Springer Proceedings in Physics 199

Mohamed Belhaq *Editor*

Recent Trends in Applied Nonlinear Mechanics and Physics

Selected Papers from CSNDD 2016

Springer

Springer Proceedings in Physics

Volume 199

The series Springer Proceedings in Physics, founded in 1984, is devoted to timely reports of state-of-the-art developments in physics and related sciences. Typically based on material presented at conferences, workshops and similar scientific meetings, volumes published in this series will constitute a comprehensive up-to-date source of reference on a field or subfield of relevance in contemporary physics. Proposals must include the following:

- name, place and date of the scientific meeting
- a link to the committees (local organization, international advisors etc.)
- scientific description of the meeting
- list of invited/plenary speakers
- an estimate of the planned proceedings book parameters (number of pages/articles, requested number of bulk copies, submission deadline).

More information about this series at http://www.springer.com/series/361

Mohamed Belhaq
Editor

Recent Trends in Applied Nonlinear Mechanics and Physics

Selected Papers from CSNDD 2016

Springer

Editor
Mohamed Belhaq
University Hassan II - Casablanca
Casablanca
Morocco

ISSN 0930-8989 ISSN 1867-4941 (electronic)
Springer Proceedings in Physics
ISBN 978-3-319-63936-9 ISBN 978-3-319-63937-6 (eBook)
https://doi.org/10.1007/978-3-319-63937-6

Library of Congress Control Number: 2017951414

Printed on acid-free paper

This Springer imprint is published by Springer Nature
The registered company is Springer International Publishing AG
The registered company address is: Gewerbestrasse 11, 6330 Cham, Switzerland

Preface

This book presents selected contributions from the 4th International Conference on Structural Nonlinear Dynamics and Diagnosis in the most active current lines of recent advanced research in the field of nonlinear mechanics and physics. A wide audience of scientists in this field may have an advantage of the material presented in this book proceeding. The book includes fifteen chapters contributed by outstanding scientists covering various aspects of applications, including road tankers dynamics and stability, simulation of abrasive wear, energy harvesting, modeling and analysis of flexoelectric nanoactuator, periodic Fermi–Pasta–Ulam problem, nonlinear stability in Hamiltonian systems, nonlinear dynamics of rotating composite, nonlinear vibrations of a shallow arch, extreme pulse dynamics in mode-locked lasers, localized structures in a photonic crystal fiber resonator, nonlinear stochastic dynamics, linearization of nonlinear resonances, hysteresis across different material scales, treatment of a linear delay differential equation, and fractional nonlinear damping. Researchers and engineers interested in challenges posed by nonlinearities in the development of the topics considered in the book will find here an outstanding introduction.

Casablanca, Morocco — Mohamed Belhaq

Contents

Contributors

Nail Akhmediev Optical Sciences Group, Research School of Physics and Engineering, The Australian National University, Acton, Australia

E. Averlant Département de Physique, Faculté des Sciences, Université Libre de Bruxelles (U.L.B.), Bruxelles, Belgium; Brussels Photonics Team, Department of Applied Physics and Photonics (B-PHOT TONA), Vrije Universiteit Brussels, Brussels, Belgium

L. Bahloul Laboratoire of Instrumentation, University of Sciences and Technology Houari Boumediene (USTHB), Bab Ezzouar, Algeria

José M. Balthazar Mechanical Engineering Division Research on Nonlinear Dynamics, Chaos and Control, Aerospace Science and Technology Department, Aeronautics Institute of Technology, Praça Mal al Eduardo Gomes 50, Vila das Acácias, São José dos Campos, São Paulo, Brazil

José Manoel Balthazar Instituto Tecnológico de Aeronáutica, São José dos Campos, Brazil

Sourour Baroudi Applied Mechanics and Systems Research Laboratory, Tunisia Polytechnic School, University of Carthage, La Marsa, Tunisia

Florian Beck Institute of Engineering and Computational Mechanics, University of Stuttgart, Stuttgart, Germany

Mohamed Belhaq University Hassan II - Casablanca, Casablanca, Morocco; Laboratory of Renewable Energy and Dynamics of Systems, Faculty of Sciences Ain Chock, University Hassan II Casablanca, Maarif, Casablanca, Morocco

Roelof Bruggeman Mathematisch Instituut, Utrecht, Netherlands

Biagio Carboni Department of Structural and Geotechnical Engineering, Sapienza University of Rome, Rome, Italy

Wonkeun Chang Optical Sciences Group, Research School of Physics and Engineering, The Australian National University, Acton, Australia

L. Cherbi Laboratoire of Instrumentation, University of Sciences and Technology Houari Boumediene (USTHB), Bab Ezzouar, Algeria

Abdelbassit Chtouki Laboratory of Renewable Energy and Dynamics of Systems, Faculty of Sciences Ain Chock, University Hassan II Casablanca, Maarif, Casablanca, Morocco

Americo Cunha Jr Universidade do Estado do Rio de Janeiro, Rio de Janeiro, Brazil

Peter Eberhard Institute of Engineering and Computational Mechanics, University of Stuttgart, Stuttgart, Germany

Jorge Luis Palacios Felix Universidade Federal da Fronteira Sul, Chapecó, Brazil

Giuseppe Habib Budapest University of Technology and Economics, Budapest, Hungary

Mustapha Hamdi Faculty of Sciences and Technology-Al Hoceima, University Mohammed I Oujda, Al-Hoceima, Morocco

A. Hariz Laboratoire of Instrumentation, University of Sciences and Technology Houari Boumediene (USTHB), Bab Ezzouar, Algeria

Raouf A. Ibrahim Department of Mechanical Engineering, Wayne State University, MI, Detroit, USA

Ahmed Jemai Applied Mechanics and Systems Research Laboratory, Tunisia Polytechnic School, University of Carthage, La Marsa, Tunisia

Gaetan Kerschen University of Liege, 1, Chemin des Chevreuils, Liege, Belgium

Walter Lacarbonara Department of Structural and Geotechnical Engineering, Sapienza University of Rome, Rome, Italy

Faouzi Lakrad Laboratory of Renewable Energy and Dynamics of Systems, Faculty of Sciences Ain Chock, University Hassan II Casablanca, Maarif, Casablanca, Morocco

Giulia Lanzara Department of Engineering, University of RomeTre, Rome, Italy

Jaroslaw Latalski Department of Applied Mechanics, Lublin University of Technology, Lublin, Poland

A. Makhoute Physique du Rayonnement et des Interactions Laser-Matière, Faculté des Sciences, Université Moulay Ismail, Zitoune, Meknès, Morocco

Peter A. Meleshenko Communication Department, Zhukovsky–Gagarin Air Force Academy, Voronezh, Russia

Fehmi Najar Applied Mechanics and Systems Research Laboratory, Tunisia Polytechnic School, University of Carthage, La Marsa, Tunisia

Richard H. Rand Department of Mathematics, Department of Mechanical & Aerospace Engineering, Cornell University, Ithaca, NY, USA

Si Mohamed Sah Nanostructure Physics, KTH Royal Institute of Technology Stockholm, Stockholm, Sweden

Mikhail E. Semenov Geophysical Survey of Russia Academy of Sciences, Obninsk, Russia

Andrey M. Solovyov Geophysical Survey of Russia Academy of Sciences, Obninsk, Russia; Digital Technologies Department, Voronezh State University, Universitetskaya st. 1, Voronezh, Russia; Applied Mathematics and Mechanics Department, Voronezh State Technical University, Voronezh, Russia

José M. Soto-Crespo Instituto de Óptica, C.S.I.C., Madrid, Spain

Michela Talò Department of Structural and Geotechnical Engineering, Sapienza University of Rome, Rome, Italy

M. Tlidi Département de Physique, Faculté des Sciences, Université Libre de Bruxelles (U.L.B.), Bruxelles, Belgium

Ferdinand Verhulst Mathematisch Instituut, Utrecht, Netherlands

Peter Vouzas Optical Sciences Group, Research School of Physics and Engineering, The Australian National University, Acton, Australia

Jerzy Warminski Department of Applied Mechanics, Lublin University of Technology, Lublin, Poland

Chapter 1
Road Tanker Dynamics Interacting with Liquid Sloshing Dynamics

Raouf A. Ibrahim

Abstract Research activities pertaining to road tankers dynamics and stability may be classified into three groups. These are liquid sloshing dynamics in moving containers, trucks dynamics carrying solids, and dynamic coupling of liquid-vehicle systems. The most serious problems of road tankers is rollover accidents due to lateral acceleration during vehicle maneuvers. For this reason many countries have imposed regulations for the minimum threshold of vehicle lateral acceleration during its maneuvers. This threshold value is usually estimated on quasi-dynamic approach which assumes that the liquid free surface takes a position orthogonal to the total body forces due to gravity and lateral acceleration. The modal analysis of liquid free surface on common tank cross-section geometries, such as horizontal circular, elliptic and generic cross section is presented together with the corresponding equivalent mechanical models. In particular, the Trammel equivalent pendulum received extensive research activities and the main results are discussed. The most difficult problem of road tankers is the coupling dynamics of liquid and vehicle dynamics under different conditions such as braking and lateral acceleration. In view of its complex nature, computer numerical simulations have been developed.

1.1 Introduction

A road tanker is a vehicle that has a tank whose capacity is greater than $3\,m^3$ and is structurally attached to (or an integral part of) the vehicle. Aside from its own liquid fuel, these vehicles usually transport non-hazardous liquids such as water and milk, or hazardous liquids such as gasoline, liquefied petroleum gas (LPG) and anhydrous ammonia. The hydrodynamic loads generated by the liquid sloshing in road tankers can have a significant influence on their driving dynamics and stability. In particular, lateral fluid sloshing during turning and sudden lane change maneuvers is the main cause for low rollover threshold while longitudinal fluid sloshing due to braking

R.A. Ibrahim (✉)
Department of Mechanical Engineering, Wayne State University, Detroit, MI 48098, USA
e-mail: ibrahim@eng.wayne.edu

M. Belhaq (ed.), *Recent Trends in Applied Nonlinear Mechanics and Physics*,
Springer Proceedings in Physics 199, https://doi.org/10.1007/978-3-319-63937-6_1

or accelerating maneuvers can cause yaw instability or loss of directional control. Liquid sloshing in a highway maneuver can lead to lateral and roll instabilities, decreased controllability/maneuverability, and increased stress on tank structures. This results in serious accidents and fireballs of fuel tanks. The problem has drawn the attention of designers and engineers to examine different aspects of road tankers' safety. The literature showed that considerations were given to predicting the liquid slosh in various containers and vehicle stability based upon simplified mechanical models or computational fluid dynamics codes. The study of dynamic interactions of the liquid motion and vehicle stability is thus very important and is not a simple task.

The most serious problem of road tankers is roll instability. Transport Canada's Transport Dangerous Goods Directorate documented a database of crashes involving a vehicle carrying dangerous goods [17]. During the period 1990–1998 there were 810 (43%) of 1,874 incidents resulted in rollover, and 671 (83%) of the 810 vehicles that rolled over were tank trucks [123]. Tilt tests to determine the rollover threshold and rollover characteristics of tank truck configurations were reported by Billing and Patten [17]. A computer simulation was used to project the lowest roll threshold of each vehicle, with tanks full and loaded to its allowable gross weight. The main reason that liquid tankers possess an elliptical cross-section, rather than circular cross-section, is due to the fact the elliptic shape lowers the center of gravity resulting in increasing the roll stability. Many countries introduced restrictions on the height of the center of gravity for non-pressurized flammable liquid tankers. This is why many studies were devoted to develop optimum design of tank cross-section geometry.

Road tanker dynamics is based on three basic problems. These are liquid sloshing dynamics in typical road tank geometries, rollover dynamics and stability, and interaction of road tankers with liquid sloshing during vehicle maneuvers. Thses three major problems will be discussed in the next sections.

1.2 Sloshing Modal Analysis

The theory of liquid sloshing dynamics in partially filled containers is based on developing the fluid field equations, estimating the fluid free surface motion, and the resulting hydrodynamic forces and moments. The boundary value problem is usually solved for modal analysis and the dynamic response characteristics to external excitations. The modal analysis of a liquid free surface motion in a partially filled container constitutes estimating the natural frequencies and the corresponding mode shapes. The knowledge of the natural frequencies is essential in the design process of liquid tanks. The natural frequencies of the free liquid surface appear in the combined boundary condition (kinematic and dynamic) rather than in the fluid continuity (Laplace's) equation. Explicit solutions are possible only for a few special cases such as upright circular cylindrical and rectangular containers. This section deals with the sloshing natural frequencies and free surface mode shapes in circular

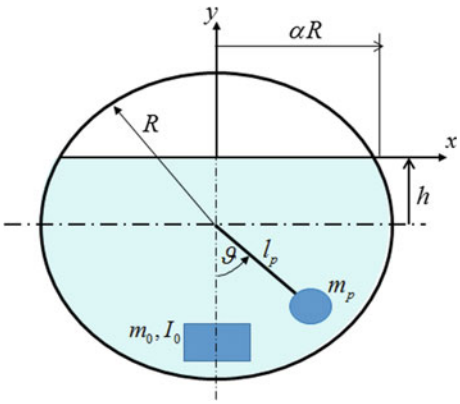

Fig. 1.1 Schematic diagram of a horizontal circular container of radius R and length L, showing the equivalent mechanical model of a simple pendulum and rigid mass

and elliptic cross-section horizontal containers as they are the most common used for road tanker containers.

1.2.1 Circular Horizontal Cylinders

Lamb [59] presented an energy approach to determine the natural frequency of the first transverse mode of liquid free surface in a half-filled horizontal cylinder, i.e., $h = -R$, see Fig. 1.1. The following expression for the kinetic energy T, of the fluid free surface experiencing small oscillations of frequency ω was obtained,

$$T = \frac{1}{2}\pi\rho R^4 \left(\frac{4}{\pi^2} - \frac{1}{4}\right)\omega^2 \tag{1.1}$$

From this expression one can write the effective mass moment of inertia of the liquid about the center of the cylinder

$$I_{o(eff)} = \pi\rho R^4 \left(\frac{4}{\pi^2} - \frac{1}{4}\right) \tag{1.2}$$

which is much less than the moment of inertia of the frozen liquid. The potential energy, U, is

$$U = \frac{1}{3}\rho g R^3 \theta^2 \tag{1.3}$$

Equating the maximum kinetic energy to the maximum potential energy, and assuming sinusoidal oscillation, gives the natural frequency of the first sloshing mode

$$\omega_1^2 = \frac{8\pi}{48 - 3\pi^2}\frac{g}{R} = 1.36656\frac{g}{R} \tag{1.4}$$

Budiansky [26] formulated the boundary value problem of free liquid surface asymmetric motion in two-dimensional cross-section of a horizontal canal. In view of the geometrical symmetry, the natural modes of the free surface involve free surface displacements that are either symmetric or anti-symmetric. The analysis was restricted for the anti-symmetric modes since the symmetric modes are not generated under lateral excitation. For small liquid free surface oscillation, the mode shape may be expressed by the planar shape. Introducing the non-dimensional natural frequency parameter, $\lambda_n = \omega_n^2 R/g$, Budiansky [26] obtained the first mode natural frequency by the expression

$$\lambda_1 \approx \frac{1}{3}\left[\frac{2}{\pi} - \frac{\pi}{8}\right] = 1.367 \rightarrow \omega_1 = 1.169\sqrt{g/R} \tag{1.5}$$

This result is identical to the one reported by Lamb and given by relation (1.4). The first three modes and frequencies were evaluated numerically for different values of fluid depth ratio, h/R. The numerical results are listed in Table 1.1 and plotted in Fig. 1.2 by solid curves as a function of the fluid depth ratio, h/R. It is seen that the fundamental mode has its lowest frequency in the nearly empty state, whereas the minimum frequency of a given higher mode appears to occur slightly below the half full condition. As the fluid depth increases, the natural frequencies tend to shift to more closely packed spectra and the ratio λ_{n+1}/λ_n decreases monotonically with increasing depth ratio. McCarty and Stephen [66] obtained some numerical experimental results of the dependence of the liquid natural frequency parameter $\omega_n\sqrt{R/g}$ on the depth ratio, $h/2R$. Fig. 1.3a, b show this dependence for transverse and longitudinal (longitudinal tank length $= L$) sloshing modes, respectively.

A two-dimensional nonlinear random sloshing problem was studied by Wang and Khoo [117] who considered the fully nonlinear wave velocity potential theory based on the finite element method. A rectangular container filled with liquid sub-

Table 1.1 Liquid free-surface eigenvalues in circular canal for different fluid depth [26]

h/R	α	$\alpha\lambda_1$	$\alpha\lambda_2$	$\alpha\lambda_3$	λ_1	λ_2	λ_3
−1.0	0.0	0.0	0.0	0.0	1.0	6.0	15.0
−0.8	0.6	0.627	3.23	6.51	1.045	5.38	10.85
−0.6	0.8	0.879	3.98	7.3	1.099	4.97	9.13
−0.4	0.917	1.068	4.34	7.63	1.165	4.74	8.33
−0.2	0.980	1.224	4.56	7.82	1.249	4.65	7.99
0.0	1.0	1.360	4.70	7.96	1.360	4.70	7.96
0.2	0.98	1.482	4.81	8.06	1.513	4.91	8.23
0.4	0.917	1.596	4.89	8.15	1.742	5.34	8.89
0.6	0.8	1.706	4.97	8.22	2.13	6.22	10.23
0.8	0.6	1.822	5.05	8.30	3.04	8.42	13.84
1.0	0.0	2.018	5.20	8.44	∞	∞	∞

jected to specified horizontal random oscillations is studied. Both wave elevation and hydrodynamic force are obtained. The spectra of random waves and forces were determined together with the effects of the peak frequencies and spectral width of the specified spectrum used for the generation of the random oscillations. It was found that the energy mainly concentrates at the natural frequencies of the container and is dominant at the i-th order natural frequency when the peak frequency is close to the i-th order natural frequency. Some results are compared between the fully nonlinear solutions, the linear solutions and the linear plus second-order solutions. A numerical scheme for the analysis of liquids sloshing in horizontal cylindrical rigid containers was developed by Dai and Xu [32]. The governing equations of the liquid were transformed via three continuous coordinate transformations. The efficiency of the proposed method was demonstrated by numerical simulations using the finite difference method for two-dimensional circular containers and three-dimensional cylindrical containers.

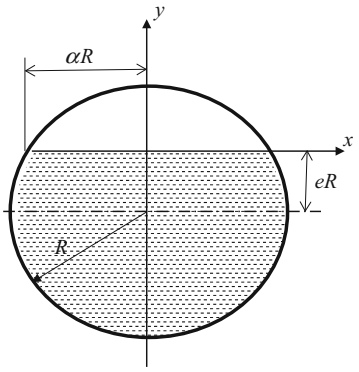

1.2.2 Elliptic Horizontal Tanks

Natural frequencies and modes of oscillation of liquids in partially filled axisymmetric ellipsoidal tanks were estimated using variational principle by Rattayya [92]. The liquid free surface natural frequencies of transverse sloshing modes in a half-filled non-deformable horizontal cylindrical container of elliptical cross-section were determined by Hasheminejad and Aghabeigi [47] based on the linear potential theory. The analysis was performed for the cases of the presence and absence of inflexible horizontal longitudinal side baffles of arbitrary extension positioned at the free liquid surface. The effects of surface-piercing or bottom-mounted vertical baffles on two-dimensional liquid sloshing characteristics in a half-full non-deformable horizontal cylindrical container of elliptical cross-section were reported by Hasheminejad and Aghabeigi [49]. The effects of vertical baffles on the hydrodynamic pressure mode shapes and sloshing flows were examined through appropriate two-dimensional images. The surface-piercing vertical baffle was demonstrated to be an effective tool in reducing the antisymmetric sloshing frequencies, especially for lower aspect ratio

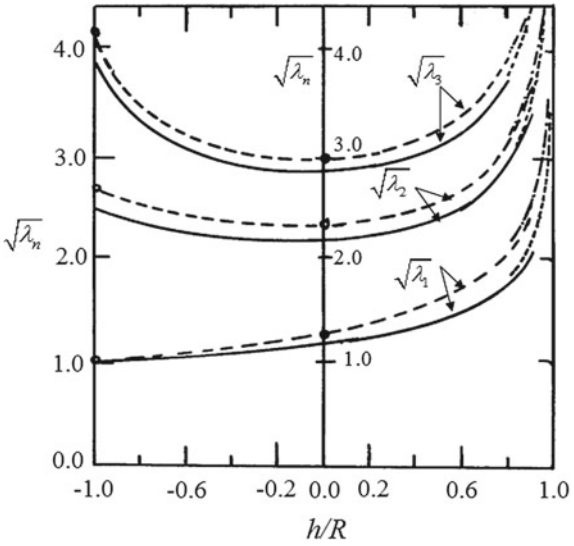

Fig. 1.2 Dependence of the liquid natural frequencies on the liquid depth ratio, h/R, for circular horizontal cylinder (*solid*) and spherical tank (*dashed*). Budiansky [26]

tanks and higher modes. On the other hand, the bottom-mounted baffle was shown to have a great influence on the higher antisymmetric slosh modes only when its tip approaches the liquid free surface. The linear theory of surface gravity–capillary waves in cylindrical containers with an elliptical cross-section was presented by Oliva-Leyva [71]. General solutions for the velocity potential and the free surface amplitude were given in terms of Mathieu functions. The numerical results showed the dependence of the natural frequencies on the fluid properties and the eccentricity of the container cross-section. The frequency shift and the wall damping ratio due to viscous dissipation in the Stokes boundary layers were evaluated numerically.

Romero et al. [94] measured the natural frequencies of three tanks of different cross-sections as shown in Fig. 1.4.The horizontal length (perpendicular to the page of each tank was 10 cm, and their cross-section dimensions were 12.5 cm radius for the circular tank (Fig. 1.4a), with semi-major and minor axes 15.1 cm and 11 cm, respectively, for the elliptic tank (Fig. 1.4b), while Fig. 1.4c shows the generic tank proposed by Kang et al. [53–55]. The generic tank periphery is obtained by composing a number of circular arcs symmetric about the vertical axis. This allows design flexibility in view of the roll stability limits than the conventional tank shapes. These tanks in their horizontal position will have variable fluid depth contrary to the uniform constant depth in a rectangular tank. Romero et al. [94] considered an average fluid depth, $\bar{h}$, so that a nonrectangular tank can be replaced by an equivalent rectangular tank. This approximation was found to result in an error within the range of 5–10%, depending on the fluid depth. For example, Fig. 1.5 shows comparison of the fluid free surface natural frequencies in a circular tank with deep-water and

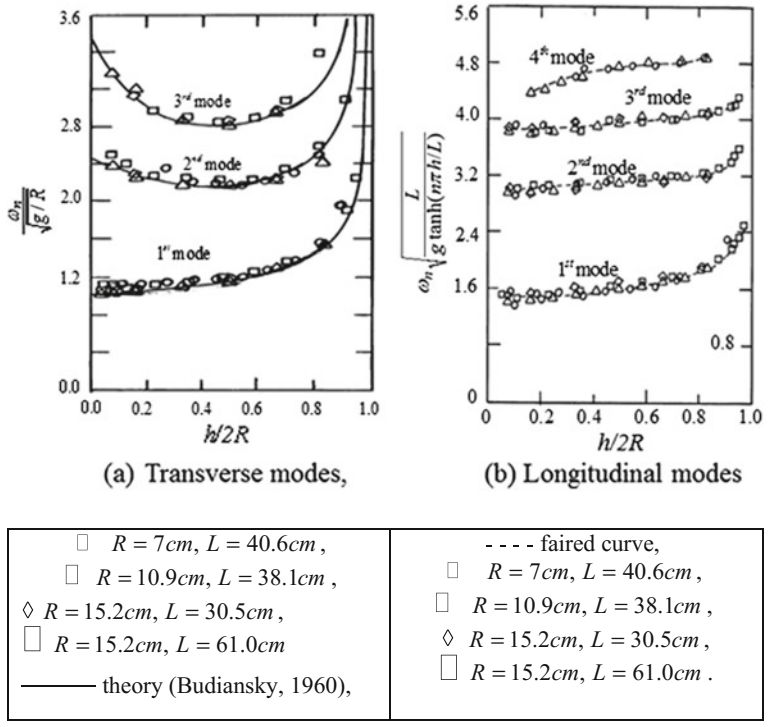

Fig. 1.3 Dependence of liquid natural frequency on depth ratio for transverse and longitudinal modes in circular canal [66]

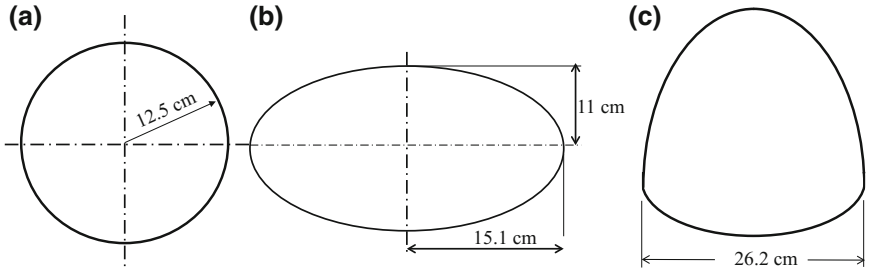

Fig. 1.4 Three different tank cross-sections: **a** circular, **b** elliptic, and **c** generic

constant (finite) depth approximation. It is seen that the deep-water approximation is only adequate for the higher fill levels. Nevertheless, the error is less than 10% for fill levels between 50 and 62.5%, and less than 5% for fills above 62.5% fill.

Figures 1.6, 1.7 and 1.8 show the measured and approximate natural frequencies for tanks of circular, elliptical, and generic cross-sections, respectively. The theoretical curve in each case represents the approximation of constant depth (average depth

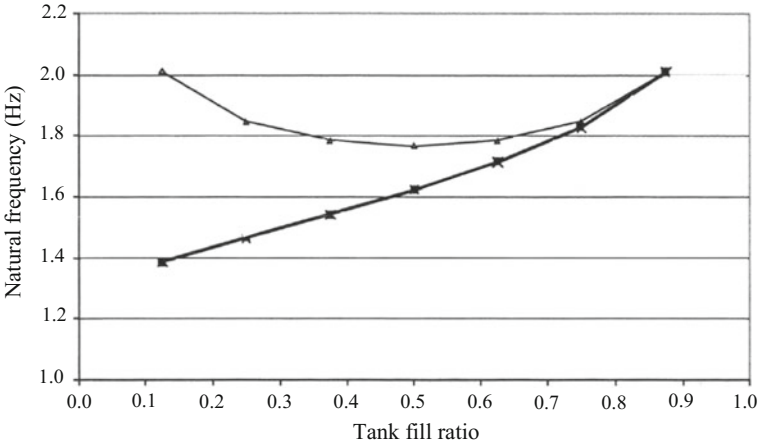

Fig. 1.5 Dependence of natural frequency on tank fill ratio in a circular tank cross-section and comparison deep-water (▲) and constant (**x**) depth approximations. Romero et al. [94]

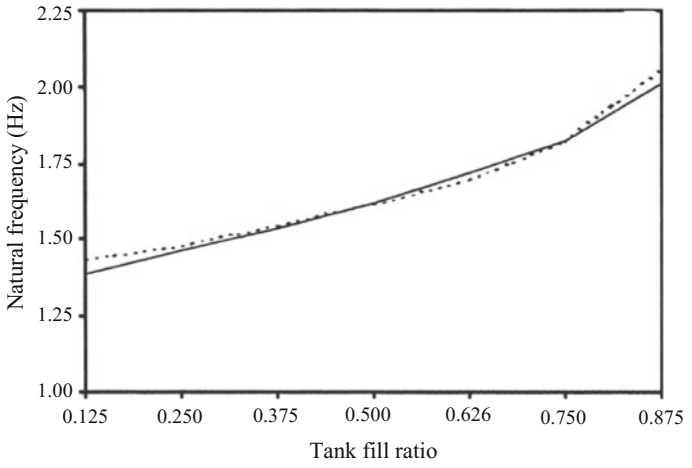

Fig. 1.6 Natural frequencies of liquid in tanks of circular cross-section of diameter 0.25 m according to …. measured and —— approximate results. Romero et al. [94]

over the cross-section). For the circular tank (Fig. 1.6), it is seen that the approximation accurately predicts the experimental results, with a maximum error of about 5% at the lowest fill level. For the elliptical tank, an improved approximation accounting for the depth variation is also included in Fig. 1.7. The constant depth approximation tends to underestimate the natural frequency, with the error decreasing as the fill level increases. The maximum error is almost 10%, which is probably acceptable in practice in most cases. For comparison purposes of the natural frequencies of the three cross-section tanks, Romero et al. [94] plotted the dependence of the natural

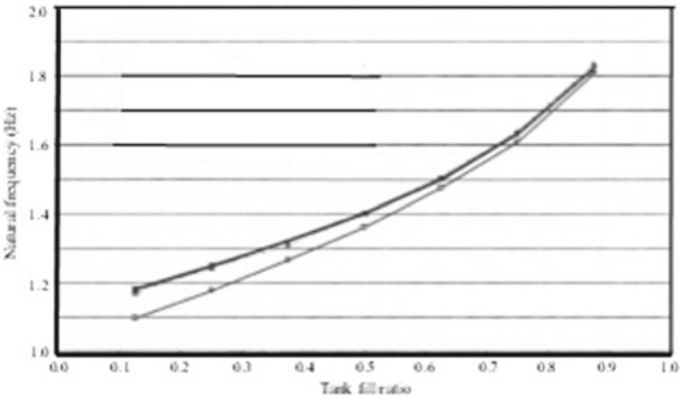

Fig. 1.7 Dependence of the fluid natural frequency on the tank fill ratio as measured (—×—) and constant depth approximation (□—□) and variable depth approximation (— — Δ — —), for a tank of elliptic cross-section of semi-axes 15.1cm × 11cm. Romero et al. [94]

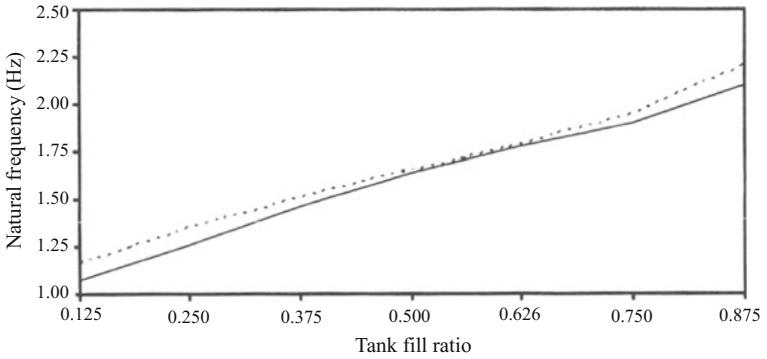

Fig. 1.8 Dependence of the fluid natural frequency on the tank fill ratio as measured (- - - -) and predicted (——) for a tank of generic cross-section of base 26.2 cm. Romero et al. [94]

frequencies on the tank fill ratio as shown in Fig. 1.9 based on the theoretical estimates of constant depth approximation. It is seen that the elliptic tank has the lowest natural frequency over the entire range of the tank fill ratio. The generic tank, on the other hand has the most rapidly increase of the natural frequency with the tank fill ratio. The circular tank has slightly lower natural frequencies for higher fill levels than the generic tank.

A semi-analytical mathematical model was developed by Hasheminejad and Aghabeigi [48] who studied the transient liquid sloshing characteristics in half-full horizontal cylindrical containers of elliptical cross-section subjected to arbitrary lateral external acceleration. A ramp-step function is used to simulate the lateral acceleration excitation during an idealized turning maneuver. The problem solution is achieved by employing the linear potential theory in conjunction with conformal

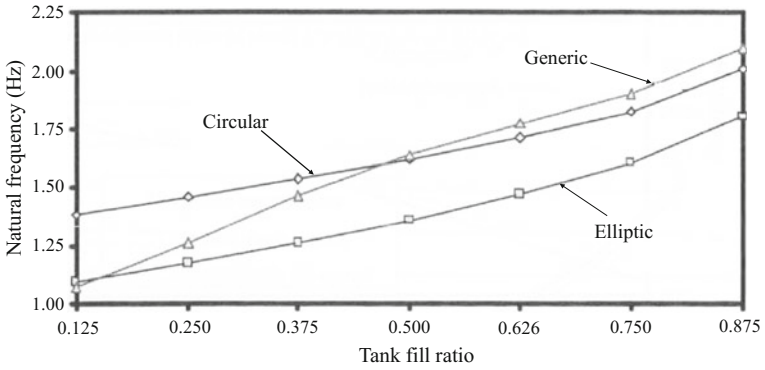

Fig. 1.9 Dependence of the fluid natural frequencies on the tank fill ratio for the circular, elliptic, and generic tank cross-sections as predicted for the scale model tanks. Romero et al. [94]

mapping were employed to yield linear systems of ordinary differential equations, which were truncated and then solved numerically by implementing Laplace transform technique followed by Durbin's numerical inversion scheme. The effects of tank aspect ratio, excitation input time, and baffle configuration on the resultant sloshing characteristics were studied. The fluid structure interaction in an elliptical tank was considered by Brar and Singh [25] who studied the movement of fluid in the tank using simulation and experimental tests. The pressure exerted by the fluid on the walls of tank was estimated over a certain period of time. The dynamic response of baffled liquid storage tank was studied to determine the influence of location and shapes of baffles under external excitation. Different baffle configurations were examined and role of combination of horizontal and vertical baffles were found to be significant in controlling the sloshing.

1.2.3 Equivalent Mechanical Models

1.2.3.1 Principles of Equivalent Models

The liquid hydrodynamic pressure in rigid containers has two distinct components. One component is directly proportional to the acceleration of the tank and is caused by part of the fluid moving in unison with the tank. The second, known as "convective" pressure, experiences sloshing at the free surface. A realistic representation of the liquid dynamics inside closed containers can be approximated by an equivalent mechanical system. The equivalence is taken in the sense of equal resulting forces and moments acting on the tank wall. By properly accounting for the equivalent mechanical system representation of sloshing, the problem of overall dynamic system behavior can be formulated more simply. For linear planar liquid motion, one

can develop equivalent mechanical models in the form of a series of mass-spring dashpot systems or a set of simple pendulums. For nonlinear sloshing phenomena, other equivalent models such as spherical or compound pendulum may be developed to emulate rotational and chaotic sloshing. The principles for constructing a mechanical model are based on the following conditions:

1. The equivalent masses and moments of inertia must be preserved.
2. The center of gravity must remain the same for small oscillations.
3. The system must possess the same modes of oscillations and produce the same damping forces.
4. The force and moment components under certain excitation must be equivalent to that produced by the actual system.

Bauer [13] developed an equivalent mechanical model consisting of a set of mass-spring-dashpot systems to describe the liquid motion in rectangular and upright circular cylindrical containers. The equivalent model possesses the same liquid natural frequencies as well as sloshing forces and moments exerted upon the various vehicles. Slibar and Troger [106] employed similar equivalent mechanical models to study the effect of liquid sloshing on the lateral wheel-load transfer of a tractor-semitrailer-system under periodic steering. Ranganathan et al. [90] developed an equivalent mass-spring system for liquid sloshing in a three-dimensional horizontal circular cylindrical tank by a summation technique to study straight-line braking performance of a tractor-semitrailer tank vehicle. A partially-filled tank was divided into a number of rectangular elements and parameters of equivalent system were calculated for each individual element based on the linear theory. The parameters of equivalent mass-spring system for entire cylindrical tank were then computed by summation of parameters calculated for each rectangular element. The proposed model was validated in terms of fundamental frequency versus liquid fill level plot obtained from experimental results of McCarty and Stephens [66].

A computational method equivalent to the method generated by Kobayashi et al. [58] was used by Xu et al. [125] who studied the ride quality of partially-filled compartmented tank trucks in presence of liquid sloshing effect. The liquid sloshing effect was modeled by a linear mass-spring-dashpot system for the pitch motion. A spatial and mechanical simulation model developed by Stedtnitz and Appel [109] who modeled the liquid sloshing by the superposition of a spring-mass model describing longitudinal sloshing and a pendulum model representing lateral sloshing in tank trucks.

Khandelwal and Nigam [57] employed the pendulum analogy including one fixed mass and one pendulum mass representing the fundamental mode of sloshing to simulate the liquid sloshing in a rectangular railway wagon moving on a random uneven railway track with constant longitudinal acceleration. The dynamic response of vehicle-liquid system was determined by two models: a heave model and a heave-pitch model. The model parameters were calculated for harmonic vertical acceleration assuming small and stable displacement of free liquid surface. The effect of damping was also considered by a viscous damper attached to the pendulum. Ranganathan et al. [86] combined a pendulum equivalent model of liquid sloshing in

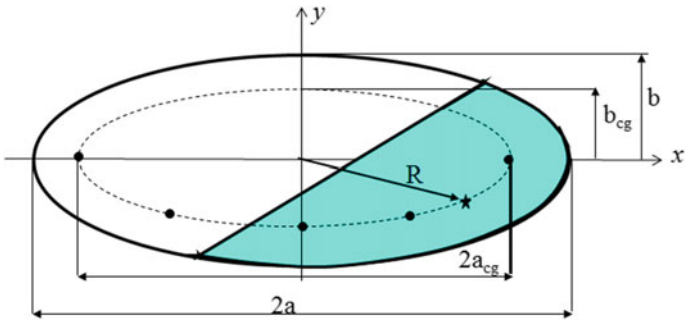

Fig. 1.10 Locus of the center of mass of the shown liquid volume in an elliptic horizontal container

two-dimensional circular tanks subjected to lateral excitation to a three-dimensional vehicle model to investigate the directional response of tank vehicle during steady state maneuver. The entire vehicle was simulated by considering five degrees of freedom for sprung mass and two degrees of freedom including roll and vertical motion for unsprung mass.

The pendulum model was used for the simulation of liquid sloshing in road tankers by Aliabadi et al. [1]. The simulation results were compared with those predicted by the finite element model for sloshing of liquids in tanker trucks. In the finite element model, the full Navier–Stokes equations were solved for two fluids to obtain the location and motion of the free surface. The comparison is for the non-dimensional radial force as a function of time exerted on the tanker during turning showed that both methods have relatively good agreements when the liquid inside the tanker is very low. However, the difference between both the amplitude and frequency of sloshing was found significant when there is a significant amount of liquid inside the tanker (near half-fill). Godderidge et al. [44] presented and validated a modified pendulum method by simulating partially filled rectangular tanks periodically excited at frequencies near the first sloshing mode. Results of the model confirmed computational dynamic methods typically within 5–10% for both magnitude and frequency.

1.2.3.2 Equivalent Trammel Pendulum Modeling

The center of gravity of a fluid volume in an elliptic horizontal container was found to follow an elliptical contour parallel to the tank wall as shown in Fig. 1.10. The tank semi major and minor axes are designated by a and b, respectively, while the corresponding semi axes of fluid center of mass contour are a_{cg} and b_{cg}. For a given orientation fluid volume its center of mass is located at distance R from the tank center. Salem [99] determined the dependence of the fluid center of mass ratio R/b on the fill volume percentage for different values of ellipse semi-axes ratio as shown in Fig. 1.11.

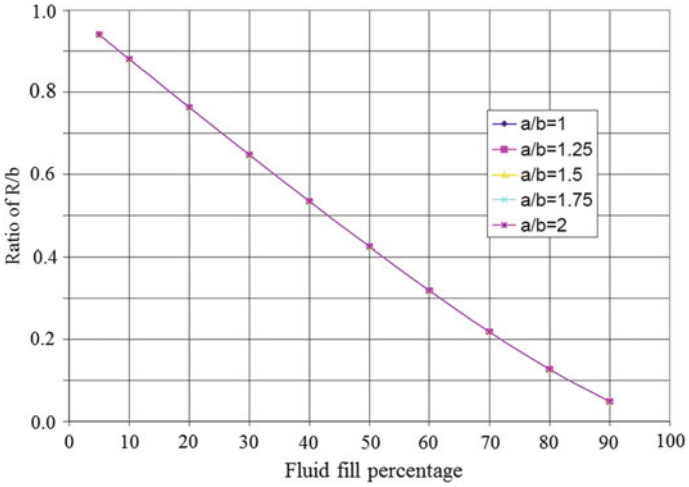

Fig. 1.11 Dependence of the location of fluid center of mass ratio R/b on the fill volume percentage for different values of ellipse semi-axes ratio. Salem [99]

In studying the rollover stability of partially filled heavy-duty elliptical tankers Gautam et al. [41] used a Trammel pendulum model to simulate the lateral motion of the fluid. The selection of the appropriate pendulum parameters was based on matching the pendulum dynamic effects with fluid sloshing dynamic effects obtained using finite element fluid models [99–101]. It was found that the Trammel pendulum model produced up to 20% more lateral forces and moments than the fluid models (FLUENT and LSDyna 3D) beyond the linear range. The numerical simulation of free-surface prediction using commercial computational fluid dynamics codes such as FLUENT (2005), has allowed the incorporation of sloshing into the design stage of tanker geometry [28]. The Arbitrary Eulerian-Lagrangian method, as embodied in MSC-Dytran is of interest when fluid-structure interaction is concerned. Sloshing in the tank may be controlled by incorporating baffles, and the effectiveness highly depends on the shape, the location, and the number of baffles inside a tank. Due to the complexities associated with the sloshing phenomenon, the CAE simulation is a desired method to meet the design intent, and shorten the development time. Several CAE codes were employed to simulate sloshing, such as, MSC-Dytran, Fluent, and LSDYNA.

The Trammel pendulum model shown in Fig. 1.12 possesses an elliptic swing trajectory, which approximately simulates the liquid sloshing in a partially filled elliptic horizontal container. The mass of the pendulum, m_p, is equivalent to the mass of the liquid first sloshing mode while m_f is the fluid fixed mass which moves in unison with the rigid container, such that $m_m + m_f = M$= the total liquid mass inside the container. The semi-major and minor axes of the Trammel pendulum are a_p and b_p, respectively. As the pendulum swings, with angle θ, its trajectory is kept elliptic by virtue of sliding on the two movable supports A and B.

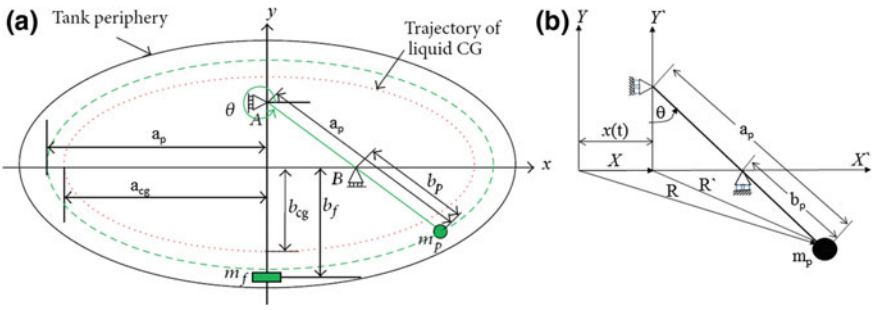

Fig. 1.12 Modeling of liquid by Trammel pendulum of mass m_p and total length a_p and minor axis b_p moving on sliding supports at A and B. **a** The pendulum angle θ is measured counterclockwise from the horizontal [61], **b** the pendulum angle θ is measured counterclockwise from the vertical axis [99]

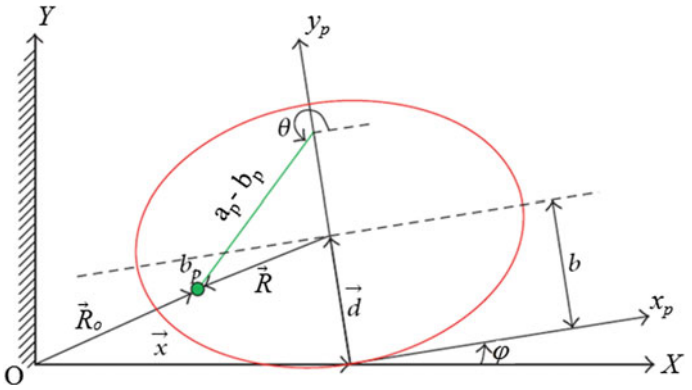

Fig. 1.13 Trammel pendulum in moving coordinate represented by the tank roll angle ϕ and lateral displacement $\vec{x}$. Li et al. [61]

The equation of motion of Trammel pendulum in fixed coordinates (inertia frame) was derived by Li et al. [61]

$$\ddot{\theta}\left(a_p^2 \sin^2\theta + b_p^2 \cos^2\theta\right) + \frac{1}{2}\dot{\theta}^2\left(a_p^2 - b_p^2\right)\sin 2\theta + g b_p \cos\theta = 0 \tag{1.6}$$

Note that both a_p and b_p depend on the tank fill ratio. Also the ratio of semi-axes is constant, i.e.,

$$\frac{a}{b} = \frac{a_{cg}}{b_{cg}} = \frac{a_p}{b_p}.$$

In terms of moving coordinates, represented by the roll angle, ϕ and lateral motion x, shown in Fig. 1.13, the equation of motion of the Trammel pendulum was obtained in the form:

$$\ddot{\theta}\left(\mathrm{a}_p^2\sin^2\theta + b_p^2\cos^2\theta\right) + \ddot{\phi}\left(\mathrm{a}_p b_p + \mathrm{a}_p b\sin\theta\right) + \dot{\phi}^2\left[\frac{1}{2}\sin 2\theta\left(\mathrm{a}_p^2 - b_p^2\right) - b_p b\cos\theta\right]$$

$$+\frac{1}{2}\dot{\theta}^2\left(a_p^2 - b_p^2\right)\sin 2\theta + g\left(b_p\cos\theta\cos\phi - \mathrm{a}_p\sin\theta\sin\phi\right) = \ddot{x}\left(\mathrm{a}_p\sin\theta\cos\phi + b_p\cos\theta\sin\phi\right) \tag{1.7}$$

On the other hand, the equation of motion in terms of the tank roll angle, ϕ, is

$$\ddot{\phi}\left[\left(b - b_p\sin\theta\right)^2 + \mathrm{a}_p^2\cos^2\theta\right] + 2\dot{\theta}\dot{\phi}\left[\frac{1}{2}\sin 2\theta\left(b_p^2 - \mathrm{a}_p^2\right) + b_p b\cos\theta\right] + \ddot{\theta}\left(\mathrm{a}_p b_p + \mathrm{a}_p b\sin\theta\right)$$

$$= \ddot{x}\left(b\cos\phi + a_b\cos\theta\sin\phi + b_p\sin\theta\cos\phi\right) \tag{1.8}$$

For the special case, when the tank is subjected only to lateral motion, x, and measuring the pendulum angle from the vertical axis counterclockwise (see Fig. 1.12b), (1.7) can be reduced to the form after setting θ by $\theta + 270^\circ$ and yields the same equation obtained by Salem [99]

$$\ddot{\theta}\left(\mathrm{a}_p^2\cos^2\theta + b_p^2\sin^2\theta\right) - \frac{1}{2}\dot{\theta}^2\left(a_p^2 - b_p^2\right)\sin 2\theta + g b_p\sin\theta = -\ddot{x}\mathrm{a}_p\cos\theta \tag{1.9}$$

Setting the righthand side to zero in (1.9), gives the free oscillation of the pendulum for small angle

$$\theta$$

$$\ddot{\theta} + \dot{\theta}^2\left(\frac{b_p^2 - a_p^2}{a_p^2}\right)\theta + \frac{g b_p}{a_p^2}\theta = 0 \tag{1.10}$$

One may notice that (1.6) through (1.10) are independent of the mass of the pendulum as known in the dynamics of simple pendulum. The linearized natural frequency of the Trammel pendulum model is given by the expression

$$\omega_{np} = \sqrt{\frac{g b_p}{a_p^2}} \tag{1.11}$$

The dependence of the Trammel pendulum natural frequency on the pendulum initial angle, θ is shown in Fig. 1.14 for different values of the tank aspect ratio as estimated by Salem [99]. It is seen that for the case of a circular cross-section, $a/b = 1.0$, the natural frequency decreases with the increase of the pendulum angle. On the other hand, the natural frequency increases gradually and peaks at a certain angle for aspect ratios more than 1. This angle is close to 90° for $a/b = 2.0$. Similar results were obtained by Zheng et al. [134] who also found that with an increase in the pendulum amplitude its oscillation becomes periodic non-harmonic and nonlinear particularly for the amplitude $\theta > 170^\circ$.

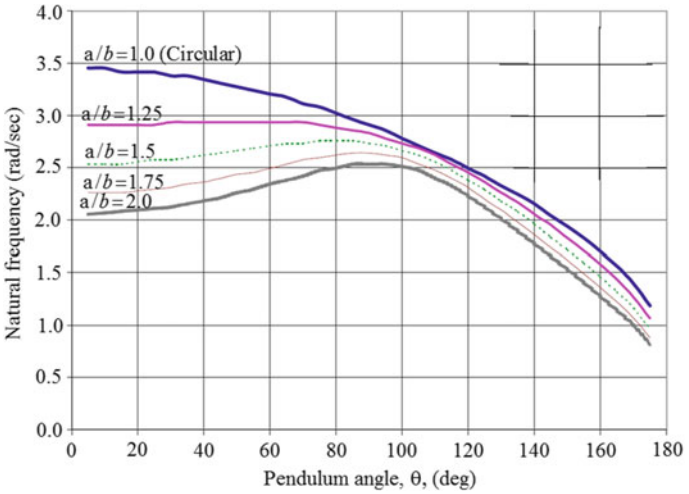

Fig. 1.14 Dependence of the Trammel pendulum natural frequency on its initial angle for different values of the tank semi-axes ratio. Salem [99]

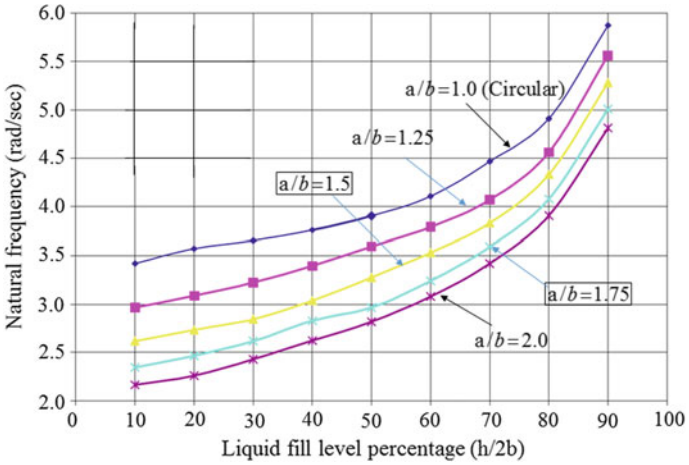

Fig. 1.15 Dependence of the fluid free surface natural frequency on the fluid fill level for a fluid volume in an elliptical tank for different values of the semi-axes ratio a/*b* at initial fluid surface angle 5° as estimated numerically by Salem [99]

Note that Bohn et al. [18] obtained another expression of the fluid natural frequency in a partially filled elliptic container in the form

$$\omega_n = \sqrt{\frac{3Ag}{2\bar{V}^3}} \tag{1.12}$$

where A is the fluid cross-section area and $\bar{V}$is half width of fluid surface at the static equilibrium position. Equation (1.12) was checked using a half-full cylindrical tank of radius R as a special case of a partially filled elliptical tank studied earlier by Budiansky [26]. For example, the fundamental frequency obtained by Rayleigh is $\omega_n = 1.1644\sqrt{g/R}$, by Lamb is $\omega_n = 0.8266\sqrt{g/R}$, by Budiansky is $\omega_n = 1.169\sqrt{g/R}$, and by Bohn et al. is $\omega_n = 1.535\sqrt{g/R}$. Salem [99] employed a finite element model for a sloshing fluid in half full cylindrical tank using LSDyna 3D and his result was close to the expression $\omega_n = 1.1\sqrt{g/R}$. Figure 1.15 shows the dependence of the fluid free surface natural frequency on the fluid fill level for a fluid volume in an elliptical tank for different values of the semi-axes ratio a/b at initial fluid surface angle 5° as estimated numerically by Salem [99].

Salem [99] and Salem et al. [101] simulated the lateral fluid sloshing in two-dimensional partly-filled elliptical containers using equivalent Trammel pendulums. The parameters of equivalent pendulum model including arms of Trammel pendulum, fixed mass and pendulum mass, and the height of fixed mass with respect to the tank base were calculated by matching of pendulum natural frequency, horizontal force component and static moment around the tank base to those calculated from finite element simulation of fluid motion. The proposed Trammel pendulum approach represented an approximation of nonlinear liquid sloshing dynamics and provided a computationally effective tool for coupled simulation of liquid sloshing and vehicle dynamics compared to computational fluid dynamics simulation of liquid sloshing. The multibody computer-aided engineering software packages DynaFlexPro (DFP) and DynaFlexPro/Tire was used by [45] to model the Trammel pendulum and the tractor and articulated tanker vehicle. The fundamental basis of selecting the appropriate pendulum parameters were obtained by matching the pendulum dynamic effects with fluid sloshing dynamic effects as predicted by finite element fluid models in the work of Salem [99]. A two-dimensional tanker model was developed and the Trammel pendulum model was integrated to study the effect of sloshing on the roll stability of heavy duty tankers. The rollover threshold of two-dimensional models ranged from 0.9 to 0.25 g.

Casasanta [27] developed mathematical models that could be utilized in MATLAB and implemented in real-time simulators to simulate the sloshing of low viscosity fluids in partially filled truck tanks to study the resulting semi-tanker truck rollover behavior. A Trammel pendulum model was adopted to simulate the fluid sloshing effects for partially filled elliptical tank of semi-tanker trucks experiencing lateral maneuvers. The Trammel pendulum model's kinematic and dynamic effects were studied and verified against fluid sloshing dynamic results obtained through finite element analysis. The sloshing model was coupled to a two-dimensional rigid body semi-tanker truck lateral dynamics model to determine the rollover stability of commercial semi-tanker trucks when performing double lane change and constant radius turn maneuvers. The rollover stability threshold of the rigid body vehicle model ranged from 0.2 to 0.8 g's, depending on the lateral maneuver and the tank aspect ratio being considered. These results agreed with the rollover stability threshold data reported in commercial vehicle rollover literature and research. The quasi-static dynamic analysis was employed in the initial research phase of studying roll stabil-

ity of partially filled road tankers and some improved algorithms were developed to increase the accuracy of the predicted results [60, 122]. An equivalent Trammel pendulum was utilized to analyze the dynamic characteristics of liquid sloshing in a partially filled tank by Li et al. [61]. The dynamics of the Trammel pendulum in the tank was described in terms of the tank-fixed coordinate system and its equation of motion under the non-inertia coordinate system was derived using the Lagrangian formulation. A typical tank truck was used to study its driving stability under steering angle step test.

Dynamic behavior of the large amplitude lateral sloshing in partially filled elliptical tankers was analytically studied by Younesian et al. [131, 132]. The equivalent mechanical elliptical Trammel pendulum was employed for modeling of the large oscillation of the fluid inside the elliptical container. Nonlinear governing equation of the motion is derived employing the Hamilton principle. Natural frequencies of the free oscillation were analytically obtained as a function of the initial amplitude. It was shown that the nonlinear dynamical system can behave mutually as a hardening and softening system based on the tanker aspect ratio.

1.3 Rollover of Road Tankers

1.3.1 Overturning Metrics

When the steering frequency is close to the natural frequency of the free liquid surface, the liquid mass will act like a pendulum swinging with the vehicle. This will result in a distinct increase in load transfer. The load transfer is usually expressed by the overturning risk factor $\Re$ or the (load transfer factor) defined by the expression

$$\Re = \left| 1 - \frac{F_l}{F_{lo}} \right| \tag{1.13}$$

where F_l is the instantaneous wheel load on the left side, and F_{lo} is the static wheel load on the left side. As $\Re \to 1$ the vehicle is close to experience overturning. The value of $\Re$ depends on the lateral acceleration whose critical value, known as the *overturning limit*, is reached when $\Re = 1$. Lidström [62] and Strandberg [110] generated the dependence of the overturning limit on the lateral acceleration for different values of harmonic oscillation frequencies and for 50% liquid volume in an elliptic tank without baffles or cross walls. The roll dynamic performance of a vehicle combination may also be evaluated in terms of the dynamic load transfer ratio (*LTR*), defined as ratio of the sum of instantaneous absolute value of the difference between right-wheel loads and left-wheel loads, to the sum of all the wheel loads, and (1.13) may be expressed as [35, 82]:

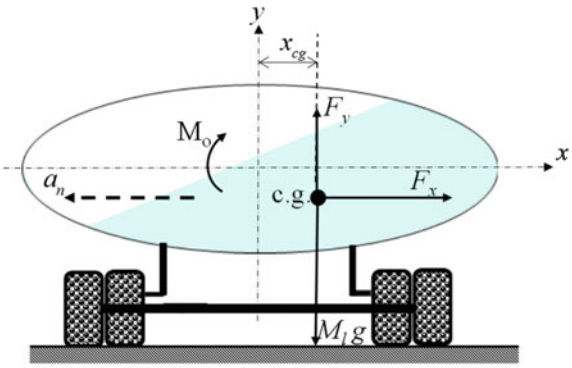

Fig. 1.16 Schematic diagram of liquid displacement in a moving tanker (from [110])

$$LTR = \sum_{i=1}^{N} \frac{|F_{zri} - F_{zli}|}{F_{zri} + F_{zli}} \tag{1.14}$$

where N is number of axles and F_{zr}, F_{zl} are instantameous vertical loads on the right and left wheels of an axle, respectively. The front steering axle is usually excluded from the calculations because of its relatively high roll compliance. The *LTR* assumes an initial value of zero and approaches unity when the wheels on the inside track lift-off the ground.

If the steering frequency is greater than the natural frequency, the liquid pendulum motion will lag the tank motion. Close to resonance, this may be especially dangerous if the risk factor with sloshing load is still close to its resonance level and thus will exceed the corresponding peak for rigid loads. Above resonance, the liquid will oscillate against the tank and stabilize the vehicle. Unfortunately, this stabilization is not effective in real practice because the actual high steering frequencies are very rare. Furthermore, roll motions act like a low-pass filter suppressing high frequency motions in chassis before they reach the tank.

Large liquid displacement inside the tank will cause larger overturning moment due to pure displacement of the center of mass and larger overturning forces when the relative motion of the liquid is reversed by the tank wall. With reference to Fig. 1.16, Strandberg [110] defines the side force coefficient (*SC*) by the expression

$$SC = \frac{m_e a_n - F_x}{(m_e + m_l)g - F_y} \tag{1.15}$$

where m_e is the empty vehicle mass, m_l is the liquid mass, F_x is the resultant force to the left from the liquid load, F_y is the resultant upward force from the load after subtracting the weight, and a_n is the lateral acceleration.

Lidström [62] examined the distinct stabilization effect from cross walls under harmonic excitation and for a half filled tank. Consideration of tank cross-sectional shape, while maintaining the tank bottom at the same level shows the center height is higher for the circular horizontal tank than for the elliptic tank. The value of

overturning limit and the worst oscillation frequency are found to be smaller for the elliptic tanks than for the circular horizontal one. It was shown that the compartment width is an important parameter in conventional tanks and it was recommended that the compartment width must not exceed 0.6 m for a peak lateral acceleration of 0.1 g in order to ensure safe operation of the vehicle under cornering or lane change maneuvers.

In studying the dynamic characteristics of heavy commercial vehicles, the likelihood of vehicle rollover was described by Ranganathan [82] and El-Gindy [35] in terms of lateral load transfer. This load transfer is usually given by the dynamic load transfer ratio (LTR) and dynamic vertical load factor (DLF). The dynamic vertical load factor is defined as ratio of instantaneous vertical load on the left or right track of a given axle to the static vertical load on that track, expressed as:

$$DLF_r = \frac{2F_{zr}}{F_{zr} + F_{zl}}, \text{ and } DLF_l = \frac{2F_{zl}}{F_{zr} + F_{zl}} \tag{1.16}$$

where F_{zr} and F_{zl} are instantaneous vertical loads on the right- and left-wheels of an axle. The *DLF* assumes a unity value under static conditions and may approach zero during a directional maneuver, when tires on the inner track lose contact with the road. The *DLF* due to outer track tires in this situation will attain a maximum value of two. This measure describes the roll dynamics of a particular axle.

The dynamic load shift were evaluated in terms of variations in the liquid center of mass coordinates and mass moments of inertia, moments induced by cargo shift, and dynamic normal load factor (DLF) defined as the instantaneous ratio of dynamic vertical load on a wheel to its static vertical load, expressed as [53]:

$$DLF_k = \frac{F_{zk}}{F_{zko}}, \text{ k=1,2,...,N} \tag{1.17}$$

is unity and may approach zero when it loses contact with the road under directional maneuver. F_{zk} and F_{zk0} are the instantaneous dynamic and static vertical loads on wheel k, respectively. The dynamic load shift characteristics in terms of dynamic load factors (*DLF*) of different tires, was determined using (1.17) for 0.5° and 1.0° ramp-step steer input and a braking treadle pressure of 68.95 KPa (10 psi). The time history records of the dynamic load factor of tires on different axles for liquid and frozen liquid for both trailer and tractor wheels revealed that for 1° steer angle and upon applying the brakes at 4 s, the dynamic load factor of the left tires of the trailer reaches its maximum value close to 1.92, while its value vanishes at the right tires. The influence of liquid dynamics is less dramatic for the case of tractor wheels.

Papadogiannis et al. [73] estimated the load share on groups of axles (bogies) and the individual axles of the bogies in relation to the tank center of gravity positioning on the vehicle chassis in both the longitudinal and the vertical plane. It was assumed that the vehicle structure is rigid, symmetric about its centerline, the lateral deflection of the suspension is negligible and the reaction forces from the road are applied at the center of the tires. Robinson et al. [93] presented an assessment of petroleum road

fuel tankers in the UK. A wide range of evidence points to rollover as a contributing factor in major fuel spillage incidents of petroleum road fuel tankers. When a rollover results in major spillage, a combination of overturning and sliding was associated with tank rupture caused by puncturing impacts with road-side objects, as the tanker slides on its side.

1.3.2 Quasi-Dynamic Approach

It was indicated by [68] that heavy vehicles exhibit unstable behavior at lateral acceleration over the range 0.0–0.4 g. The quasi-dynamic approach assumes the liquid volume moves such that the free surface takes a position orthogonal to the total body forces due to gravity and lateral acceleration [82, 103]. Note that the liquid free surface is a tilted flat surface whose gradient is a function of vehicle's lateral acceleration and tank's roll angle [83, 86, 105, 110]. It was found that the liquid load shift depends on the fill level, vehicle speed, and steer input. The liquid load was found to reach its maximum level at a liquid fill of 70%. Using the quasi-static fluid slosh, it was demonstrated that the destabilizing roll moment of a partly-filled vehicle subject to an idealized lane change excitation is considerably higher than that of an equivalent rigid cargo vehicle. The effect of liquid load shift on stopping distance performance of tank vehicles was examined by [91] who used the quasi-static liquid slosh solution under a straight-line braking input.

The relationship between the liquid sloshing effect obtained by calculating the movement of the liquid bulk center of mass and the actual liquid sloshing observed effect was studied by some researchers (see, e.g., [67, 133, 134]). It was found that the mean values of sloshing forces and the coordinates of the liquid bulk center of mass are quite close between the estimated and observed results. This conclusion demonstrates the validity of the quasi-static method. The location of the center of mass of the liquid domain experiencing a lateral acceleration can be specified by replacing the free liquid surface by a flat surface. The liquid center of mass experiences a shift as shown in Fig. 1.17. This shift gives rise to an additional roll moment due to liquid about the entire vehicle center of mass. With reference to Fig. 1.17, the position of free surface in a model of a partially-filled tank truck experiencing lateral acceleration due to the motion of the truck in a circular path of radius of curvature R_c can be determined by writing the equations of motion along $x-$ and $y-$ axes of a mass particle of mass $\rho d\upsilon$, where ρ is the fluid density and $d\upsilon = dxdydz$ is an elemental volume of the fluid

$$\rho(d\upsilon)a_n \cos\theta = \rho(d\upsilon)g \sin\theta + \Delta P(dydz) \tag{1.18a}$$

$$\rho(d\upsilon)a_n \sin\theta = -\rho(d\upsilon)g \cos\theta + \Delta P(dxdz) \tag{1.18b}$$

Dividing both sides by $d\upsilon = dxdydz$ and rearranging

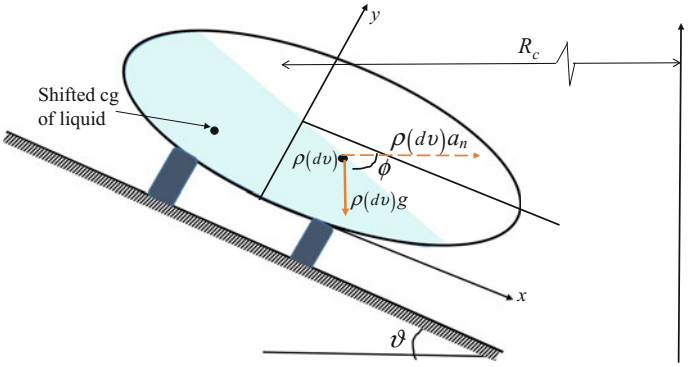

Fig. 1.17 Schematic diagram of a fluid volume whose free surface assume a flat surface during lateral acceleration due to vehicle turning

$$\frac{\partial P}{\partial x} = \rho a_n \cos\theta - \rho g \sin\theta \tag{1.19a}$$

$$\frac{\partial P}{\partial y} = \rho a_n \sin\theta + \rho g \cos\theta \tag{1.19b}$$

Dividing (1.19a) by (1.19b), gives the slope of the free surface

$$\frac{dy}{dx} \approx \frac{(a_n/g) - \theta}{(a_n/g)\,\theta + 1} = \tan\phi \tag{1.20}$$

Note that the quasi-static approach cannot reflect the dynamic characteristics of liquid sloshing. Furthermore, the dynamic liquid sloshing using the fluid potential theory is not straightforward in elliptic and arbitrary geometric containers as in the case of upright circular and rectangular containers. Alternatively, equivalent mechanical models have proven very convenient in describing the dynamic characteristic of liquid sloshing in partially filled containers [50, 51].

Strandberg [110] studied experimentally the influence of large amplitude movements of the contents on the overturning and skidding stability of road tankers. Considerable reductions of the effective capacity due to dynamic liquid motions were found for partly loaded tanks. Steady state shifting of the liquid cargo center of mass CG was modelled by different approaches, including geometrical modeling and experimental methods. However, no straightforward formulation has been proposed for the calculation of the overturning moments due to the quasi-static shifting of the cargo. When a partly filled tank truck is subjected to a constant lateral acceleration, the free surface of the liquid inclines at a slope φ. This slope is numerically equal to the lateral acceleration, when $\theta = 0$ as given by (1.20).

Under lateral acceleration the liquid center of mass CG shifts along an elliptical path having an aspect ratio equivalent to the aspect ratio of the tank cross-section. There is a geometric description of the liquid free surface orientation, which remains

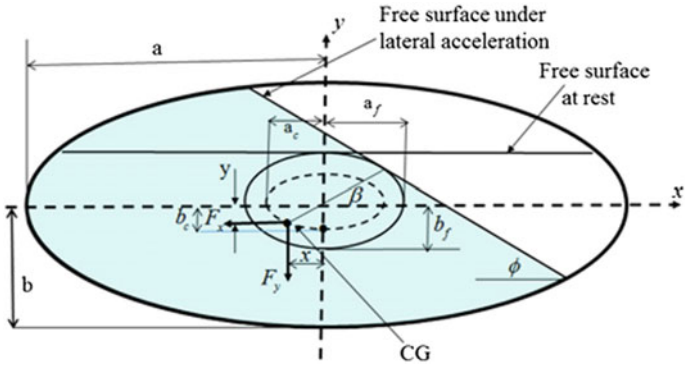

Fig. 1.18 Fluid free surface configuration under steady lateral acceleration according to quasi-static approach

tangential to an ellipse that has the same aspect ratio as of the tank itself. Note that the three ellipses of the tank cross-section, free-surface tangent, and CG path are concentric and $b_f/\mathrm{a}_f = b_c/\mathrm{a}_c = b/\mathrm{a} = \Lambda$. The position $(x_f, y_f)$of the liquid in the elliptic container depends on the dimensions of the ellipse that describes its position, and on the angle β shown in Fig. 1.18. From the definition of the ellipse geometry, we can write

$$x_f = \mathrm{a}_f \cos\beta; \quad \text{and } y_f = b_f \sin\beta \tag{1.21}$$

where a_f and b_f are the semi-axes of the ellipse. The slope of the liquid free surface φ is

$$\frac{dy_f}{dx_f} = \frac{b_f \cos\beta}{-\mathrm{a}_f \sin\beta} = -\Lambda\left(\frac{1}{\tan\beta}\right) = \varphi \tag{1.22}$$

The liquid center of mass CG is described by the parametric equations

$$x = \mathrm{a}_c \cos\beta; \quad \text{and } y = b_c \sin\beta \tag{1.23}$$

Thus the coordinates of the liquid CG are

$$x = \mathrm{a}_c \cos\left(\tan^{-1}\left(-\frac{\Lambda}{\varphi}\right)\right) \text{ and } y = \mathrm{a}_c \sin\left(\tan^{-1}\left(-\frac{\Lambda}{\varphi}\right)\right) \tag{1.24}$$

where a_c and b_c are known from the original position of the undisturbed liquid.

1.3.3 Rollover of Road Tankers

A broad-range of simulations of the dynamics of tank-vehicle rollover was reported by Winkler et al. [121] who used the TruckSim[1] [116] computer simulation. Seven cargo tank motor vehicles, two tank trucks, and five tractor semitrailer combinations were simulated. Each was subjected to 126 simulated maneuvers intended to result in rollover. Test maneuvers included mild, low-speed turns that just barely produced rollover, more dynamic maneuvers on smooth surfaces, and high-speed impacts with curbs and guardrails that result in rapid rollover combined with substantial pitch and yaw. A nonlinear fluid slosh analysis of a partially filled circular tank was developed by Modaressi-Tehrani et al. [67] to study the transient fluid motion on the resulting destabilizing forces and moments imposed on the tank vehicle. The analysis was performed on a clean bore tank of circular cross-section for various fill volumes and subject to different magnitudes of steady as well as harmonic lateral acceleration using the FLUENT software. A relationship between the lateral force and the resulting roll moment was derived, which suggests that the roll moment could be defined as a function of the horizontal force and tank radius. The deviations of the forces and overturning moment from those predicted using quasi-static load shift analysis were also presented. The results of the study suggested that the magnitude of transient roll moment could be 1.57 times larger than corresponding mean values that are very close to those predicted using the quasi-static analysis. The magnitude of the peak overturning moment was found to be strongly dependent on the frequency of the lateral acceleration excitation.

The critical lateral acceleration for overturning of a typical tank truck was found to be 5.4 m/s^2 when the tank is fully loaded, and only 2.4 m/s^2 when the tank is 50% full. Note that although the center of gravity associated with the half-filled tank is lower than the one for the fully filled tank, the critical lateral acceleration is smaller due to the sloshing of the free surface. The danger of rollover is particularly severe when the frequency content of driving maneuvers is close to the natural frequency of the free surface as indicated by Strandberg [110], Ervin et al. [39], Aquaro [2] and Aquaro et al. [2]. In view of the adverse influence of liquid sloshing on road tanker stability and safety performance, some attempts were made to reduce sloshing effects. These include separating walls or baffles as proposed by Strandberg [110] and Bauer [14, 15] and Ibrahim [51]. The number, location and sizes of separating walls and baffles, as well as the size of baffle orifices and their effect on slosh loads were documented by Ibrahim [51].

Cargo load movement in cylindrical tanks was incorporated into the static roll model by Southcombe et al. [107]. A "generalized ellipse" equation allows a variety of cylindrical tank profiles to be analyzed. For a partially filled tank, the locus of

[1] TruckSim computer simulation system is a software package for predicting braking, steering, and roll behavior of heavy trucks and combination vehicles. The models range in complexity from a 26-degree-of-freedom two-axle truck model to a 67-degree-of-freedom tractor-semitrailer model. TruckSim does not have capabilities to simulate liquid loads, but in large part liquid motion is not at issue for full loads. The exception is in regards to the roll moment of inertia of the payload.

the cargo center of gravity locations was determined as a function of the cargo surface slope. The cargo was then modeled as a single point mass that moves along a curved guide shaped. The safety performance measures may be strongly affected by the dynamic load shift and variations in mass moments of inertia of the moving cargo and are evaluated in terms of dynamic load shift. In an effort of predicting the dynamics of a fluid transport system, Wendel et al. [120] and Thomassy et al. [112] reported the results of a multiphase program to develop and demonstrate the use of computational fluid dynamics analysis coupled with vehicle dynamics analysis encountering typical maneuvers. A one-quarter-scale model of a Tank Unit Liquid Dispensing (TULD) tank was constructed, as well as a test fixture to simulate a five-ton Family of Medium Tactical Vehicles (FMTV) truck. The reaction forces and the fluid motions of the computational fluid dynamics analysis and the laboratory test were compared for six simulated vehicle maneuvers including lane changes and bumps. The computational fluid dynamics analysis was conducted with the FLOW-3D software package. The net fluid force and moment predictions were added to the force and moment predictions of a rigid body dynamic analysis of the empty tank alone to compare to the corresponding measured values for the test tank. Figure 1.19 shows the time history records of predicted and measured of rear axle roll moment exerted by the tank half full of water mounted on a vehicle negotiating an Allied Vehicle Test Publication (AVTP) lane change at 40-mph as reported by Wendel et al. [120]. This figure demonstrates that the effect of liquid sloshing is significant and will have significant effect on vehicle dynamics.

Rollover threshold is an essential factor in the study and design of road tanker. Tesar [111] presented a method of identifying the influence of liquid motion in a partially filled road tanker based on simulation using the Multi-body System Analysis software. The road tanker model was tested in compliance with the results obtained by measuring carried out on a SCANIA 124 L truck combined with a ZVVZ trailer. Simulation tests were carried out for the drive on a circular track and in a drive around a roundabout, which is considered the most dangerous manoeuver that causes vehicle rollover. A combined experimental and calculation method was presented by Chondros et al. [30] to determine the overall torsion-angular displacement relation for a road tanker on an inclined level under its own weight. Pape et al. [75] examined the heavy truck rollover characterization. They considered a tanker-trailer used for the on-track testing specially designed and fabricated so that the desired test load distributions could be obtained with minimal complexity in terms of loading the tanks with water and sand. The results provided insight into the relationship of torsional stiffness to roll stability. It also provided insight into the roll stability and design changes which can enhance roll stability.

The simulation of the liquid cargo–truck interaction was studied by Romero et al. [96]. It was found that the rollover trend of the vehicle can increase due to fluid sloshing, up to 50% for the container half full. The experimental assessment of lateral sloshing forces developed within scaled road tankers as a function of fill level and container shape was presented by Romero et al. [95] for high fill levels (from 90 to 98%) and three container shapes (oval, modified oval, and circular). The lateral dimensional characteristics of the containers represented a reduction scale of road tankers

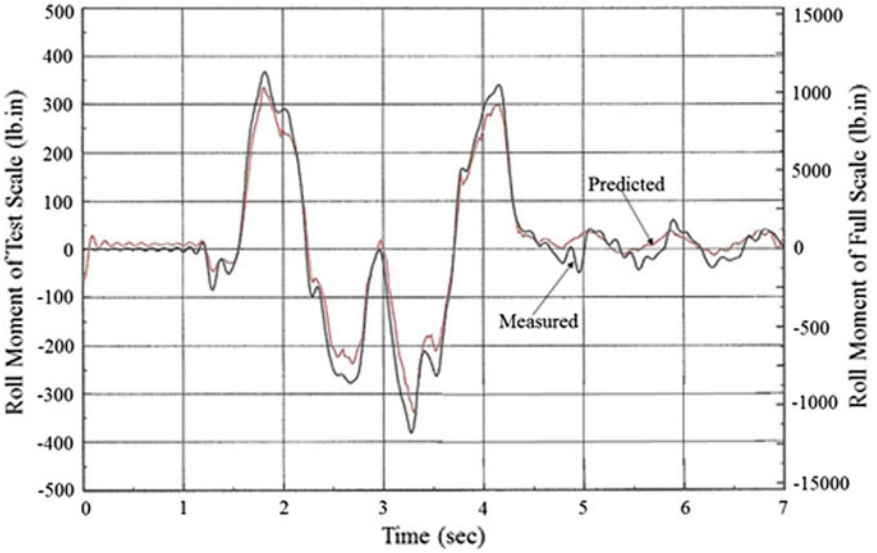

Fig. 1.19 Time history records of predicted and measured of rear axle roll moment exerted by the tank with fluid of the vehicle under 40-mph lane change. Wendel et al. [120]

in the range of 1:5. Containers were subjected to a lateral excitation imparted by a sinusoidal electromagnetic shaker that moved a wheeled container/support assembly at a range of frequencies. Application of these normalized forces to actual size tank trucks further suggests that the rollover threshold acceleration of a rigidly suspended tank truck, due to sloshing, can be reduced by 2% for the 98% fill level, and around 10% for the 90% fill level. The rollover propensity of road tankers when subjected to lateral perturbations derived from steering manoeuvers was experimentally measured by Romero et al. [97]. The testing principle involved a scaled down sprung tank to analyze its rollover propensity as a function of various vehicle's operational and design parameters. Initial acceleration was generated a tilt table supported by a hydraulic piston. The controlled release of the fluid in the hydraulic system generates a perturbation situation for the tank, similar to the one that a vehicle experiences when leaving a curved section of the road and going to a straight segment. Durations for the maneuver and initial tilt angles were used to characterize both the corresponding intensities of the steering maneuver.

1.3.4 International Standards of Roll Threshold and Drivers Training

The basic measure of roll stability is the static rollover threshold, expressed as lateral acceleration in gravitational units. A number of standards were proposed in several

countries. For example, the Canadian National regulatory authorities adopted 0.40 g as the minimum roll threshold for tank trucks. New Zealand and Australia have a minimum roll threshold of 0.35 g, while the United Nations Economic Commission for Europe has a minimum roll threshold of 0.40 g for tank trucks by tilt test. The threshold value 0.35 g seems to be the lower limit for the roll threshold for all vehicles, with 0.40 g for tank trucks among many nations. An on-scene study of 42 road tanker incidents with flammable loads was conducted in New South Wales over a period of fifteen months [46]. Roll instability was a common factor and rollover of the tankers occurred frequently. The reduced stability appeared to result from high center of gravity, "soft" roll stiffness from suspension and turntables, and sloshing loads of the liquid cargo. Road geometry factors contributing to the 42 incidents occurred nine times and included curvature, cross-section, grade and width. The results of a study of cryogenic tanker roll stability of a fleet of tankers, operated by the Linde Division of the Union Carbide Corporation were reported by Ervin and Nisonger [38]. It was found the Linde fleet is low in roll stability compared to tractor-semitrailers in common freight service in USA. Rollover thresholds for the Linde fleet were found to range from 0.26 g to 0.36 g. By way of contrast, MC 306 gasoline tankers in the USA showed rollover thresholds around 0.32 g and tractor-semitrailers in general freight service were estimated to register typical values around 0.37 g.

The handling- performance capability of most large commercial vehicles operating on US highways is generally established by the limits of roll stability [121]. For heavy trucks, suspension properties play an important role in establishing the basic roll stability of the vehicle. The inherent susceptibility of a given vehicle to rollover was described by the rollover threshold [37, 42, 43].

Four complementary approaches to reducing the incidence of cargo tank truck rollovers were evaluated by Pape et al. [74]. These includes improving the training of drivers, deploying electronic stability aids, implementing new vehicle designs, and learning lessons from highway designs. The safety of driving cargo tank trucks was strongly addressed on rollover prevention [70, 76]. The emphasis is on the driver's role in an overall corporate safety culture. To the extent that a skill is emphasized, it is the importance of avoiding sudden maneuvers that can induce slosh.

It is known that rollovers are among the most serious crashes of cargo tank motor vehicles carrying hazardous materials [74]. In Battelle [9, 10, 12] extensive studies were conducted to assess the additional risks posed by hazardous materials transportation when compared to non-hazardous shipments. The average annual enroute hazardous materials accident frequency was estimated to be 2,484 accidents. On the other hand, non-hazardous materials shipments experienced an estimated 126,880 accidents in the portrait year. Total hazardous materials annual impacts for the portrait year were estimated at about $1.2 billion. Enroute accidents with total impacts of just over $1 billion account for about 89% of the total impacts. The safety benefits of an improved version of the Roll Advisor and Controller (RA&C) on-board safety system were considered [11]. The RA&C, comprised of two components that perform two distinct functions: (1) To inform drivers when they have performed a maneuver with a high risk of rollover (the roll stability advisor [RSA] component). (2) To initiate autonomous braking to prevent a rollover (the Field Operational Test Roll Stability

Control [RSC] component). The new safety standard, Federal Motor Vehicle Safety Standard, FMVSS 136 (NHTSA, 2012), is designed to reduce rollovers and to mitigate severe understeer or oversteer conditions that lead to loss of control. It will require the use of automatic computer-controlled braking and reduced engine torque output to achieve its objectives.

1.3.5 Directional Stability and Dynamics

The stability of a vehicle about an axis which is perpendicular to its direction of motion is usually referred to as directional stability. It is defined as the tendency of a vehicle to return to its original direction in relation to the on-coming road medium when rotated away from that original direction. If a vehicle is directionally stable, a restoring moment is produced which is in a direction opposite to the rotational disturbance. This "pushes" the vehicle to return it to the original orientation.

Dynamic response and stability characteristics of a partly filled articulated liquid cargo vehicle with tanks of arbitrary cross-section were studied under braking-in-a-turn manoeuver. Tanks with circular, modified-oval and arbitrary cross-sections were considered for deriving the longitudinal and lateral cargo shifts under longitudinal as well as lateral acceleration fields. The three-dimensional quasi-static model of the partly filled tanks was integrated to the dynamic model of the vehicle to study the role of tank geometry and road adhesion on the dynamic behavior of the partly filled liquid cargo vehicle. The directional dynamic characteristics under a braking-in-a-turn manoeuver were evaluated in terms of moments induced by the moving cargo, wheel dynamic load factor; load transfer ratio, yaw and roll response and braking performance of the vehicle. The results showed that dynamic performance of the partly filled liquid cargo vehicle deteriorates significantly due to considerable magnitudes of roll, pitch and yaw moments imposed by the moving cargo. A partly filled articulated tank vehicle, subject to braking-in-a-turn, is more susceptible to rollover on dry roads, while it exhibits a higher propensity of trailer swing on slippery roads. The results further indicate that tank cross-section yields certain influence on the dynamic characteristics of the partly filled articulated liquid cargo vehicle under braking-in-a-turn.

The directional response characteristics of double tankers (i.e., two articulated tank-trailers in Tandem) were studied by Mallikarjunarao and Fancher [63]. It was indicated that the double-trailer gasoline tanker configuration corresponding to that used in Michigan has a lightly damped mode of "pup-trailer" (i.e., the second trailer) oscillation that can be unstable at highway speeds. This occurred when the rear compartment of the pup trailer is loaded and the other compartments of the pup trailer are empty. The lateral acceleration of the pup-trailer was found much larger than that of the tractor of the vehicle train in obstacle-avoidance maneuvers at highway speeds. The influence of size and weight of heavy vehicles on handling and control characteristics of liquid tank vehicles was examined by Sankar et al. [102]. The influence of liquid motion within the tank, on the static stability behavior of the

vehicle was investigated in terms of the lateral shift of center of mass and the tank shape.

Roll stability issues involving the operation of heavy tanker combinations on two segments of curved roadway were evaluated by Ervin and Mathew [40]. Two vehicle configurations were examined, representing tankers for transporting petroleum products. The analyses showed the comparison in static stability between the selected vehicles and the performance of these vehicles on an existing and a proposed road segment. The study provided recommendations for setting maximum speed values for trucks operating on the subject curves. The dynamic stability limits of partially-filled tank vehicle combination using computer simulation and field testing were reported by SS [108]. Overturning limits of tank vehicles were investigated using a kineto-static roll plan model. A three-dimensional tank-vehicle model, incorporating a steady-state fluid slosh model, was developed and computer simulation was performed to determine directional stability for various maneuvers, fill levels, vehicle speeds, and tank design factors. A comparison of directional response characteristics of tank vehicles with liquid and equivalent rigid cargo was conducted. As well, the influence of dynamic slosh loads on the dynamic stability and directional response characteristics of tank vehicles was investigated.

The directional dynamics of partially filled articulated tank vehicles was studied by Sankar et al. [103, 104] using computer simulation under constant forward velocity. The directional response characteristics of an articulated tank vehicle was examined for various steering manoeuvers and compared to that of an equivalent rigid cargo vehicle to demonstrate the destabilizing effects of liquid load shift. It was found that during a steady steer input, the distribution of cornering forces caused by the liquid load shift yields considerable deviation of the path followed by the tank vehicle. The lateral load shift encountered in a partially filled tank vehicle during lane change and evasive type of highway manoeuvers was found to give rise to roll and lateral instabilities. The nonlinear fluid slosh equations were solved in an Eulerian mesh to determine dynamic fluid slosh loads caused by the dynamic motion of the vehicle. The dynamic fluid slosh forces and moments were coupled with the vehicle dynamics model to study the directional response characteristics of tank vehicles. Simulation results revealed that during a steady steer maneuver, the dynamic fluid slosh loads introduce oscillatory directional response about a steady-state value calculated from the quasi-dynamic vehicle model. It was concluded that the quasi-dynamic model can predict the directional response characteristics of tank vehicles quite close to that evaluated using the comprehensive fluid slosh model.

The vertical and lateral translation of the liquid cargo due to vehicle roll angle and lateral acceleration, encountered during steady turning, were evaluated by Rakheja et al. [78]. The adverse influence of the unique interactions of the liquid within the tank vehicle, on the rollover limit of the articulated vehicle is demonstrated. The influence of tank geometry and liquid fill level on the rollover immunity of the tank vehicles was studied by Ranganathan et al. [85]. The rollover threshold levels of the tank vehicle were compared to that of an equivalent rigid cargo vehicle for various loading conditions. The influence of compartmenting of the tank and the influence of the location of the trailer axles on the rollover immunity levels was also studied and an

optimal order to unloading the various compartments was established. The influence of the lateral load shift on the dynamic response characteristics of an articulated tank vehicle was studied under braking by Ranganathan and Yang [84] and Ranganathan et al. [82]. The destabilizing effects of liquid load shift were studied by comparing the directional dynamics of the partially filled tank vehicle to that of an equivalent rigid cargo vehicle subject to steady steer input. The liquid load shift occurring in the pitch plane of the vehicle during a braking maneuver was characterized using the change in the gradient of the free surface of liquid and the corresponding shift in the center of gravity of the fluid bulk. The braking characteristics of the tank vehicle were compared to those of an equivalent rigid cargo vehicle in order to study the impact of liquid load shift. Influence of various vehicle and tank design parameters on the braking behavior and wheel lock-up condition is also investigated for typical braking maneuvers. The distribution of cornering forces caused by the liquid load shift yielded considerable deviation of the path followed by the liquid tank vehicle. The influence of the vehicle speed on the dynamics of the liquid tank vehicle is also investigated for variations in the fill levels and fluid density.

The directional dynamics of a partially filled tank truck was studied by Rakheja et al. [79] using computer simulation of a three-dimensional vehicle model incorporating a quasi-dynamic roll plane model of the tank. Field tests were performed for typical lane change and turning manoeuvers, and the corresponding directional response data were compared to the computer simulation results to validate the analytical model. The rollover threshold of partially filled liquid cargo vehicles was estimated by Rakheja and Ranganathan [80]. The primary overturning moment caused by the lateral motion of the liquid cargo within the circular, elliptic or modified-oval cross-section tanks was derived as a function of the lateral acceleration, roll angle, fill level, and the tank geometry. The estimated values of rollover threshold were compared to those obtained from a comprehensive kineto-static roll plane model of the tank vehicle. Directional dynamics of a B-train[2] tank vehicle was studied by Ranganathan et al. [88] by integrating the three-dimensional vehicle model to the dynamics of free surface of liquid cargo. The influence of liquid motion on the dynamic response of the rearmost trailer was examined for both constant and transient steer inputs, assuming constant forward speed. Directional response characteristics of the B-train tank vehicle were compared to those of an equivalent rigid cargo vehicle.

The dynamics of vehicles subject to liquid slosh loads was modeled as a multibody system by Rumold [98]. The sloshing liquid dynamics was determined by solving the Navier–Stokes equations. The concept of modular simulation was applied decomposing the dynamic system into subsystems. The system of equations resulting from a finite volume discretization was solved by a multigrid method while the location of free surfaces was determined by a volume-of-fluid approach. The interaction of liquid sloshing and vehicle motion was used to determine the braking characteristics of partially liquid-filled tank vehicles. It was shown that a loss of directional control due

[2]B-Train consists of two trailers linked together by a fifth wheel, which is located at the rear of the lead, or first, trailer and is mounted on a "tail" section commonly located immediately above the lead trailer axles. In North America this area of the lead trailer is often referred to as the "bridge".

to wheel lock-up is more likely for tank vehicles with sloshing liquid cargo than for vehicles loaded with equivalent rigid cargo because of the dynamic liquid load shift. The stability of articulated suspended cargo vehicles was studied by Mangialardi and Mantriota [64] to characterize possible conditions of instability that can be induced by the presence of oscillating cargo. A linear mathematical model of the articulated vehicle was used to determine the critical speed and to analyze the sensitivity of the critical speed to the variation of some characteristic parameters of the vehicle. Suspended cargo movements within articulated vehicles were found to cause the greatest potential risk of road accidents. A mathematical model was proposed by Mantriota [65] for studying the dynamics of articulated vehicles carrying suspended cargoes. For different operational conditions, the effect of the suspended cargo for the vehicle's stability was assessed in terms of the critical speeds and the frequencies of the vehicle. Later, Mantriota [65] proposed another analytical model to study the directional stability of articulated tank vehicles. The liquid in the tank was simulated through elementary pendulums distributed longitudinally. The critical speed of the tank vehicle was calculated for different values of fill level. The most critical condition was obtained for a fill level equal to approximately 70%, with a frequency of 0.38 Hz. The decay time for the oscillations of the liquid was found strongly influenced by the vehicle's forward speed. The stability of the vehicle was examined by varying the geometric greatness of the tank demonstrating a predominant effect of the length compared to the radius.

The coupling of a mechanical subsystem model with a fluid subsystem model was developed by Elliott et al. [36] and Barton et al. [8]. The approach was to link a vehicle simulation based on ADAMS software [36] with the computational fluid dynamics software Dytran. The result was a fully coupled tank truck simulation that used state-of-the-art models for both the vehicle and the fluid. The method was not easy to implement since vehicle simulations and fluid simulations are generally solved using very different methods. Vehicle simulations use an implicit method in which time within the simulation is virtually continuous whereas fluid simulations use an explicit method in which the simulation time is broken into discrete instants. In order to pass variables between the two simulations Elliott developed "glue code," which handles the exchange of data between the two solvers.

1.4 Coupled Dynamics of Liquid-Tanker Systems

1.4.1 Overview

The motion of road tanker affects the motion of liquid free surface inside its tank. At the same time the resulting motion of liquid inside the tank will impart hydrodynamic loads on the vehicle that affects its dynamics and stability. The interaction between the liquid with the vehicle dynamics has been the subject of many studies. For heavy trucks without liquid tanks, Yang et al. [130] applied a system identifi-

cation technique to determine the lateral dynamics of an articulated freight vehicle subjected to three different steering excitations and levels of measurement noise. An algorithm was proposed to extract an estimate of significant vehicle parameters. It was found that the directional dynamics of the vehicle is influenced mostly by the lateral and yaw dynamics, while the contributions due to roll dynamics are relatively small. Thomassy et al. [112] developed a co-simulated software (referred to CoSim), which simultaneously simulate vehicle dynamics and fluid slosh so that the highly coupled behavior of fluid and vehicle motion is realized. The CoSim involves a master program that manages the exchange of data between and synchronization of two separate simulation codes. These codes are the vehicle dynamics and tank slosh simulations. The master program (called the Glue Code) provides motion data from the vehicle dynamics simulation to the tank slosh simulation and force data from the tank slosh simulation to the vehicle dynamics simulation.

Solid–fluid interaction in vehicles carrying liquids was examined by Biglarbegian and Zu [16]. The equations of motion for the vehicle system were coupled with solid fluid interaction coupled. The coupled equations were solved to determine the dynamic behavior of the system under different braking moments. As the braking moments increase, braking time decreases. It was shown that vehicles carrying fluids need a greater amount of braking moments in comparison to vehicles carrying solids during braking. In addition, as the level of the fluid inside the tanker increases, from one-third to two-third of the tanker's volume, the sloshing forces applied to the tanker's walls increase.

The dynamic coupling between shallow-water fluid sloshing and the motion of the transport vehicle was studied analytically by Ardakani and Bridges [4, 5]. Horizontal motion, translation and rotation of the vessel coupled to shallow-water sloshing were considered. For the case of coupling with horizontal motion, the governing equations of motion were derived by Cooker [31]. The coupling was nonlinear while the vehicle model is linear (linear spring).

Wu and Lin [124] studied the yaw/roll dynamics of tractor-trailer with multi-axle-steering carrying a partial load of liquid during a transient steering operation for various levels of tank filling. The lateral inertia forces and the vertical and lateral translations of the center of mass of a liquid-carrying tanker fitted with multi-wheel steering under conditions of steady-state steering response are presented. The transient directional responses of yaw and roll angles were studied under lane change maneuvers. The results demonstrated that the use of multi-axle-steering reduces the lateral forces caused by shifts of the liquid during steady turning, hence reducing roll and lateral instabilities of the vehicle. The results were compared with those of a conventional tanker fitter with a single front wheel steerable axle. The transient forces and roll moment caused by fluid slosh within partly filled circular and conical cross-section tanks, subject to a time-varying lateral acceleration field, were estimated numerically by Yan et al. [127]. The variations in the center of mass coordinates, vertical and lateral forces and roll moment were applied to the roll-moment model of a 6-axle tractor-semi-trailer articulated tank vehicle for analysis of the steady-turning rollover threshold. It was found that the magnitudes of transient lateral force and roll moment approach significantly higher values, than those estimated from the quasi-

static formulations. The mean values of the force and moment, however, were found similar to those predicted from the quasi-static solution. The steady-turning rollover-threshold accelerations of the vehicle combination with partly filled tanks were thus considerably lower when transient slosh forces and moment are considered in the moment equilibrium, specifically for the intermediate fill volumes. It was found that the static roll stability limits for a conical cross-section tank are considerably higher than that with a circular cross-section tank.

The nonlinear dynamic behavior of partially filled tank vehicles under large-amplitude liquid sloshing was studied by Dai et al. [33]. A nonlinear impact model for liquid sloshing in partially filled liquid tank vehicles was developed to examine the longitudinal dynamic characteristics of tank vehicles under typical driving conditions. The dynamic fluid motion within the tank was modelled by utilizing an analogy system together with an impact subsystem for longitudinal oscillations. The forces on the fifth wheel and the axles of the vehicle were determined taking into account the effects of the liquid sloshing in the tank. The nonlinear dynamic behavior of the tank vehicle involving liquid sloshing, running over rough roads were analyzed and compared with those of linear models.

A time-based finite element model for predicting the coupled dynamic response of tanker trucks and their liquid payloads validated experimentally was presented by Wasfy el al. [118, 119]. The tanker truck components were modeled using rigid bodies, flexible bodies, joints and actuators. The model was validated using a full-scale army heavy class tactical trailer carrying a water tank. The trailer is placed on an n-post motion base simulator which was used to perform harmonic/ramp pitch, roll and stir excitations of the trailer in order to simulate typical road maneuvers. Experiments were carried out with an empty tank and a 65%-filled tank. The experimental measurements were compared with the results predicted using the computational model and it was shown that the model can predict with reasonably good accuracy the test tanker-trailer's dynamic response.

The liquid motion inside a road tank vehicle and its analytical modeling for stability limits was studied by Bottiglione and Mantriota [19, 20]. The experimental study employed visual technique of the free surface of the fluid, accompanied by several measurements of vehicle motion parameters. The analytical model, validated by the experimental results, predicted the influence of several design and operative parameters on dynamical properties of partially filled tank vehicles. It was shown that the dynamical interaction between liquid and rigid cargo is considerably influenced by the type of maneuver performed and the sharpness of the steering inputs applied. In another study [21], the trailer was equipped with further instruments providing the analysis of the vehicle dynamics. Experimental tests about a trial manoeuver consisting of a 90° degrees curve of an articulated car-tank trailer system were performed. The measured results were compared with the calculated results of a mathematical model of an articulated vehicle including a dynamic model for liquid motion. Later, the work was extended by Bottiglione and Mantriota [22, 23] to experimentally study the handling performance of an articulated vehicle carrying liquid cargo. The test vehicle consists of a car with a single-axle trailer carrying a cylindrical tank, fully instrumented to measure the interested parameters of vehicle dynamics

and liquid-vehicle interactions. An original device for the visualization of the liquid free surface inside the tank is also described. Comparisons between three different kinds of mechanical models and test results revealed that the dynamical interaction between liquid and rigid cargo is considerably influenced by the type of manoeuver performed and the sharpness of the steering inputs applied.

An analytical model of longitudinal liquid sloshing was developed by Toumi et al. [113] who used the Navier-Stokes equations and the principle of work and energy for tank models with lateral orifice baffles. The analysis was performed under varying the magnitude of the tank longitudinal acceleration for two different values of liquid fills. The results obtained were compared with the simulation results and were presented in terms of mean and peak of longitudinal and vertical shift of the center-of-mass coordinates. Later, the stability and the behavior of the dynamics of tank vehicles carrying liquid fuel cargo were studied by Toumi et al. [114, 115] and Bouazara et al. [24]. A simplified analytical model of liquid sloshing was developed using the Navier–Stokes equations. Simulation results obtained using the full complex Navier–Stokes equations modulated with numerical commercial software are compared to the simplified analytical model. The results showed a good correlation under single or double lane change and turning manoeuvers. An analytical model of a modular tank vehicle has been developed. The model included all the vehicle systems and subsystems. Simulation results obtained using this model were compared with those obtained using the popular TruckSim software. Simulated directional response results obtained for a vehicle transporting liquid load with that transporting rigid load under several directional manoeuvers such as step steer, single lane and double lane change revealed that the vehicle transporting liquid experiences more load transfer and the difference was found to be 15–20%.

Jafari and Samadian [52] developed a dynamic model of a tractor semi-trailer vehicle coupled with a three-dimensional full scale tank's fluid dynamics to study the dynamic behaviors of the vehicle subject to liquid slosh loads during steady and transient steering inputs. The fluid forces and moments were derived from computational fluid dynamic model based on volume-of-fluid technique. The steady state turning and lane-change maneuvers were performed and dynamic responses compared with equivalent rigid cargo. It was found that the vehicle responses are affected by fluid slosh. The roll angles highly affected by fluid movement but the yaw rate changes would be small. Roll stability of vehicle was also affected by fluid movement inside the tank, describing by dynamic load factor and load transfer ratio. The results showed the fluid sloshing model interaction with the vehicle dynamic increases probability of roll over occurrence. This probability is higher in the lane change maneuver especially in the second half of lane-change maneuver. The directional response and roll stability characteristics of a partly filled tractor semi-trailer vehicle were studied by Azadi et al. [6, 7]. The effective parameters and conditions in the stability of a tractor semi-trailer carrying liquid were found essentially to be the tank shape, fill volume and vehicle steering input. The dynamic interaction of liquid cargo with the tractor semi-trailer vehicle was evaluated by integrating a dynamic slosh model of the partly filled tank with five-degrees-of-freedom of a tractor semi-trailer tank. The vehicle model was analyzed for the different tank cross-sections, circular, modified-

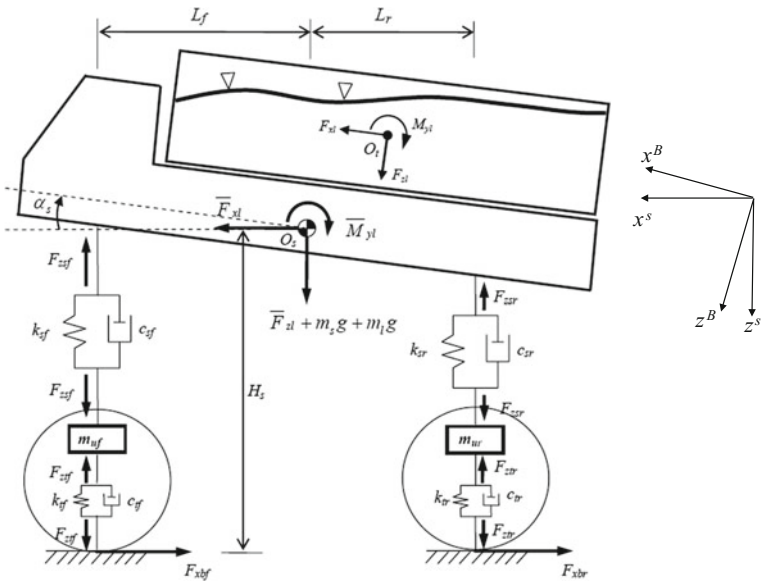

Fig. 1.20 Schematic diagram of the seven-degree of freedom pitch-plane vehicle model as proposed by Yan and Rakheja [129]

oval and reuleaux triangle. The dynamic fluid slosh within the tank is modelled using three-dimensional Navier-Stokes equations, coupled with the volume-of-fluid equations and analyzed using the FLUENT software.

1.4.2 Liquid-Vehicle Coupling During Braking

The coupling between fluid and vehicle body during straight line braking of a partially-filled tank truck was developed by Yan and Rakheja [128, 129]. The analysis was based on a seven-degree-of-freedom pitch-plane model in which the rear three axles are represented by a single composite axle as shown in Fig. 1.20. The model considers longitudinal, vertical and pitch motions of the sprung mass, vertical motions of the two unsprung masses, and angular motions of the wheels. The floating fluid cargo within the tank is represented by its resultant transient dynamic forces along the longitudinal and vertical axis, and the pitch moment, which are derived from the slosh model and assumed to act on the vehicle sprung mass center of gravity (Os). Figure 1.20 shows the resultant longitudinal and vertical forces, $\bar{F}_{xl}$, $\bar{F}_{zl}$, respectively, and pitch moment, $\bar{M}_{yl}$, due to the liquid sloshing. The resultant liquid sloshing forces and moment were computed along the $(xyz)^L$ coordinate system and transformed to the inertial reference $(xyz)^s$. The fluid slosh was modeled in the computational fluid dynamics and experimentally validated for the scale model tank by

Yan [126]. The resultant pitch moment due to the slosh forces was computed about the center of gravity of sprung mass, O_s. The resultant slosh forces and moments were derived from the absolute slosh forces and moment by appropriately adjusting for the inertial forces and moment due to an equivalent rigid cargo.

The equations of motion describing the longitudinal x_s, vertical z_s and pitch α_s motions of the sprung mass can be expressed as:

$$\left(m_s + m_{uf} + m_{ur} + m_l\right)\ddot{x}_s = \bar{F}_{xl} - \left(F_{xbf} + F_{xbr}\right) - \left(m_s g + m_l g + \bar{F}_{zl}\right)\alpha_s \tag{1.25}$$

$$\left(m_s + m_l\right)\ddot{z}_s = \bar{F}_{zl} - \left(F_{zsf} + F_{zsr}\right) + \left(m_s + m_l\right) g \tag{1.26}$$

$$\left(I_{yys} + I_{yyl}\right)\ddot{\alpha}_s = \bar{M}_{yl} + F_{zsf} L_f - F_{zsr} L_r - \left(H_s - z\right)\left(F_{xbf} + F_{xbr}\right) \tag{1.27}$$

where F_{xbf} and F_{xbr} are the braking forces developed at the front and rear tire-road interfaces, respectively. Assuming no wheel lockup, the longitudinal braking forces developed on the tire-road contact were derived from the widely used 'Magic Tire Formula' developed originally by Pacejka and Bakker [72]. m_s is the sprung mass of the vehicle consisting of the chassis structure and the tank structure. m_l is the liquid mass, m_{uf} and m_{ur} are the front and rear unsprung masses, respectively. I_{yys} and I_{yyl} are the pitch mass moments of inertia of the sprung mass and the floating cargo. H_s is the height of the sprung mass center of gravity position at the static equilibrium position, L_f and L_r are the longitudinal positions of the front and rear axles, respectively, from the center of gravity of the sprung mass, as shown in Fig. 1.20. F_{zsf} and F_{zsr} are the vertical forces developed due to the front and rear suspensions, respectively. Assuming linear stiffness and damping properties of the suspension system, the suspension forces are derived from:

$$F_{zsf} = k_{sf}\left(z_s - L_f\alpha_s - z_{uf}\right) + c_{sf}\left(\dot{z}_s - L_f\dot{\alpha}_s - \dot{z}_{uf}\right) \tag{1.28}$$

$$F_{zsr} = k_{sr}\left(z_s + L_r\alpha_s - z_{ur}\right) + c_{sr}\left(\dot{z}_s + L_f\dot{\alpha}_s + \dot{z}_{ur}\right) \tag{1.29}$$

where a dot denotes derivative with respect to time, k_{sf}, and k_{sr} are the stiffness coefficients of the front and rear lumped axles, respectively, while c_{sf} and c_{sr} are the corresponding damping coefficients. z_{uf} and z_{ur} are the vertical displacements of the front and rear unsprung masses measured from the respective static equilibrium position. The equations of motion for the unsprung masses, m_{uf} and m_{ur} describing the vertical motion can be expressed from the suspension and inertial forces in the form:

$$m_{uf}\ddot{z}_{uf} = F_{zsf} - F_{ztf} + m_{uf} g, \text{ and } m_{ur}\ddot{z}_{ur} = F_{zsr} - F_{ztr} + m_{ur} g \tag{1.30a, b}$$

where F_{ztf} and F_{ztr} are the vertical force components due to tires on the front and rear axles, respectively, and can be written by the expressions

$$F_{ztf} = k_{tf} z_{uf} + c_{tf} \dot{z}_{uf}, \text{ and } F_{ztr} = k_{tr} z_{ur} + c_{tr} \dot{z}_{ur} \quad (1.31a, b)$$

where k and c are the linear tire stiffness and damping coefficients, respectively.

Assuming uniform tire-road adhesion and that the braking forces remain below the limit of tire-road adhesion (i.e., no wheel lockup), the angular motion of the wheel/tire combination can be related to the braking force and braking torque by the equations of motion:

$$I_f \dot{\Omega}_f = F_{xbf} R_f - T_f, \quad \text{and} \quad I_r \dot{\Omega}_r = F_{xbr} R_r - T_r \quad (1.32)$$

where R is the effective radius of the indicated wheel, and I is the corresponding polar mass moment of inertia of the tire-wheel assembly. The torque distribution was assumed to be proportional to the static normal load on the front and rear axles. The driver's reaction time and the braking system time lag were taken as $0.75 - s$, while the braking torque gain of the braking system was set to be 98.2 Nm/kPa. Yan and Rakheja [129] considered the tridem tank truck with 6.65-m wheel base, 3.5-m overall height and 11-m overall length. The gross mass of the truck was about 25,840-kg (including the liquid cargo). The sprung mass of the vehicle without the cargo was 5250-kg, while the vehicle full payload capacity is 16,400-kg. The tridem axles were assumed to have identical properties and responses, and were lumped to a single composite axle. Three different liquid products were selected to achieve three different fill volumes but nearly identical cargo load. These included: sulfuric acid, dichloromethane and water, which resulted in fill volume ratios of 38.1%, 52.1% and 69.5%, respectively. The fill heights for the three different fill volumes were 0.63, 0.85 and 1.14-m from the tank bottom. The weight densities of the three fluids were 1826.3, 1326 and 998.2-kg/m^3.

The measured liquid sloshing forces due to external harmonic excitation were analyzed in terms of frequency and transient forces and moments for 50%-filled multiple-orifice baffled tank and clean-bore tank subject to 1 m/s^2 lateral excitation at 0.7 Hz. Figure 1.21 shows the power spectral density of measured slosh forces. It is seen that the two tanks reveal similar magnitudes of the spectral energy of lateral slosh force, while considerable differences is evident for the longitudinal force responses. Two predominant peaks near the excitation frequency, $f_e \approx 0.7$ Hz, and the lateral mode fundamental frequency, $f_{n,y} = 1$ Hz, are observed in the spectra of lateral force as shown in Fig. 1.21a. The spectra of the longitudinal slosh force shown in Fig. 1.21b exhibit prominent peaks near the excitation frequency, f_e, longitudinal mode resonant frequency, $f_{n,x} = 0.45$ Hz, and lateral mode frequency, $f_{n,y} = 1$ Hz. This suggests that the variations of transient slosh forces are closely dependent on the external excitation and the liquid sloshing natural frequency. Note that the longitudinal mode resonance of the baffled tank is approximately 1.1 Hz, close to the lateral mode resonance. The higher frequency peaks exhibited in the spectra may be related to higher slosh modes and structural modes. The three-dimensional slosh model of a partly-filled tank with and without baffles was also integrated to a 7-DOF pitch plane model of a tridem truck to analyze its straight-line braking characteristics in the

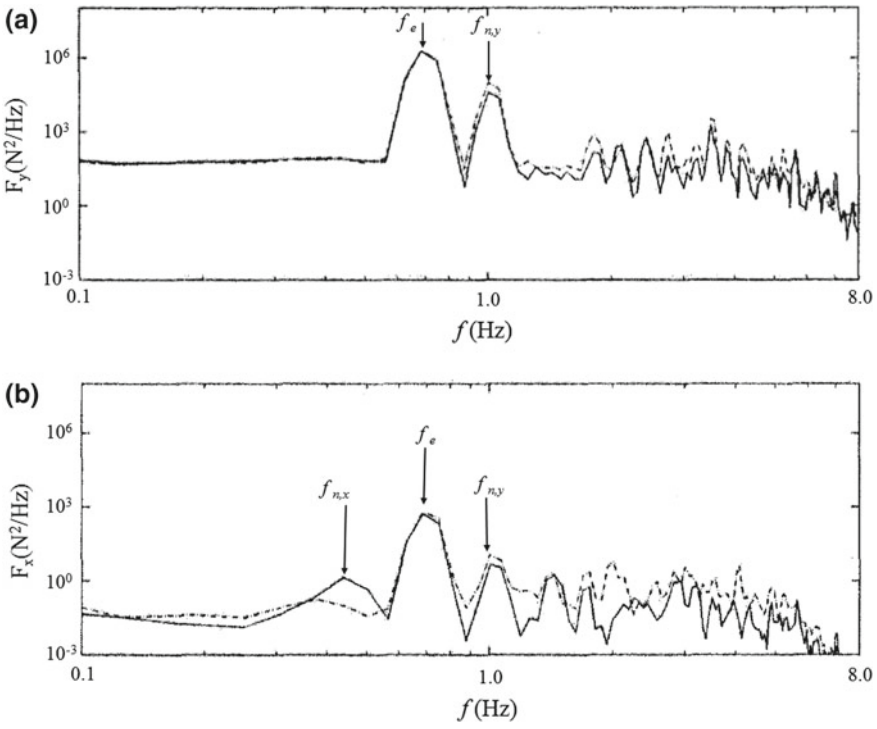

Fig. 1.21 Frequency spectra of slosh force components measured on the 50%-filled un-baffled (*dashed-dotted plots*) and baffled (*solid plots*) tanks subject to 1m/s^2 lateral acceleration excitation at 0.7 Hz: **a** lateral force, **b** longitudinal force. Yan and Rakheja [129]

presence of fluid slosh. A degradation of the braking performance of the partly filled tank truck was evident in the presence of transient fluid slosh, particularly in the absence of baffles. The braking performance, however, was highly dependent upon fill volume, presence of baffles, and severity of the braking input.

Dynamic behavior of a partly-filled liquid cargo vehicle subject to simultaneous application of cornering and braking maneuvers was studied using computer simulation by Kang et al. [55]. A three-dimensional quasi-dynamic model of a partly-filled tank of circular cross-section was developed and integrated into a three-dimensional model of an articulated vehicle to study its directional response under varying steering and braking inputs, fill volumes and road surface friction. The liquid load movement encountered under combined steering and braking was expressed in terms of variations in the instantaneous center of mass coordinates and mass moments of inertia of the liquid bulk. The dynamic response characteristics of the partly-filled tank vehicle under braking and turning were presented in terms of resulting cargo load shift, moments induced by the cargo movement, load transfer ratio, yaw and roll response, and braking performance of the vehicle. It was found that a partly-filled articulated tank vehicle, subject to braking in a turn, is more susceptible to rollover

on dry roads, while it exhibits a higher propensity of trailer swing on slippery roads. The directional dynamic characteristics under a braking-in-a-turn manoeuver were evaluated by Rakheja et al. [81] in terms of moments induced by the moving cargo, wheel dynamic load factor, load transfer ratio, yaw and roll response, and braking performance of the vehicle. Tanks with circular, modified-oval and arbitrary cross-sections are considered for deriving the longitudinal and lateral cargo shifts under longitudinal as well as lateral acceleration fields. It was shown that the dynamic performance of the partly filled liquid cargo vehicle deteriorates significantly due to considerable magnitudes of roll, pitch and yaw moments imposed by the moving cargo. A partly filled articulated tank vehicle, subject to braking-in-a-turn, is more susceptible to rollover on dry roads, while it exhibits a higher propensity of trailer swing on slippery roads.

Steady-state fluid slosh model was applied by Rakheja [77] to derive the dynamic response and stability characteristics of a partly-filled articulated liquid cargo vehicle with tanks of arbitrary cross-section under steering and braking-in-a-turn maneuvers. The directional dynamic characteristics under a braking-in-a- turn maneuver were evaluated in terms of moments induced by the moving cargo, wheel dynamic load factor, load transfer ratio, yaw and roll response, and braking performance of the vehicle. The results of the study revealed that a partly-filled articulated tank vehicle, subject to braking-in-a-turn, is more susceptible to rollover on dry roads, while it exhibits a higher propensity of trailer swing on slippery roads.

A computational fluid dynamics slosh model coupled with a lumped truck model was developed by D'Alessandro [34]. The computational fluid dynamics model, based on the Navier-Stokes equations, was incorporated with the volume-of-fluid technique to model two immiscible fluids. A 14° of freedom truck model coupled with the computational fluid dynamics model were combined to evaluate the vehicle behavior in a lane change manoeuver in a braking maneuver. In both cases tests were made at different velocities and different fill volumes and compared with experimental results available in literature. Moreover, the tilt table test have been simulated for different fill volume in order to assess the influence of the fill volume on the Static Rollover Threshold. The performed braking manoeuvers revealed that load transfers, due to the fluid sloshing, can cause premature rear wheels locking up and then effectiveness of baffles has been investigated. A comparison of simulations results, between liquid and an equivalent rigid cargo, in a lane change manoeuvers have allowed to evaluate how much the fluid sloshing affects the rollover in dynamical conditions. During braking manoeuvers, fluid sloshing may lead to load transfers causing rear wheels to lock up and loss of directional control, while during turning or lane changes, it may cause rollover. A methodology for evaluating the interaction between fluid sloshing and vehicle dynamics was proposed by Cheli et al. [29]. The fluid and the tank were modelled using the computational fluid dynamics code FLUENT, based on the Navier-Stokes equations and incorporating the volume-of-fluid and the moving mesh techniques. The motion of the tank was determined based on the response of a 14° of freedom vehicle model subjected to the forces due to the fluid sloshing. Straight line braking manoeuvers and lane change manoeuvers were introduced to evaluate the effects of fill level, baffles and tank shape.

1.5 Conclusions and Closing Remarks

Road tankers constitute a complex dynamical system and its dynamic analysis requires combined background of fluid dynamics in containers with cross-sections that are difficult to analyze and dynamics of articulated vehicles. The dynamic interaction of these two systems is not a simple task. This article addressed some problems and results of road tankers dynamics, stability and related problems.

The design of liquid containers of road vehicles requires full knowledge of the liquid sloshing natural frequencies for different values of fill depth and tank cross-section. The liquid natural frequencies in containers with cross-sections commonly used in road tankers have been presented with more emphasis on elliptic and generic cross-sections. Within the frame work of linear theory, equivalent mechanical models of liquid sloshing mass in the form of mass-spring-dashpot systems, simple pendulum, and Trammel pendulum have been developed. Mass-spring-dashpot and simple pendulum equivalent models are well documented by Ibrahim [51]. However, the Trammel pendulum, convenient for elliptic containers, has been presented in details. With reference to the design of tank cross-section, many researchers developed optimum design of liquid containers geometry, which results in a minimum overturning moment in certain ranges of the fill level and lateral acceleration. The results of these studies have been discussed.

The rollover scenarios of road tankers based on computer simulations indicated that the vehicle may fall onto its side but continue to rotate in roll on the flat ground surface. During rollover, the dynamic load factor time evolution of tires on different axels in the presence of liquid cargo and frozen liquid cargo were generated to identify the influence of liquid sloshing loads on rollover. Equally important is the transient liquid motion on the resulting destabilizing forces and moments imposed on the tank vehicle. For this reason, there are international criteria and regulations established to set a static rollover threshold for the lateral acceleration. Note that if a vehicle is directionally stable, a restoring moment is produced in a direction opposite to the rotational disturbance. The directional stability, which measures the tendency of a vehicle to return to its original direction in relation to the on-coming road medium when rotated away from that original direction has received many studies.

Most of the work was based on the quasi-dynamics approach although some efforts have been devoted for computer simulation of utilizing computational fluid dynamics incorporated with truck computer simulation. Note computational fluid dynamics has its limitations, in particular when the fluid free surface experiences breaking waves and hydrodynamic impact. The introduction of the power law for simulating the hydrodynamic impact has not been utilized in the literature. Potential research activities should be devoted to modify the Trammel pendulum to accommodate the power law and to develop its equivalent parameters such as mass and its dimensions for the first sloshing mode. One of the serious problems is the impact and rollover of vehicles carrying hazardous liquids. Hydraulic jumps can result in extremely high impact pressures acting on the tank walls in gasoline. This may considerably endanger the stability and maneuvering quality of the vehicle and may cause accidents of road

tankers carrying hazard materials. It is vital that designers understand how the road tankers behave under a wider range of impact and roll-over conditions. The study of impact resistance of road tankers carrying hazardous materials may include the severity of damage from a range of impacts on various parts of the tank, the effect of changes to tank material, thickness and baffle spacing and the effect of tank side protection.

Some research activities have been devoted to study the dynamic coupling of liquid sloshing dynamics with the vehicle dynamics under different maneuver scenarios. For example, during vehicle braking, the analytical model of 11 equations of motion based on the work of Yan and Rakheja [129] is presented. In view of complexity of the coupled system, most studies were performed using computer simulations in parallel to actual road experiments on test tracks. However, as mentioned, computer simulations have their limitations.

References

1. Aliabadi, S., Johnson, A., Abedi, J.: Comparison of finite element and pendulum models for simulation of sloshing. Comput. Fluids **32**, 535–545 (2003)
2. Aquaro, M.: Stability of Partially Filled Tanker Trucks using a Finite Element Modeling Approach, MS Thesis, West Virginia University (1999)
3. Aquaro, M.J., Mucino, V.H., Gautam, M., Salem, M.: A finite element modeling approach for stability analysis of partially filled tanker trucks. SAE paper 1999-01-3708 (1999)
4. Ardakani, H.A., Bridges, T.J.: Dynamic coupling between shallow-water sloshing and a vehicle undergoing planar rigid-body motion, Technical Report, University of Surrey: available electronically http://personal.maths.surrey.ac.uk/st/T.Bridges/SLOSH/ (2009)
5. Ardakani, H.A., Bridges, T.J.: Dynamic coupling between shallow-water sloshing and horizontal vehicle motion. Eur. J. Appl. Math. **21**(6), 479–517 (2011)
6. Azadi, S., Jafari, A., Samadian, M.: Effect of tank shape on roll dynamic response of an articulated vehicle carrying liquids. Int. J. Heavy Veh. Dyn. **21**(3), 221–240 (2014a)
7. Azadi, S., Jafari, A., Samadian, M.: Effect of parameters on roll dynamic response of an articulated vehicle carrying liquids. J. Mech. Sci. Tech. **28**(3), 837–848 (2014b)
8. Barton, M.S., Corson, D., Quigley, J., Emami, B., Kush, T.: Tanker truck sloshing simulation using Bi-directionally coupled CFD and multi-body dynamics solvers. SAE Tech Paper 2014-01-2442 (2014)
9. Battelle: Comparative risks of hazardous materials and non-hazardous materials truck shipment accidents/ incidents. Final Report. Contract No. DTFH61-98-C-00060. http://www.fmcsa.dot.gov/Pdfs/HMRiskFinalReport.pdf. Related Tech Brief at http://www.fmcsa.dot.gov/facts-research/research-technology/tech/HAZMAT-Technical-Briefing.htm (2001)
10. Battelle: Hazardous Materials Serious Crash Analysis: Phase 2. Final report. Contract DTMC75-01-D-00003/TO No. 02 (2005)
11. Battelle: A simulation approach to estimate the efficacy of meritor WABCO's improved Roll Stability Control (RSC), by Houser, A., Pape, D., McMillan, N., Task 5.4 Report. Contract DTFH61-96-C-00077, Task Order 7732, Report No. FMCSA-MCRR -06-006, 48p (2006)
12. Battelle: Analysis and documentation of industry benefits and costs for the improved roll advisor and controller technology, Murray, D., Shakelford, S., Houser, A., Task 5.5 Report. Contract DTFH61-96-C-00077, Task Order 7732, Report No. FMCSA-RRT-09-020, 69p (2009)
13. Bauer, H.F.: On the destabilizing effect of liquids in various vehicles, part I. Vehicle Syst. Dyn. Int. J. Veh. Mech. Mobility **1**, 227–260 (1972)

14. Bauer, H.F.: Dynamic behavior of an elastic separating wall in vehicle containers: Part I. Int. J. Vehicle Des. **2**(1), 44–77 (1981)
15. Bauer, H.F.: Dynamic behavior of an elastic separating wall in vehicle container: Part II. Int. J. Vehicle Des. **3**, 307–332 (1982)
16. Biglarbegian, M., Zu, J.: Tractor-semitrailer model for vehicles carrying liquids. Vehicle Syst. Dyn. **44**(11), 871–885 (2006)
17. Billing, J.R., Patten, J.D.: An assessment of tank truck roll stability. Technical report, Transport Dangerous Goods Directorate, Ottawa (2005)
18. Bohn, P.F. Butler, M.C., Dunkle, H.D., Eshleman, R.L.: Computer simulation of the effect of cargo shifting on articulated vehicles performing braking and cornering maneuvers, Technical Report, Vol. 2, The John Hopkins University (1981)
19. Bottiglione, F., Mantriota, G.: Simplified model and experimental insight of partially filled, tank vehicles dynamics. In: Proceedings 12^{th} International Federation for the Promotion of Mechanism and Machine Science (IFToMM) World Congress Besançon (France), 6p (2007a)
20. Bottiglione, F., Mantriota, G.: Tank vehicles: modeling and testing, 10p. www.dipmat.univpm.it/aimeta2009/Atti%20Congresso/MECCANICA_MACCHINE/Bottiglione_paper171.pdf (2007b)
21. Bottiglione, F., Foglia, M., Mantriota, G., Mastrovito, M.: Liquid slosh in articulated tank vehicles: image-based investigation in field test. Int. J. Heavy Vehicle Syst. **14**(4), 441–459 (2007)
22. Bottiglione, F., Mantriota, G.: Field tests and validation of dynamical models of tank vehicles Part I: mathematical model and experimental apparatus. Int. J. Heavy Vehicle Syst. **19**(1), 1–22 (2012a)
23. Bottiglione, F., Mantriota, G.: Field tests and validation of dynamical models of tank vehicles Part II: experimental tests and results. Int. J. Heavy Vehicle Syst. **19**(1), 23–39 (2012b)
24. Bouazara, M., Toumi, M., Richard, M.J.: Study of the directional stability of fully articulated tank-vehicle under random excitation. Int. J. Vehicle Syst. Model. Test. **9**(2), 193–205 (2014)
25. Brar, G.S., Singh, S.: An Experimental and CFD Analysis of Sloshing in a Tanker, Procedia Technology. In: 2nd International Conference on Innovations in Automation and Mechatronics Engineering (ICIAME-2014), 14, pp. 490–496 (2014)
26. Budiansky, B.: Sloshing of liquids in circular canals and spherical tanks. J. Aerosp. Sci. **27**(3), 161–173 (1960)
27. Casasanta, J.D.: Rollover stability analysis of commercial semi-tanker trucks utilizing a Trammel pendulum model to simulate fluid sloshing, Master's thesis, M.S. Thesis, Binghamton University, State University of New York, Binghamton, NY
28. Chaudhari, C.D., Deshmukh, D., Kulkarni, S.S.: Assessing sloshing effect of fluid in tanker geometry through deployment of CAE. Int. J. Adv. Eng. Res. Stud. /III/I/Oct.–Dec., 33–37 (2013)
29. Cheli, F., D'Alessandro, V., Premoli, A., Sabbioni, E.: Simulation of sloshing in tank trucks. Int. J. Heavy Vehicle Syst. **20**, 1–16 (2013)
30. Chondros, T.G., Michalos, G., Michaelides, P., Fainekos, E.: An approximate method for the evaluation of the roll stiffness of road tankers. J. Automobile Eng. **221**(12), 1499–1512 (2007)
31. Cooker, M.J.: Water waves in a suspended container. Wave Motion **20**, 385–395 (1994)
32. Dai, L., Xu, L.: A numerical scheme for dynamic liquid sloshing in horizontal cylindrical containers. Proc. Inst. Mech. Eng. Part D: J. Automobile Eng. **220**, 901–918 (2006)
33. Dai, L., Xu, L., Setiawan, B.: A new nonlinear approach to analyzing the dynamic behavior of tank vehicles subjected to liquid sloshing. Proc. Inst. Mech. Eng. Part K. J. Multi-body Dyn. **219**(1), 75–86 (2005)
34. D'Alessandro, V.: Modeling of Tank Vehicle Dynamics by Fluid Sloshing Coupled Simulation. Ph.D, Politecnico di Milano, Italy (2011)
35. El-Gindy, M.: An overview of performance measures for heavy commercial vehicles in North America. Int. J. Vehicle Des. **16**(4–5), 441–463 (1995)
36. Elliott, A.S., Slattengren, J., Bujik, A.: Fully coupled fluid/mechanical response prediction for truck-mounted tank sloshing using co-simulation of MSC.Adams and MSC.Dytran. SAE International, Warrendale, Penn, 13p (2006)

37. Ervin, R.D., Mallikarunaroa, C., Gillespie, T.D.: Future configuration of tank vehicles hauling flammable liquids in Michigan, Final Report to Michigan Department of Transportation, Agreement # 78-2230, Highway Safety Research Institute, University of Michigan, Report No. UM-HSRI-80-73, December (1980)
38. Ervin, R.D. Nisonger, R.L.: Analysis of the Roll Stability of Cryogenic Tankers, Final Report to Union Carbide Corp., P.O. No. 131-423003-4-CNiI1, Highway Safety Res. Inst., Univ. of Mich., Report No. UM-HSRI-82-32, September (1982)
39. Ervin, R.D., Barnes, M., Wolfe, A.: Liquid cargo shifting and the stability of cargo tank trucks. Report UMTRI-85-35/1, University of Michigan Transportation level. Research Institute (1985)
40. Ervin, R.D., Mathew, A.: Stability of tank truck combinations on curved road segments in the Yukon, Report UMTRI-87-9. University of Michigan, Ann Arbor, Transportation Research Institute (1987)
41. Gautam, M., Mucino, V., Salem, M., Saunders, E., Aquaro, M.: Automotive stability of heavy-duty truck tractor-tanker combination. Final Report, Fredrick Manufacturing, March (1999)
42. Gillespie, T.D.: The Influence of Slosh and Shifting Loads on Turning and Rollover Behavior, Course Notes, Mechanics of Heavy-Duty Trucks and Truck Combinations, Engineering Summer Conference, University of Michigan, June 15–19 (1985)
43. Gillespie, T.D., Ervin, R.D.: Comparative study of vehicle roll stability, University of Michigan Transportation Research Institute, UMTRI 83–25, Final Report, An Arbor, 74p (1983)
44. Godderidge, B., Turnock, S.R., Tan, M.: Evaluation of a rapid method for the simulation of sloshing in rectangular and octagonal containers at intermediate filling levels. Comput. Fluids **57**, 1–24 (2012)
45. Goru, V. G., 2007, Analysis of the Potential of DynaFlexPro as a Modeling Software by its Application in the Roll Stability of Heavy-Duty Elliptical Tankers using Trammel Pendulum to Simulate Fluid Sloshing, Memoire- Thesis, Erasmus Mundus Master of Mechanical Engineering, Institut National Des Sciences Appliquées De Lyon—France
46. Griffiths, M., Linklater, D.R.: Accidents involving road tankers with flammable loads, traffic authority of new south wales, Research Report 1/84, Jan (1984)
47. Hasheminejad, S.M., Aghabeigi, M.: Liquid sloshing in half-full horizontal elliptical tanks. J. Sound Vib. **324**, 332–349 (2009)
48. Hasheminejad, S.M., Aghabeigi, M.: Transient sloshing in half-full horizontal elliptical tanks under lateral excitation. J. Sound Vib. **330**(14), 3507–3525 (2011)
49. Hasheminejad, S.M., Aghabeigi, M.: Sloshing characteristics in half-full horizontal elliptical tanks with vertical baffles. Appl. Math. Model. **36**, 57–71 (2012)
50. Ibrahim, R.A., Pilipchuk, V.N., Ikeda, T.: Recent advances in liquid sloshing dynamics. ASME Appl. Mech. Rev. **54**(2), 133–199 (2001)
51. Ibrahim, R.A.: Liquid Sloshing Dynamics: Theory and Applications. Cambridge University Press, Cambridge, U.K. (2005)
52. Jafari, S.A., Samadian, M.: Roll dynamic response of an articulated vehicle carrying liquids. Int. J. Automot. Eng. **3**(3), 508–522 (2013)
53. Kang, X.: Optimal Tank Design and Directional Dynamic Analysis of Liquid Cargo Vehicles under Steering and Braking, Ph.D. Thesis, Concordia University, Department of Mechanical Engineering, Montreal, Quebec, Canada (2001)
54. Kang, X., Rakheja, S., Stiharu, I.: Optimal tank geometry to enhance static roll stability of partially filled tank vehicles, SAE Tech Paper 1999-01-3730, 14p (1999)
55. Kang, X., Rakheja, S., Stiharu, I.: Directional dynamics of a partially-filled tank vehicle under braking and steering. In: Proceedings SAE 2000 Bus & Truck Meeting, Portland, Oregon, December, 13p (2000)
56. Kang, X., Rakheja, S., Stihani, I.: Cargo load shift and its influence on tank vehicle dynamics under braking and turning. Heavy Vehicle Syst. Int. J. Vehicle Des. **9**(3), 173–203 (2001)
57. Khandelwal, R.S., Nigam, N.C.: Digital simulation of the dynamic response of a vehicle carrying liquid cargo on a random uneven surface. Vehicle Syst. Dyn. **11**(4), 195–214 (1982)

58. Kobayashi, N., Mieda, T., Shibata, H., Shinozaki, Y.: A study of the liquid slosh response in horizontal cylindrical tanks. ASME J. Press. Vessel Tech. **111**(1), 32–38 (1989)
59. Lamb, M.: Hydrodynamics, Section 259. Dover Publications, N.Y. (1945)
60. Li, X.S, Zheng, X.L, Liu, H.F.: Improved algorithm on roll stability evaluation of partially filled tractor-tank semitrailer, (in Chinese) J. Jilin University **42**(5), 1089–1094 (2012)
61. Li, X.S., Zheng, X.L., Ren, Y.Y., Wang, Y.N., Cheng, Z.Q.: Study on driving stability of tank trucks based on equivalent Trammel pendulum for liquid sloshing. Discrete Dyn. Nat. Soc. **2013**, Article ID 659873, 15p (2013)
62. Lidström, M.: Road tanker overturning: with and without longitudinal baffles, (in Swedish) National Road and Traffic research Institute. Linköping, Sweden, Report No 115 (1977)
63. Mallikarjunarao, C., Fancher, P.: Analysis of the directional response characteristics of double tankers. SAE paper No. 781064 (1978)
64. Mangialardi, L., Mantriota, G.: Stability of an articulated vehicle with suspended cargo. Heavy Vehicle Syst. **8**(l), 83–102 (2001)
65. Mantriota, G.: Influence of suspended cargoes on dynamic behavior of articulated vehicles. Heavy Vehicle Syst. **9**(l), 52–75 (2002)
66. McCarty, J.L., Stephens, D.G.: Investigation of the natural frequencies of fluid in spherical and cylindrical tanks, NASA TN D-252 (1960)
67. Modaressi-Tehrani, K., Rakheja, S., Sedaghati, R.: Analysis of the overturning moment caused by transient liquid slosh inside a partly filled moving tank. Proc. Inst. Mech. Eng. Part D: J. Automob. Eng. **220**(3), 289–301 (2006)
68. Nalecz, A.G., Genin, J.: Dynamic stability of heavy articulated vehicles. Int. J. Veh. Des. **5**(4), 417–426 (1984)
69. NHTSA (2012) FMVSS No. 136: Electronic Stability Control Systems on Heavy Vehicles, National High Traffic Safety Administration, National Center for Statistics and Analysis, US Dept Transportation, Washington, DC, 125p
70. NTSB: Rollover of a truck-tractor and cargo tank semitrailer carrying liquefied petroleum gas and subsequent fire. National Transportation Safety Board (NTSB). Indianapolis, Indiana, Washington, D.C. (2011)
71. Oliva-Leyva, M.: Free wave modes in elliptic cylindrical containers. Eur. J. Mech. B/Fluid **43**, 185–190 (2014)
72. Pacejka, H., Bakker, E.E.: The magic formula tire model. In: Pacejka, H. (ed.) Tyre Models for Vehicle Dynamics Analysis, pp. 1–18. Swets & Zeitlinger, Amsterdam (1993)
73. Papadogiannis, A.S., Farmakopoulos, A.G., Chondros, T.G.: Road tankers axles load share design. Int. J. Heavy Vehicle Syst. **17**(2–4), 256–275 (2010)
74. Pape, D.B., Harback, K., McMillan, N., Greenberg, A., Mayfield, H., Chitwood, J.C., Barnes, M., Winkler, C.B., Blower, D., Gordon, T., Brock, J.: Cargo Tank Roll Stability Study, Final Report, Battelle, U.S. Department of Transportation, Federal Motor Carrier Safety Administration, Washington, D.C (2007)
75. Pape, D., Arant, M., Franzese, O., Attanyake, U., LaClair, T.: U19: Heavy truck rollover characterization (Phase B), Final Report University Transportation Center, Knoxville, TN. National Transportation Research Center, Inc.; Battelle Columbus Div., OH; Oak Ridge National Lab., TN.; Western Michigan Univ., Kalamazoo, 418p (2009)
76. Pape, D.B., Fredman, S.R., Murray, D.C., Lueck, M., Abkowitz, M.D., Fleming, J.: Role of human factors in preventing cargo tank truck rollovers, HMCRP Report 7. Transportation Research Board, Washington, D.C. (2012)
77. Rakheja, S.: Safety dynamics of partly-filled road tankers. In: Proceedings of the 2012 IEEE Intelligent Vehicles Symposium Workshops, Alcalá de Henares, Spain (2012)
78. Rakheja, S., Sankar, S., Ranganathan, R.: Roll plane analysis of articulated tank vehicles during steady turning. Vehicle Syst. Dyn. **17**(1–2), 81–104 (1988)
79. Rakheja, S., Ranganathan, R., Sankar, S.: Field testing and validation of directional dynamics model of a tank truck. Int. J. Vehicle Des. **13**(3), 251–275 (1992)
80. Rakheja, S., Ranganathan, R.: Estimation of the rollover threshold of heavy vehicles carrying liquid cargo: a simplified approach. Heavy Vehicle Syst. A Series Int. J. Vehicle Des. **1**(1), 79–98 (1993)

81. Rakheja, S., Stiharu, I., Kang, X., Romero, J.A.: Influence of tank cross-section and road adhesion on dynamic response of partly filled tank trucks under braking-in-a-turn. J. Vehicle Des. **9**, 223–240 (2002)
82. Ranganathan, R.: Stability Analysis and Directional Response Characteristics of Heavy Vehicles Carrying Liquid Cargo, Ph.D. Thesis, Concordia University, Montreal, Canada (1990)
83. Ranganathan, R.: Rollover threshold of partially filled tank vehicles with arbitrary tank geometry. Proc. Inst. Mech. Eng. Part D J. Automot. Eng. **207**(3), 241–244 (1993)
84. Ranganathan, R., Yang, Y.S.: Impact of liquid load shift on the braking characteristics of partially filled tank vehicles. Vehicle Syst. Dyn. **26**(3), 223–240 (1989)
85. Ranganathan, R., Rakheja, S., Sankar, S.: Kineto-static roll plane analysis of articulated tank vehicles with arbitrary tank geometry. Int. J. Vehicle Des. **10**(1), 89–111 (1989a)
86. Ranganathan, R., Rakheja, S., Sankar, S.: Steady turning stability of partially filled tank vehicles with arbitrary tank geometry. ASME J. Dyn. Syst. Measur. Control **111**(3), 481–489 (1989b)
87. Ranganathan, R., Rakheja, S., Sankar, S.: Influence of liquid load shift on the dynamic response of articulated tank vehicles. Vehicle Syst. Dyn. **19**(4), 177–200 (1990)
88. Ranganathan, R., Rakheja, S., Sankar, S.: Directional response of a B-train vehicle combination carrying liquid cargo. ASME J. Dyn. Syst. Measur. Control **115**(1), 133–139 (1993a)
89. Ranganathan, R., Ying, Y., Miles, J.B.: Analysis of fluid slosh in partially filled tanks and their impact on the directional response of tank vehicles. SAE Trans. **102**, 502–505 (1993b)
90. Ranganathan, R., Ying, Y., Miles, J.B.: Development of a mechanical analogy model to predict the dynamic behavior of liquids in partially filled tank vehicles, p. 942307. SAE Tech Paper, SAE International Truck and Bus Meeting (1994)
91. Ranganathan, R., Yang, Y.: Impact of liquid load shift on the braking characteristics of partially filled tank vehicles. Vehicle Syst. Dyn. **26**, 223–240 (1996)
92. Rattayya, J.V.: Sloshing of liquids in axisymmetric ellipsoidal tanks. In: Proceedings 2nd AIAA Aerospace Science Meeting, New York, AIAA Paper 65–114, 20p (1965)
93. Robinson, B., Webb, D., Hobbs, J., London, T.: Technical assessment of petroleum road fuel tankers, Report PPR724. Wokingham, Berkshire, U.K, Transport Research Laboratory (2014)
94. Romero, J.A., Hildebrand, R., Martinez, M., Ramirez, O., Fortanell, J.M.: Natural sloshing frequencies of liquid cargo in road tankers. Int. J. Heavy Vehicle Syst. **12**(2), 121–138 (2005)
95. Romero, J.A., Ramirez, O., Fortanell, J.M., Martinez, M., Lozano, A.: Analysis of lateral sloshing forces within road containers with high fill levels. Proc. Inst. Mech. Eng. Part D: J. Automob. Eng. **220**, 302–312 (2006)
96. Romero, J.A., Lozano, A., Ortiz, W.: Modelling of liquid cargo—vehicle interaction during turning maneuvers. In: Proceedings 12th International Federation for the Promotion of Mechanism and Machine Science (IFToMM) World Congress, Besançon (France), 5p (2007)
97. Romero, J., Betanzo-Quezada, E., Lozano-Guzman, A.: A methodology to assess road tankers rollover trend during turning. SAE Int. J. Commercial Vehicles **6**(1), 93–98 (2013)
98. Rumold, W.: Modeling and simulation of vehicles carrying liquid cargo. Multibody Syst. Dyn. **5**(4), 351–374 (2001)
99. Salem, M. I.: Rollover Stability of Partially Filled Heavy-Duty Elliptical Tankers Using Trammel Pendulums to Simulate Fluid Sloshing, Ph.D. Thesis, West Virginia University, Department of Mechanical and Aerospace Engineering (2000)
100. Salem, M.I., Mucino, V., Aquaro, M., Gautam, M.: Review of parameters affecting stability of partially filled heavy duty tankers. In: Proceedings of the SAE International Truck & Bus Meet Expo, Detroit, MI, paper no. 1999-01-3709 (1999)
101. Salem, M.I., Mucino, V.H., Saunders, E., Gautam, M.: Lateral sloshing in partially filled elliptical tanker trucks using a Trammel pendulum. Int. J. Heavy Vehicle Syst. **16**(1–2), 207–224 (2009)
102. Sankar, S., Rakheja, S., Sabounghi, R.N.: Stability analysis of liquid tank vehicle. In: Proceedings International Symposium on Heavy Vehicle Weights and Dimensions, pp. 131–138(June), pp. 8–13: Kelowna. British Columbia, Transportation Association of Canada (1988)

103. Sankar, S., Rakheja, S., Ranganathan, R.: Directional response of partially filled tank vehicles. SAE Tech Paper No. **892481**, 12p (1989)
104. Sankar, S., Ranganathan, R., Rakheja, S.: Impact of dynamic fluid slosh loads on the directional response of tank vehicles. Vehicle Syst. Dyn. **21**, 385–404 (1992)
105. Sankar, S., Surial, S.: Sensitivity analysis approach for fast estimation of rollover stability of heavy articulated vehicles during steady state turning. Int. J. Heavy Vehicle Syst. **1**(3), 282–303 (1994)
106. Slibar, A., Troger, H.: The steady state behavior of tank trailer system carrying rigid or liquid cargo. VSD-IUTAM Symp Dynamics of Vehicles on Roads & Trucks, Vienna, 256–264 (1977)
107. Southcombe, E.J., Ruhl, R.L., Kuznetsov, E.: Fluid load analysis within the static roll model. Paper 2000-01-3476, Society of Automotive Engineers Truck and Bus Meeting (2000)
108. SS: Liquid tanker stability, S and S Inc., Montreal (Quebec), Transportation Development Center, Montreal (Quebec), Concordia University. Concave Research Center (Canada). 1350 (1990)
109. Stedtnitz, W., Appel, H.: Experimental and analytical simulation of liquid sloshing in tank trucks. SAE Tech Paper 885110, 12p (1988)
110. Strandberg, L.: Lateral stability of road tankers, National Road and Traffic Research Institute, VIT Report 138A. Linköping, Sweden (1978)
111. Tesar, M.: The influence of liquid load motion on rollover stability of road tankers. Int. J. Heavy Vehicle Syst. **12**(2), 121–138 (2005)
112. Thomassy, F.A., Wendel, G.R., Green, S.T., Jank, A. C.: Coupled simulation of vehicle dynamics and tank slosh. Phase 2 interim Report, TLRF no. 368. Technical report, U.S. Army TARDEC Fuels and Lubricants Research Facility (SwRI), Southwest Research Institute, San Antonio, TX, (2003)
113. Toumi, M., Bouazara, M., Richard, M.J.: Analytical and numerical analysis of the liquid longitudinal sloshing impact on a partially filled tank-vehicle with and without baffles. Int. J. Vehicle Syst. Model. Test. **3**(3), 229–249 (2008)
114. Toumi, M., Bouazara, M., Richard, M.J.: Impact of liquid sloshing on the behavior of vehicles carrying liquid cargo. Eur. J. Mech. A/Solids **28**(5), 1026–1034 (2009)
115. Toumi, M., Bouazara, M., Richard, M.J.: Development of analytical model for modular tank vehicle carrying liquid cargo. World J. Mech. **3**(2), 122–138 (2013)
116. TruckSim: TruckSim User Reference Manual, Version 4.0.2. Mechanical Simulation Corporation, Ann Arbor, MI, 287p (1997)
117. Wang, C.Z., Khoo, B.C.: Finite element analysis of two-dimensional nonlinear sloshing problems in random excitations. Ocean Eng. **32**(2), 107–133 (2005)
118. Wasfy, T.M., O'Kins, J., Smith, S.: Experimental validation of a time-accurate finite element model for coupled multibody dynamics and liquid sloshing. SAE Congress and Exhibition, SAE Paper No. 2007-01-0139, 18p. Also Trans. J. Passenger Cars: Mechanical Systems (2007)
119. Wasfy, T.M., O'Kins, J., Smith, S.: Experimental validation of a coupled fluid-multibody dynamics model for tanker trucks. SAE Int. J. Commercial Vehicles **1**(1), 71–88 (2008)
120. Wendel, G.R., Green, S.T., Burkey, R.C.: Coupled Simulation of Vehicle Dynamics and Tank Slosh, Phase 1: Report Testing and Validation of Tank Slosh Analysis, Southwest Research Institute, San Antonio, TX, Interim Report, TFLRF No. 364, Defense Technical Information Center, Fort Belvoir, 59p (2002)
121. Winkler, C.B., Karamihas, S.M., Bogard, S.E.: Roll stability performance of heavy vehicle suspensions. SAE Tech Paper Series International Truck and Bus Meeting and Exposition, pp. 1–14. Toledo, OH (1992)
122. Winkler, C.B.: Rollover of heavy commercial vehicles. UMTRI Research Review, University of Michigan, An Arbor, MI **31**(4), 20p (2000)
123. Woodrooffe, J.H.F.: Evaluation of Dangerous Goods Vehicle Safety Performance, Report TP 13678E. Report for Transport Canada, Transport Dangerous Goods Directorate, Ottawa (2000)

124. Wu, D.H. and Lin, Y.H.: Directional response analysis of tractor-trailer with multi-axle-steering carrying liquid load. SAE Paper 2005-01-0415 (2005)
125. Xu, L., Dai, L., Dong, M., Setiawan, B.: Influence of liquid slosh on ride quality of liquid cargo tank vehicles. Proc. Inst. Mech. Eng. Part D: J. Automob. Eng. **218**, 675–684 (2004)
126. Yan, G. R.: Liquid Slosh and its Influence on Braking and Roll Responses of Partly Filled Tank Vehicles, Ph.D. thesis, Department of Mechanical and Industrial Engineering, Concordia University, Montreal, Canada (2008)
127. Yan, G.R., Siddiqui, K., Rakheja, S., Modaressi, K.: Transient fluid slosh and its effect on the rollover-threshold analysis of partially filled conical and circular tank trucks. Int. J. Heavy Vehicle Syst. **12**(4), 323–343 (2005)
128. Yan, G.R., Rakheja, S.: Straight-line braking dynamic analysis of a partly filled baffled and unbaffled tank truck. Proc. Ins.t Mech. Eng. Part D: J. Automob. Eng. **223**(1), 11–26 (2009)
129. Yan, G.R., Rakheja, S.: Fluid structure interaction induced by liquid slosh in partly filled road tankers. World Acad. Sci. Eng. Technol. **4**(10), 701–706 (2010)
130. Yang, X., Rakheja, S., Stiharui, I.: Identification of lateral dynamics and parameter estimation of heavy vehicles. Mech. Syst. Sig. Proc, **125**, 611–626 (1998)
131. Younesian, D., Abedi, M., Hazrati Ashtiani, I.: Dynamic analysis of a partially filled tanker train travelling on a curved track. Int. J. Heavy Vehicle Syst. **17**, 331–358 (2010)
132. Younesian, D., Askari, H., Saadatnia, Z., Esmailzadeh, E.: Analytical solutions for nonlinear lateral sloshing in partially-filled elliptical tankers. In: Proceedings of the ASME International Technical Conference and Computers and Information in Engineering Conference, 23rd Biennial Conf Mechanical Vibration and Noise, Parts A & B, Vol. 1, pp. 135–139. Washington, DC, Paper No. DETC2011-48468 (2011)
133. Zheng, X.L., Li, X.S., Ren, Y.Y.: Analysis of rollover threshold for partially-filled tank vehicles impacted by transient liquid sloshing. J. Beijing Inst. Technol. **21**(supplement 2), 169–174 (2012a)
134. Zheng, X.L., Li, X.S., Ren, Y.Y.: Equivalent mechanical model for lateral liquid sloshing in partially filled tank vehicles. Math. Probl. Eng. **2012**, Article ID 162825, 22p (2012b)

Chapter 2
Simulation of Abrasive Wear with a Coupled Approach Considering Particles of Different Sizes

Florian Beck and Peter Eberhard

Abstract Abrasive wear is a damage caused by small solid particles which are transported by the working fluid of a hydraulic machine. In case of an impact of an abrasive particle, material of the boundary surface is removed or deformed. Several material parameters have an influence on the amount of the removed material. In complex industrial applications, like the impact of a free jet with particle loading on a pelton bucket of a turbine in a water power plant, the abrasive particles, i.e. the loading of the fluid, often consist of geomaterials. In this paper a new approach is presented for accurately modelling abrasive wear due to a loading consisting of particles of geomaterials with different sizes. The fluid is modelled with the Smoothed Particle Hydrodynamics method. This method is a complete meshless method which is very suitable for highly transient flows with free surfaces. The loading is described with two different methods depending on the size of the particle. Smaller particles are modelled with a transport equation and larger ones with the Discrete Element Method. In this study the resulting wear patterns, due to the impact of a free jet with loading consisting of particles with different diameters, are presented.

2.1 Introduction

There are various reasons for the loss of efficiency of a hydraulic machine. One of them is damage due to abrasive wear. Of course there are several other damage mechanisms, e.g. like cavitation, but in this work the focus is on abrasive wear. Small solid particles can cause damage to the surface of a hydraulic machine when they have a contact with the surface. The small solid particles are the loading of the fluid as it is the case in many engineering systems, e.g. small sand particles from the reservoir in a water power plant. Besides geomaterials like sand particles, the loading can consist of other small particles, e.g. metall chips which are already removed from the surface. Especially in closed systems this is a problem, because they are not removed from the

F. Beck · P. Eberhard (✉)
Institute of Engineering and Computational Mechanics, University of Stuttgart,
Pfaffenwaldring 9, 70569 Stuttgart, Germany
e-mail: peter.eberhard@itm.uni-stuttgart.de

M. Belhaq (ed.), *Recent Trends in Applied Nonlinear Mechanics and Physics*,
Springer Proceedings in Physics 199, https://doi.org/10.1007/978-3-319-63937-6_2

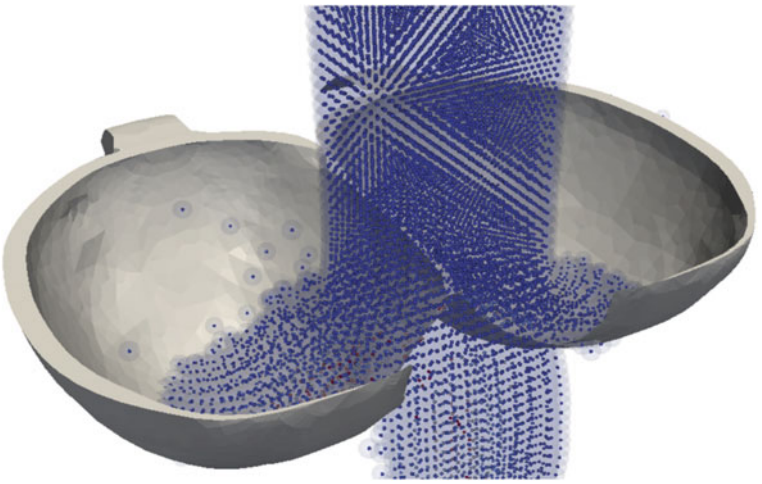

Fig. 2.1 Impact of a free jet on a pelton bucket

cycle and can cause new damage. Here, it is assumed that the loading consists only of geomaterials. Besides the loading of the fluid, the accurate modelling of the free surface of a transient sloshing fluid can be a challenging task, like e.g. the scenario with an impact of a free jet shown in Fig. 2.1.

In classical fluid dynamics a mesh is used for calculating the flow field. In case of the impact of a free jet the free surface of the fluid is strongly deformed. The mesh has to be remeshed, or a simulation method like the Volume of Fluid (VOF) method has to be applied. Disadvantages of methods like the VOF method are, that large areas have to be discretized and the surface has to be tracked. Here, an approach for modelling abrasive wear is presented which consists only of mesh-free methods. The fluid is described as in classical fluid dynamics simulations with the Navier-Stokes equations and for the discretisation the Smoothed Particle Hydrodynamics (SPH) method is applied. The loading is assumed to consist of geomaterials and is modelled with two different methods. The newly developed approach which is presented is able to handle various particle sizes simultaneously. The large particles of the loading are simulated with the Discrete Element Method (DEM) and the smaller ones with a transport equation. They are not resolved in detail like the larger ones. The boundary geometry is described with triangles which are in the program also handled as particles. The removed material due to the impact of a solid particle from the loading of the fluid, is calculated with a wear model.

The article is structured as follows. First, the most important details of the SPH method are presented. A typical example for the validation of the SPH method is discussed, the lid driven cavity. This is a commonly used example in classical fluid dynamics. Here, two different methods for modelling the loading of the fluid are applied. The first one is the DEM which was successfully applied in [1]. Therefore, some details about the DEM and the coupling of the DEM with the SPH method

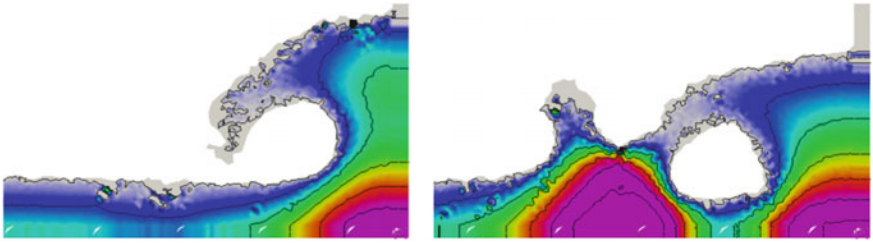

Fig. 2.2 Example of a heavily sloshing fluid simulated with the SPH method

are explained. Then, the second one, the transport equation which was successfully applied in [2], is presented. Two different examples are shown where a fluid with loading is simulated. The purpose is to demonstrate the use of a transport equation for modelling a fluid with loading. These are a two dimensional sloshing simulation of a collapsing water column and a multiphase flow problem. After the discussion of the details for handling a fluid with loading which consists of solid particles of different sizes, the results of a three dimensional collapsing water column with loading are shown. Then the abrasive wear model for calculating the damage on the boundary geometry is presented. Finally, in the end a simulation of free jet with loading, impacting on a pelton bucket is discussed and conclusions are drawn.

2.2 Simulation Method

In the following section, the important details for the applied simulation methods are introduced. Besides, some simulation results for the validation of the newly developed and implemented methods are discussed.

2.2.1 Smoothed Particle Hydrodynamics Method

The SPH method, which was introduced by different groups, see e.g. [14] and [24], can be used for the discretisation of partial differential equations. Commonly simulated examples are highly transient sloshing processes in engineering systems which have free surfaces with large deformations. Exemplarily, a two dimensional breaking wave simulated with the SPH method is shown in Fig. 2.2. In this figure, the fluid is color coded with the pressure (red maximum pressure and blue minimum pressure) and for the visualisation a surface plot is chosen. For plotting a continuous surface a Delaunay triangulation is applied.

The free surface of the wave can be accurately modelled without any additional computational methods. This is possible due to the mesh-less character of the SPH

method. The computation of complex interfaces with large deformations is one of the strengths of the SPH method. Other examples, where the SPH method is applied for modelling fluid flow, are scenarios with fluid-solid interaction [5, 21], free complex surfaces [27, 28] or [38], and multi-phase flow [6, 18]. A detailed review about some more research studies can be found in [22].

The fluid is described with the Navier-Stokes equations. Taking into account that a fluid flow of an engineering process is investigated, turbulence is modelled like in [44]. The conservation of mass of the fluid method requires

$$\nabla \cdot \mathbf{v} = 0 \tag{2.1}$$

and the conservation of the momentum is ensured by

$$\rho \left(\frac{\partial \mathbf{v}}{\partial t} + \mathbf{v} \cdot \nabla \mathbf{v} \right) = \mu \nabla^2 \mathbf{v} - \nabla p + \mathbf{f} + \nabla \mathbf{R}. \tag{2.2}$$

In these equations, p is the pressure, $\mathbf{f}$ are the body forces acting on the fluid, $\mathbf{v}$ is the velocity, ρ the density, μ the viscosity of the fluid and $\mathbf{R}$ are the Reynolds turbulence stresses. They are calculated by

$$R_{ij} = \rho \left(2\nu_t S_{ij} - \frac{2}{3} k \delta_{ij} \right). \tag{2.3}$$

In this equation ν_t is the turbulence eddy viscosity, k is the turbulence kinetic energy, S_{ij} are the components of the strain rate tensor and δ_{ij} is the Kronecker delta function [23]. Other possibilities for modelling turbulence flows are the direct numerical simulation or the large eddy simulation, but in this work we are only interested in the forces and not the turbulent structures itself and so a simple description is sufficient.

There are two different approaches for calculating the pressure when applying the SPH method. The first one is the use of an equation of state (EoS). When an EoS is applied, it is called the weakly compressible approach. The pure weakly compressible approach suffers from a noisy pressure field. For improving the accuracy a Riemann solver can be applied, see [16, 45] or [34]. The second approach is to use the Poisson equation

$$\nabla \cdot \left(\frac{1}{\rho} \nabla p \right) = \frac{1}{\Delta t} \nabla \cdot \mathbf{v}^*, \tag{2.4}$$

proposed by [7]. Here, $\mathbf{v}^*$ is the intermediate velocity and t the time.

The basic steps for transforming the Navier-Stokes equations are the kernel and the particle approximation. For details see [22]. One important point herein is the choice of the so-called kernel function. In this work, mainly a Wendland kernel [40] is used, because lower order kernel functions have a negative influence on the accuracy of the simulation [30].

A commonly used example for the validation of the simulation methods for classical mesh-based methods is the lid driven cavity. A small cavity is filled with a

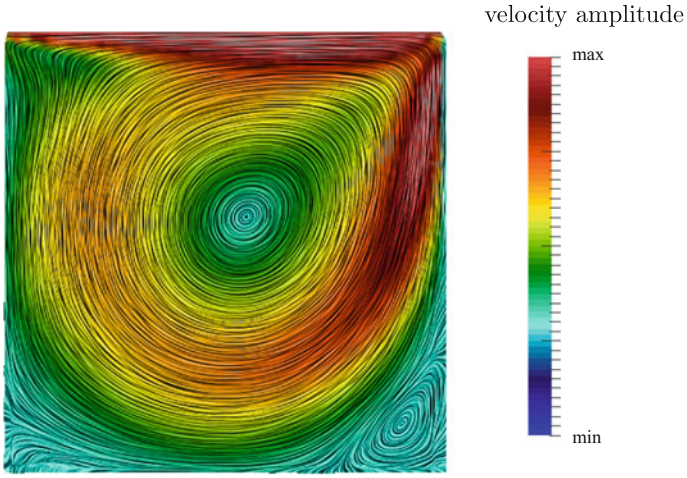

Fig. 2.3 Velocity amplitude of the lid driven cavity

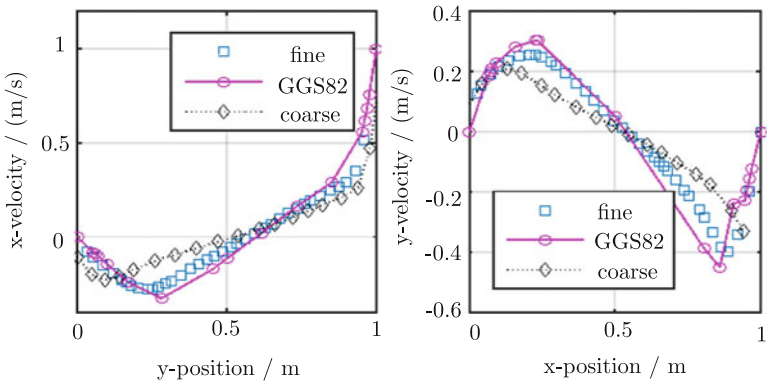

Fig. 2.4 Velocity profile in x and y direction

fluid and at the top a constant horizontal fluid flow velocity is defined as boundary condition. At the beginning the fluid is at rest and then a static flow is evolving, as shown in Fig. 2.3.

The fluid is shown as a surface plot and color coded with the velocity amplitude. For more details on the example see [46]. For the validation, the velocity profiles along the x- and y-axis are compared. Here, the velocity profiles are compared with [15]. In Fig. 2.4 the velocity profiles in x- and y-direction are shown.

The velocity profiles for two discretisations with different numbers of SPH particles and data from literature [15] (GGS82) are shown. It can be seen that the results are in good agreement. The accuracy of the simulation results can be increased with a finer discretisation. It can be observed that the SPH method is able to handle the initial transient process and to describe the quasi-static solution of this example.

2.2.2 Discrete Element Method

When simulating granular material, e.g. like the angle of repose of a sand pile, the DEM is a suitable method. The method was introduced for the modelling of bulk material [8], but it is also possible to describe particles that are freely moving inside the simulation scenario [11]. Also, it is possible to model failure of geomaterials, like e.g. breakable railway ballast [12]. The basic idea behind the method is, to describe a single grain of a geomaterial, e.g. a sand grain, with a particle or apply some coarse-graining approach [31]. The forces between adjacent particles are calculated with a force law, e.g. a Hertzian contact law. The dynamics of a single particle is described with the Newton-Euler equations, see [36], which yield

$$m_i \mathbf{a}_i = \mathbf{f}_i, \tag{2.5}$$

$$\mathbf{I}_i \cdot \dot{\boldsymbol{\omega}}_i + \boldsymbol{\omega}_i \times \mathbf{I}_i \cdot \boldsymbol{\omega}_i = \mathbf{l}_i. \tag{2.6}$$

Here, $\mathbf{I}_i$ is the inertia tensor, m_i is the mass, $\mathbf{l}_i$ and $\mathbf{f}_i$ are applied torques and forces, $\mathbf{a}_i$ is the translational acceleration and $\boldsymbol{\omega}_i$ is the angular velocity.

One approach for calculating the contact force between two adjacent particles is, to take into account the distance and the velocity difference between the two particles and multiply them with constant factors. These constant factors have to be calibrated for each simulation scenario. An approach which is more accurate is to apply a Hertzian contact law where the force is calculated by

$$F_{ij} = k_{ij} \psi_{ij}^{\frac{3}{2}} + d\dot{\psi}_{ij} \tag{2.7}$$

with the abbreviations

$$k_{ij} = \frac{4}{3\pi(h_i + h_j)} \left(\frac{r_i r_j}{r_i + r_j} \right)^{\frac{1}{2}} \text{ and } h_j = \frac{1 - \nu_j^2}{\pi E_j}. \tag{2.8}$$

Here, E_j is the Young's modulus of the granular material, r_j is the radius of a particle, ν_j the Poisson number, d a damping parameter and ψ_{ij} the overlap of two particles.

2.2.3 DEM-SPH Coupling

There are different approaches for coupling DEM particles with SPH particles. Depending on the simulation scenario the method for coupling the particles has to be chosen. One possibility is to distinguish the approaches by the ratio of the initial distance of the SPH particles to the diameter of the DEM particles. The diameter of the DEM particles depends on the geomaterials. For a ratio, where the initial distance of the SPH particle is larger than the diameter of the DEM particles an approach like [35] has to be applied. In this approach the force between two adjacent particles is

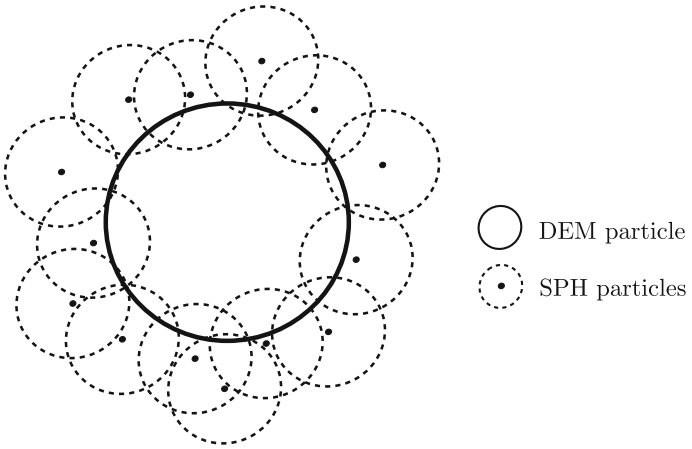

Fig. 2.5 Sketch of the coupling of a DEM particle and SPH particles

modelled with a force law that takes into account drag, buoyancy, and shear stress without resolving the flow around a single DEM particle. For a ratio where the initial distance is significantly smaller, the contact forces can be modelled as penalty forces like in [33]. In Fig. 2.5, the principle of this approach is shown.

The DEM particle is visualised with a circle and the SPH particles are visualised with a point which represents the center and a dotted circle which marks the smoothing length.

This approach is applied here for coupling DEM with SPH particles. The ratio of the initial distance has to be chosen as shown in Fig. 2.5 to be able to resolve the flow around the DEM particle accurately. The coupling force $\mathbf{f}_c$ is calculated taking into acount the distance and velocity difference. It is applied to the equation for the conservation of momentum for the fluid which changes to the form

$$\rho\left(\frac{\partial \mathbf{v}}{\partial t} + \mathbf{v}\cdot\nabla\mathbf{v}\right) = -\nabla p + \mu\nabla^2\mathbf{v} + \mathbf{f} + \mathbf{f}_c \tag{2.9}$$

and for a DEM particle i

$$m_i\mathbf{a}_i = \mathbf{f}_i + \mathbf{f}_c. \tag{2.10}$$

This approach for coupling DEM and SPH particles has the advantage that it is not limited to a certain Reynolds number due to the choice of the formula for the settling-velocity in other approaches. However, the computational effort can increase significantly depending on the flow and the geomaterials. The initial distance of the SPH particles depends on the fluid flow, which has to be resolved in the simulation scenario, and the diameter of the DEM particle, which depends on the geomaterials to be modelled. Taking these factors into account the ratio of the initial distance of

the SPH particles to the diameter of the DEM particles for the discretisation has to be chosen.

2.2.4 Transport Equation

The other approach for handling the loading of the fluid besides the DEM is using a transport equation. The idea behind this approach is, that a sand particle is not resolved in detail but considered as a ratio of the amount of fluid to sand particles at every SPH particle. Every SPH particle has therefore an additional property, the loading concentration. In Fig. 2.6, a sloshing fluid with loading is shown, whereby the loading is modelled with the transport equation. The SPH particles are visualised with a dot and a transparent sphere which visualises the smoothing length.

At the beginning only a few SPH particles inside the water column are initialized with a concentration greater than zero. The fluid sloshes then inside a closed tank from the left to the right. The loading is distributed in the whole fluid due to this highly transient sloshing process. The change in time of the concentration between adjacent SPH particles during the simulation in this flow is calculated by

$$\frac{\partial C}{\partial t} = -\mathbf{v}_\mathrm{s} \cdot \nabla C + \frac{1}{\rho} \nabla (D \nabla C) + J. \tag{2.11}$$

In this equation C is the concentration, $\mathbf{v}_\mathrm{s}$ is the sedimentation velocity of the sand phase, D the diffusion coefficient, and a source term J. In this paper, the source term is neglected in this equation, because there is no exchange of abrasive particles with the boundary geometry.

The idea to describe the second phase of a multiphase flow with the transport equation was also successfully applied for simulating salt diffusion [29], erosion [20] or transport of sediment in coastal areas [37].

One important point of this approach is the choice of the sedimentation velocity. One formula was used in [20] where the velocity is calculated by

$$\mathbf{v}_\mathrm{s} = \frac{2}{9} r_\mathrm{s}^2 \frac{\rho_\mathrm{s} - \rho_\mathrm{f}}{\mu} \mathbf{g} f(C) \tag{2.12}$$

with influence of the concentration

$$f(C) = 1 - (C/C_\mathrm{max})^y. \tag{2.13}$$

In these equations, r_s is the radius of a sand grain, $\mathbf{g}$ the gravity, ρ_s is the density, ρ_f is the density of the fluid and C_max is the maximal concentration. The changing concentration over the height of the fluid is taken into account with $y = 4.5$ for the sedimentation velocity. A simplification would be to assume a constant value for

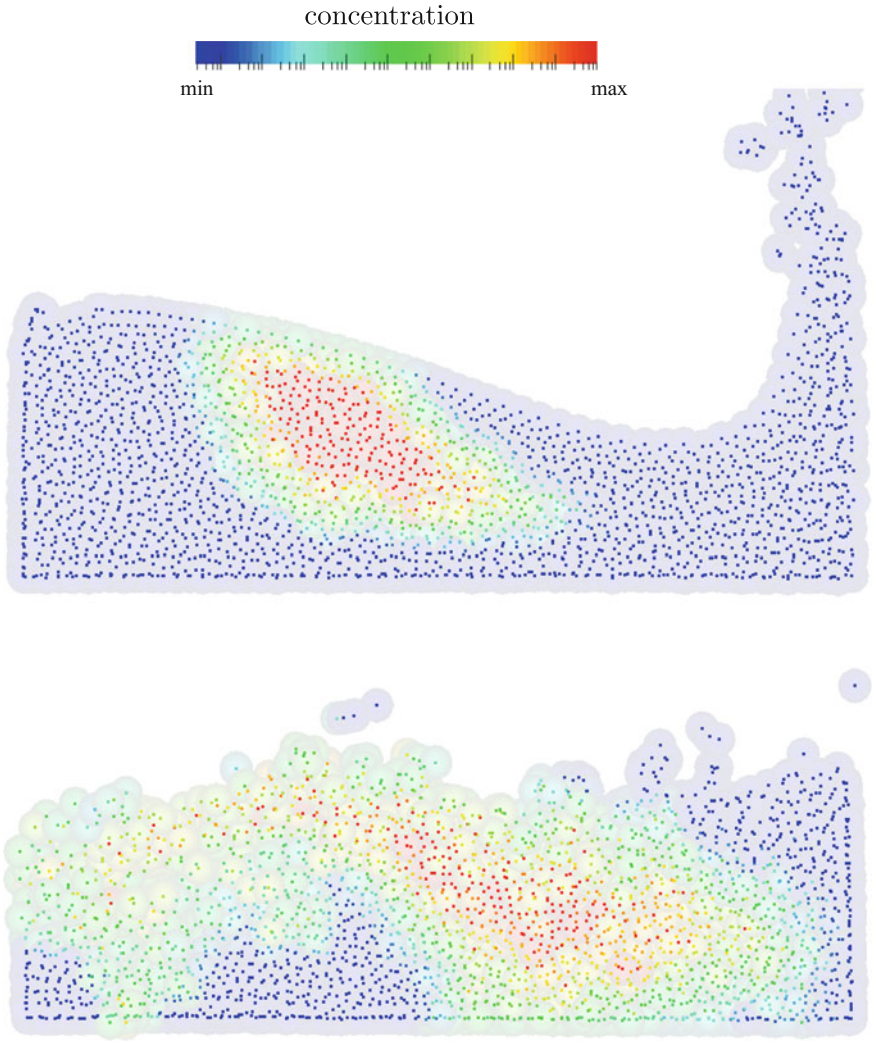

Fig. 2.6 Example of a collapsing water column with loading inside a closed tank. The loading is modelled with the transport equation

the velocity [19]. One crucial point is that (2.12) is only valid for a small range of Reynolds numbers.

Therefore, here the sedimentation velocity is calculated with a different equation which is valid for a larger range. The velocity is calculated according to [43] by

$$\mathbf{v}_\mathrm{s} = \frac{M\nu}{Nd}\left[\sqrt{\frac{1}{4} + \left(\frac{4N}{3M^2}D_*^3\right)^{1/n}} - \frac{1}{2}\right]^n \mathbf{w} f(C) \tag{2.14}$$

with the scaled abrasive particle diameter

$$D_* = d\left[(\rho_\mathrm{s}/\rho - 1.0)\,\frac{g}{\nu^2}\right]^{1/3}, \tag{2.15}$$

the coefficients

$$M = 53.5 \cdot 10^{-0.65 S_\mathrm{f}},\ N = 5.65 \cdot 10^{-2.5 S_\mathrm{f}} \tag{2.16}$$

for taking the shape of the abrasive particle into account and

$$n = 0.7 + 0.9 S_\mathrm{f}. \tag{2.17}$$

Here, the shape factor is calculated as $S_\mathrm{f} = c/\sqrt{ab}$. Thereby, a is the longest, b the intermediate and c is the shortest axis of an abrasive particle. The gravity field $\mathbf{w}$ describes the direction of the sedimentation velocity. Equation (2.14) is valid for Reynolds numbers which are not only < 0.5 and one of the other advantages is that the surface shape of the abrasive particles is considered.

Then, convective term of (2.11) can be calculated as

$$-\mathbf{v}_\mathrm{s} \cdot \nabla C_i = -\sum_j \begin{cases} m_j \dfrac{C_j}{\rho_j} T_{ij} \text{ for } 0 \leq \mathbf{v}_\mathrm{s} \cdot \mathbf{r}_{ij} \\ m_i \dfrac{C_i}{\rho_i} T_{ij} \text{ else} \end{cases} \tag{2.18}$$

with the abbreviation

$$T_{ij} = \left(\mathbf{v}_\mathrm{s} \cdot \frac{\mathbf{r}_{ij}}{|\mathbf{r}_{ij}|}\right) \nabla W(\mathbf{r}_{ij}, h). \tag{2.19}$$

Here, W is the kernel function, h is the smoothing length, ρ_j is the density, m_j is the mass, and C_j is the concentration of a particle j. The particle distance $\mathbf{r}_{ij}$ is calculated as $\mathbf{r}_{ij} = \mathbf{r}_i - \mathbf{r}_j$. Equation (2.18) was introduced by [20], another possibility was proposed in [37], but the approach there is computationally more expensive.

The diffusive term of (2.11) is calculated as

$$\frac{1}{\rho}\nabla(D\nabla C) = \sum_j \frac{m_j D}{\rho_i \rho_j} C_{ij} \frac{\mathbf{r}_{ij}}{|\mathbf{r}_{ij}|^2 + \eta} \nabla W(\mathbf{r}_{ij}, h) \tag{2.20}$$

with the diffusion coefficient $D = 0.1$ and the difference of the concentration C_{ij} of particle i and j. With this approach it is possible to describe a multiphase flow problem including a fluid with loading. With respect to engineering processes it is

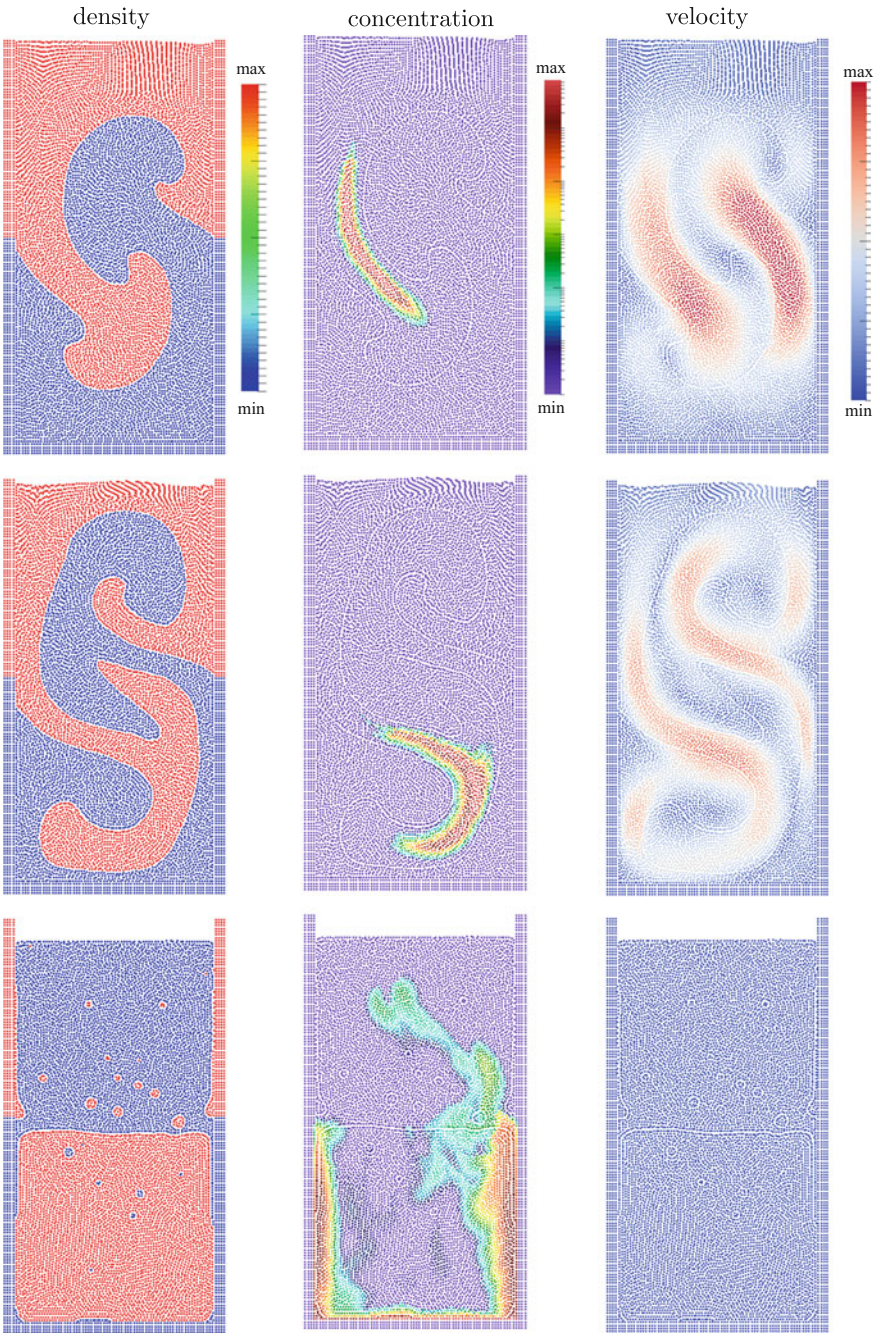

Fig. 2.7 Simulation of three different phases, a light and a heavier fluid and sand particles as loading ($t_1 = 1.4s$, $t_2 = 2.0s$ and $t_3 = 13.2s$)

Table 2.1 Sand grain size after DIN EN ISO 14688-1 [9]

Name	Size (mm)
Fine sand	0.063−0.2
Middle sand	0.2−0.63
Coarse sand	0.63−2

also possible that the fluid is a mixture of different fluids, e.g. water and oil. In doing so the proposed modelling approach for the loading can also be applied to a scenario with three phases, two fluids and a solid phase. Exemplarily in Fig. 2.7, a multiphase flow problem with three different phases is shown.

This example shows that it is possible to model the complex interface between two different fluids and that the approach can handle three different phases. The simulation is inspired by the Raylor-Taylor instability. The data for the fluids are from [7]. At the beginning the heavier fluid is in the upper part of a two dimensional fluid column and the lighter fluid in the lower part. The interface of the two fluids is disturbed by a sine function. Only some of the particles of the heavier fluid are initialized with a concentration greater than zero. The fluids are mixing up during the simulation and in the end the lighter fluid is completely in the upper part. The concentration is also mixed up inside the fluids, but the sedimentation process is much slower and therefore the sediment is still distributed inside the fluid after the segregation of the two fluids.

2.2.5 Loading with Different Particle Sizes

The loading of the fluid is assumed to consist of geomaterials like sand. The classification of sand particles after DIN EN ISO 14688-1 [9] is shown in Table 2.1. In engineering scenarios the loading consists of grains of different diameters, like e.g. in a turbine [32], which can be classified after Table 2.1. If the sand particles are modelled only with DEM particles, the SPH discretisation, i.e. the initial distance of the SPH particles, has to be chosen depending on the size of the smallest sand particle.

The computational cost would not be acceptable using only these very fine DEM and SPH particles. Therefore, here an approach, which couples different methods, is applied for handling sand grains of different sizes. For an accurate modelling of an engineering process it is necessary to take into account all particle sizes. Larger particle can cause, e.g. blockage or a deadlock of a hydraulic machine and the load spectrum due to several small particles can not be neglected.

In Fig. 2.8, three different states of a collapsing water column with loading are shown. The loading consists of small and large sand particles.

The larger ones are described with the DEM and the smaller ones with the transport equation. The DEM particles are scaled in the visualisation. The fluid sloshes inside

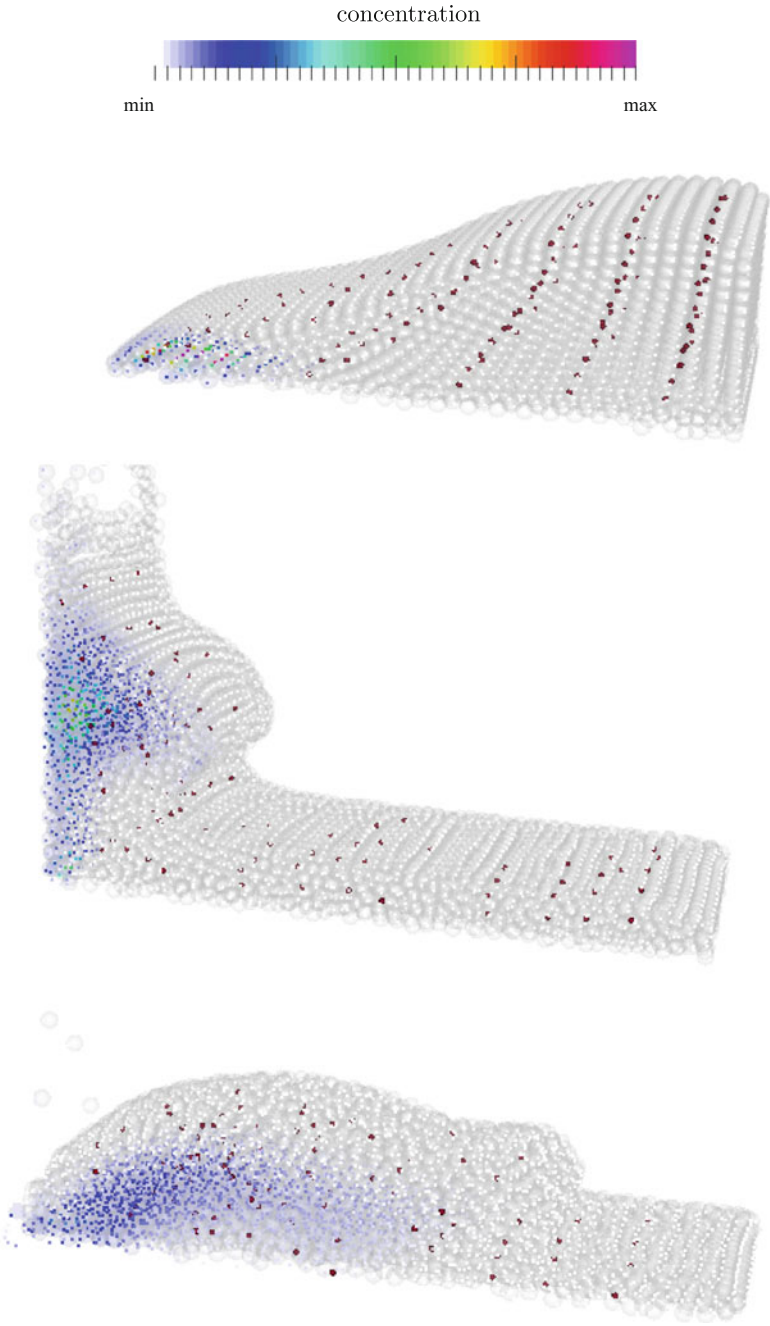

Fig. 2.8 Simulation of a sloshing fluid with loading inside a closed tank

a closed tank from left to right. The loading is transported by the fluid and distributed inside the whole tank together with the fluid.

2.2.6 Abrasive Wear Model

Resulting from an impact of an abrasive particle on the boundary geometry the surface will be damaged. The damage can be distinguished into different mechanisms, such as crack building, deformation, cutting mechanisms, or sliding mechanisms [10]. The damage or amount of removed material from the surface is depending on different parameters like, e.g. the velocity of the particle, the impact angle or different material parameters of the abrasive particle and the target. Here, a wear model for calculating the damage on the boundary geometry is used. There exist many different wear models in literature, which consider different wear mechanisms and have various advantages as well as disadvantages. An overview of wear models can be found in [26] or [25]. Here, a wear model is applied which was originally introduced in [3, 4]. This model was modified and extended by [13, 17, 42] and [41]. The removed material is calculated by

$$W = \frac{100}{2\sqrt{29}} r_{\mathrm{p}}^3 \left(\frac{U}{C_{\mathrm{k}}}\right)^n \sin 2\alpha \sqrt{\sin\alpha} + \frac{M_{\mathrm{p}}(U\sin\alpha - D_{\mathrm{k}})^2}{2E_{\mathrm{f}}} \tag{2.21}$$

with the characteristic cutting velocity

$$C_{\mathrm{k}} = \sqrt{\frac{3\sigma R_{\mathrm{f}}^{0.6}}{\rho_{\mathrm{p}}}} \tag{2.22}$$

and the characteristic deformation velocity

$$D_{\mathrm{k}} = \frac{\pi^2}{2\sqrt{10}} (1.59Y)^{2.5} \left(\frac{R_{\mathrm{f}}}{\rho_{\mathrm{t}}}\right)^{0.5} \left[\frac{1-q_{\mathrm{p}}^2}{E_{\mathrm{p}}} + \frac{1-q_{\mathrm{t}}^2}{E_{\mathrm{t}}}\right]^2. \tag{2.23}$$

Here, r_{p} is the radius, M_{p} the mass, q_{p} the Poisson ratio, U the absolut impact velocity of the particle, α the impact angle, E_{p} Young's modulus, ρ_{p} the density and R_{f} the roundness factor of the particle, ρ_{t} the density, q_{t} the Poisson ratio, Y the yield stress and E_{f} is the Young's modulus of the boundary, σ the plastic flow stress, E_{f} the deformation erosion factor, and n the velocity exponent.

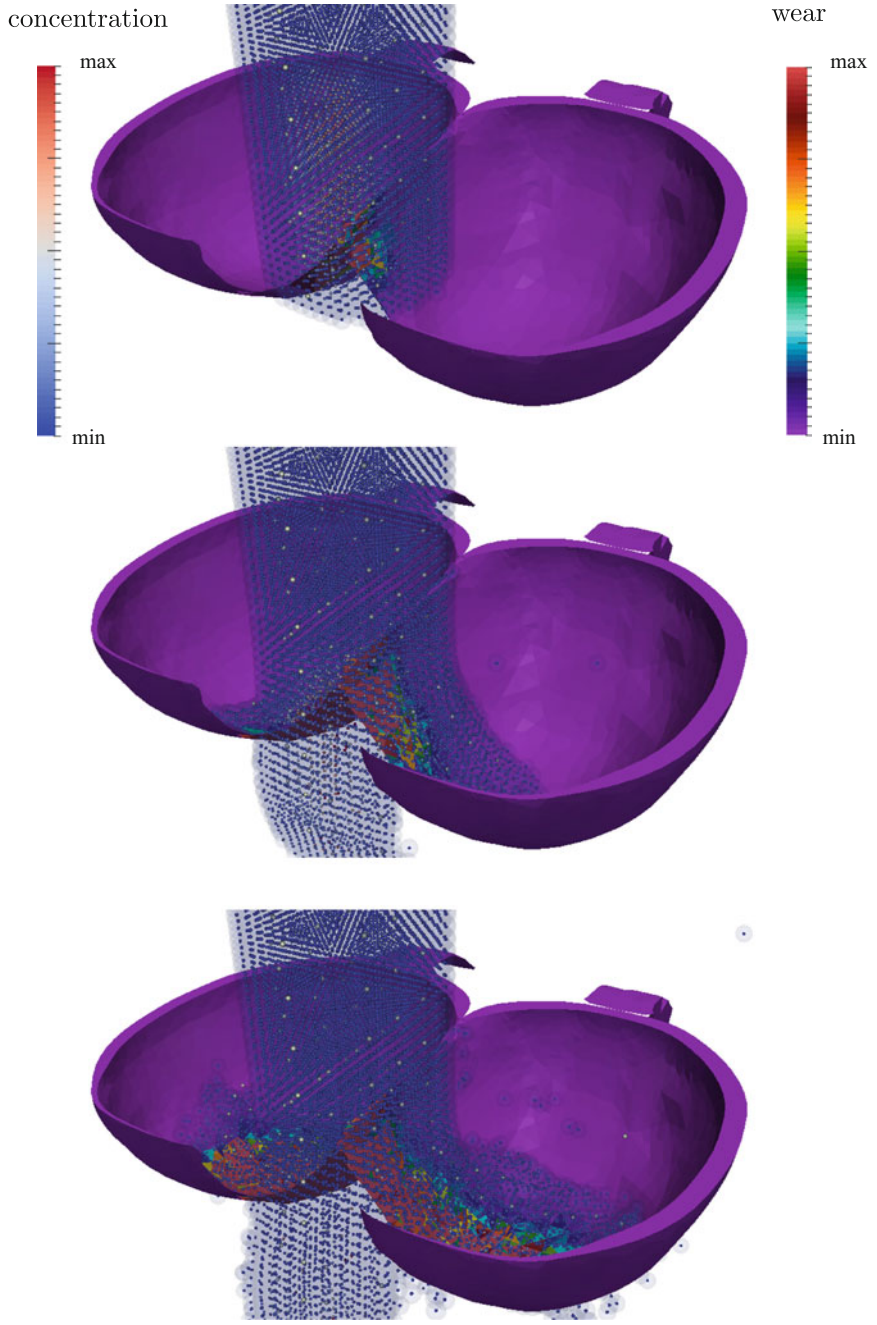

Fig. 2.9 Simulation of impact of a free jet with loading

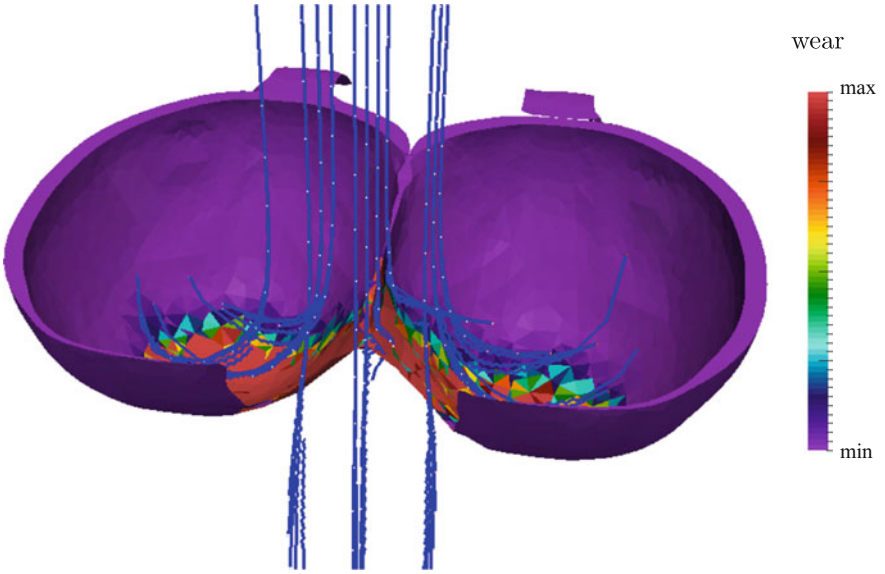

Fig. 2.10 Trajectories of the DEM particles

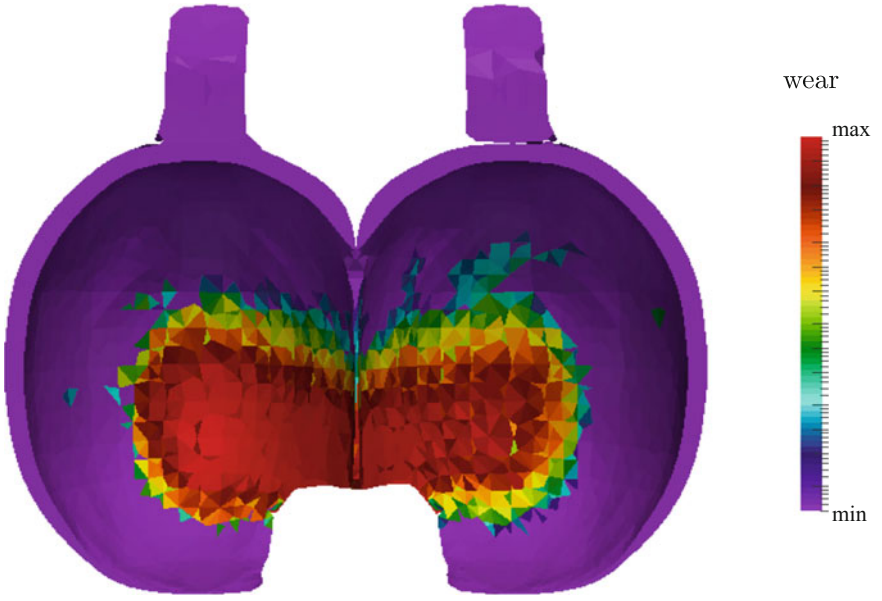

Fig. 2.11 Damage pattern with the Bitter model

2.3 Results for the Pelton Turbine

A free jet with loading, which consists of geomaterials with particles of different sizes, is simulated. The boundary geometry is a simplified pelton bucket. In Fig. 2.9, three states of the simulation are shown.

The fluid is color coded with the concentration. The DEM particles in white are scaled in their size for a better visibility. The boundary geometry is color coded with the removed material. In Fig. 2.10, the trajectories of the DEM particles are shown.

With the newly proposed approach it is possible to track larger particles and investigate their trajectories. Thereby, it is possible to predict the places where they cause damage or settle down. Abrasive particles which settle down at certain places can cause a binding of the hydraulic machine. In Fig. 2.11, exemplarily the damage pattern of the simulation is shown.

It can be observed that most of the material is removed in the middle at the upper part of the bucket, which also corresponds to experiments [32]. In the presented approach only the shape of the pattern is investigated. The analysis of the absolute amount of the removed material needs further improvements of the applied damage model.

2.4 Conclusion

A new meshless simulation approach for predicting wear patterns is presented. The fluid is modelled with the SPH method. It is assumed that the loading consists of geomaterials with particles of very different sizes. It is modelled, depending on the size of the abrasive particles, with two different methods, a DEM approach and a transport equation, respectively. It is possible to simulate a complex engineering scenario like the impact of a free jet with loading on a pelton bucket. The highly transient flow can be accurately simulated with the SPH method and it is possible to model the wear pattern on the boundary geometry. In this study wear models from literature were applied. In future further developments of the wear models are necessary for the prediction of the absolute amount of the removed material.

Acknowledgements This research has been partially made possible by funding from the German Research Foundation (DFG) under the program SFB 716 ‘Dynamic simulation of systems with large particle numbers’, subproject A5 with the title ‘Simulation of abrasive damage processes using hybrid smoothed particle hydrodynamics’. This financial support is highly appreciated.

References

1. Beck, F., Eberhard, P.: Predicting abrasive wear with coupled Lagrangian methods. Comput. Part. Mech. **2**(1), 51–62 (2015)
2. Beck, F., Eberhard, P.: Study on abrasive wear with a Lagrangian SPH approach. In: Proceedings of the 11th International Smoothed Particle Hydrodynamics European Research Interest Community SPH Workshop (SPHERIC 2016), pp. 39–46 (2016)
3. Bitter, J.: A study of erosion phenomena: part I. Wear **6**(1), 5–21 (1963)
4. Bitter, J.: A study of erosion phenomena: part II. Wear **6**(3), 169–190 (1963)
5. Campbell, J., Vignejevic, R., Libersky, L.: A contact algorithm for smoothed particle hydrodynamics. Comput. Meth. Appl. Mech. Eng. **184**, 49–65 (2000)
6. Colagrossi, A., Landrini, M.: Numerical simulation of interfacial flows by smoothed particle hydrodynamics. J. Comput. Phys. **191**, 448–475 (2003)
7. Cummins, S.J., Rudman, M.: An SPH projection method. J. Comput. Phys. **152**(2), 584–607 (1999)
8. Cundall, P.A., Strack, O.D.L.: A discrete numerical model for granular assemblies. Géotechnique **29**(1), 47–65 (1979)
9. DIN EN ISO 14688-1: Geotechnische Erkundung und Untersuchung Benennung, Beschreibung und Klassifizierung von Boden Teil 1: Benennung und Beschreibung. Deutsches Institut für Normung, pp. 1–20 (2011)
10. Duan, C., Karelin, V.: Abrasive Erosion Corrosion of Hydraulic Machinery. Imperial College Press, London, Series on Hydraulic Machinery (2002)
11. Ergenzinger, C., Seifried, R., Eberhard, P.: A discrete element model to describe failure of strong rock in uniaxial compression. Granular Matter **13**(4), 341–364 (2011)
12. Ergenzinger, C., Seifried, R., Eberhard, P.: A discrete element approach to model breakable railway ballast. J. Comput. Nonlinear Dyn. **7**(4), 041010–1–8 (2012)
13. Forder, A., Thew, M., Harrison, D.: A numerical investigation of solid particle erosion experienced within oilfield control valves. Wear **216**(2), 184–193 (1998)
14. Gingold, R.A., Monaghan, J.J.: Smoothed particle hydrodynamics: theory and application to non-spherical stars. Mon. Not. R. Astron. Soc. **181**, 375–389 (1977)
15. Ghia, U., Ghia, K.N., Shin, C.T.: High-Re solutions for incompressible flow using the Navier-Stokes equations and a multigrid method. J. Comput. Phys. **48**, 387–411 (1982)
16. Guilcher, P.M., Ducrozet, G., Alessandrini, B., Ferrant, P.: Water wave propagation using SPH models. In: Proceedings 2nd International Spheric Workshop, pp. 119–122 (2007)
17. Hashish, M.: An improved model of erosion by solid particle impact. In: Proceedings of the 7th International Conference on Erosion by Liquid and Solid Impact, pp. 66.1–66.9 (1987)
18. Hu, X., Adams, N.: A multi-phase SPH method for macroscopic and mesoscopic flows. J. Comput. Phys. **213**, 844–861 (2005)
19. Kos'Yan, R., Divinskiy, B., Krylenko, M., Vincent, C.: Modelling of the Vertical Distribution of Suspended Sediment Concentration Under Waves with a Group Structure. Oceans 2007—Europe, pp. 1–6 (2007)
20. Kristof, P., Benes, B., Krivanek, J., Stava, O.: Hydraulic erosion using smoothed particle hydrodynamics. Comput. Grap. Forum Proc. Eurographics **28**(2), 219–228 (2009)
21. Kulasegaram, S., Bonet, J., Lewis, R.W., Profit, M.: A variational formulation based contact algorithm for rigid boundaries in two-dimensional SPH applications. Comput. Mech. **33**, 316–325 (2004)
22. Liu, M., Liu, G.: Smoothed particle hydrodynamics (SPH): an overview and recent developments. Arch. Comput. Meth. Eng. **17**, 25–76 (2010)
23. Liu, X., Xu, H., Shao, S., Lin, P.: An improved incompressible SPH model for simulation of wave structure interaction. Comput. Fluids **71**, 113–123 (2013)
24. Lucy, L.B.: A numerical approach to the testing of the fission hypothesis. Astron. J. **82**(12), 1013–1024 (1977)
25. Lyczkowski, R.W., Bouillard, J.X.: State-of-the-art review of erosion modeling in fluid/solids systems. Prog. Ener. Combust. Sci. **28**(6), 543–602 (2002)

26. Meng, H., Ludema, K.: Wear Models and Predictive Equations: Their Form and Content. Wear **181–183**, Part 2, 443–457 (1995)
27. Monaghan, J.J., Kocharyan, A.: SPH simulation of multi-flow. Comput. Phys. Commun. **87**, 225–235 (1995)
28. Monaghan, J.J.: Simulating free surface flows with SPH. J. Comput. Phys. **110**, 399–406 (1994)
29. Monaghan, J.J.: Smoothed particle hydrodynamics. Rep. Prog. Phys. **68**, 1703–1759 (2005)
30. Morris, J.P., Fox, P.J., Zhu, Y.: Modeling low Reynolds number incompressible flows using SPH. J. Comput. Phys. **136**, 214–226 (1997)
31. Nasato, D.S., Goniva, C., Pirker, S., Kloss, C.: Coarse graining for large-scale DEM simulations of particle flow–an investigation on contact and cohesion models. Proc. Eng. **102**, 1484–1490 (2015)
32. Padhy, M., Saini, R.: Effect of size and concentration of silt particles on erosion of pelton turbine buckets. Energy **34**(10), 1477–1483 (2009)
33. Potapov, A.V., Hunt, M.L., Campbell, C.S.: Liquid-solid flows using smoothed particle hydrodynamics and the discrete element method. Powder Technol. **116**(2–3), 204–213 (2001)
34. Rafiee, A., Cummins, S., Rudman, M., Thiagarajan, K.: Comparative study on the accuracy and stability of sph schemes in simulating energetic free-surface flows. Eur. J. Mech. - B/Fluids **36**, 1–16 (2012)
35. Robinson, M., Ramaioli, M., Luding, S.: Fluid particle flow simulations using two-way-coupled mesoscale SPH-DEM and validation. Int. J. Multiph. Flow **59**, 121–134 (2014)
36. Schiehlen, W., Eberhard, P.: Applied Dynamics. Springer, Heidelberg (2014)
37. Shan, Z.: Coastel Sediment Transport Simulation by Smoothed Particle Hydrodynamics. PhD thesis, The Johns Hopkins University, (2007)
38. Takeda, H., Miyama, S., Sekiya, M.: Numerical simulation of viscous flow by smoothed particle hydrodynamics. Prog. Theor. Phys. **92**(5), 939–960 (1994)
39. Wang, Y., Yang, Z.: A coupled finite element and meshfree analysis of erosive wear. Tribol. Int. **42**(2), 373–377 (2009)
40. Wendland, H.: Piecewise polynomial, positive definite and compactly supported radial functions of minimal degree. Adv. Comput. Math. **4**(1), 389–396 (1995)
41. Wood, R., Jones, T., Ganeshalingam, J., Miles, N.: Comparison of predicted and experimental erosion estimates in slurry ducts. Wear **256**(9–10), 937–947 (2004)
42. Wood, R., Jones, T., Miles, N., Ganeshalingam, J.: Upstream swirl-induction for reduction of erosion damage from slurries in pipeline bends. Wear **250**, 770–778 (2001)
43. Wu, W., Wang, S.S.Y.: Formulas for sediment porosity and settling velocity. J. Hydraul. Eng. **8**(132), 858–862 (2006)
44. Violeau, D., Issa, R.: Numerical modelling of complex turbulent free-surface flows with the SPH method: an overview. Int. J. Numer. Methods Eng. **53**, 277–304 (2007)
45. Vila, J.P.: On particle weighted methods and smooth particle hydrodynamics. Math. Models Methods Appl. Sci. **9**(2), 161–209 (1999)
46. Xu, R., Stansby, P.K., Laurence, D.R.: Accuracy and stability in incompressible SPH (ISPH) based on the projection method and a new approach. J. Comput. Phys. **18**(228), 6703–6725 (2009)

Chapter 3
Energy Harvesting in a Hybrid Piezoelectric-Electromagnetic Harvester with Time Delay

Mustapha Hamdi and Mohamed Belhaq

Abstract The effect of time delay on the energy harvesting (EH) performance is studied in a class of hybrid EH systems. The delayed hybrid energy harvester consists in a nonlinear mono-stable harvester device composed of a forced mechanical component coupled to piezoelectric and electromagnetic energy harvesting mechanisms in which the time delay is introduced in the mechanical component of the harvester. Analytical approximations of the steady-state amplitude as well as the amplitudes of piezoelectric and electromagnetic powers output are obtained using a perturbation method and the effect of delay parameters on the powers output performance is examined. The optimal values of delay parameters and coupling coefficients at which the EH performance is maximum are determined. To appreciate the influence of the delay amplitude on the powers output performance, the results obtained in the presence of time delay are compared to those obtained in the case without delay. It is shown that in the presence of time delay the powers output performance is significantly improved at certain ranges of time delay and delay amplitude.

3.1 Introduction

Delay feedback mechanism is usually used to reduce or suppress large-amplitude vibrations [1–3]. For instance, in delayed self-excited oscillator [4, 5], limit cycle oscillations can be suppressed for appropriate values of time delay and delay amplitude. Likewise, in delayed forced nonlinear oscillators [6, 7], large-amplitude vibrations can be quenched for appropriate combination of time delay parameters. Similar studies were carried out to suppress limit cycle oscillations in the case where the time delay is combined with a fast excitation [8–10]. However, large-amplitude vibrations

M. Hamdi
Faculty of Sciences and Technology-Al Hoceima, University Mohammed I Oujda, Al-Hoceima, Morocco
e-mail: hamustapha2000@yahoo.fr

M. Belhaq (✉)
Faculty of Sciences Ain Chock, University Hassan II Casablanca, Casablanca, Morocco
e-mail: mbelhaq@yahoo.fr

M. Belhaq (ed.), *Recent Trends in Applied Nonlinear Mechanics and Physics*,
Springer Proceedings in Physics 199, https://doi.org/10.1007/978-3-319-63937-6_3

can be desirable in certain applications, as in vibration-based EH. This is because large-amplitude vibrations can be exploited to extract power from ambient sources of vibration. As time delayed feedback can be used to reduce or suppress large-amplitude vibrations, it can also be used to increase the amplitude of vibrations near the resonance for certain range of delay parameters. Indeed, the concept of using time delay has been used recently considering a delayed pure self-excited oscillator and it was concluded that modulated delay amplitude increases significantly the amplitude of vibrations [11]. This result was exploited positively to enhance the EH performance in a delayed van der Pol harvester system using quasi-periodic vibrations [12]. The concept of using delayed feedback mechanism was also used to extend the dynamic range of an energy harvester with nonlinear damping [13] demonstrating that this method can provide substantial performance in the EH capacity.

In this chapter we consider a hybrid harvester device consisting in a delayed nonlinear mono-stable oscillator coupled to electric circuits through piezoelectric and electromagnetic couplings. The objective is to study the influence of time delay on the performance of a general class of hybrid energy harvester. The hybrid harvester device consists of a nonlinear forced mechanical subsystem coupled to both piezoelectric and electromagnetic EH mechanisms. This class of hybrid energy harvesters has been examined in the absence of time delay [14]. The authors in [14] established a unified approximation method to illustrate the effect of electromechanical coupling on the EH systems. Here, the time delay in the position is present in the mechanical subsystem and the influence of the delay parameters on the power output of the hybrid harvester system is studied. The contribution of the present work is highlighted through a systematic comparison with the case without time delay considered in [14].

This study can be useful for certain applications in which delayed state feedback is present in the mechanical component of the harvester. For instance, in milling and turning operations the inherent time delay in the position commonly arises in the process [15–18] such that the time delay is not considered as an additional input power in the harvester. Instead, when time delay is introduced in the system as an input power, the problem of energy balance between the generated and the consumed average powers should be examined.

The chapter is structured as follows. In Sect. 3.2, we present the delayed hybrid energy harvester. Using a perturbation method, the steady-state response and the harvested powers extracted from piezoelectric and electromagnetic energy harvesting mechanisms are derived near the primary resonance. The influence of delay parameters of the harvesting system on the EH performance is examined in Sect. 3.3 for both piezoelectric and electromagnetic coupling mechanisms. A summary of the results is provided in the concluding section.

3.2 Harvester System and Powers Output

The energy harvester system under consideration consists of a delayed nonlinear mono-stable oscillator coupled to electric circuits through piezoelectric and electro-

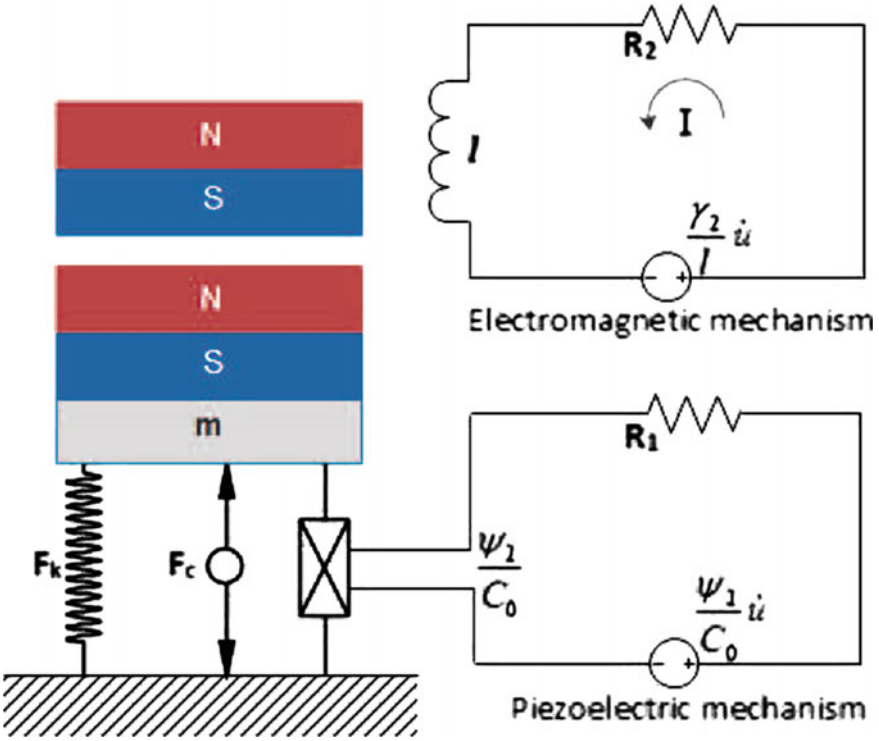

Fig. 3.1 Schematic of the energy harvesting model

magnetic couplings. The schematic view of the harvester is given in Fig. 3.1. The governing equations can be written as

$$\begin{cases} m\dfrac{d^2u^*}{dt^{*2}} + \xi\dot{u^*} + ku^* + \tilde{b}u^{*3} = \tilde{\lambda}u(t^* - \tau) - \tilde{\psi}_1 V_1{}^* + \tilde{\gamma} i_2{}^* - \hat{m}\ddot{r} \\ \dfrac{dV_1{}^*}{dt^*} + \dfrac{V_1{}^*}{R_1 C_0 \omega_n} = \dfrac{\psi_2}{C_0}\dfrac{du^*}{dt} \\ \dfrac{di_2{}^*}{dt^*} + \dfrac{R_2}{\ell\omega_n} i_2{}^* = -\dfrac{\gamma_2}{\ell}\dfrac{du^*}{dt} \end{cases} \tag{3.1}$$

where the variable u^* represents the relative displacement of the mass m, ξ is the damping coefficient, k and b are the linear and nonlinear stiffness of the restoring force, $\tilde{\Psi}_1$, Ψ_2 and $\tilde{\gamma}$, γ_2 are the piezoelectric and electromagnetic coupling coefficients, respectively, $\tilde{\lambda}$ is the delay amplitude, τ is the time delay, while i_2^*, V_1^*, $\frac{di_2^*}{dt^*}$ and $\frac{dV_1^*}{dt^*}$ have been substituted for electrical charge coordinate q ($i_2^* = \dot{q}$ and $V_1^* = -R_1\dot{q}$). The quantities R_1, R_2 represent piezoelectric and electromagnetic loads, C_0 and ℓ are, respectively, the capacitance and the inductance of the coils.

In the absence of time delay, the hybrid energy harvester system (3.1) has been considered and the effect of electromechanical coupling on vibration-based energy

harvesting was examined [14]. Here we explore the influence of time delay on the EH performance of the harvester. As mentioned in the introduction, in certain applications, in milling and turning operations, the time delay in the position is an inherent characteristic of the process and cannot be considered as an additional input power in the harvester.

In the case of harmonic excitations of the base, the forcing term in system (3.1) takes the form $\hat{m}\ddot{r} = 2F\cos(\omega t)$. To obtain a dimensionless form of (3.1), we introduce the following non-dimensional parameters: $t = \omega_n t^*, u = \frac{u^*}{u_{max}}, V_1 = \frac{C_0}{\Psi_2 u_{max}} V_1^*$, $i_2 = \frac{\ell}{\gamma_2 u_{max}} i_2^*, \zeta = \frac{\xi}{2m\omega_n}, b = \frac{\tilde{b}u_{max}^2}{m\omega_n^2}, \Psi = \frac{\psi_1\psi_2}{C_0}, \gamma = \frac{\gamma_1\gamma_2}{\ell}, f = \frac{F}{\omega_n^2 u_{max}}, k_1 = \frac{1}{R_1 C_0 \omega_n}$, $k_2 = \frac{R_2}{\ell\omega_n}, \lambda = \frac{\lambda}{m\omega_n^2}$ and $\Omega = \frac{\omega}{\omega_n}$ where u_{max} is the maximum displacement of the oscillator and $\omega_n = \sqrt{k/m}$ is the natural frequency of the mechanical oscillator.

Introducing a bookkeeping parameter ε, scaling the parameters $\zeta, b, \Psi, \gamma, \lambda$ and f, and considering the case of primary resonance, i.e. $1 = \Omega + \varepsilon\sigma$, where σ is a detuning parameter from the resonance, Eq. (3.1) can be rewritten in terms of the non-dimensional parameters as

$$\begin{cases} \dfrac{d^2u}{dt^2} + \varepsilon 2\zeta\dfrac{du}{dt} + \Omega^2 u = \varepsilon\left(2\Omega\sigma u - bu^3 - \Psi V_1 + \gamma i_2 - 2f\cos(\Omega t) + \lambda u(t-\tau)\right) \\ \frac{dV_1}{dt} + k_1 V_1 = \frac{du}{dt} \\ \frac{di_2}{dt} + k_2 i_2 = -\frac{du}{dt} \end{cases} \tag{3.2}$$

To approximate the steady-state response of the system, we use the method of multiple scales [19, 20] by expanding the solution in terms of powers of ε as

$$\begin{cases} u(T_0, T_1) = u_0(T_0, T_1) + \varepsilon u_1(T_0, T_1) + \ldots \\ V_1(T_0, T_1) = V_{10}(T_0, T_1) + \varepsilon V_{11}(T_0, T_1) + \ldots \\ i_2(T_0, T_1) = i_{20}(T_0, T_1) + \varepsilon i_{21}(T_0, T_1) + \ldots \end{cases} \tag{3.3}$$

where $T_0 = t, T_1 = \varepsilon t$. The time derivatives become $\frac{d}{dt} = D_0 + \varepsilon D_1, \frac{d^2}{dt^2} = D_0^2 + 2\varepsilon D_0 D_1 + D_1^2 + o(\varepsilon^2)$.

Substituting (3.3) into (3.2), extracting systems of equation at different order of ε and eliminating secular terms as usual, one obtains the following modulation equations

$$\begin{cases} \dot{a} = \dfrac{f}{\Omega}\sin\theta - a(\xi + \Gamma + \dfrac{\lambda}{2\Omega}\sin\Omega\tau) \\ a\dot{\theta} = \frac{f}{\Omega}\cos\theta + a(\eta - \sigma - \frac{\lambda}{2\Omega}\cos\Omega\tau) + \frac{3b}{8\Omega}a^3 \end{cases} \tag{3.4}$$

where a and θ are, respectively, the amplitude and the phase of the modulation, while $\Gamma = \frac{k_1\Psi}{k_1^2+\Omega^2} + \frac{k_2\gamma}{k_2^2+\Omega^2}$ and $\eta = \frac{\Psi\Omega}{k_1^2+\Omega^2} + \frac{\gamma\Omega}{k_2^2+\Omega^2}$ represent, respectively, the real and imaginary parts of the coupling expression.

The steady-state response of the modulation equations, corresponding to periodic oscillations of (3.2), are determined by setting $\dot{a} = \dot{\theta} = 0$. Eliminating θ and define

$\rho = a^2$, we obtain the following algebraic equation on ρ

$$S_3^2\rho^3 - 2S_2S_3\rho^2 + (S_1^2 + S_2^2)\rho - \frac{f^2}{\Omega^2} = 0 \tag{3.5}$$

where $S_1 = \xi + \Gamma + \frac{\lambda}{2\Omega}\sin(\Omega\tau)$, $S_2 = \sigma - \eta + \frac{\lambda}{2\Omega}\cos(\Omega\tau)$ and $S_3 = \frac{-3b}{8\Omega}$.

Note that in the absence of time delay ($\lambda = 0$), we recover the results obtained in [14]. Next, we fix the damping parameter $\zeta = 0.01$, the coupling terms $\Psi = 2$ and $\gamma = 0.9$ and the forcing amplitude $f = 1$.

The first order approximation of the steady-state solution reads

$$u_0 = a\cos(\Omega t - \theta) \tag{3.6}$$

$$V_{10} = \frac{a\Omega^2}{\Omega^2 + k_1^2}\cos(\Omega t - \theta) - \frac{a\Omega k_1}{\Omega^2 + k_1^2}\sin(\Omega t - \theta) \tag{3.7}$$

$$i_{20} = \frac{a\Omega^2}{\Omega^2 + k_2^2}\cos(\Omega t - \theta) + \frac{a\Omega k_2}{\Omega^2 + k_2^2}\sin(\Omega t - \theta) \tag{3.8}$$

and the non-dimensional instantaneous piezoelectric and electromagnetic powers are given, respectively, by

$$P_P(t) = k_1 V_1(t)^2 \tag{3.9}$$

$$P_M(t) = k_2 i_2(t)^2 \tag{3.10}$$

It follows that the average piezoelectric and electromagnetic powers can be obtained by averaging over a single excitation period. This leads to

$$P_{avP} = \frac{1}{T}\int_0^T k_1 V_1(t)^2 dt \tag{3.11}$$

$$P_{avM} = \frac{1}{T}\int_0^T k_2 i_2(t)^2 dt \tag{3.12}$$

Using (3.6), (3.10) and the maximization procedure, one obtains, respectively, the maximum piezoelectric and electromagnetic powers response as

$$P_{maxP} = \frac{k_1\Omega^2}{k_1^2 + \Omega^2}a^2 \tag{3.13}$$

$$P_{maxM} = \frac{k_2\Omega^2}{k_2^2 + \Omega^2}a^2 \tag{3.14}$$

and using (3.6), (3.12) the average piezoelectric and electromagnetic powers response reads

$$P_{avP} = \frac{\Omega^2 a^2 k_1}{2(\Omega^2 + k_1^2)} \tag{3.15}$$

$$P_{avM} = \frac{\Omega^2 a^2 k_2}{2(\Omega^2 + k_2^2)} \tag{3.16}$$

3.3 Main Results

In this section, the influence of time delay parameters λ, τ on the powers output extracted from the piezoelectric and electromagnetic mechanisms is analyzed.

Figure 3.2 shows in the absence of time delay ($\lambda = 0$) and for different negative values of the delay amplitude ($\lambda = -0.5, -1$) the frequency-response curve near the primary resonance, as given by (3.5). The plots indicate clearly that increasing negative delay amplitude increases significantly the peak of the frequency response. The analytical predictions (solid lines) are compared to results obtained by numerical simulations (circles) using `dde23` [21] algorithm. The box inset in the figure shows time history for a given choice of parameters.

Figure 3.3a–d illustrate, respectively, the effect of the delay amplitude on the maximum and average output piezo-powers, P_{maxP}, P_{avP} and output electromagnetic powers P_{maxM}, P_{avM}, versus the detuning parameter σ for the same values of λ

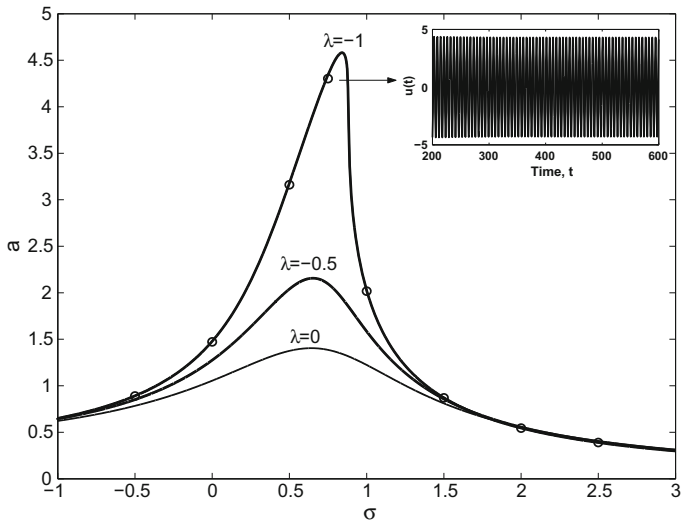

Fig. 3.2 Frequency response for different values of λ and for $b = 0.04$, $\tau = 1.58$, $k_1 = 1$ and $k_2 = 1.7$. Analytical approximation: *solid lines*. Numerical simulation: *circles*

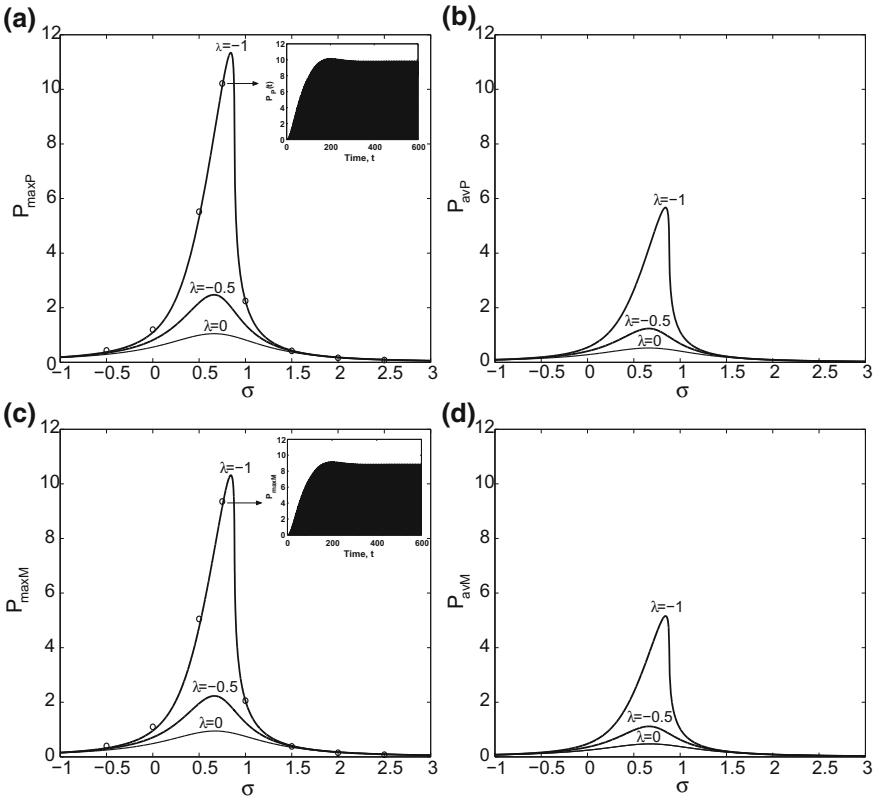

Fig. 3.3 Powers amplitude versus σ for different values of λ and for $b = 0.04$, $\tau = 1.58$, $k_1 = 1$ and $k_2 = 1.7$; **a**–**c** maximum powers response and **b**–**d** average powers response. Analytical approximation: *solid lines*. Numerical simulation: *circles*

considered in Fig. 3.2. The results show that increasing negative λ the performance of the output powers is significantly improved near the resonance. The powers amplitude corresponding to the case without delay ($\lambda = 0$) are also reported for comparison. The analytical approximations (solid lines) are compared to results obtained using numerical simulations (circles). Inset in Fig. 3.3a, c are shown, respectively, time histories of the output powers $P_{max\,P}$ and $P_{max\,M}$ obtained by integrating numerically (3.2) and using (3.9), (3.10). It can be observed from Fig. 3.3 that the maximum and average powers extracted from the piezoelectric mechanism ($P_{max\,P}$, $P_{av\,P}$) are slightly larger that those extracted from the electromagnetic harvester ($P_{max\,M}$, $P_{av\,M}$). The plots also show that for a small value of the nonlinear stiffness parameter ($b = 0.04$), the frequency response (Fig. 3.2) and the response of the powers amplitudes (Fig. 3.3) have a linear behavior.

The variation of the steady-state amplitude versus the delay amplitude λ, as given by (3.5), is presented in Fig. 3.4a for two different values of time delay ($\tau = 0.8, 1$).

Figure 3.4b–e show the effect of time delay on the maximum and average output powers, P_{maxP}, P_{avP}, P_{maxM}, P_{avM}, as function of λ. It can be observed that the EH performance is maximum in a certain range of negative λ, negligible in the absence of time delay ($\lambda = 0$) and insignificant for increasing positive values of λ. Inset in Fig. 3.4a, b, d are shown, respectively, time histories of the steady-state response and of the harvested powers obtained by integrating numerically (3.2) and using (3.9)–(3.10).

It can also be observed from Fig. 3.4 that the output piezo-powers are larger that the output electromagnetic powers.

In order to obtain the optimal values of delay parameters, λ and τ, at which the EH performance is maximum, we plot in Fig. 3.5 the variation of the steady-state amplitude as well as the maximum and average output powers versus time delay τ for different negative values of λ. The plots show that the optimal values of delay amplitude and time delay are obtained in certain small alternate ranges of time delay τ and for increased negative values of λ. Inset in Fig. 3.5a, b, d are shown, for certain values of λ and τ, time histories of the steady-state response and of the harvested powers obtained by numerical simulations.

Figure 3.6 shows the variation of the steady-state amplitude and the output powers amplitude P_{maxP}, P_{avP}, P_{maxM} and P_{avM} versus the coupling coefficient k_1 indicating the improvement of the EH performance in the presence of time delay. It can be seen that increasing k_1, the steady-state amplitude increases to a certain optimal value ($k_1 = 1$) and then decreases for large values of k_1. Time histories of the steady-state response and of the harvested powers are shown inset in Fig. 3.6a, b, d.

Similarly, Fig. 3.7 depicts the variation of the amplitude of the periodic response and the output powers amplitude versus the coupling term k_2 in the presence and absence of delay. The results show that the performance of the energy harvester system is also improved in the presence of time delay.

Finally, it is interesting to evaluate in the presence of time delay the optimal values of the nonlinear stiffness parameter, b, at which the performance of the harvester system is improved. Figure 3.8 presents the variation of the amplitude of the periodic response and the output power versus b showing that there exists an optimal value of b (≈ 0.05) at which the output power is maximum.

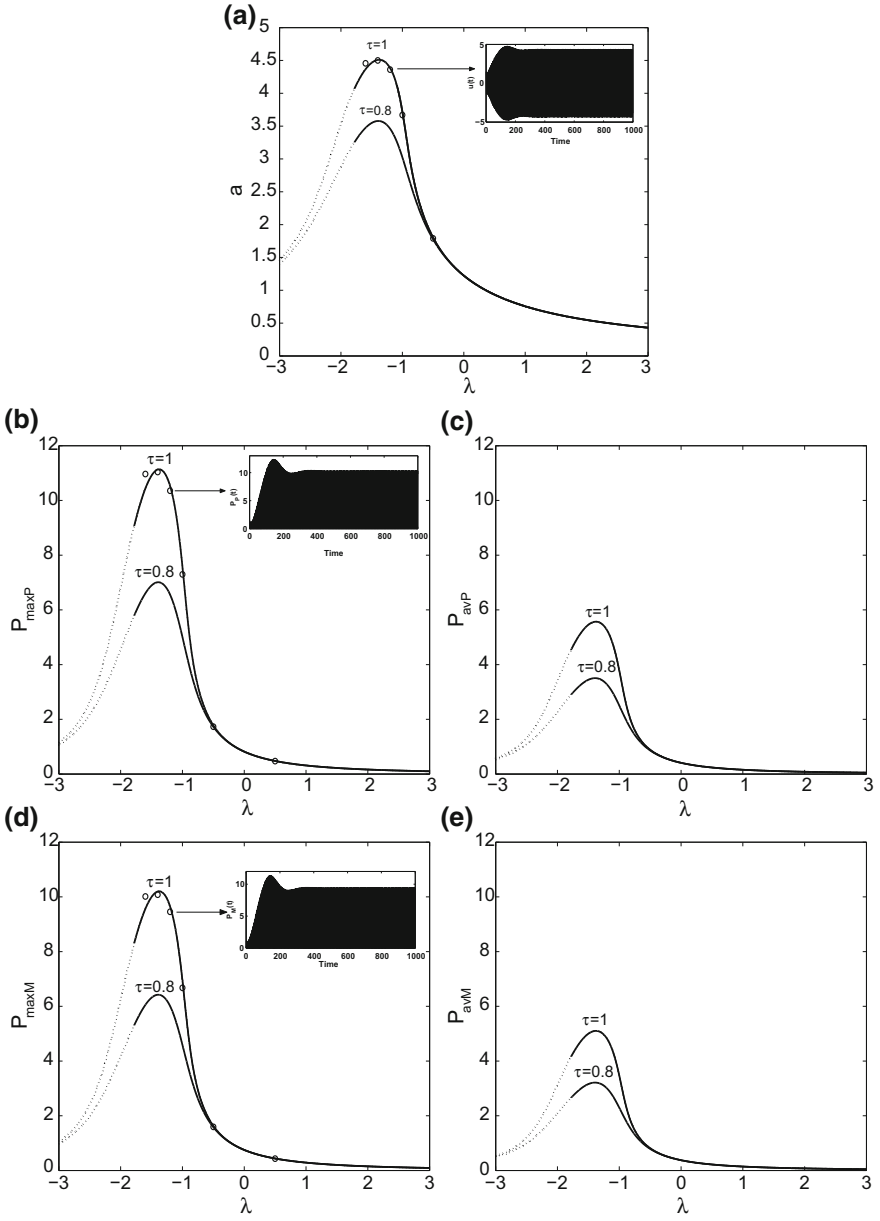

Fig. 3.4 Vibration and powers amplitude versus λ for different values of τ and for $b = 0.04$, $\Omega = 1.1, k_1 = 1$ and $k_2 = 1.7$; **a** vibration response; **b**, **d** maximum powers response; **c**, **e** average powers response. *Solid line* for stable, *doted line* for unstable. Numerical simulation: *circles*

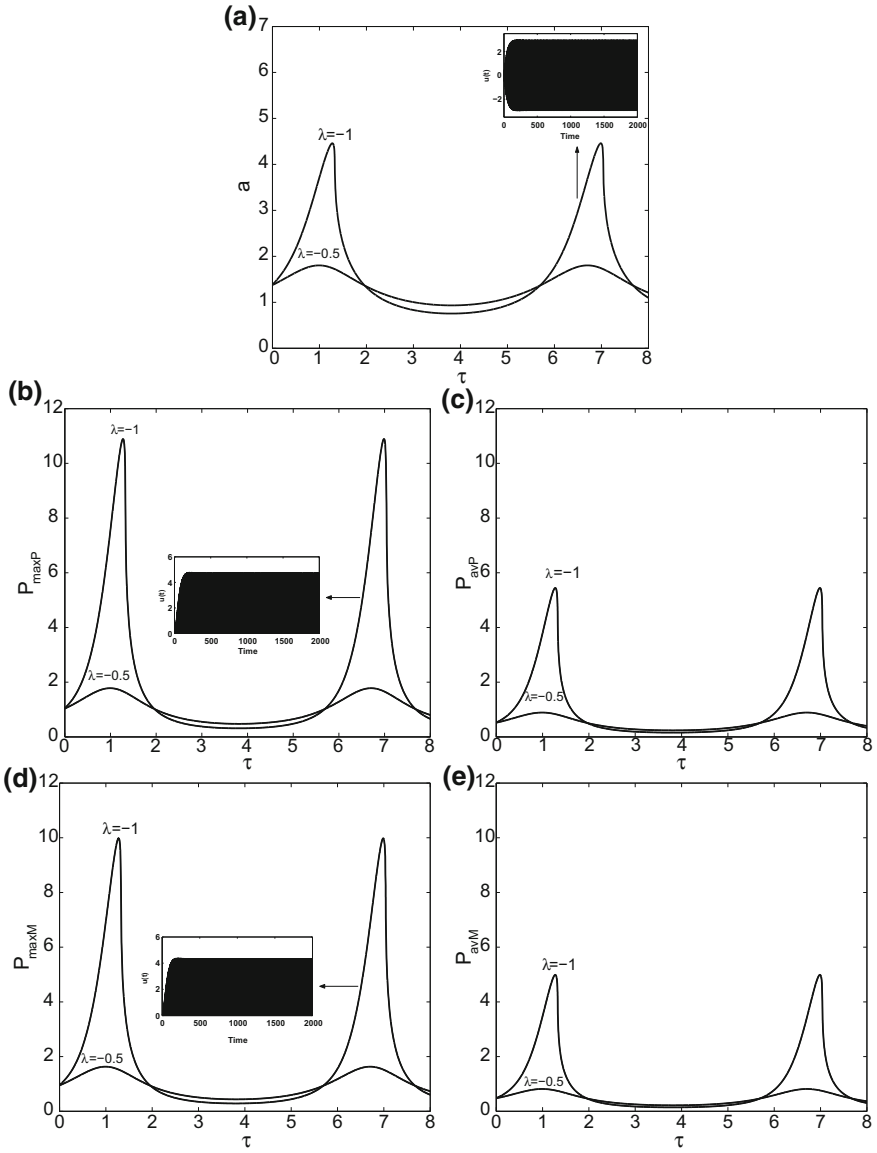

Fig. 3.5 Vibration and powers amplitude versus τ for different values of λ and for $b = 0.04$, $\Omega = 1.1, k_1 = 1$ and $k_2 = 1.7$; **a** vibration response; **b**, **d** maximum powers response; **c**, **e** average powers response. Analytical prediction: *solid line*

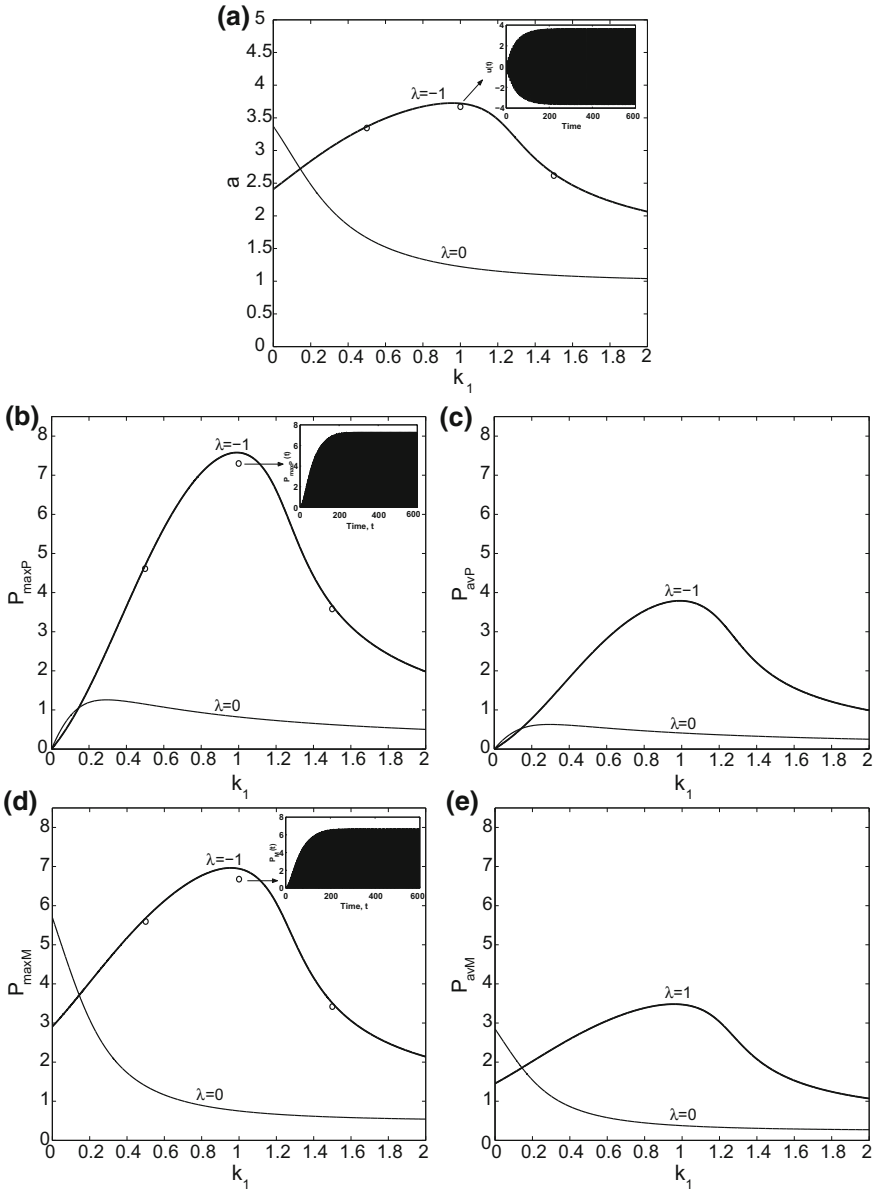

Fig. 3.6 Vibration and powers amplitude versus k_1 for $b = 0.04$, $\Omega = 1.1$, $\lambda = -1$, $\tau = 1$ and $k_2 = 1.7$; **a** vibration response; **b**, **d** maximum powers response; **c**, **e** average powers response. Analytical prediction: *solid line*. Numerical simulation: *circles*

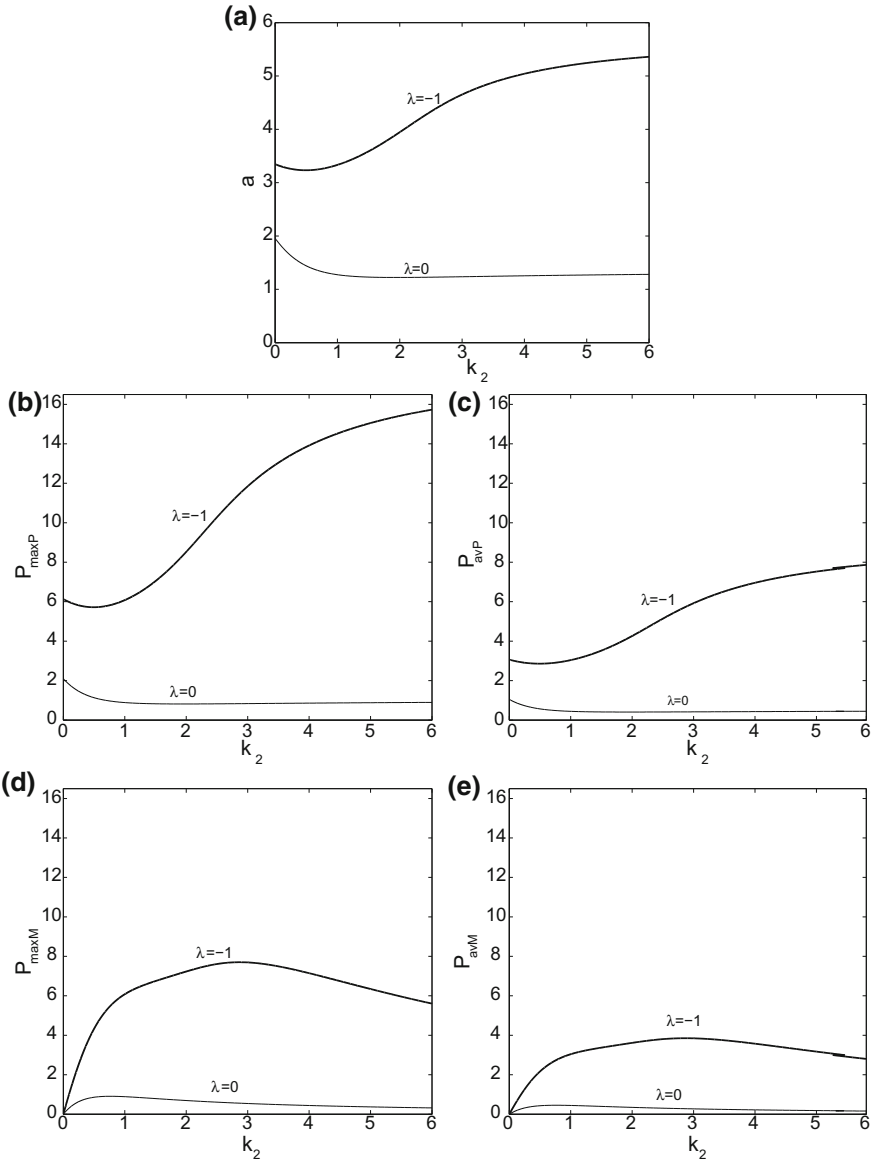

Fig. 3.7 Vibration and powers amplitude versus k_2 for $b = 0.04, \Omega = 1.1, \lambda = -1, \tau = 1$ and $k_1 = 1$; **a** vibration response; **b**, **d** maximum powers response; **c**, **e** average powers response. Analytical prediction: *solid line*

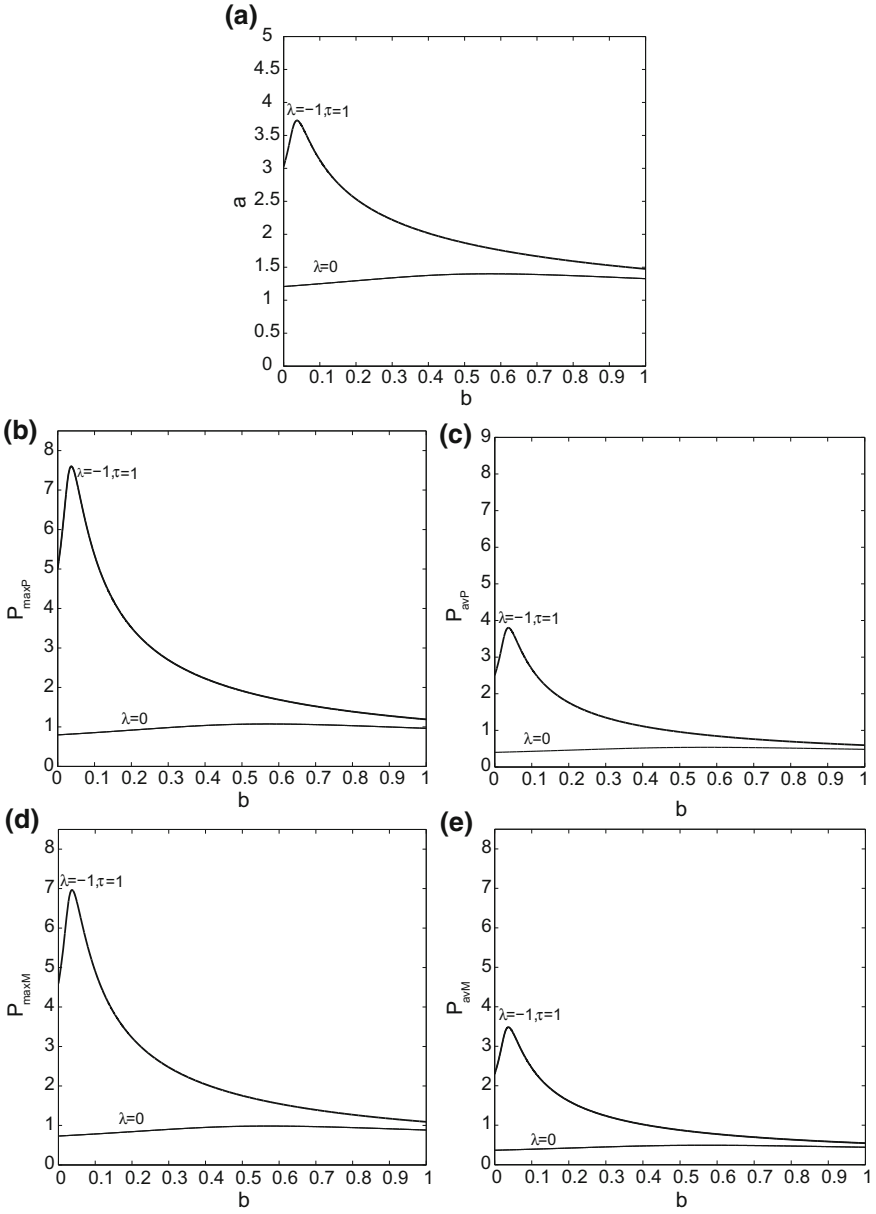

Fig. 3.8 Vibration and powers amplitude versus b for $\Omega = 1.1$, $k_1 = 1$ and $k_2 = 1.7$; **a** vibration response; **b**, **d** maximum powers response; **c**, **e** average powers response

3.4 Conclusions

In this chapter, the effect of time delay on the EH performance of a hybrid energy harvester system is investigated. The delayed hybrid energy harvester consists in a nonlinear mono-stable harvester device composed of a forced mechanical component coupled to piezoelectric and electromagnetic energy harvesting mechanisms in which the time delay in the position is present. This can be found in certain applications as in milling and turning operations in which the time delay in the position is inherently present in the process. Using the multiple scales method, the frequency-response of the harvester is derived and the amplitudes of piezoelectric and electromagnetic powers output are obtained near the primary resonance. The influence of the delay and coupling parameters on the steady-state response and the powers output is described analytically and validated using numerical simulations. Specifically, it was shown that the performance of the piezoelectric and electromagnetic output powers in the presence of time delay is significantly improved over certain ranges of delay and coupling parameters near the resonance with an advantage for the output piezo-powers over the electromagnetic output power. This is confirmed by comparison to the case in which the time delay is absent.

Moreover, the results indicate that increasing the coupling coefficient of the piezoelectric component k_1, the piezoelectric and electromagnetic output powers increase to a certain maximum value and then decrease significantly. Instead, increasing the coupling coefficient of the electromagnetic component k_2 increases the output piezo-power, while the electromagnetic output power decreases for large values of the coupling. The optimal values of the nonlinear stiffness parameter b producing maximin powers input are also obtained.

References

1. Olgac, N., Holm-Hansen, B.T.: A novel active vibration absorption technique: delayed resonator. J. Sound Vib. **176**, 93–104 (1994)
2. Mokni, L., Belhaq, M.: Reducing Transmitted Vibration Using Delayed Hysteretic Suspension. Advances in Acoustics and Vibration 546280. https://doi.org/10.1155/2011/546280 (2011)
3. Mokni, L., Belhaq, M.: Using delayed damping to minimize transmitted vibrations. Commun. Nonlinear Sci. Numer. Simul. **17**, 1980–1985 (2012)
4. Atay, F.M.: van der Pol's oscillator under delayed feedback. J. Sound Vib. **218**, 333–339 (1998)
5. Suchorsky, M.K., Sah, S.M., Rand, R.H.: Using delay to quench undesirable vibrations. Nonlinear Dyn. **62**, 407–416 (2010)
6. Hu, H., Dowell, E.H., Virgin, L.N.: Resonances of a harmonically forced Duffing oscillator with time delay state feedback. Nonlinear Dyn. **15**, 311–327 (1998)
7. Maccari, M.: The response of a parametrically excited van der Pol oscillator to a time delay state feedback. Nonlinear Dyn. **26**, 105–119 (2001)
8. Belhaq, M., Sah, S.M.: Horizontal fast excitation in delayed van der Pol oscillator. Commun. Nonlinear Sci. Numer. Simul. **13**, 1706–1713 (2008)
9. Belhaq, M., Sah, S.M.: Fast parametrically excited van der Pol oscillator with time delay state feedback. Int. J. Non-linear Mech. **43**, 124–130 (2008)

10. Sah, S.M., Belhaq, M.: Control of a delayed limit cycle using the tilt angle of a fast excitation. J. Vib. Control **17**, 163–173 (2011)
11. Hamdi, M., Belhaq, M.: On the delayed van der Pol oscillator with time-varing feedback gain. Appl. Mech. Mater. **706**, 149–158 (2015)
12. Belhaq, M., Hamdi, M.: Energy harvesting from quasi-periodic vibrations. Nonlinear Dyn. **86**, 2193–2205 (2016)
13. Kammer, A.S., Olgac, N.: Delayed-feedback vibration absorbers to enhance energy harvesting. J. Sound Vib. **363**, 54–67 (2016)
14. Karami, M.A., Inman, D.J.: Equivalent damping and frequency change for linear and nonlinear hybrid vibrational energy harvesting systems. J. Sound Vib. **330**, 5583–5597 (2011)
15. Stepan, G., Kalmer-Nagy, T.: Nonlinear regenerative machine tool vibrations. In: Proceedings of the 1997 ASME Design Engineering Technical Conferences, 16th ASME Biennial Conference on Mechanical Vibration and Noise (Sacramento, 1997), DETC97/VIB-4021 1-11 (1997)
16. Kalmer-Nagy, T., Stepan, G., Moon, F.C.: Subcritical Hopf bifurcation in the delay equation model for machine tool vibrations. Nonlinear Dyn. **26**, 121–142 (2001)
17. Stepan, G., Szalai, R., Insperger, T.: Nonlinear dynamics of high-speed milling subjected to regenerative effect. In: Radons, G., Neugebauer, R. (eds.) Nonlinear Dynamics of Production Systems, pp. 111–127. Wiley-VCH, Weinheim (2004)
18. Rusinek, R., Weremczuk, A., Warminski, J.: Regenerative model of cutting process with nonlinear Duffing oscillator. Mech. Mech. Eng. **15**, 129–143 (2011)
19. Nayfeh, A.H., Mook, D.T.: Nonlinear Oscillations. Wiley, New York (1979)
20. Nayfeh, A.H.: Introduction to Perturbation Techniques. Wiley, New York (1981)
21. Shampine, L.F., Thompson, S.: Solving delay differential equations with dde23. PDF available on-line at http:www.radford.edu/thompson/webddes/tutorial.pdf (2000)

Chapter 4
Modeling and Parametric Analysis of a Piezoelectric Flexoelectric Nanoactuator

Sourour Baroudi, Ahmed Jemai and Fehmi Najar

Abstract We investigate the piezoelectric flexoelectric response at the nanoscale level of a cantilever beam made of $BaTiO_3$. In fact, the flexoelectric effect in dielectric solids couples polarization and strain gradient, rather than polarization and strain for piezoelectricity. We develop a comprehensive electromechanical analytical model of the nanobeam taking into account the piezoelectric and the flexoelectric effects. The distribution of the electrical potential inside the nanobeam is also solved analytically while considering the self-field effect. Starting from the enthalpy density function, the Hamilton's principle is applied to derive the governing coupled equations with the appropriate boundary conditions. The free vibration problem is solved first to extract the mode shapes and natural frequencies associated to the transverse deflection and the electrical potential along the longitudinal axis. Using a Galerkin procedure, we use the obtained mode shapes to develop a reduced-order analytical time dependent model valid for the static and dynamic responses of the nanobeam. The results are validated with results found in the literature, without the self-field effect. The obtained static and dynamic results show that the flexoelectric effect significantly increases the performance of the nanoactuator for high aspect ratio of the nanobeam. Finally, we calculate analytically the electromechanical coupling coefficient and verified that high values can be obtained when correctly tunning the geometry.

4.1 Introduction

Flexoelectricity, referring to the spontaneous polarization in response to strain gradient, is a universal effect in all classes of dielectric materials even for centrosymmetric crystals. This phenomenon can be interpreted as a local dissymmetry of the material structure caused by the strain gradient, allowing the creation of a dipole moments and thus the induced polarization [2].

S. Baroudi (✉) · A. Jemai · F. Najar
Applied Mechanics and Systems Research Laboratory, Tunisia Polytechnic School, University of Carthage, La Marsa 2078, BP743, La Marsa, Tunisia
e-mail: sourour.baroudi@gmail.com

M. Belhaq (ed.), *Recent Trends in Applied Nonlinear Mechanics and Physics*, Springer Proceedings in Physics 199, https://doi.org/10.1007/978-3-319-63937-6_4

Recently, Zubko et al. [3], Nguyen et al. [4] and Yudin and Tagantsev [5] have conducted a thorough and comprehensive review elaborating the fundamentals of the flexoelectricity in solids, its consequences in the physical properties of nanoscale systems and the potential applications of this electromechanical phenomenon. Moreover, at the nanoscale, where large strain gradients are expected, the flexoelectric effect becomes more appreciable. Thus the size-dependent flexoelectricity may contribute significantly to the electro-mechanical coupling of piezoelectric materials at the nanoscale and it is necessary to incorporate such an effect when investigating the static and dynamic behaviors of those materials. Indeed, a comprehensive theoretical framework incorporating flexoelectricity, surface effects and electrostatic force was developed by Hu and Shen [9].

Then, the size-dependent electroelastic responses and dynamic behaviors of one-dimensional piezoelectric nanostructures were investigated by Yan and Jiang in their works [11, 12]. Recently, Deng et al. [13] was particularly interested by the possibility of using the phenomenon of flexoelectricity for energy harvesting and showed that flexoelectric based energy harvesting can be a viable alternative to piezoelectricity. In their work, Deng et al. [13] adopted a linear form of the electric potential and considered only the strain gradient along the beam thickness direction.

Here we aim to study the electroelastic responses and dynamic behaviors of a nanoactuator in which both the flexoelectricity and piezoelectricity effects are considered. Also, we propose to take into account the effect of the self-generated electrical potential.

4.2 Problem Formulation

We consider a nanobeam with length L, width b and thickness h, covered by two metallic electrodes where an electric potential $v(t)$ is applied (Fig. 4.1). The nanobeam is modeled using the Euler-Bernoulli beam theory. Thus the displacement vector $\mathbf{u}$ of an arbitrary point located at $(x, 0, z)$ of the nanobeam is given by

$$\begin{aligned} \mathbf{u} &= -z\frac{\partial w(x,t)}{\partial x}\mathbf{x} + w(x,t)\mathbf{z} \\ &= -zw'(x,t)\mathbf{x} + w(x,t)\mathbf{z} \end{aligned} \tag{4.1}$$

where $w(x,t)$ represent the transverse displacement component, $(\mathbf{x}, \mathbf{y}, \mathbf{z})$ is the rectangular orthonormal Cartesian basis, t is the time and the prime corresponds to derivative with respect to x. From this displacement field, the only non-zero strain component is $\varepsilon_{xx} = -zw''$. Therefore, the non-zero strain gradient components are $\varepsilon_{xx,x} = -zw'''$ and $\varepsilon_{xx,z} = -w''$. The polarization density field within the cantilever beam is considered to be along the two axis: x-axis and z-axis, as follows:

$$\mathbf{P} = P_x(x,z,t)\mathbf{x} + P_z(x,z,t)\mathbf{z} \tag{4.2}$$

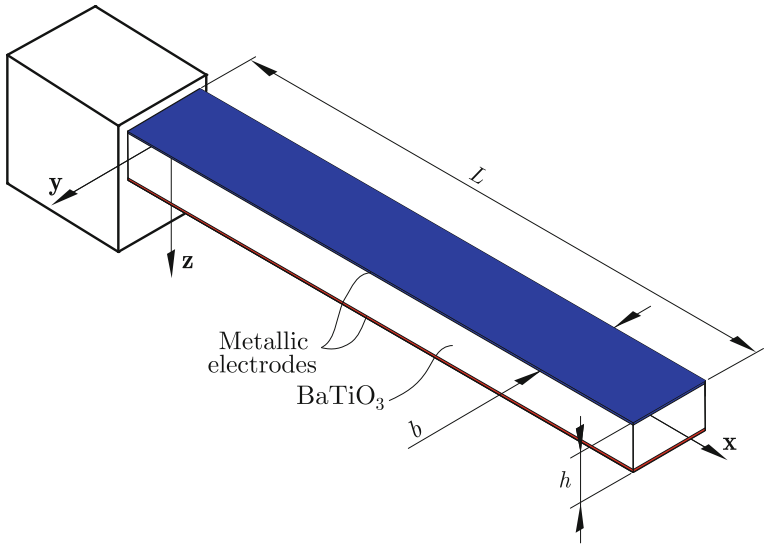

Fig. 4.1 Nanobeam actuator

We assume that the potential ϕ is approximated by the following formula [14]

$$\phi(x,z,t) = \varphi(x,t)\cos(\frac{\pi}{h}z) + \frac{z+h/2}{h}v(t)(H(x) - H(x-L)) \tag{4.3}$$

where $v(t)$ is the voltage across the electrodes and $H(x)$ is the Heaviside step function.

Referring to [8], given the above assumptions, the expression of the internal energy density W^L can be written as:

$$\begin{aligned} W^L = \; & \frac{1}{2}a_{11}P_x^2 + \frac{1}{2}a_{33}P_z^2 + \frac{1}{2}c_{11}\varepsilon_{xx}^2 + d_{11}\varepsilon_{xx}P_x + d_{13}\varepsilon_{xx}P_z \\ & + f_{11}\varepsilon_{xx,x}P_x + f_{14}\varepsilon_{xx,z}P_z \end{aligned} \tag{4.4}$$

We obtain then the explicit expressions of the nonzero components of the stress tensor $\mathbf{T}$, the higher order stress tensor $\tilde{\mathbf{T}}$ and the electric filed $\mathbf{E}$ as follows:

$$T_{11} = c_{11}\varepsilon_{xx} + d_{11}P_x + d_{13}P_z \tag{4.5}$$

$$\tilde{T}_{111} = f_{11}P_x \tag{4.6}$$

$$\tilde{T}_{113} = f_{14}P_z \tag{4.7}$$

$$-\mathrm{E}_1 = a_{11}P_x + d_{11}\varepsilon_{xx} + f_{11}\varepsilon_{xx,x} \tag{4.8}$$

$$-\mathrm{E}_3 = a_{33}P_z + d_{13}\varepsilon_{xx} + f_{14}\varepsilon_{xx,z} \tag{4.9}$$

To derive the governing electroelastic equations and the boundary conditions of the system, we apply the extended Hamilton principle as follows:

$$\int_{t_1}^{t_2} \left(\delta K - \int_V \delta H \, dV + \delta W_{nc} \right) dt = 0 \tag{4.10}$$

where K is the kinetic energy, H is the enthalpy density and W_{nc} is the work done by the external nonconservative forces.

According to Toupin [8], the enthalpy density of perfectly elastic dielectrics is defined as:

$$H = W^L - \frac{1}{2}\varepsilon\phi_{,i}^2 + P_i\phi_{,i} \quad i = x, y, z \tag{4.11}$$

where W^L is the internal energy density, ε is the permittivity of the medium and the index following a coma in the subscript corresponds to the derivative with respect to the ith-direction.

Then the variation of the electric enthalpy density is given by:

$$\begin{aligned} \delta H &= \delta W^L + \left(P_x - \varepsilon\phi_{,x}\right)\delta\phi_{,x} + \left(P_z - \varepsilon\phi_{,z}\right)\delta\phi_{,z} + \phi_{,x}\delta P_x + \phi_{,z}\delta P_z \\ &= \left(-zT_{11} - \tilde{T}_{113}\right)\delta w'' - z\tilde{T}_{111}\delta w''' + \left(\phi_{,x} - E_1\right)\delta P_x + \left(\phi_{,z} - E_3\right)\delta P_z \\ &\quad + \left(P_x - \varepsilon\phi_{,x}\right)\delta\phi_{,x} + \left(P_z - \varepsilon\phi_{,z}\right)\delta\phi_{,z} \end{aligned} \tag{4.12}$$

The expression of the variation of the kinetic energy is reduced to

$$\delta K = -\int_0^L m_0\ddot{w}\,\delta w dx \tag{4.13}$$

where m_0 is the principal inertia given by $m_0 = \rho A$.

Assuming that the applied external force F is constant and concentrated at the free end of the nanobeam, the variation of W_{nc} is given by

$$\delta W_{nc} = \int_V F\delta(x - L)\delta w dV \tag{4.14}$$

Inserting the expressions of K, H and W_{nc} in (4.10), setting the quantities δw, δP_x, δP_z and $\delta\phi$ as arbitrary yields to the following governing equations:

$$m_0\ddot{w} + M'' = F\delta(x - L)A \tag{4.15}$$

$$P_{x,x} + P_{z,z} - \epsilon\phi_{,xx} - \epsilon\phi_{,zz} = 0 \tag{4.16}$$

$$\phi_{,x} - E_1 = 0 \tag{4.17}$$

$$\phi_{,z} - E_3 = 0 \tag{4.18}$$

The following boundary conditions are associated with (4.15).

$$\begin{cases} w(0) = 0 \\ w'(0) = 0 \\ w''(0) = 0 \end{cases} \quad \text{and} \quad \begin{cases} M(L) = 0 \\ M'(L) = 0 \\ \tilde{M}(L) = 0 \end{cases} \tag{4.19}$$

where M is the bending moment and $\tilde{M}$ is a higher-order stress component given by

$$M = \int_A \left(-zT_{11} - \tilde{T}_{113} + z\tilde{T}'_{111}\right) dA \tag{4.20}$$

$$\tilde{M} = \int_A z\tilde{T}_{111} dA \tag{4.21}$$

Now let us derive the equation in terms of the deflection $w(x,t)$ and the potential $\varphi(x,t)$. In fact, combining equations (4.17) and (4.18) with equations (4.8) and (4.9), we can obtain the following formulas of both P_x and P_z as follows

$$P_x = -\frac{\phi_{,x}}{a_{11}} - \frac{d_{11}}{a_{11}}\varepsilon_{xx} - \frac{f_{11}}{a_{11}}\varepsilon_{xx,x} \tag{4.22}$$

$$P_z = -\frac{\phi_{,z}}{a_{33}} - \frac{d_{13}}{a_{33}}\varepsilon_{xx} - \frac{f_{14}}{a_{33}}\varepsilon_{xx,z} \tag{4.23}$$

Using equation (4.3), we deduce the explicit expressions of P_x and P_z as functions of the two unknowns: the deflection w and the potential φ as follows:

$$P_x = -\frac{1}{a_{11}}\cos(\frac{\pi}{h}z)\varphi'(x,t) - \frac{z+h/2}{a_{11}h}v(t)\left(\delta(x) - \delta(x-L)\right) \tag{4.24}$$

$$+\frac{d_{11}}{a_{11}}zw'' + \frac{f_{11}}{a_{11}}zw'''$$

$$P_z = \frac{\pi}{a_{33}h}\sin(\frac{\pi}{h}z)\varphi(x,t) - \frac{v(t)}{a_{33}h}\left(H(x) - H(x-L)\right) \tag{4.25}$$

$$+\frac{d_{13}}{a_{33}}zw'' + \frac{f_{14}}{a_{33}}w''$$

Then inserting the above expressions of both P_x and P_z into equation (4.16) gives the differential equation in terms of the potential φ coupled with the deflection w as follows

$$\varphi''(x,t) = \frac{\pi^2\varepsilon_{r33}}{h^2\varepsilon_{r11}}\varphi(x,t) + \frac{\pi d_{13}}{2a_{33}\varepsilon_{r11}}w'' - \frac{\pi}{4}v(t)\left(\delta'(x) - \delta'(x-L)\right) \tag{4.26}$$

where $\varepsilon_{r11} = (\frac{1}{a_{11}} + \varepsilon)$ and $\varepsilon_{r33} = (\frac{1}{a_{33}} + \varepsilon)$. Equation (4.26) is associated with the following boundary conditions

$$\varphi(0,t)=0 \quad \text{and} \quad \varphi(L,t)=0 \tag{4.27}$$

Considering the bending moment M as given in equation (4.20) and inserting the expressions of P_x, $P_{x,x}$ and P_z gives the explicit expression of M as follows:

$$\begin{aligned} M=-\Bigg[&\left(\left(-c_{11}+\frac{{d_{11}}^2}{a_{11}}+\frac{d_{13}^2}{a_{11}}\right)J+\frac{{f_{14}}^2}{a_{33}}A\right)w''-\frac{{f_{11}}^2}{a_{11}}Jw''''\\ &+\frac{2d_{13}bh}{a_{33}\pi}\varphi(x,t)-\frac{d_{11}}{a_{11}}J\frac{v(t)}{h}\left(\delta(x)-\delta(x-L)\right)\\ &+\frac{f_{11}}{a_{11}}J\frac{v(t)}{h}\left(\delta'(x)-\delta'(x-L)\right)\\ &-\frac{f_{14}}{a_{33}}A\frac{v(t)}{h}\left(H(x)-H(x-L)\right)\Bigg] \end{aligned} \tag{4.28}$$

For convenience we introduce the following normalizing variables

$$\hat{w}=\frac{w}{h},\ \hat{\varphi}=\frac{\varphi}{\varphi_0},\ \hat{x}=\frac{x}{L} \quad \text{and} \quad \hat{t}=\frac{t}{\tau} \tag{4.29}$$

where

$$\tau=\sqrt{\frac{L^4m_0}{K_1^*}} \quad \text{and} \quad \varphi_0=\frac{\pi K_1^*a_{33}}{2bL^2d_{13}} \tag{4.30}$$

Then, dropping the hats, we obtain the following nondimensional system of coupled partially derivative equations describing the transverse deflection and the electrical potential variations of the considered nanobeam:

$$\begin{aligned} \ddot{w}+w^{iv}-\alpha_0w^{vi}=&\varphi''+\alpha_1v(t)\left(\delta'''(x)-\delta'''(x-1)\right)\\ &-\alpha_2v(t)\left(\delta''(x)-\delta''(x-1)\right)\\ &-\alpha_3v(t)\left(\delta'(x)-\delta'(x-1)\right)+\alpha_4F\delta(x-1) \end{aligned} \tag{4.31}$$

$$\varphi''-\beta_0\varphi=\beta_1w''-\beta_2v(t)\left(\delta'(x)-\delta'(x-1)\right) \tag{4.32}$$

The nondimensional coefficients in equations (4.31) and (4.32) are given as follows

$$\alpha_0=\frac{K_2^*}{L^2K_1^*},\ \alpha_1=\frac{f_{11}J}{K_1^*h^2a_{11}},\ \alpha_2=\frac{Ld_{11}J}{K_1^*h^2a_{11}},\ \alpha_3=\frac{L^2f_{14}A}{K_1^*a_{33}h^2}$$
$$\alpha_4=\frac{L^3}{K_1^*h},\ \beta_0=\frac{L^2\pi^2\varepsilon_{r33}}{h^2\varepsilon_{r11}},\ \beta_1=\frac{d_{13}A\pi}{2a_{33}\varepsilon_{r11}b\varphi_0},\ \beta_2=\frac{A\pi}{4bh\varphi_0}$$

where the quantities K_1^*, K_2^* and K_3^* are defined here by

$$K_1^* = -\left(-c_{11} + \frac{d_{11}^2}{a_{11}} + \frac{d_{13}^2}{a_{33}}\right) J - \frac{f_{14}^2}{a_{33}} A, \quad K_2^* = -\frac{f_{11}^2}{a_{11}}, \quad K_3^* = \frac{f_{11} d_{11}}{a_{11}} J$$

where $A = bh$ and $J = \frac{bh^3}{12}$.

The governing equations (4.31) and (4.32) are associated with the following normalized boundary conditions

$$\begin{cases} w(0,t) = 0 \\ w'(0,t) = 0 \\ w''(0,t) = 0 \\ \varphi(0,t) = 0 \end{cases} \text{ and } \begin{cases} w''(1,t) - \alpha_0 w^{iv}(1,t) - \varphi(1,t) = 0 \\ w'''(1,t) - \alpha_0 w^{v}(1,t) - \varphi'(1,t) = 0 \\ -w'''(1,t) + \gamma_0 w^{iv}(1,t) = 0 \\ \varphi(1,t) = 0 \end{cases} \tag{4.33}$$

where $\gamma_0 = \frac{K_2^*}{K_3^* L}$.

4.3 Free Vibration Analysis

We propose to solve the eigenvalue problem associated to equations (4.31) and (4.32) and their boundary conditions in order to calculate the natural frequencies and mode shapes of the considered nanobeam at free vibration conditions, i.e. $v(t) = 0$ and $F = 0$. Let's first consider a harmonic response in the form

$$w(x,t) = W(x)e^{i\omega t}, \text{ and } \varphi(x,t) = \psi(x)e^{i\omega t} \tag{4.34}$$

For reason of simplicity, we propose to neglect the sixth order derivative of W representing the nonlocal gradient influence. In such way the system of coupled equations (4.31) and (4.32) are transformed to

$$-\omega^2 W + W^{iv} = \psi'' \tag{4.35}$$

$$\psi'' - \beta_0 \psi = \beta_1 W'' \tag{4.36}$$

The general solution of (4.35) and (4.36) are obtained by considering an exponential form of the solution. Therefore

$$W(x) = \sum_{i=1}^{6} C_i e^{\lambda_i x}, \text{ and } \psi(x) = \sum_{i=1}^{6} C_i D_i e^{\lambda_i x} \tag{4.37}$$

where C_i is a vector of constant to be determined and $(D_i)_{(i=1..6)} = \frac{\beta_1 \lambda_i^2}{\lambda_i^2 - \beta_0}$. The circular eigenfrequencies ω_n for the nth mode can be obtained by solving the following equation

$$Det\,([\mathbf{J}_0]) = 0 \tag{4.38}$$

Table 4.1 The first three nondimensional natural frequencies

ω_1	ω_2	ω_3
3.5208	22.0731	61.7811

where the matrix $\mathbf{J}_0$ is given by

$$[\mathbf{J}_0] = \begin{bmatrix} 1 & 1 & 1 & 1 & 1 & 1 \\ \lambda_1 & \lambda_2 & \lambda_3 & \lambda_4 & \lambda_5 & \lambda_6 \\ \lambda_1^2 e^{\lambda_1} & \lambda_2^2 e^{\lambda_2} & \lambda_3^2 e^{\lambda_3} & \lambda_4^2 e^{\lambda_4} & \lambda_5^2 e^{\lambda_5} & \lambda_6^2 e^{\lambda_6} \\ \Lambda_1 e^{\lambda_1} & \Lambda_2 e^{\lambda_2} & \Lambda_3 e^{\lambda_3} & \Lambda_4 e^{\lambda_4} & \Lambda_5 e^{\lambda_5} & \Lambda_6 e^{\lambda_6} \\ D_1 & D_2 & D_3 & D_4 & D_5 & D_6 \\ D_1 e^{\lambda_1} & D_2 e^{\lambda_2} & D_3 e^{\lambda_3} & D_4 e^{\lambda_4} & D_5 e^{\lambda_5} & D_6 e^{\lambda_6} \end{bmatrix} \tag{4.39}$$

in which $(\Lambda_i)_{(i=1..6)} = -\lambda_i^3 + D_i \lambda_i$.

Considering the proposed general solutions (4.37), applying the boundary conditions appearing in (4.33) and setting C_1 as arbitrary constant, the constants C_2 to C_6 can be calculated.

For numerical results, we use $BaTiO_3$ whose material properties are obtained from [15]. Considering the plane stress condition, we calculate the material constants as follows: the elastic constant $c_{11} = 131\text{GPa}$, the dielectric constants $a_{11} = 0.897 \times 10^8\text{Vm/C}$, $a_{33} = 0.788 \times 10^8\text{Vm/C}$, the piezoelectric constants $d_{11} = -18.52 \times 10^8\text{V/m}$ and $d_{13} = 1.87 \times 10^8\text{V/m}$. The mass density is $\rho = 6.02 \times 10^3\text{kg/m}^3$. We refer to [16] to deduce the flexoelectric constant $f_{11} = -0.013\text{V}$ and following Yan et al. [11, 12] we set the flexoelectric coefficient $f_{14} = 5\text{V}$.

Table 4.1 gives the first three non-dimensional natural frequencies of piezoelectric flexoelectric cantilever nanobeam. Figures 4.2 and 4.3 show the first three mode shapes of the transverse deflection W and the potential ψ, respectively.

4.4 Static Response

We apply the Galerkin approximation method and rewrite the static nondimensional transverse deflection and the electrical potential as

$$w(x) = \sum_{i=1}^{N_i} Q_i W_i(x), \text{ and } \varphi(x) = \sum_{j=1}^{N_j} U_j \psi_j(x) \tag{4.40}$$

Substituting (4.40) into (4.31) and (4.32) multiplying the outcome by the corresponding mode shape, integrating over the domain and applying the orthogonality condition, we end up with two uncoupled equations in terms of the generalized amplitudes $(Q_i)_{(i=1..N_i)}$ and $(U_j)_{(j=1..N_j)}$ as follows:

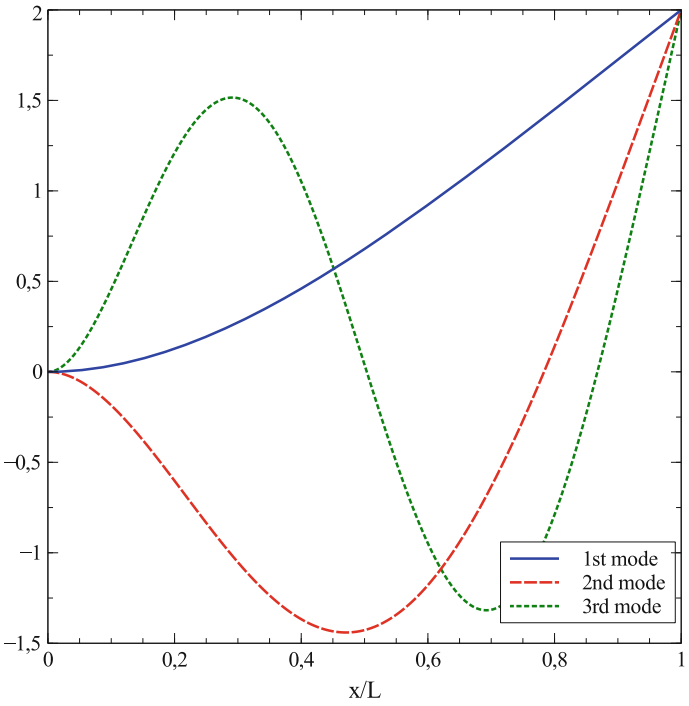

Fig. 4.2 First three transverse deflection mode shapes

$$Q_i J_{in}^{(1)} = \alpha_0 Q_i J_{in}^{(2)} + U_j J_{jn}^{(3)} + \left(\alpha_1 \Theta_n^{(1)} - \alpha_2 \Theta_n^{(2)} - \alpha_3 \Theta_n^{(3)}\right) v + \alpha_4 \bar{f}_n \tag{4.41}$$

$$U_j J_{jm}^{(4)} = \beta_0 U_m + \beta_1 Q_i J_{im}^{(5)} - \beta_2 V \Theta_m^{(4)} \tag{4.42}$$

$$i, n = 1..N_i \quad \text{and} \quad j, m = 1..N_j$$

where

$$\begin{aligned}
J_{in}^{(1)} &= \int_0^1 W_i''''(x) W_n(x) dx \\
J_{in}^{(2)} &= \int_0^1 W_i^{vi}(x) W_n(x) dx \\
J_{jn}^{(3)} &= \int_0^1 \psi_j''(x) W_n(x) dx \\
J_{jm}^{(4)} &= \int_0^1 \psi_j''(x) \psi_m(x) dx \\
J_{im}^{(5)} &= \int_0^1 W_i''(x) \psi_m(x) dx \\
\Theta_n^{(1)} &= \int_0^1 W_n^{iv}(x) dx \\
\Theta_n^{(2)} &= -\int_0^1 W_n'''(x) dx \\
\Theta_n^{(3)} &= \int_0^1 W_n''(x) dx \\
\Theta_m^{(4)} &= \int_0^1 \psi_m''(x) dx \\
\bar{f}_n &= F W_n(1)
\end{aligned} \tag{4.43}$$

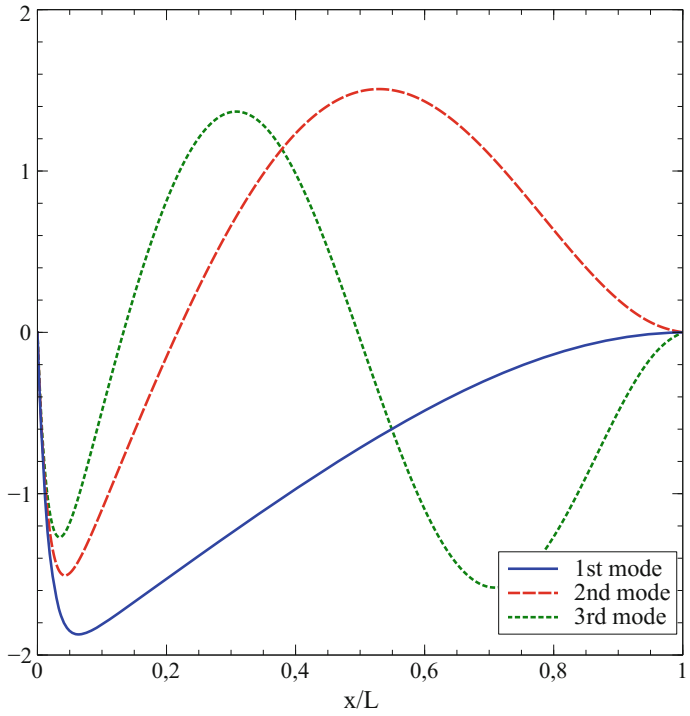

Fig. 4.3 First three electrical potential modes

For numerical results, we consider that the nanobeam is loaded with a concentrated force $F = 1\text{nN}$ and a constant voltage $v = -0.1\text{V}$. The dimensions of the nanobeam are chosen so that $b = h$.

Figure 4.4 represents the normalized deflection in comparison with Yan et al. [11] showing a good convenience with our model if we consider only one dimensional model and linear distribution of the electrical potential ϕ (i.e. $\varphi(x) = 0$). When the full model is considered (red curve in Fig. 4.4), a mismatch is observed demonstrating that effect of the self-field induced potential cannot be neglected, and that, under these conditions, the model used by Yan et al. [11] underestimates the effect of the flexoelectricity.

4.5 Dynamic Response

Here the dynamic behavior of the structure is investigated by considering an applied voltage of the form $v(t) = Ve^{i\Omega t}$ and by setting the static force $F = 0$. We consider the time variation of the two variables $w(x, t)$ and $\varphi(x, t)$ as follows

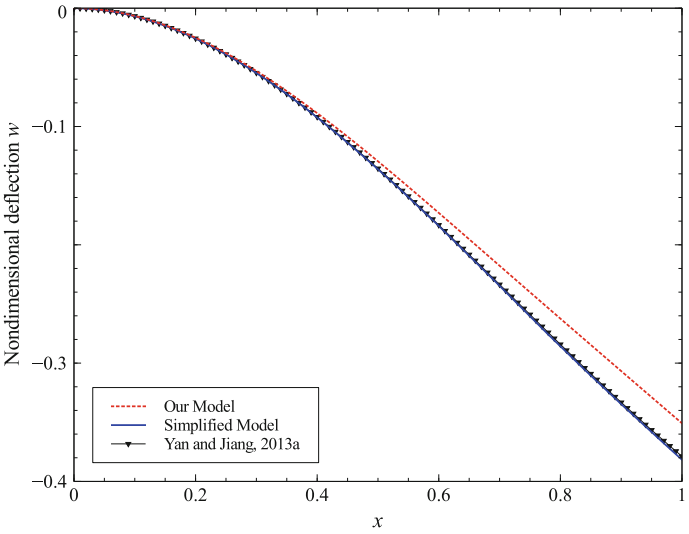

Fig. 4.4 Normalized defection variation in comparison with previous work [11] (V = −0.1, L/h=20, h = 20 nm, F = −1nN)

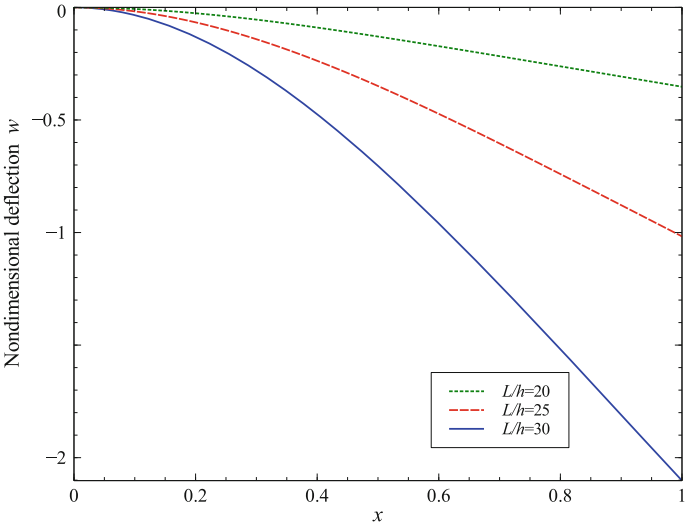

Fig. 4.5 Normalized deflection for different aspect ratios L/h ($V = -0.1$V, $h = 20$nm, $F = -1$nN)

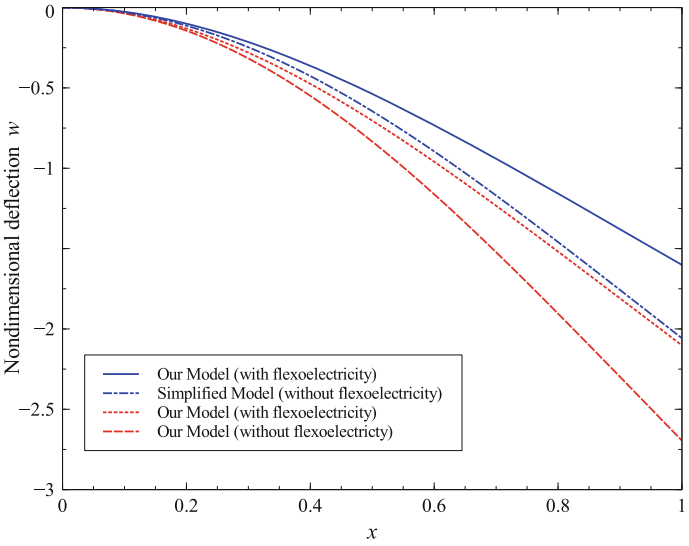

Fig. 4.6 Effect of flexoelectriciy in the distribution of the normalized deflection in comparison with the simplified model ($V = -0.1$V, $L/h = 30$, $h = 20$nm)

$$w(x,t) = \sum_{i=1}^{N_i} q_i(t) W_i(x), \text{ and } \varphi(x,t) = \sum_{j=1}^{N_j} u_j(t)\psi_j(x) \tag{4.44}$$

Introducing the diagonal damping matrix ξ defined as $\xi_n = \frac{\omega_n}{Q}$ where Q is the quality factor chosen equal to 10 and considering a harmonic behavior for the generalized coordinate of displacement **q(t)**, the generalized coordinate of the potential **u(t)**, and the voltage v(t), as follows $\mathbf{q}(t) = \mathbf{Q}e^{j\omega t}$, $\mathbf{u}(t) = \mathbf{U}e^{j\omega t}$, $\mathbf{v}(t) = \mathbf{V}e^{j\omega t}$, we deduce the dynamic response of our system in terms of the amplitude of the displacement $\mathbf{Q}(t)$ and the amplitude of the electric potential $\mathbf{U}(t)$ as follows:

$$(-\omega^2 + j\omega\xi_n) Q_n + Q_i J_{in}^{(1)} = \alpha_0 Q_i J_{in}^{(2)} + U_j J_{jn}^{(3)} \tag{4.45}$$

$$+ \left(\alpha_1 \Theta_n^{(1)} - \alpha_2 \Theta_n^{(2)} - \alpha_3 \Theta_n^{(3)}\right) V$$

$$U_j J_{jm}^{(4)} = \beta_0 U_m + \beta_1 Q_i J_{im}^{(5)} - \beta_2 V \Theta_m^{(4)} \tag{4.46}$$

$$i, n = 1..N_i \quad \text{and} \quad j, m = 1..N_j$$

Figure 4.5 represents the normalized defection for different aspect ratios L/h and a thickness equal to 20×10^{-9}. It is clear that the response of the nanoactuator is well accentuated for slender beam ($L/h = 30$ for example). Figure 4.6 shows the effect of the flexoelectric coupling for both the current model and the simplified one.

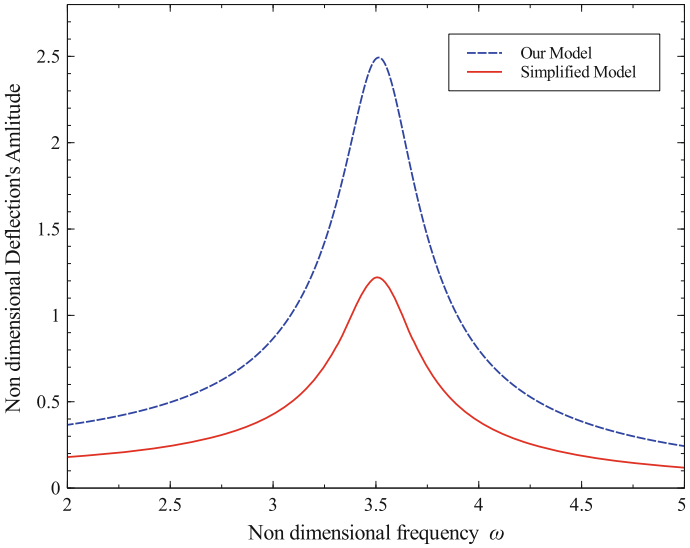

Fig. 4.7 Comparison of nondimensional dynamic defection's amplitude for different models (V= −0.1, L/h=20, h=20 nm)

One can clearly see that the flexoelectricity coupling tends to decrease the predicted deflection since the stiffness of the structure is well modified. Figure 4.7 represents the normalized dynamic deflection for a thickness equal to 20×10^{-9} and an aspect ratios L/h equal to 20. It is clear that the response of the nanoactuator of the nanoactuator is well increased when considering our comprehensive model. The discrepancy between the two models indicates that more accurate and exact results are obtained thanks to our complete model and shows the necessity of taking into consideration the current assumptions.

4.6 Electromechanical Coupling Coefficient

The Electromechanical Coupling Coefficient (EMCC) can be obtained by measuring the variations of the energy stored in the nanobeam at open circuit (OC) and short circuit (SC) conditions [17].

$$\kappa = \sqrt{\frac{U_{OC} - U_{SC}}{U_{OC}}} \tag{4.47}$$

where U_{OC} is the total energy measured at the OC, (i.e. the electric displacement $\mathbf{D}$ is equal to zero), and U_{SC} is the total energy measured at the SC, (i.e. the electric field $\mathbf{E}$ is equal to zero).

Considering equations (4.8) and (4.9) and knowing that $\mathbf{P} = \epsilon\mathbf{E} + \mathbf{D}$, we can deduce the expression of $\mathbf{P}$ for both electric conditions.

4.6.1 Stored Energy at SC Conditions

For SC conditions, the expression of the polarization components $P_{x_{SC}}$ and $P_{z_{SC}}$ are obtained by using their general expressions in (4.24) and (4.25), that is

$$P_{x_{SC}} = \frac{d_{11}}{a_{11}} z w'' + \frac{f_{11}}{a_{11}} z w'''' \tag{4.48}$$

$$P_{z_{SC}} = \frac{d_{13}}{a_{33}} z w'' + \frac{f_{14}}{a_{33}} w'' \tag{4.49}$$

Therefore, the total energy U_{SC} stores at SC condition is expressed as follows

$$\begin{aligned} U_{SC} &= \int_V W_{SC}^L dV = \int_V \left[\frac{1}{2} a_{11} P_{x_{SC}}^2 + \frac{1}{2} a_{33} P_{z_{SC}}^2 + \frac{1}{2} c_{11} \varepsilon_{xx}^2 + d_{11} \varepsilon_{xx} P_{x_{SC}} + d_{13} \varepsilon_{xx} P_{z_{SC}} \right. \\ &\left. + f_{11} \varepsilon_{xx,x} P_{x_{SC}} + f_{14} \varepsilon_{xx,z} P_{z_{SC}} \right] dV \\ &= \frac{1}{2} \left[K_1^* \int_0^L w''^2(x,t) dx + K_2^* \int_0^L w''''^2(x,t) dx - K_3^* \int_0^L w''(x,t) w''''(x,t) dx \right] \end{aligned} \tag{4.50}$$

4.6.2 Stored Energy at OC Conditions

For OC conditions, the the total energy is given by

$$P_{x_{OC}} = \frac{d_{11}}{a_{11} + \frac{1}{\varepsilon}} z w'' + \frac{f_{11}}{a_{11} + \frac{1}{\varepsilon}} z w'''' \tag{4.51}$$

$$P_{z_{OC}} = \frac{d_{13}}{a_{33} + \frac{1}{\varepsilon}} z w'' + \frac{f_{14}}{a_{33} + \frac{1}{\varepsilon}} w'' \tag{4.52}$$

Therefore, the total energy U_{OC} stored at OC condition is expressed as follows

$$\begin{aligned} U_{OC} &= \int_V W_{OC}^L dV = \int_V \left[\frac{1}{2} a_{11} P_{x_{OC}}^2 + \frac{1}{2} a_{33} P_{z_{OC}}^2 + \frac{1}{2} c_{11} \varepsilon_{xx}^2 + d_{11} \varepsilon_{xx} P_{x_{OC}} + d_{13} \varepsilon_{xx} P_{z_{OC}} \right. \\ &\left. + f_{11} \varepsilon_{xx,x} P_{x_{OC}} + f_{14} \varepsilon_{xx,z} P_{z_{OC}} \right] dV \\ &= \frac{1}{2} \left[K_4^* \int_0^L w''^2(x,t) dx + K_5^* \int_0^L w''''^2(x,t) dx + K_6^* \int_0^L w''(x,t) w''''(x,t) dx \right] \end{aligned} \tag{4.53}$$

where K_4^*, K_5^*, K_6^* are defined as follows:

$$\begin{aligned}
K_4^* =& 2\left(c_{11} + \frac{a_{11}\varepsilon_0^2}{(1+a_{11}\varepsilon_0)^2}d_{11}^2 + \frac{a_{33}\varepsilon_0^2}{(1+a_{33}\varepsilon_0)^2}d_{13}^2\right)J + \frac{2a_{33}\varepsilon_0^2}{(1+a_{33}\varepsilon_0)^2}f_{14}^2 A \\
&- \left(\frac{d_{11}^2}{1+a_{11}\varepsilon_0} + \frac{d_{13}^2}{1+a_{33}\varepsilon_0}\right)4\varepsilon_0 J - \frac{4\varepsilon_0}{1+a_{33}\varepsilon_0}f_{14}^2 A \\
K_5^* =& -\frac{(2-a_{11}\varepsilon_0)\,2\varepsilon_0 f_{11}^2 J}{\left(1+a_{11}\varepsilon_0)^2\right)} \\
K_3^* =& \left(\frac{2a_{11}\varepsilon_0^2}{(1+a_{11}\varepsilon_0)^2} - \frac{\varepsilon_0}{3\,(1+a_{11}\varepsilon_0)}\right)2 f_{11} d_{11} J
\end{aligned}$$

4.6.3 Approximation of the Electromechanical Coupling Coefficient

Applying the Galerkin approximation, we end up with the following expressions of U_{SC} and U_{OC}

$$U_{SC} = \frac{1}{2}\left[K_1^*\Xi_{in}^{(1)} + K_2^*\Xi_{in}^{(2)} - K_3^*\Xi_{in}^{(3)}\right]Q_i^2(t) \tag{4.54}$$

$$U_{OC} = \frac{1}{2}\left[K_4^*\Xi_{in}^{(1)} + K_5^*\Xi_{in}^{(2)} + K_6^*\Xi_{in}^{(3)}\right]Q_i^2(t) \tag{4.55}$$

where $\Xi_{in}^{(1)}$, $\Xi_{in}^{(2)}$ and $\Xi_{in}^{(3)}$ are integral terms given by

$$\Xi_{in}^{(1)} = \frac{L^3}{h^2}\int_0^1 W_i''(x)^2 W_n(x)dx \tag{4.56}$$

$$\Xi_{in}^{(2)} = \frac{L^5}{h^2}\int_0^1 W_i'''(x)^2 W_n(x)dx \tag{4.57}$$

$$\Xi_{in}^{(3)} = \frac{L^4}{h^2}\int_0^1 W_i''(x) W_i'''(x) W_n(x)dx \tag{4.58}$$

Finally the EMCC κ is given by

$$\kappa = \sqrt{\frac{\left(K_4^* - K_1^*\right)\Xi_{in}^{(1)} + \left(K_5^* - K_2^*\right)\Xi_{in}^{(2)} + \left(K_6^* + K_3^*\right)\Xi_{in}^{(3)}}{K_4^*\Xi_{in}^{(1)} + K_5^*\Xi_{in}^{(2)} + K_6^*\Xi_{in}^{(3)}}} \tag{4.59}$$

In Fig. 4.8 the variation of the electromechanical coupling coefficient κ of the nanobeam with the beam thickness h is illustrated. One can remark that κ is highly

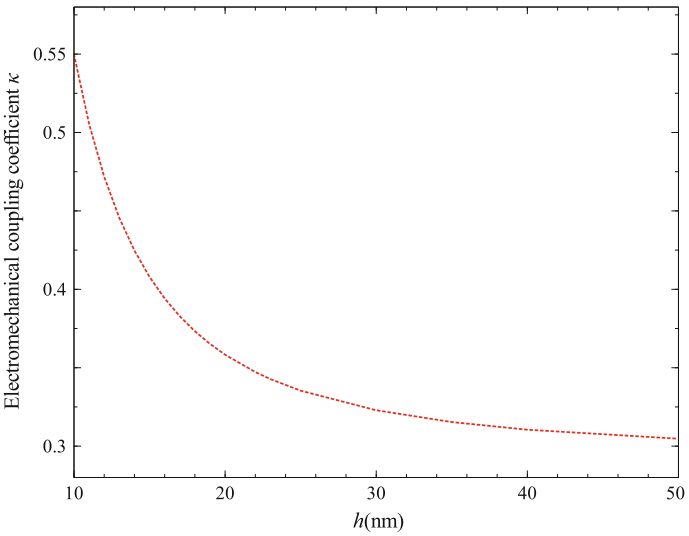

Fig. 4.8 Variation of the electromechanical coupling coefficient κ with the thickness h (L/h=20)

affected by the aspect ratio of the nanobeam. As it is predicted, the efficiency of the flexoelectric device increases with the decrease of the beam thickness showing the necessity of taking into consideration the flexoelectric coupling when designing piezoelectric devices at the nanoscale.

4.7 Conclusion

In this work, a flexoelectric piezoelectric cantilever nanobeam is modeled to investigate the static and dynamic response of $BaTiO_3$ nanoactuator. Starting with the strain gradient linear theory of piezoelectricity and applying the extended Hamilton principle, the governing system of coupled differential equations is derived for the transverse deflection and a two dimensional distribution of the electric potential inside the nanobeam. An eigenvalue problem is established to study the free vibration of the device. Finally, using the Galerkin method, the static and dynamic bending responses are studied and compared to previous and simplified works. Our results show that considerable effect are observed especially when considering self-field effect of the induced electric potential, which was not the case in previous published analyses. We illustrate also that the flexoelectric coupling effect can be responsible for increasing the size-dependent properties of dielectric materials at the nanoscale. This conclusion was also verified by calculating the electromechanical coupling coefficient.

Acknowledgements Part of the material of this chapter was presented in the Third International Conference on Structural Nonlinear Dynamics and Diagnosis (CSNDD'2016), Marrakech, Morocco, May 23–25, 2016. The organizers are acknowledged for partial support.

References

1. Yang, J.S.: Appl. Mech. Rev **59**, 335–345 (2006)
2. Maranganti, R., Sharma, N.D., Sharma, P., P.: Phys. Rev. B **74**, 014110 (2009)
3. Zubko, P., Catalan, G., Tagantsev, A.K.: Annu. Rev. Mater. **43**, 387–421 (2013)
4. Nguyen, T.D., Mao, S., Yeh, Y.W., Purohit, P.K., McAlpine, M.C.: Adv. Mater. **25**, 946–974 (2013)
5. Yudin, P.V., Tagantsev, A.K.: Nanotechnology **24**, 432001 (2013)
6. Majdoub, M.S., Sharma, P., Çağin, T.: Phys. Rev. B **78**(12), 121407 (2008)
7. Liang, X., Hu, S., Shen, S.: Smart Mater. Struct. **23**, 035020 (2013)
8. Toupin, R.A.: J. Rational Mech. Anal. **5**(6), 849–915 (1956)
9. Hu, S.L., Shen, S.P.: Science China physics. Mech. Astron. **53**, 1497–1504 (2010)
10. Liu, C.C., Hu, S.L., Shen, S.P.: Smart Mater. Struct. **21**, 115024 (2012)
11. Yan, Z., Jiang, L.Y.: J. Appl. Phys. **113**, 194102 (2013)
12. Yan, Z., Jiang, L.Y.: J. Appl. Phys. **46**, 355502 (2013)
13. Deng, Q., Kammoun, M., Erturk, A., Sharma, P.: Int. J. Solids Struct. **51**, 3218–3225 (2014)
14. Wang, Q.: Eng. Struct. **24**, 199–205 (2002)
15. Tagantsev, A.K., Yurkov, A.S.: J. Appl. Phys. **112**, 044103 (2012)
16. Maranganti, R., Sharma, P.: Phys. Rev. B **80**, 054109 (2009)
17. Trindade, M.A., Benjeddou, A.: Mech. of Adv. Mat. Struct. **16**, 210223 (2009)

Chapter 5
Dynamics of a Chain with Four Particles, Alternating Masses and Nearest-Neighbor Interaction

Roelof Bruggeman and Ferdinand Verhulst

Abstract We formulate the periodic FPU problem with four alternating masses which is the simplest nontrivial version. The analysis involves normal form calculations to second order producing integrable normal forms with three timescales. In the case of large alternating mass the system is an example of dynamics with widely separated frequencies and three timescales. The presence of approximate integrals and the stability characteristics of the periodic solutions lead to weak interaction of the modes of the system.

5.1 Introduction

For the mono-atomic case of the original periodic FPU-problem (Fermi-Pasta-Ulam problem) with all masses (or particles) equal it was shown in [4] for up to six degrees-of-freedom (dof) and for an arbitrary number of dof in [5], that the corresponding normal forms are governed by $1:1$ resonances and that these Hamiltonian normal forms are integrable. This explains the recurrence phenomena near stable equilibrium for long intervals of time.

In [1] we have studied the inhomogeneous FPU-problem which contains many different resonance cases. In [9] and [10] recurrence and near-integrability aspects of FPU cells were studied. The alternating case was studied in [2] for a FPU chain with fixed end-points using analytic and numerical tools to obtain insight in the equipartition of energy, in particular between the low (acoustic) frequency and the high (optical) frequency part. A preliminary but important conclusion in [2] is that for the masses considered and on long timescales no equipartition takes place; the evidence is numerical. Inspired by [2] we will study the periodic FPU-problem in the case of alternating masses. The simplest nontrivial form of this problem is for four particles, it is necessary to understand this problem first. In a subsequent paper we

R. Bruggeman (✉) · F. Verhulst
Mathematisch Instituut, 3508TA, PO Box 80.010 Utrecht, Netherlands
e-mail: r.w.bruggeman@uu.nl

F. Verhulst
e-mail: f.verhulst@uu.nl

M. Belhaq (ed.), *Recent Trends in Applied Nonlinear Mechanics and Physics*,
Springer Proceedings in Physics 199, https://doi.org/10.1007/978-3-319-63937-6_5

will study the more general problem with an even number of particles. The emphasis will be on periodic solutions, integrability of the normal forms (near-integrability of the original system), invariant manifolds and recurrence phenomena; for recurrence see also [9].

In a periodic chain, for (even) n particles with arbitrary masses $m_j > 0$, position q_j and momentum $p_j = m_j \dot{q}_j$, $j = 1 \ldots n$, the Hamiltonian (see [1]) is of the form:

$$H(p,q) = \sum_{j=1}^{n} \left(\frac{1}{2m_j} p_j^2 + V(q_{j+1} - q_j) \right) \text{ with } V(z) = \frac{1}{2}z^2 + \frac{\alpha}{3}z^3 + \frac{\beta}{4}z^4. \tag{5.1}$$

If $\alpha = 1, \beta = 0$ we will call this an α-chain, if $\alpha = 0, \beta = 1$ a β-chain. The quadratic part of the Hamiltonian is not in diagonal form; for $n = 4$ the linearized equations of motion can be written as:

$$\begin{cases} m_1 \ddot{q}_1 + 2q_1 - q_2 - q_4 = 0, \\ m_2 \ddot{q}_2 + 2q_2 - q_3 - q_1 = 0, \\ m_3 \ddot{q}_3 + 2q_3 - q_4 - q_2 = 0, \\ m_4 \ddot{q}_4 + 2q_4 - q_1 - q_3 = 0. \end{cases} \tag{5.2}$$

In system (5.2) the 4 alternating masses are $1, m, 1, m$, with $m > 1$. Although this number of particles is small, the problem of the dynamics of such a periodic chain is by no means trivial. Moreover we will indicate that the dynamics of a small number of particles in the chain is in a certain sense typical for much larger systems.

The mass ratio $m : 1$ is the important parameter, we put $a = 1/m$, $0 < a < 1$. The eigenvalues of system (5.2) will be indicated by λ_i, $i = 1, \ldots, 4$, the corresponding frequencies of the linear normal modes are $\omega_i = \sqrt{\lambda_i}$. The numerical value of H_2 for given initial conditions is indicated by E_0. We will use symplectic transformation to put the linear part of the equations of motion in quasi-harmonic form. The solutions in the eigendirections of the equations of motion linearized near the origin are called the linear normal modes of the system, they can be continued for the nonlinear system. The transformation to quasi-harmonic form is natural but introduces an interpretation problem. Intuitively we expect the masses 1 to be more excitable than the masses m. However, after symplectic transformation we have in the resulting equations of motion a mix of both sets of particles and at the same time a splitting of the spectrum in $O(1)$ frequencies with modes that we will call 'optical' and $O(\sqrt{a})$ frequencies called 'acoustical'. The behaviour of the solutions within the two sets of particles can not in a simple way be identified with the normal mode (quasi-harmonic) equations corresponding with the optical and acoustical part of the spectrum.

In the following sections the analysis by averaging-normal forms is a basic tool. For the general theory and results in the case of Hamiltonian systems see [6]. Resonances in the frequency-spectrum of the linearized equations of motion, generated

by the quadratic part of the Hamiltonian H_2, play a fundamental part in the analysis. The cubic part H_3 and if necessary the quartic part H_4 will be normalized to $\bar{H}_3$, $\bar{H}_4$.

In [1] we have discussed a number of technical normal form aspects of averaging for Hamiltonian systems. In a system of n perturbed harmonic equations we will often transform to polar coordinates. If the frequencies are $\omega_j,\ 1 \le j \le n$ we introduce

$$x_j = r_j \cos(\omega_j t + \varphi_j)\,, \quad y_j = -r_j\,\omega_j \sin(\omega_j t + \varphi_j) \qquad (1 \le j \le 7) \qquad (5.3)$$

to produce an equivalent first-order system in the variables

$$X = (r_1, r_2, \ldots, r_n, \varphi_1, \ldots, \varphi_n)\,.$$

This system is equivalent with the n dof system of perturbed harmonic equations outside the normal mode planes.

The numerical experiments were carried out by MATCONT under MATLAB with ode solver 78. The precision was increased until the picture did not change anymore with typical relative error e^{-15}, absolute error e^{-17}. A number of algebraic manipulations were carried out using MATHEMATICA.

It will turn out that for the α- and β-chain especially the analysis for large mass is interesting. The normal form systems are in this case examples of integrable systems with widely separated frequencies. The dynamics involves periodic solutions, among which three normal modes; their stability can be established from the equations and the integrals. The normal form analysis has to be carried out to second order and uses three timescales. Using these results we can sketch a global picture of the phase-flow with a number of characteristic examples of recurrence phenomena. In the discussion we will mention the relevance of our results for FPU-systems with many more particles.

5.2 Periodic FPU Chains with 4 Alternating Masses

We find from the equations of motion, both for an α- and for a β-chain, the momentum integral:

$$\dot{q}_1 + m\dot{q}_2 + \dot{q}_3 + m\dot{q}_4 = \text{constant}. \qquad (5.4)$$

For the linear system (5.2) we find the 4 eigenvalues:

$$\lambda_i = 2(a+1),\ 2,\ 2a,\ 0.$$

with frequencies $\omega_i^2 = \lambda_i$, $i = 1, \ldots, 4$. We perform a symplectic transformation to eigenmodes of the form $q = L_a x$, $p = K_a y$, with the matrices

$$L_a = \begin{pmatrix} -\frac{1}{\sqrt{2a+2}} & -\frac{1}{\sqrt{2}} & 0 & \sqrt{\frac{a}{2\ a+2}} \\ \frac{a}{\sqrt{2a+2}} & 0 & -\frac{\sqrt{a}}{\sqrt{2}} & \sqrt{\frac{a}{2a+2}} \\ -\frac{1}{\sqrt{2a+2}} & \frac{1}{\sqrt{2}} & 0 & \sqrt{\frac{a}{2\ a+2}} \\ \frac{a}{\sqrt{2a+2}} & 0 & \frac{\sqrt{a}}{\sqrt{2}} & \sqrt{\frac{a}{2a+2}} \end{pmatrix}, \tag{5.5}$$

$$K_a = \begin{pmatrix} -\frac{1}{\sqrt{2a+2}} & -\frac{1}{\sqrt{2}} & 0 & \sqrt{\frac{a}{2\ a+2}} \\ \frac{1}{\sqrt{2a+2}} & 0 & -\frac{1}{\sqrt{2}\sqrt{a}} & \frac{1}{\sqrt{a}\sqrt{2a+2}} \\ -\frac{1}{\sqrt{2a+2}} & \frac{1}{\sqrt{2}} & 0 & \sqrt{\frac{a}{2\ a+2}} \\ \frac{1}{\sqrt{2a+2}} & 0 & \frac{1}{\sqrt{2}\sqrt{a}} & \frac{1}{\sqrt{a}\sqrt{2a+2}} \end{pmatrix}. \tag{5.6}$$

The coordinates $(x_4,\ y_4)$ correspond to the momentum integral (5.4). We proceed with the reduced system $(x_j,\ y_j)$, $1 \le j \le 3$, in which the components of the Hamiltonian take the following form:

$$\begin{cases} H_2 = (1+a)x_1^2 + x_2^2 + ax_3^2 + \frac{1}{2}(y_1^2 + y_2^2 + y_3^2), \\ H_3 = -2\sqrt{2a(1+a)}x_1x_2x_3, \\ H_4 = \frac{1}{4}((1+a)^2x_1^4 + x_2^4 + 6ax_2^2x_3^2 + a^2x_3^4 + 6(1+a)x_1^2(x_2^2 + ax_3^2)). \end{cases} \tag{5.7}$$

The usual procedure for normalization as an approximation procedure is to rescale in a neighborhood of equilibrium, in this case $x_i \to \varepsilon x_i,\ y_i \to \varepsilon y_i,\ i = 1, 2, 3$ with ε a small positive parameter. This procedure yields, after dividing by ε^2 in the Hamiltonian a system with a small parameter which is a measure for the distance to equilibrium. The procedure will be implicit in our statements in the case that a is not a small parameter. If $0 < a \ll 1$ (large mass m) we will also leave out the scaling with ε as a will be a natural small parameter. Still, also in this case, we will assume for the solutions to be in a neighborhood of equilibrium; when starting closer to equilibrium (small energy) the normal form results will improve.

5.3 The α-Chain

The equations of motion are for the α-chain with $\gamma = 2\sqrt{2a(1+a)}$:

$$\begin{cases} \ddot{x}_1 + 2(1+a)x_1 = \gamma x_2x_3, \\ \ddot{x}_2 + 2x_2 = \gamma x_1x_3, \\ \ddot{x}_3 + 2ax_3 = \gamma x_1x_2. \end{cases} \tag{5.8}$$

Special solutions are the normal modes associated with the eigenvalues $2(1+a)$, 2 and $2a$. These exact solutions are harmonic for an α-chain. The equilibria of system (5.8) are the origin in phase-space and the points with coordinates:

$$(x_1, x_2, x_3, y_1, y_2, y_3) = \left(\frac{\delta_1}{\sqrt{2(1+a)}}, \frac{\delta_2}{\sqrt{2}}, \frac{\delta_3}{\sqrt{2a}}, 0, 0, 0 \right),$$

with $\delta_i = \pm 1, i = 1, 2, 3$ with $\delta_1\delta_2\delta_3 = 1$. The energy value of the four equilibria outside the origin is in all cases 0.5. The energy manifold bifurcates geometrically in the critical points of the energy manifold, the corresponding equilibria of the equations of motion are unstable. For values of the energy between 0 and 0.5, the energy manifold is compact.

The first order resonances in a three dof system like (5.8) are $1:2:1$, $1:2:2$, $1:2:3$ and $1:2:4$. Considering the spectrum of the linearized system (5.8) we find no three dof first order resonances in a cell with four particles.
Two dof first order resonances occur if $a = \frac{1}{4}, \frac{1}{3}$. Second order resonances arise if $a = \frac{1}{8}, \frac{1}{9}$ and if $0 < a \ll 1$. It was shown in [6] Sect. 10.4, that the normal form of a two dof Hamiltonian system is integrable. Adding a third dof with non-commensurable third frequency as is the case here keeps to high order these normal forms integrable as the added terms remain separated from the resonant two dof.

We conclude that for $0 < a < 1$ a periodic FPU α-chain with four alternating masses is in normal form near-integrable. The dynamics (periodic solutions and stability) of the two dof cases can be found in the literature (for references see [6]) but is in this case fairly degenerate. The case of values of a very close to zero have to be considered separately.

5.3.1 The α-Chain for Large Mass m

For large values of the mass we have a in a neighborhood of zero. Two of the frequencies will be near $\sqrt{2}$, one will be $\sqrt{2a}$, the associated modes will be called the optical group (x_1, x_2) and the acoustical group (x_3). System (5.8) is an example of a system with widely separated frequencies, see [7] and further references there. Following the analysis in [7] we apply normalization considering x_3 as slowly varying. The slow dynamics of x_3 becomes more transparent when rescaling the Hamiltonian to a related standard form by

$$x_3 \to (2a)^{-\frac{1}{4}} x_3, \; y_3 \to (2a)^{+\frac{1}{4}} y_3. \tag{5.9}$$

This results in:

$$H_2 = (1+a)x_1^2 + x_2^2 + \frac{1}{2}(y_1^2 + y_2^2) + \frac{1}{2}\sqrt{2a}(x_3^2 + y_3^2)$$

and

$$H_3 = -\bar{\gamma} x_1 x_2 x_3, \; \bar{\gamma} = 2^{\frac{5}{4}} \sqrt{1+a}\, a^{\frac{1}{4}}.$$

In the equations of motion we rescale $x_i \to a^{\frac{1}{8}} x_i$, $i = 1, 2$; this choice is optimal for keeping as many interactive terms in the approximations as possible. In [8] this is called a significant degeneration of the differential operator. System (5.8) becomes with the rescalings:

$$\begin{cases} \ddot{x}_1 + 2x_1 = \bar{\gamma} x_2 x_3 - 2a x_1, \\ \ddot{x}_2 + 2x_2 = \bar{\gamma} x_1 x_3, \\ \dot{x}_3 = \sqrt{2a}\, y_3,\ \dot{y}_3 = \bar{\gamma} a^{\frac{1}{4}} x_1 x_2 - \sqrt{2a} x_3. \end{cases} \tag{5.10}$$

The terms with small parameter $\bar{\gamma} = O(a^{\frac{1}{4}})$ dominate. Introducing polar coordinates

$$x_1 = r_1 \cos(\sqrt{2}t + \phi_1),\ \dot{x}_1 = -\sqrt{2} r_1 \sin(\sqrt{2}t + \phi_1),$$

$$x_2 = r_2 \cos(\sqrt{2}t + \phi_2),\ \dot{x}_2 = -\sqrt{2} r_2 \sin(\sqrt{2}t + \phi_2),$$

we find after transformation and normalization to $O(\bar{\gamma})$:

$$\begin{cases} \dot{r}_1 = -\frac{\bar{\gamma}}{2\sqrt{2}} r_2 \sin(\phi_1 - \phi_2) x_3,\ \dot{\phi}_1 = -\frac{\bar{\gamma}}{2\sqrt{2}} \frac{r_2}{r_1} \cos(\phi_1 - \phi_2) x_3, \\ \dot{r}_2 = +\frac{\bar{\gamma}}{2\sqrt{2}} r_1 \sin(\phi_1 - \phi_2) x_3,\ \dot{\phi}_2 = -\frac{\bar{\gamma}}{2\sqrt{2}} \frac{r_1}{r_2} \cos(\phi_1 - \phi_2) x_3, \\ \dot{x}_3 = 0,\ \dot{y}_3 = 0. \end{cases} \tag{5.11}$$

For the third mode we find with $y_3(0) = 0$:

$$x_3 = x_3(0),\ y_3 = 0.$$

We put $\chi = \phi_1 - \phi_2$. The solutions of the normal form have error $O(a^{\frac{1}{4}})$ on the timescale $a^{-\frac{1}{4}}$, see the appendix.

Integrals of the normalization. System (5.11) has the integral of motion $E_3 = \frac{1}{2}\sqrt{2a}(x_3^2 + y_3^2)$ and the second integral

$$\frac{1}{2}(r_1^2 + r_2^2) = E_1 \tag{5.12}$$

with E_1 a positive constant. This integral is valid with error $O(a^{\frac{1}{4}})$. The choice of polar coordinates means that we have to exclude normal modes, but we know already that the original system (5.8) has three normal mode solutions. We have

$$\frac{d}{dt}\chi = -\frac{\bar{\gamma}}{2\sqrt{2}} \left(\frac{r_2}{r_1} - \frac{r_1}{r_2} \right) x_3 \cos\chi.$$

From the equations for r_1 in system (5.11) and the equation for χ we find

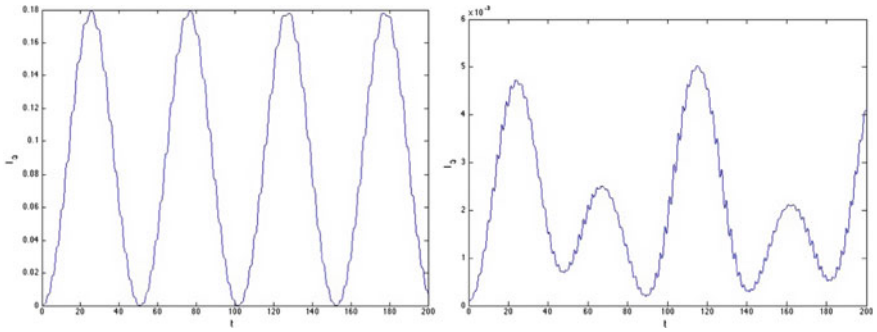

Fig. 5.1 Interactions with the x_3 mode for $a = 0.01$ in system (5.8). *Left* the action $I_3 = \frac{1}{2}(\dot{x}_3^2 + 2ax_3^2)$ with initial conditions $x_1(0) = x_2(0) = 0.5$, $x_3(0) = 0.1$ and initial velocities zero so $I_1(0) = I_2(0) = 0.25$, $I_3(0) = 10^{-4}$ resulting in $0 < I_3 < 0.18$. *Right* I_3 if $x_1(0) = 0.1$, $x_2(0) = 0.5$, $x_3(0) = 0.1$ so $I_1(0) = 0.01$, $I_2(0) = 0.25$, $I_3(0) = 10^{-4}$ resulting in (much smaller) $0 < I_3 < 0.005$

$$\frac{dr_1}{d\chi} = r_2 \frac{\sin\chi}{\left(\frac{r_2}{r_1} - \frac{r_1}{r_2}\right)\cos\chi}.$$

Eliminating r_2 with integral (5.12) the equation becomes separable. We find:

$$r_1 r_2 \cos\chi = C, \tag{5.13}$$

which is a third integral of motion of system (5.11); C is a constant determined by the initial conditions. We conclude that to first order of approximation we have no interaction between the first two modes (the optical part) and the third mode (the acoustical part). However, a numerical experiment suggests that the x_3 mode is interacting with the other modes, see Fig. 5.1, so to show this analytically we will compute a second order approximation later on.

Periodic solutions. At first order a special solution arises if

$$\chi = 0, \pi.$$

This is possible if

$$\frac{d}{dt}\chi = -\frac{\bar{\gamma}}{2\sqrt{2}}\left(\frac{r_2}{r_1} - \frac{r_1}{r_2}\right) x_3 \cos\chi = 0. \tag{5.14}$$

We conclude for this special solution $r_1 = r_2$ with solutions for x_1, x_2 given by:

$$x_1(t) = \sqrt{E_1}\cos(\sqrt{2}t + \phi_0),\ x_1(t) = \pm x_2(t), \tag{5.15}$$

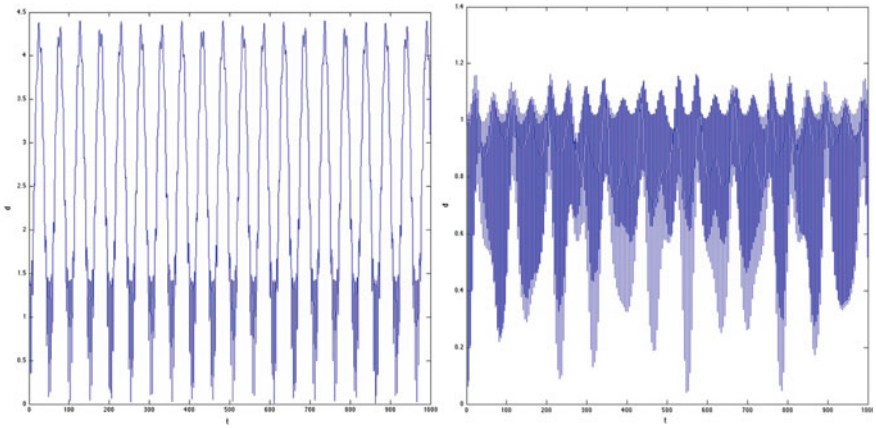

Fig. 5.2 Recurrence indicated by the Euclidean distance d with respect to the initial values as a function of time in the α-chain with the conditions as in Fig. 5.1. If $x_1(0) \neq x_2(0)$ (*right*) the recurrence takes longer

an approximation valid on the timescale $a^{-1/4}$. Choosing $x_3(0)$, $y_3(0)$, solutions (5.15) are determined uniquely. These solutions $(x_i, y_i, i = 1, 2, 3)$ form manifold M_1 embedded in the energy manifold defined by the quadratic integrals E_3 and E_1 of system (5.11).

Another special solution of (5.14) arises if

$$\chi = \frac{\pi}{2}, \, 3\frac{\pi}{2}.$$

In this case the solutions of system (5.11) are determined by:

$$\begin{cases} r_1(t) = A\cos(\frac{\tilde{\gamma}}{2\sqrt{2}}x_3(0)t) + B\sin(\frac{\tilde{\gamma}}{2\sqrt{2}}x_3(0)t), \\ r_2(t) = \mp A\frac{\tilde{\gamma}}{2\sqrt{2}}x_3(0)\sin(\frac{\tilde{\gamma}}{2\sqrt{2}}x_3(0)t) \pm B\frac{\tilde{\gamma}}{2\sqrt{2}}x_3(0)\cos(\frac{\tilde{\gamma}}{2\sqrt{2}}x_3(0)t), \end{cases} \tag{5.16}$$

with $x_3(t) = x_3(0)$, $\phi_1(0) - \phi_2(0) = \pi/2, 3\pi/2$ and constants A, B; analogously to the case of M_1, the solutions x_i, y_i, $i = 1, 2, 3$ form manifold M_2 embedded in the energy manifold.

Both for special solution (5.15) and (5.16) we have families of periodic solutions on the energy manifold. This may signal a degeneration of the normal form at first order in the sense of Poincaré [3] vol. 1. This gives another reason to compute a second order approximation.

Integrability and recurrence. The normal form (5.11) of the α-chain for large mass is clearly integrable. The three normal form integrals can be written as quadratic expressions:

$$\frac{1}{2}\sqrt{2a}(x_3^2+y_3^2)=E_3,\ \dot{x}_1^2+2x_1^2+\dot{x}_2^2+2x_2^2=2E_1,\ 2x_1x_2+\dot{x}_1\dot{x}_2=2C. \tag{5.17}$$

The three integrals are exact integrals of the normal form (5.11) and approximate integrals of the original equations (5.10). Remarkably enough the recurrence properties of the phase flow are different in the two cases of Fig. 5.1. In the case where $x_1(0)=x_2(0)=0.5$, we have rather strong recurrence, see Fig. 5.2 left, in the case $x_1(0)=0.1, x_2(0)=0.5$ the recurrence times are longer; see Fig. 5.2. The two special solutions obtained above suggest an explanation. Starting at the first special solution we have to first approximation periodicity with period $\sqrt{2}\pi$, for the second special solution we find a modulation of the period $O(\bar{\gamma}x_3(0))$.
We conclude that even if we have a system with integrable normal form, its recurrence properties depend strongly on the initial conditions. We will return to this in Sect. 5.6.

5.3.2 *Second Order Approximation for the α-Chain*

A second order approximation according to [6] can be computed using MATHEMATICA. As before we do not change the notation for the variables r_1, ϕ_1 etc. to avoid too many new symbols. We find with $\bar{\gamma}=O(a^{\frac{1}{4}})$ (and a mix of variables):

$$\begin{cases}\dot{r}_1=-\frac{\bar{\gamma}}{2\sqrt{2}}r_2x_3\sin\chi,\ \dot{\phi}_1=-\frac{\bar{\gamma}}{2\sqrt{2}}\frac{r_2}{r_1}x_3\cos\chi-\frac{1}{4}a^{\frac{1}{2}}x_3^2,\\ \dot{r}_2=+\frac{\bar{\gamma}}{2\sqrt{2}}r_1x_3\sin\chi,\ \dot{\phi}_2=-\frac{\bar{\gamma}}{2\sqrt{2}}\frac{r_1}{r_2}x_3\cos\chi-\frac{1}{4}a^{\frac{1}{2}}x_3^2,\\ \dot{x}_3=(2a)^{\frac{1}{2}}y_3,\ \dot{y}_3=-(2a)^{\frac{1}{2}}x_3+(2)^{\frac{1}{4}}(a)^{\frac{1}{2}}r_1r_2\cos\chi.\end{cases} \tag{5.18}$$

We deduce from system (5.18) that the quadratic integral (5.12) persists; $d\chi/dt$ does not change at second order, so also the quadratic integral (5.13) persists. The two special solutions (5.15) and (5.16) are slightly modified but correspond at second order still with manifolds of special solutions. For x_3, y_3 we can write

$$\ddot{x}_3+2ax_3=2ar_1r_2\cos\chi.$$

Using integral (5.13) we have with $y_3(0)=0$ as second order approximation:

$$x_3(t)=(x_3(0)-C)\cos(\sqrt{2a}\,t)+C \tag{5.19}$$

with $C=r_1(0)r_2(0)\cos\chi(0)$. This establishes the interaction with the x_3 normal mode as for initial values of x_1, x_2 producing an $O(1)$ value of C, the amplitude of x_3 will grow even if $x_3(0)$ is small.
From system (5.8), so before rescaling, we can find the equivalent integral equation for $x_3(t)$ which also holds for the rescaled quantities:

$$x_3(t) = x_3(0)\cos\sqrt{2a}t + 2\sqrt{1+a}\int_0^t x_1(\tau)x_2(\tau)\sin(\sqrt{2a}(t-\tau))d\tau, \quad (5.20)$$

where we have chosen $\dot{x}_3(0) = 0$. The oscillating integral can be evaluated using approximations for $x_1(t)$, $x_2(t)$ for instance the special solutions (5.15) (interaction timescales t and $a^{1/2}t$) and (5.16) (interaction timescales t, $a^{1/4}t$ and $a^{1/2}t$).
Note that inspection of system (5.10) shows that neglecting terms $O(a)$, we have $x_1(t) = \pm x_2(t)$ exactly. This means that in this particular case $x_1(t)x_2(t)$ will be sign definite in the integral of (5.20) at this level of approximation.

5.4 The β-Chain for Large Mass m

The Hamiltonian given by (5.7) is positive definite outside the origin, so the origin is the only equilibrium. The energy manifolds are compact. The remarks on the possible resonances of the α-chain apply also to the β-chain. So we restrict ourselves to the case of large mass m. The equations of motion are more complicated and are without scaling of the coordinates:

$$\begin{cases} \ddot{x}_1 + 2(1+a)x_1 &= -(1+a)^2x_1^3 - 3(1+a)x_1(x_2^2 + ax_3^2), \\ \ddot{x}_2 + 2x_2 &= -x_2^3 - 3ax_2x_3^2 - 3(1+a)x_1^2x_2, \\ \ddot{x}_3 + 2ax_3 &= -3ax_2^2x_3 - a^2x_3^3 - 3a(1+a)x_1^2x_3. \end{cases} \quad (5.21)$$

The three normal modes are exact solutions (elliptic functions) of the system. To apply normalization we will assume that a is small and will rescale with respect to equilibrium:

$$(x_i, y_i) \to a^{\frac{1}{4}}(x_i, y_i) i = 1, 2, x_3 \to (2a)^{-\frac{1}{4}}x_3,\ y_3 \to (2a)^{+\frac{1}{4}}y_3.$$

This scaling keeps as many interaction terms as possible. We find after scaling:

$$\begin{cases} \ddot{x}_1 + 2x_1 &= -2ax_1 - \sqrt{a}(1+a)^2x_1^3 - 3\sqrt{a}(1+a)x_1(x_2^2 + \frac{1}{2}\sqrt{2}x_3^2)), \\ \ddot{x}_2 + 2x_2 &= -\sqrt{a}x_2^3 - \frac{3}{2}\sqrt{2a}x_2x_3^2 - 3\sqrt{a}(1+a)x_1^2x_2, \\ \dot{x}_3 &= \sqrt{2a}y_3,\ \dot{y}_3 = -\sqrt{2a}x_3 - a(\frac{3}{2}\sqrt{2}x_2^2x_3 + \frac{1}{2}x_3^3 + \frac{3}{2}\sqrt{2}(1+a)x_1^2x_3). \end{cases} \quad (5.22)$$

Neglecting terms $O(a)$ we find with $\chi = \phi_1 - \phi_2$ the normal form:

$$\begin{cases} \dot{r}_1 = +\frac{3\sqrt{a}}{8\sqrt{2}}r_1r_2^2\sin 2\chi,\ \dot{\phi}_1 = \frac{\sqrt{a}}{16}\left(3\sqrt{2}(r_2^2\cos 2\chi + 2r_2^2 + r_1^2) + 12x_3^2\right), \\ \dot{r}_2 = -\frac{3\sqrt{a}}{8\sqrt{2}}r_1^2r_2\sin 2\chi,\ \dot{\phi}_2 = \frac{\sqrt{a}}{16}\left(3\sqrt{2}(r_1^2\cos 2\chi + 2r_1^2 + r_2^2) + 12x_3^2\right), \\ \dot{x}_3 = \sqrt{2a}y_3,\ \dot{y}_3 = -\sqrt{2a}x_3. \end{cases} \quad (5.23)$$

We find again the integral $E_3 = \frac{1}{2}\sqrt{2a}(x_3^2 + y_3^2)$ and the second normal form integral (5.12). The equation for χ becomes

$$\frac{d}{dt}\chi = -\frac{3\sqrt{2}}{8}\sqrt{a}(r_1^2 - r_2^2)\cos^2\chi.$$

From system (5.23) we find also the third integral (5.13):

$$r_1 r_2 \cos\chi = C,$$

with C determined by the initial conditions.
A special solution with constant amplitudes r_1 and r_2 may arise if

$$\chi = \varphi_1 - \phi_2 = 0, \pi/2, \pi, 3\pi/2.$$

From the equation for $\chi = \phi_1 - \phi_2$ we find the requirement $r_1 = r_2$ corresponding with four periodic solutions of the first order normal form. The initial values $x_3(0)$, $y_3(0)$ are still free, the solutions x_i, y_i, $i = 1, 2, 3$ produce manifold M_1 embedded in the energy manifold.
Analogous to the case of the α-chain we find solutions from the equation for $d\chi/dt$ with constant phase difference. These are found if

$$r_1 \neq r_2,\ \chi = \frac{\pi}{2},\ 3\frac{\pi}{2}.$$

For $r_1(t), r_2(t)$ we find in this case goniometric functions of $\sqrt{a}t$ and, as for the α-chain, a manifold M_2 of special solutions x_i, y_i, $i = 1, 2, 3$ embedded in the energy manifold.

At this level of approximation we find no interaction between the optical and the acoustical group. This motivates us to compute the second order normal form.

5.4.1 *Second Order Approximation for the β-Chain*

A second order approximation according to [6] can be computed using again MATHEMATICA. We do not change the notation for the variables r_1, ϕ_1 etc. to avoid too many new symbols. We find for the $O(a)$-terms to be added to the derivatives $\dot{r}_1, \dot{\phi}_1, \dot{r}_2, \dot{\phi}_2, \dot{x}_3, \dot{y}_3$ in the normal form of system (5.23):

$$\begin{cases} -\frac{3}{512}r_1r_2^2\sin(2\chi)\left(17\sqrt{2}\left(r_1^2+r_2^2\right)+48x_3^2\right) \\ \frac{-288x_3^2\left(r_2^2(\cos(2\chi)+2)+r_1^2\right)-51\sqrt{2}\left(2r_2^2r_1^2(2\cos(2\chi)+3)+r_2^4(2\cos(2\chi)+3)+r_1^4\right)-144\sqrt{2}x_3^4}{1024}+\frac{1}{\sqrt{2}} \\ \frac{3}{512}r_1^2r_2\sin(2\chi)\left(17\sqrt{2}\left(r_1^2+r_2^2\right)+48x_3^2\right) \\ \frac{-288\ x_3^2\left(r_1^2(\cos(2\chi)+2)+r_2^2\right)-51\sqrt{2}\left(r_1^4(2\cos(2\chi)+3)+2r_2^2r_1^2(2\cos(2\chi)+3)+r_2^4\right)-144\sqrt{2}x_3^4}{1024} \\ 0 \\ -\frac{1}{4}x_3\left(3\sqrt{2}\left(r_1^2+r_2^2\right)+2x_3^2\right) \end{cases} \tag{5.24}$$

Integral (5.12) is conserved again to second order. The condition for constant amplitudes r_1 and r_2 is again

$$\chi = \varphi_1 - \phi_2 = 0, \pi/2, \pi, 3\pi/2.$$

The requirement $d\chi/dt = 0$ is satisfied for $r_1 = r_2 + O(\sqrt{a})$, producing four periodic solutions.
For the third mode we find with integral (5.12) the equation:

$$\ddot{x}_3 + (2a + 3a^{\frac{3}{2}}E_1)x_3 = -\frac{1}{2}\sqrt{2}a^{\frac{3}{2}}x_3^3. \tag{5.25}$$

The only critical point (equilibrium) is $(0, 0)$ which is stable. This means that starting near the origin, the solution will not move away. The results show for the β-chain weak interaction between acoustical and optical group and dependence on the initial conditions. In general the solutions for the β-chain depend on the timescales $t, \sqrt{a}t, at$.

5.5 Stability of the Periodic Solutions for Large Mass *m*

The first and second order normal form analysis enables us to establish the stability of the periodic solutions. Note however that for three and more dof instability in Hamiltonian systems from a perturbation (normal form) analysis is conclusive, stability is not. Purely imaginary eigenvalues guarantee 'stability on a certain timescale'.

- The x_1 and x_2 normal modes.
  If either $x_1(0)$ or $x_2(0)$ is small, we conclude with integral (5.13) that C is small. For the α- and the β-chain this implies with (5.19) and (5.25) that if $x_3(0)$ is small, $x_3(t)$ remains small.
  Consider now a neighborhood of the x_1 normal mode for the α-chain.
  Choose $x_3(0) > 0, \chi(0) = 0$ and $\varepsilon > 0$ such that if $r_2(0) = \varepsilon$ we have $C = x_3(0)/2$. From integral (5.13) we have that $\cos\chi(t)$ can not vanish so that $\chi(t)$ has to oscillate between $-\pi/2$ and $+\pi/2$. As $x_3(t)$ may only change sign on

the timescale $1/\sqrt{a}$, we have that $d\chi/dt$ is sign definite unless $r_2(t)$ grows. We conclude to instability of the x_1 normal mode.
The same reasoning applies to the x_2 normal mode of the α-chain.
For the β-chain the reasoning is similar but simpler as the equation for χ does not depend on x_3. With $\chi(0) = 0$ we have that $\chi(t)$ has to oscillate between $-\pi/2$ and $+\pi/2$. The second order normal form for $d\chi/dt$ can only change sign if $r_1^2 - r_2^2 + O(\sqrt{a})$ changes sign. Both normal modes are unstable for the β-chain.

- The x_3 normal mode.
If both x_1 and x_2 are small we conclude with integral (5.12) that these modes remain small. The normal mode x_3 is stable both for the α- and the β-chain.

- The solution manifold M_1 for $r_1 = r_2$, $\chi = 0, \pi$.
We will use the first order approximations as using the second order does not change the results qualitatively. We can consider the stability behavior with respect to the x_1, x_2 modes and the x_3 mode in the first order approximations separately.
The α-chain. Regarding the behaviour with respect to the x_1, x_2 modes we eliminate r_2 with integral (5.12) after which we linearize the normal form equations of motion (5.11) and (5.23) in a neighborhood of $r_1 = r_2$, $\chi = 0, \pi$. For the α-chain we have the system:

$$\dot{r}_1 = -\frac{\bar{\gamma}}{2\sqrt{2}} x_3 \sqrt{2E_1 - r_1^2} \sin\chi, \ \dot{\chi} = \frac{\bar{\gamma}}{2\sqrt{2}} x_3 \left(\frac{\sqrt{2E_1 - r_1^2}}{r_1} - \frac{r_1}{\sqrt{2E_1 - r_1^2}} \right) \cos\chi. \tag{5.26}$$

The Jacobian matrix yields if $r_1 = r_2 = \sqrt{E_1}$, $\chi = 0, \pi$ the eigenvalue equation:

$$\lambda^2 - 4\frac{\bar{\gamma}^2}{2} x_3^2 = 0.$$

This produces eigenvalues with opposite signs, we have instability.
From integral (5.12) we find $C = \pm E_1$. The approximation for x_3 of the α-chain (5.19) shows that also x_3 will grow in size.
The β-chain. Repeating the analysis for the β-chain we find for the x_1, x_2 modes the corresponding equations:

$$\dot{r}_1 = +\frac{3\sqrt{a}}{8\sqrt{2}} r_1 (2E_1 - r_1^2) \sin 2\chi, \ \dot{\chi} = -\frac{3\sqrt{2}}{4} \sqrt{a} (r_1^2 - E_1) \cos^2\chi.$$

The Jacobian matrix yields if $r_1 = r_2 = \sqrt{E_1}$, $\chi = 0, \pi$ the eigenvalue equation:

$$\lambda^2 + \frac{9}{8} a E_1^2 = 0$$

and purely imaginary eigenvalues; the second order does not change this.
The second order approximation of x_3 for the β-chain described by (5.25) does not grow in size; we have stability of M_1 for the β-chain.

- The solution manifold M_2 for $\chi = \pi/2, 3\pi/2$.
  In this case there is no restriction on r_1, r_2. We can expand the normal form equation for χ near $\chi = \pi/2, 3\pi/2$. We find from the equations obtained above for $d\chi/dt$ that if $r_1 \neq r_2$, χ will change. The case $r_1 = r_2$ produces eigenvalues zero and is left as a degenerate case. Both for the α-chain and the β-chain we find instability if $r_1 \neq r_2$.

5.6 The Global Picture for Large Mass

We consider compact energy manifolds for the α-chain (energy between 0 and 0.5) and the β-chain not too far from the origin of phase-space. The energy manifolds and of course the manifold corresponding with $H_2 = E_0$ (constant), are topologically the sphere S^5. Both for the α- and the β-chain, we have that the x_1 and x_2 modes for fixed E_1 are restricted to the ellipsoid M_{12} which is S^3 described by integral (5.12) and is embedded in the energy manifold with in general $0 < E_1 < E_0$.

A transversal of the flow on S^5 will be 4-dimensional. Consider the transversal D determined by $y_3 = 0$ with x_3 eliminated using the integral $H_2 = E_0$. The coordinate plane x_1, y_1 is located in D containing as boundary the x_1 normal mode which is S^1. Perpendicular to this plane is the coordinate plane x_2, y_2 in D with as a boundary the normal mode x_2; the boundary does not belong to the transversal. As for the x_2 normal mode we have $x_1 = y_1 = 0$, the x_2 normal mode will go through this point in the centre of the x_1, y_1 coordinate plane. This means that the x_1 and x_2 normal modes are linked. We can repeat this reasoning for a transversal containing the x_3 normal mode. We conclude that the three normal modes are linked on S^5. The stable normal modes are surrounded by invariant tori embedded in the energy manifold.

The x_3 mode plays a special part. The dynamics on M_{12} is still determined by the third mode through the phases (or angles in action-angle representation). The integral (5.13) restricts the dynamics on manifold M_{12}. The solutions around the x_3 normal mode move on tori on the 5-dimensional energy manifold that extend to the normal modes x_1 and x_2 and of which the size depends on the initial conditions of all variables.

The special solution (5.15) produces a torus M_1 on the energy manifold with $r_1 = r_2$ and shrinking diameter as $x_3(t)$ becomes more prominent. For the α-chain, the torus is unstable, for the β-chain we have stability if $x_3(0)$ is small enough.

The special solution (5.16) of the normal form produces a torus M_2 for which in general $r_1 \neq r_2$. It is unstable and may not persist under higher order perturbations. For the α-chain the instability poses a problem when connecting the stable normal mode x_3 with the unstable tori. Note however that the instability of M_1 arises only if C of integral (5.13) is not small which it is near the x_3 normal mode. As a further illustration consider the linearization of the normal form (5.26). If $r_1, r_2 = O(a^{\frac{1}{4}})$ and $r_1 \neq r_2$ we have near the x_3 normal mode that $\dot{r}_1 = O(\sqrt{a})$, $\dot{\chi} = O(a^{\frac{1}{4}})$ which is an obstruction to the validity of linearization.
For an illustration of the stability results by an amplitude-simplex see Fig. 5.3.

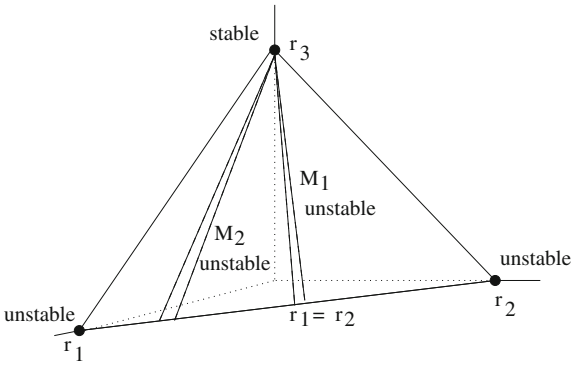

Fig. 5.3 The amplitude-symplex for the α-chain that is a projection omitting the phases (or angles). The front triangle corresponds with $H_2 =$ constant. The *dots* at the vertices indicate normal mode periodic solutions. The manifolds M_1 ($r_1 = r_2$) corresponds with tori that are unstable in the case of the α-chain, stable for the β-chain. M_2 is unstable if $r_1 \neq r_2$ with $r_1 = r_2$ undecided

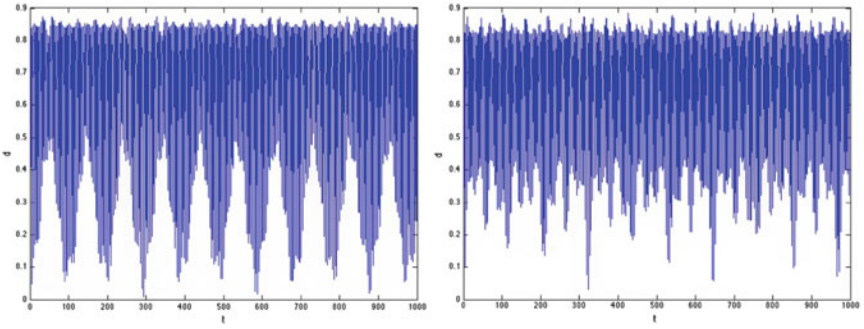

Fig. 5.4 Recurrence for 1000 timesteps indicated by the Euclidean distance d with respect to the initial values as a function of time in the α-chain with $a = 0.04$, energy 0.1762. *Left* the conditions $x_1(0) = 0.05, x_2(0) = 0.4168, x_3(0) = 0.01$ near the x_2 normal mode; we have recurrence with $0 \leq d \leq 0.9$. *Right* the case where $x_3(0)$ is also small but more removed from the normal modes with $x_1(0) = 0.4, x_2(0) = 0.1, x_3(0) = 0.01$; the instability weakens the recurrence ($0 \leq d \leq 0.9$)

Consequences for recurrence

Recurrence of the flow as guaranteed by the Poincaré recurrence theorem, provides us with additional information about the dynamics in phase-space. We will consider some aspects for the α-chain as this chain has most instability. In Fig. 5.4 we start near the stable x_2 normal mode which results in relatively strong recurrent motion, as expected. The result is rather different when starting away from the normal modes with $x_1(0) \neq x_2(0)$; the recurrence is weakened by the instability of M_2 although the normal form is integrable.

In Fig. 5.5 we start near manifold M_1 to observe good short-time recurrence. Right we move to more general position on the energy manifold with $x_1(0) \neq x_2(0)$; this produces rather bad recurrence.

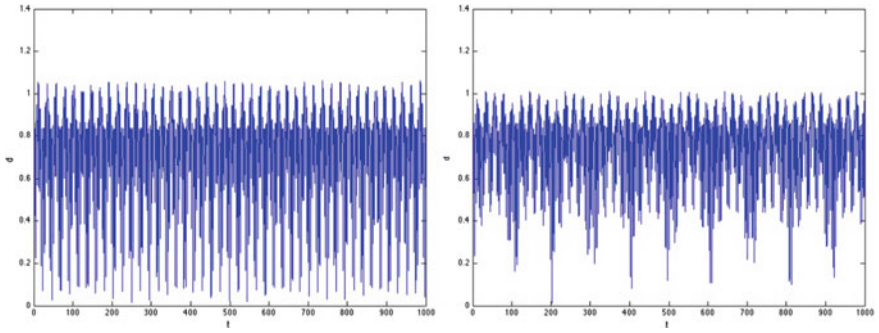

Fig. 5.5 Recurrence for 1000 timesteps indicated by the Euclidean distance d with respect to the initial values as a function of time in the α-chain with $a = 0.04$, energy 0.1762. *Left* the conditions $x_1(0) = 0.2943$, $x_2(0) = 0.2943$, $x_3(0) = 0.01$; starting near M_1 we have fairly good recurrence with $0 \leq d \leq 1.1$. *Right* the case where $x_1(0) = 0.37$, $x_2(0) = 0.2167$ and $x_3(0) = 0.5$, away from the normal modes; the motion along the tori weakens the recurrence ($0 \leq d \leq 1.1$). Extending the picture to 5000 time steps does not improve the recurrence

5.7 Conclusions and Discussion

1. The periodic FPU-problem with 4 particles and alternating masses can be reduced to a three dof Hamiltonian problem. The normal modes are exact periodic solutions of the reduced system both for the α- and the β-chain.
2. Normal form calculations lead to an integrable system with three normal form integrals and additional periodic solutions.
3. A second order normal form calculation is necessary to characterize the phase-flow. This involves three timescales with the conclusion that we have weak interaction between the acoustical and the optical part of the system.
4. The integrability of the normal form, corresponding with approximate integrability of the original system, keeps the system recurrent with fairly short intervals of time.
5. We will show in a subsequent paper the important fact that the dynamics of the four particles problem is in a certain sense typical for periodic FPU problems with alternating masses and many more particles.

Appendix

In the error estimates of the normal form analysis integral inequalities can be useful. We will use the *specific Gronwall lemma* formulated in [6], lemma 1.3.3.

Lemma 5.1 *Let ϕ be a real-valued continuous (or piecewise continuous) functions on a real t interval $I : t_0 \leq t \leq T$. Assume $\phi(t) > 0$ on I and $\delta_1(\varepsilon)$, $\delta_2(\varepsilon)$ positive order functions (ε a small, positive parameter). If the inequality*

$$\phi(t) \leq \delta_2(\varepsilon)(t - t_0) + \delta_1(\varepsilon) \int_{t_0}^{t} \phi(s)ds,$$

holds on I, then

$$\phi(t) \leq \frac{\delta_2(\varepsilon)}{\delta_1(\varepsilon)} e^{\delta_1(\varepsilon)(t-t_0)}.$$

We apply the *specific Gronwall lemma* to obtain:

Lemma 5.2 *Consider the perturbation problem:*

$$\dot{x} = \delta_1(\varepsilon) f(t, x) + \delta_2(\varepsilon) R(t, x), x(t_0) = x_0,$$

for $I : t_0 \leq t \leq T, x \in D \subset \mathbb{R}^n$, $\delta_1, \delta_2, \delta_3(\varepsilon)$ order functions with $\delta_2(\varepsilon) = o(\delta_1(\varepsilon))$ as $\varepsilon \to 0$ and continuous differentiability of the vector fields f, R on $I \times D$; in particular we have $||R(t, x)|| \leq M$, $M > 0$ for $t \geq 0$. We neglect small terms to consider the solution of

$$\dot{y} = \delta_1(\varepsilon) f(t, y), y(t_0) = x_0$$

and we approximate $y(t)$ by a procedure (averaging) for which we know that $||y(t) - \bar{y}(t)|| = O(\delta_3(\varepsilon))$ on the timescale $1/\delta_1(\varepsilon)$. Then we have on the timescale $1/\delta_1(\varepsilon)$ the estimate

$$x(t) - y(t) = O(\frac{\delta_2(\varepsilon)}{\delta_1(\varepsilon)} + \delta_3(\varepsilon)) \text{ on the timescale } 1/\delta_1(\varepsilon).$$

Proof We formulate the equivalent integral equations for $x(t)$, $y(t)$:

$$x(t) = x_0 + \delta_1(\varepsilon) \int_{t_0}^{t} f(x(s), s)ds + \delta_2(\varepsilon) \int_{t_0}^{t} R(x(s), s)ds,\ y(t) = x_0 + \delta_1(\varepsilon) \int_{t_0}^{t} f(y(s), s)ds.$$

Subtracting the two equations we have:

$$x(t) - y(t) = \delta_1(\varepsilon) \int_0^t (f(x(s), s) - f(y(s), s))ds + \delta_2(\varepsilon) \int_0^t R(x(s), s)ds.$$

Using the Lipschitz continuity of f (Lipschitz constant L) and the estimate for R we have:

$$||x(t) - y(t)|| \leq \delta_1(\varepsilon) L \int_{t_0}^{t} ||x(s) - y(s)||ds + \delta_2(\varepsilon) M t,$$

and with Lemma 5.1:

$$||x(t) - y(t)|| \leq \delta_1(\varepsilon) \frac{M}{L} e^{\delta_1(\varepsilon) L t} - \frac{\delta_2(\varepsilon)}{\delta_1(\varepsilon)} \frac{M}{L}.$$

We conclude that $y(t)$ approximates $x(t)$ with error $O(\frac{\delta_2(\varepsilon)}{\delta_1(\varepsilon)})$ on the timescale $1/\delta_1(\varepsilon)$. We conclude with the triangle inequality that

$$||x(t) - \bar{y}(t)|| = ||x(t) - y(t) + y(t) - \bar{y}(t)|| \leq ||x(t) - y(t)|| + ||y(t) - \bar{y}(t)||,$$

or

$$||x(t) - \bar{y}(t)|| \leq O\left(\frac{\delta_2(\varepsilon)}{\delta_1(\varepsilon)}\right) + O(\delta_3(\varepsilon))$$

on the timescale $1/\delta_1(\varepsilon)$.

References

1. Bruggeman, R., Verhulst, F.: The inhomogenous Fermi-Pasta-Ulam chain, submitted (2015). arXiv:1510.00560 [math.DS]
2. Galgani, L., Giorgilli, A., Martinoli, A., Vanzini, S.: On the problem of energy partition for large systems of the Fermi-Pasta-Ulam type: analytical and numerical estimates. Phys. D **59**, 334–348 (1992)
3. Poincaré, Henri: Les Méthodes Nouvelles de la Mécanique Célèste, 3 vols. Gauthier-Villars, Paris **1892**, 1893 (1899)
4. Rink, B., Verhulst, F.: Near-integrability of periodic FPU-chains. Phys. A **285**, 467–482 (2000)
5. Rink, B.: Symmetry and resonance in periodic FPU-chains. Comm. Math. Phys. **218**, 665–685 (2001)
6. Sanders, J.A., Verhulst, F., Murdock, J.: Averaging methods in nonlinear dynamical systems. Appl. Math. Sci. vol. 59, 2nd ed., Springer (2007)
7. Tuwankotta, J.M., Verhulst, F.: Hamiltonian systems with widely separated frequencies. Nonlinearity **16**, 689–706 (2003)
8. Verhulst, F.: Methods and Applications of Singular Perturbations. Springer, Berlin (2005)
9. Verhulst, F.: A chain of FPU cells. In: Awrejcewicz, J., Kazmierczak, M., Mrozowski, J., Oleinik, P. (eds.) In: Proceedings of the 13th International Conference Dynamical Systems—Theory and Applications, vol. Control and Stability, pp. 603–612, Lodz, December 7–10 (2015). Extended version. Regular and chaotic recurrence in FPU cell-chains publ. in Appl. Math. Modelling (2016)
10. Verhulst, F.: Near-integrability and recurrence in FPU cells. Int. J. Bif. Chaos, accepted for publ. (2017)

Chapter 6
Linear Versus Nonlinear Stability in Hamiltonian Systems

Ferdinand Verhulst

Abstract The stability of periodic solutions of time-independent Hamiltonian systems is often studied by linearization techniques. In the case of two degrees of freedom near stable equilibrium this is a correct procedure, in the case of three or more degrees of freedom we present some counterexamples. The case of the classical Fermi-Pasta-Ulam chain with cubic and quartic interactions illustrates the instability phenomenon.

6.1 Introduction

It is well-known that linearizing procedures in dissipative systems produce no conclusive evidence regarding stability if the eigenvalues are purely imaginary. An example is given in [6] ex. 3.2 where a second order autonomous equation with a centre equilibrium point is perturbed by nonlinear terms. For various choices of the nonlinear terms we may obtain asymptotic stability or instability of the equilibrium.

For Hamiltonian systems the stability question is more complicated. Suppose we have a time-independent Hamiltonian $H(p,q)$ with $p,q \in \mathbb{R}^n$ so that we have n degrees of freedom and a $2n$ dimensional system of differential equations. Suppose that the system has a nontrivial periodic solution $\phi(t)$ (in fact there will be many in general). We want to establish its stability by small perturbations in a neighborhood of $\phi(t)$. The usual practice is to linearize the perturbed system and consider the characteristic exponents.

From now on we will also assume that we consider the system near stable equilibrium so that we have a family of compact energy manifolds. This will enable us to apply known theorems and, if necessary, normalization techiques. If we have one or more positive Lyapunov exponents, the periodic solution will be unstable. To have only negative parts in the Hamiltonian case is impossible because of the symmetry of the spectrum in Hamiltonian systems.

F. Verhulst (✉)
Mathematisch Instituut, 3508TA, PO Box 80.010 Utrecht, Netherlands
e-mail: f.verhulst@uu.nl

M. Belhaq (ed.), *Recent Trends in Applied Nonlinear Mechanics and Physics*,
Springer Proceedings in Physics 199, https://doi.org/10.1007/978-3-319-63937-6_6

A periodic solution corresponds with a fixed point of a suitable Poincaré map of the phase-flow. Suppose now that the spectrum of the linearized flow near this fixed point has purely imaginary parts only. In many papers it is assumed then that the periodic solution is stable. We will argue that this is correct in the case of two degrees of freedom but not necessarily if $n \geq 3$. There can be various causes for instability, for instance higher order resonance or diffusion processes in phase-space. Our analysis may also have consequences for conservative, nonlinear wave equations where Galerkin projection leads to finite-dimensional but large Hamiltonian systems.

6.2 Two Degrees of Freedom

The system of equations of motion is four-dimensional, the energy manifolds near stable equilibrium are three-dimensional and compact. Apart from degenerate cases one can quite generally apply the KAM theorem that guarantees a foliation of tori of the energy manifolds around stable periodic solutions, see for instance [1] or [2] and further references there. The Weinstein theorem [7] guarantees the existence of at least two periodic solutions on an energy manifold near stable equilibrium. One can construct a transversal to the flow on the energy manifold that results in an area-preserving map, a Poincaré map, of the transversal into itself. We can choose the map so that the periodic solution produces a fixed point of the map. Because of the area-preserving character of the map, the eigenvalues associated with the fixed point will generically be real (positive and negative) or purely imaginary. The KAM tori around the stable periodic solutions are two-dimensional, the tori separate the three-dimensional energy manifold; the solutions between the tori can not escape. This means that purely imaginary eigenvalues imply stability of the solution in the nonlinear system.

6.3 Counter-Examples for More Degrees of Freedom

In the case of three or more degrees of freedom we can also apply the KAM theorem quite generally. However, the energy manifolds are $2n-1$ dimensional, the tori at most n-dimensional. The tori do not separate the energy manifolds for $n \geq 3$. We will discuss examples showing various causes of instability but with common feature resonance.

6.3.1 The Influence of Quartic Terms

This example shows that higher order Hamiltonian perturbations may introduce instability. Indicating the quadratic, cubic and quartic parts of the Hamiltonian by

H_2, H_3, H_4 respectively we have:

$$H_2 = \frac{1}{2}(\dot{x}_1^2 + x_1^2 + \dot{x}_2^2 + 2x_2^2 + \dot{x}_3^2 + x_3^2),\ H_3 = -x_1x_2x_3,\ H_4 = -(\frac{1}{4}x_1^4 + x_1^2x_3^2 + \frac{1}{4}x_3^4).$$

The equations of motion can be written as:

$$\begin{cases} \ddot{x}_1 + x_1 &= x_2x_3 + x_1^3 + 2x_1x_3^2, \\ \ddot{x}_2 + 2x_2 &= x_1x_3, \\ \ddot{x}_3 + x_3 &= x_1x_2 + 2x_1^2x_3 + x_3^3. \end{cases} \tag{6.1}$$

The origin of phase-space corresponds with stable equilibrium. Localizing in a neighborhood of this equilibrium we can rescale $\dot{x}_i, x_i \to \varepsilon\dot{x}_i, \varepsilon x_i,\ i = 1, \ldots, 3$ resulting in:

$$\begin{cases} \ddot{x}_1 + x_1 &= \varepsilon x_2x_3 + \varepsilon^2(x_1^3 + 2x_1x_3^2), \\ \ddot{x}_2 + 2x_2 &= \varepsilon x_1x_3, \\ \ddot{x}_3 + x_3 &= \varepsilon x_1x_2 + \varepsilon^2(2x_1^2x_3 + x_3^3). \end{cases} \tag{6.2}$$

The system induced by Hamiltonian $H_2 + \varepsilon H_3 + \varepsilon^2 H_4$ admits the three normal modes in the coordinate planes. Consider the x_1 normal mode to $O(\varepsilon)$, the solution is harmonic:

$$x_1(t) = \phi(t) = r_0\cos(t + \theta_0).$$

Puttting $x_1 = y + \phi(t)$ and linearizing near the normal mode in system (6.2) to $O(\varepsilon)$ we obtain:

$$\begin{cases} \ddot{y} + y &= 0, \\ \ddot{x}_2 + 2x_2 &= \varepsilon\phi(t)x_3, \\ \ddot{x}_3 + x_3 &= \varepsilon\phi(t)x_2. \end{cases} \tag{6.3}$$

We have kept the notation x_2, x_3 to avoid too many new symbols. The righthand sides of the last two equations contain non-resonant quasi-periodic terms that keep the inhomogeneous solutions $O(|x_3|)$, $O(|x_2|)$ respectively. Put in a different way, normalizing the equations for x_2, x_3 involves non-resonant terms to any order. We conclude to linear stability of the x_1 normal mode. The higher order terms $O(\varepsilon^2)$ destroy this picture as was shown in [5] that the system induced by $H_2 + H_4$ contains two unstable normal modes; for an illustration see Fig. 6.1.

We can also linearize around the normal mode including the cubic terms of the equations. The x_1 normal mode satisfies to $O(\varepsilon^2)$ the equation

$$\ddot{x}_1 + x_1 = \varepsilon^2 x_1^3.$$

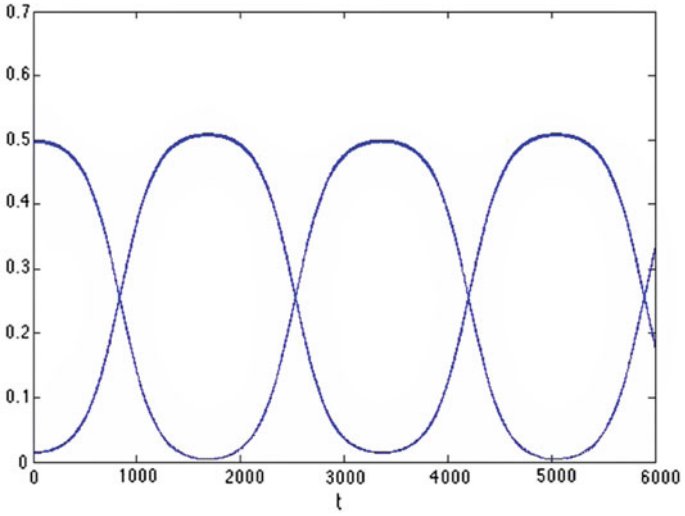

Fig. 6.1 The actions of system (6.2) with $x_1(0) = 1, x_2(0) = x_3(0) = 0.1$, velocities zero; $\varepsilon = 0.1$ and 6000 time-steps. The action $I_1 = \frac{1}{2}(\dot{x}_1^2 + x_1^2)$ associated with the x_1 normal mode starts in 0.5 and shows recurrence on around 3400 time-steps. The sum of the actions $I_2 + I_3$ associated with the x_2, x_3 modes starts near zero and shows similar recurrence

The solutions are elliptic functions that are more complicated to handle. However, for ε small we can determine the solution by the Poincaré-Lindstedt (or Poincaré continuation) method; see [6] ch. 10. The solution can be written as

$$\phi(t) = r_0(\varepsilon^2)\cos(t + \varepsilon^2\eta(\varepsilon^2)t + \phi_0)$$

where $r_0(\varepsilon^2)$, $\eta(\varepsilon^2)$ have convergent Taylor expansions with respect to their argument. In this way we find linear stability but again instability in the full, nonlinear system.

6.3.2 Instability by the Presence of Mathieu-Tongues

Consider the Hamiltonian with

$$H_2 = \frac{1}{2}(\dot{x}_1^2 + 4x_1^2 + \dot{x}_2^2 + 4x_2^2 + \dot{x}_3^2 + \omega^2 x_3^2),\ H_3 = -(x_1 + x_2)x_3^2.$$

Applying the same scaling with small, positive parameter ε as before we have:

$$\begin{cases} \ddot{x}_1 + 4x_1 & = \varepsilon x_3^2, \\ \ddot{x}_2 + 4x_2 & = \varepsilon x_3^2, \\ \ddot{x}_3 + \omega^2 x_3 & = \varepsilon 2(x_1 + x_2)x_3. \end{cases} \tag{6.4}$$

The x_1 normal mode is harmonic, we put for this solution

$$x_1(t) = \phi(t) = r_0 \cos(2t + \theta_0).$$

We assume now that ω^2 is close but not equal to 1. Puttting $x_1 = y + \phi(t)$ and linearizing near the normal mode in system (6.4) we find:

$$\begin{cases} \ddot{y} + 4y & = 0, \\ \ddot{x}_2 + 4x_2 & = 0, \\ \ddot{x}_3 + \omega^2 x_3 & = 2\varepsilon\phi(t)x_3. \end{cases} \tag{6.5}$$

Stability or instability depends now on the Mathieu instability tongues of the third equation. Given ω near 1, $x_3(0)$ can be chosen small enough to produce stability of the x_1 normal mode, see Fig. 6.2 right, so formally the x_1 normal mode is stable. However, a slightly smaller perturbation of the frequency 1 may put the solution $x_3(t)$ with the same initial conditions in the unstable Mathieu tongue, see Fig. 6.2 left. These phenomena are subtle and should be kept in mind near resonance.

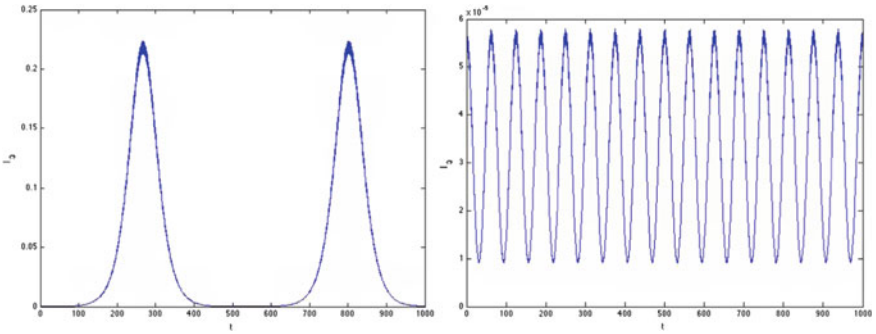

Fig. 6.2 The action $I_3 = \frac{1}{2}(\dot{x}_3^2 + \omega^2 x_3^2)$ in two cases of system (6.4) with $x_1(0) = 1, x_2(0) = 0.1, x_3(0) = 0.01$, velocities zero; $\varepsilon = 0.1$ and 1000 time-steps. *Left* the case $\omega^2 = 1.1$ leading to instability of the x_1 normal mode, $0 < I_3 < 0.23$. *Right* the slightly more detuned case $\omega^2 = 1.15$ leading to stability of the x_1 normal mode, the fluctuations of I_3 are of size 10^{-4}

6.4 Application to a Chain with 4 Interacting Particles

Consider a periodic chain consisting of four particles of equal mass ($m = 1$) with quadratic and cubic nearest-neighbor interaction. With position q_j and momentum $p_j = \dot{q}_j$, $j = 1 \ldots 4$, the Hamiltonian is of the form

$$H(p,q) = \sum_{j=1}^{4}(\frac{1}{2}p_j^2 + V(q_{j+1} - q_j)) \text{ with } V(z) = \frac{1}{2}z^2 + \frac{\alpha}{3}z^3 + \frac{\beta}{4}z^4. \quad (6.6)$$

This is a low-dimensional case of the periodic Fermi-Pasta-Ulam problem; usually many more particles are considered in this classical problem. We will choose

$$\alpha = 1, \beta = -1.$$

The corresponding equations of motion were studied in [4] where the stability and instability of the short-periodic solutions was established for arbitrary α and β. The equations induced by Hamiltonian (6.6) have a second integral of motion, the momentum integral $\sum_1^4 p_j = \text{constant}$. This enables us to reduce the 4 degrees-of-freedom equations of motion to 3 degrees-of-freedom. The symplectic transformation was carried out in [3] producing with $\alpha = 1, \beta = -1$:

$$\begin{cases} H_2 = 2x_1^2 + x_2^2 + x_3^2 + \frac{1}{2}(\dot{x}_1^2 + \dot{x}_2^2 + \dot{x}_3^2),\ H_3 = -4x_1x_2x_3, \\ H_4 = -\frac{1}{4}(4x_1^4 + x_2^4 + 6x_2^2x_3^2 + x_3^4 + 12x_1^2(x_2^2 + x_3^2)). \end{cases} \quad (6.7)$$

Rescaling as before $x_i \to \varepsilon x_i$, $\dot{x}_i \to \varepsilon \dot{x}_i$, $i = 1, 2, 3$ in a neighborhood of stable equilibrium we find the equations of motion:

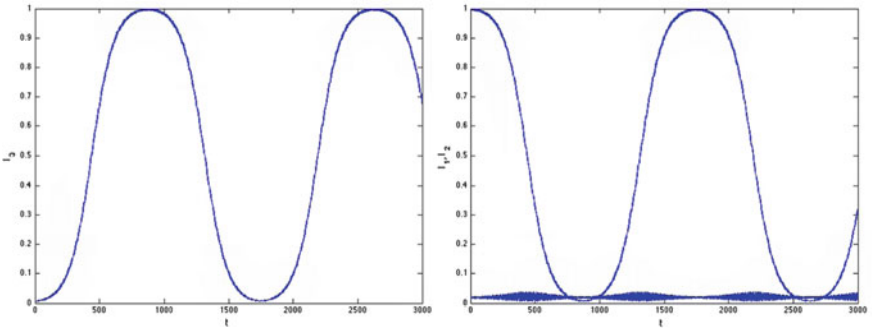

Fig. 6.3 The actions for 3000 timesteps near the unstable x_2 normal mode of system (6.8) with $\varepsilon = 0.1$, initial conditions $x_1(0) = x_3(0) = 0.1$, $x_2(0) = 1$ and initial velocities zero. *Left* the action $I_3(t) = \frac{1}{2}(\dot{x}_3^2 + 2x_3^2)$ starting near zero and increasing to values near 1. Right $I_2(t)$ starting at $I_2(0) = 1$ and $I_1(t)$ which remains small

$$\begin{cases} \ddot{x}_1 + 4x_1 = 4\varepsilon x_2 x_3 + \varepsilon^2 \left(4x_1^3 + 6x_1(x_2^2 + x_3^2)\right), \\ \ddot{x}_2 + 2x_2 = 4\varepsilon x_1 x_3 + \varepsilon^2 (x_2^3 + 3x_2 x_3^2 + 6x_1^2 x_2), \\ \ddot{x}_3 + 2x_3 = 4\varepsilon x_1 x_2 + \varepsilon^2 (x_3^3 + 3x_2^2 x_3 + 6x_1^2 x_3). \end{cases} \tag{6.8}$$

The three normal modes (in the coordinate planes) satisfy the equations of system (6.8). It was shown in [4] that the x_1 normal mode is stable, the x_2 and x_3 normal modes are unstable. Consider normal mode x_2. Linearization near the normal mode to $O(\varepsilon)$ produces stability as in the examples presented before. The instability is illustrated in Fig. 6.3.

References

1. Arnold, V.I., Kozlov, V.V., Neistadt, A.I.: Mathematical aspects of classical and celestial mechanics, Encycopedia of Math. Sciences vol. 3, Springer (1989)
2. Broer, H.W., Takens, F.: Dynamical systems and chaos. Appl. Math. Sci. **172**, Springer (2011)
3. Bruggeman, R.W., Verhulst, F.: Dynamics of a Chain with Four Particles and Nearest-neighbor Interaction, to be published
4. Rink, B., Verhulst, F.: Near-integrability of periodic FPU-chains. Phys. A **285**, 467–482 (2000)
5. Verhulst, F.: Discrete symmetric dynamical systems at the main resonances with applications to axi-symmetric galaxies. Phil. Trans. Royal Soc. A **290**, 435–465 (1979)
6. Verhulst, F.: Nonlinear Differential Equations and Dynamical Systems, 2nd rev. and expanded ed. Springer (2000)
7. Weinstein, A.: Normal modes for nonlinear Hamiltonian systems. Inv. Math. **20**, 47–57 (1973)

Chapter 7
Dynamics and Saturation Control of Rotating Composite Beam with Embedded Nonlinear Piezoelectric Actuator

Jaroslaw Latalski and Jerzy Warminski

Abstract In this research we consider a saturation adaptive control strategy to suppress vibrations of a system consisting of a rotating rigid hub and a thin-walled composite blade with an embedded piezoelectric active element. The adopted mathematical model of the beam considers non-classical effects like a circumferentially asymmetric stiffness lamination scheme that result in strong mutual coupling of the bending-twisting deformations as well as a higher order piezoceramic constitutive relation. The discussed structure has been investigated for possible levels of original system simplifications starting from the fully linearised one up-to the control applied to the nonlinear structure performing the full rotation. Obtained results of numerical simulations prove the applied nonlinear saturation control to be the robust and effective method for beam vibration suppression in near-by resonance zones for a non-rotating as well as rotating structures. It is shown that vibration of the beam can be suppressed to similar levels independently of the model simplification degree presuming the condition of proper controller tuning is preserved. However, significant differences in the width of vibration suppression zones are observed for studied subcases. Moreover, the analysis of the system response sensitivity to feedback and control gains is discussed.

7.1 Introduction

One of the most important issues in modern structures design is an enhancement of their static and dynamic characteristics. The objective might be efficient noise reduction, suppressing undesired structural vibrations, shape morphing, retrofitting existing structures, structural integrity monitoring etc. These aims can be achieved by a concept of structural control that is now becoming a standard technology.

J. Latalski · J. Warminski (✉)
Department of Applied Mechanics, Lublin University of Technology,
Nadbystrzycka 36, 20-618 Lublin, Poland
e-mail: j.warminski@pollub.pl

J. Latalski
e-mail: j.latalski@pollub.pl

M. Belhaq (ed.), *Recent Trends in Applied Nonlinear Mechanics and Physics*,
Springer Proceedings in Physics 199, https://doi.org/10.1007/978-3-319-63937-6_7

There are a huge variety of structural control strategies available to control engineer. Based on operational mechanisms these can be classified into four main groups: passive, semi-active, active, and hybrid methods.

In passive systems the control is activated by the structural motion and the input energy is dissipated by damping devices and proper isolation of the plant. No external force or energy is applied to effect the control. Semi-active control devices are a natural extension of passive ones. The embedded active elements control the properties of passive devices and adapt their behaviour based on the collected information on excitation and structural response, magneto-rheological dampers may serve as an example. In active control strategies system control is achieved by the externally activated actuators applying control load directly to the structure. The phase and magnitude of the control signal is evaluated on the basis of the measurements of external disturbance and temporary structural response.

A state of the art review of different control methods in civil and mechanical engineering was presented by Saaed et al. [21]. A comprehensive discussion on structural control strategies was supplemented by an overview of passive and active devices used in control engineering. Finally, some innovative practical implementations of modern control transducers were given. Further reading on different active vibration control methods and comparison of individual strategies performance may be found in recent review studies by Warminski et al. [30] and Orivuori et al. [13].

One of possible implementations of active control methods to suppress structural vibrations is the strategy based on a saturation phenomenon. This technique exploits the effect exhibited by two-to-one autoparametric resonance systems with quadratic nonlinearities. The strategy provides for the introduction of a second-order controller and coupling it with the plant through a sensor and an actuator, where both the feedback and control signals are quadratic. Setting the natural frequency of the controller to one-half of the plant natural frequency, the response of the excited mode gets saturated and plant vibrations are suppressed. Comparing to other control techniques, the saturation control has two important advantages [23]. In opposite to many conventional control strategies, the saturation method is very effective for controlling systems excited at near-resonant frequencies. Moreover, the saturation control is not sensitive to the amplitude of the external excitation. Thus, any increase in the energy applied to the plant is merely transferred to the controller without spilling back and keeping the plant response constant.

Since its discovery by Nayfeh in early 70s the saturation phenomenon has been the subject of extensive theoretical and experimental studies. Nayfeh and Oueini research group [14, 15] proposed a vibration absorber based on the saturation phenomena and implemented it for a cantilever beam made of isotropic material. The feedback signal was achieved from a strain gage and transferred to the control circuit assembled with analog electronic hardware. The beam actuation was accomplished through a pair of piezoceramic transducers attached to its surface. Laboratory tests for controller performance were conducted in the transient and steady-states under multifrequency resonant excitations. Conducted experiments demonstrated the strategy to be very effective in suppressing the vibration of tested beams. The saturation

phenomenon was the subject of further intense theoretical and experimental studies by other researchers [3, 16, 22, 23, 30].

The above mentioned technology of structural actuation and response sensing via distributed compact piezoelectric patches was introduced in 80-ties and since than has found a relevant role in active vibration control. A key advantage of this technology is a small weight of the control mechanism if compared to structural weight. Moreover, the controller consists of only electronic components, and a further weight saving can be achieved. More theoretical studies and investigations focused on vibration reduction achieved by piezoelectric patches and combined with the control system can be found in [16, 18, 20, 26, 28].

In most analytical models of coupled beam-controller systems developed to study the dynamics of piezoelectrically actuated structures the mass and stiffness of the piezoceramic transducers are neglected. In reality, bonding actuators onto the light-weight structure introduces non-uniformities in the studied system. To address the question whether it is reasonable to neglect the mass and stiffness contributions of the actuators when calculating the beam dynamic response Saguranrum et al. [23] performed a series of comparative studies. Authors enhanced the standard approach and included in the mathematical model of the coupled beam-controller system the non-uniformity effects resulting from bonded piezoceramic patches. Numerical simulations demonstrated that the presence of piezoelectric actuators resulted in system modal coupling and could affect the performance of a saturation controller. The difference was particularly apparent for systems having just a segment of specimen span covered by PZTs and at higher modes responses.

Further improvement in system control performance can be achieved by an exact modelling of structural kinematics and piezoceramic constitutive relations. This refers especially to commonly posed assumptions that the main features of the electro-mechanical system might be captured by a linear theory. Indeed, in most typical situations responses of the piezoelectric structures are sufficiently accurately evaluated by simple linear models. However, numerous laboratory tests of piezoceramic materials confirm that the high electrical fields and high stresses lead to the significant differences between linear and nonlinear approach to structural analysis [1, 7, 17]. Further investigations demonstrated that the inherent piezoelectric nonlinearities were not limited only to high magnitudes of electrical and mechanical loadings. Wagner and Hagedorn [29] and Stanton et al. [25] indicated that the observed discrepancies were non-negligible when the electro-elastic system was excited at its near-resonant frequencies even if amplitudes remained geometrically linear and the electric field was small. This observation seems to be critical if modelling control systems that are supposed to operate in near-resonance frequency zone.

Above referenced studies indicate the need to use a nonlinear model of the piezoceramic to obtain realistic and accurate results when modelling controlled electro-elastic structures. A complex approach to this issue was proposed by Leadenham and Erturk [11]. Authors developed a unified, two-way coupling framework accounting for softening and dissipative system nonlinearities to analyse piezoelectric cantilever structures. The elaborated analytical model was verified experimentally for sensing and dynamic actuation behaviour as well as for energy harvesting applications.

Experiments were performed over a wide (low to moderately high) range of mechanical and electrical excitation levels. Excellent agreement between the model and laboratory investigation was found, providing evidence that quadratic stiffness and electromechanical coupling effects accurately represented predominantly observed nonlinear effects in geometrically linear vibration of piezoelectric cantilever beams. Analytical model of an active piezoelectric cantilever developed by Leadenham and Erturk was used later on by Gatti et al. [4]. Authors examined the influence of nonlinear terms in piezoceramic constitutive relation on the dynamics of a structure and its energy harvesting performance. Different levels of base acceleration were tested with the intention to evaluate the limits of the linear model. It was concluded the nonlinearity played an unavoidable role in predicting charge generation for the tested systems since the observed discrepancy of the linear model was evident even for very low acceleration levels. Further reading regarding modelling of piezoceramic nonlinearities may be found in e.g. [1, 12, 19, 24, 34].

Analytical studies on electro-mechanical systems with piezoceramic constitutive nonlinearities have been done also by Latalski [8]. Author developed a fully coupled analytical model of a rotating flexible piezolaminated composite beam. In the mathematical formulation the reversible nonlinear behaviour of piezoceramic layer was considered. This nonlinearity was modelled by an up-to the third order constitutive relationship with respect to electric field. In the mathematical formulation of the problem the full two-way piezoelectric coupling effect was considered by adopting the assumption of spanwise electric field variation. Studies on system free vibration and analysis of individual components of mode shapes showed the significant diversities in electric field distribution regarding the angular speed of the plant and type of master structure deformation. Most prominent effects were observed for lower modes, where for higher speeds the difference between the electric field magnitudes at free end and the clamping point increased. For higher modes with a negligible bending/shear component the electric field spanwise distribution was almost uniform and close to zero on the full specimen span. Finally, the forced vibrations analysis confirmed the presence of the softening effect in systems with nonlinear piezoceramic material.

This paper is a continuation of the mentioned already research as well as other previous authors' studies on beams vibrations and their control methods. In particular Warmiński et al. [30, 31] discussed an application of the saturation control method as well as other control strategies to suppress vibrations of a clamped isotropic beam subjected to high levels of excitation amplitudes [30], and in conditions of two simultaneous excitations [31]. In the mathematical model of the structure, inertial as well as geometrical nonlinearities were taken into account.

Next Latalski et al. [9] studied on the performance of a rotating composite box beam exhibiting the coupled flexural-flexural vibrations. The control capabilities of the structure resulted from a piezoelectric layer distributed along the full span of the specimen inducing the boundary bending moment at the beam tip. A feedback control law was implemented to relate the control bending moment to the various kinematical response quantities of the structure. Within the performed studies various linear proportional control strategies were tested in terms of modal coupling magnitude

and possible cross-over frequency shifting. Afterwards Warmiński and Latalski [32] examined the efficiency of the nonlinear saturation control algorithm to suppress the coupled vibrations of a rotating piezolaminated composite box beam. The considered blade featured the circumferential asymmetric stiffness lamination scheme, thus it exhibited inherent coupling between bending and twisting modes. However, the linear properties of the piezoceramic material were assumed.

The idea of this research is to combine results of recent studies [32] with the mathematical modelling of nonlinear piezolaminated composite beams proposed in [8]. In particular, comparing to [32], different reinforcing fibres orientations in beam laminate are studied since this parameter strongly influences the magnitude of beam inherent flexural-torsional vibration modes coupling. Moreover, the impact of nonlinearities coming from hub-beam dynamics, as well as nonlinear properties of the PZT element is examined to evaluate the robustness and effectiveness of the saturation algorithm. Regarding the referenced papers and to the best of authors knowledge these aspects of saturation control strategy were not studied in detail yet.

7.2 Structural Model and Governing Equations

The model of the studied rotating structure (Fig. 7.1) is composed of a rigid hub with a clamped flexible beam. This has a prismatic cross section that is spanwise uniform (no taper) and without initial twist in its natural state. In the analysis it is assumed the original shape of the cross-section is maintained in its plane, but is allowed to warp out of the plane due to an elastic deformation of the specimen. The blade is clamped to the hub at the presetting angle $\theta = -\pi/2$. Therefore, the beam flapwise bending plane coincides with the plane of lead-lag structure deformation.

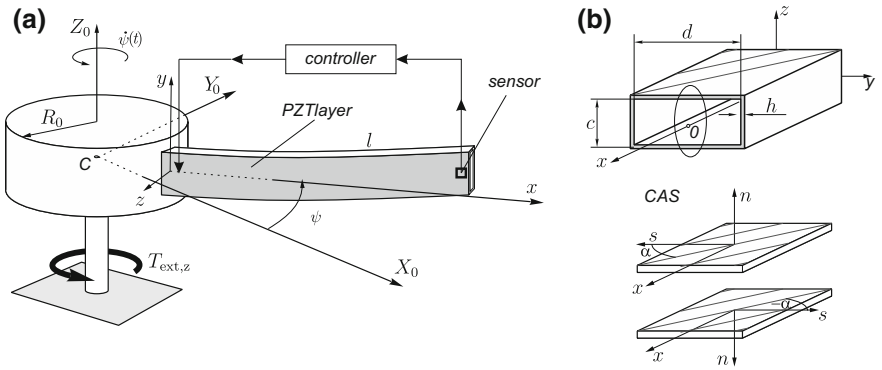

Fig. 7.1 Model of the hub-beam structure; the outer surfaces of the blade fully electroded with piezoceramic material (**a**), the circumferentially asymmetric stiffness (*CAS*) composite configuration (**b**)

The discussed blade is made of multilayered laminate with reinforcing fibres placed according to the circumferentially asymmetric stiffness (CAS) scheme—see Fig. 7.1b. This configuration results in bending-twisting deformation coupling the magnitude of which depends on the reinforcing fibres orientation [10]. Apart from the fibre unidirectional layer, there are two additional piezoceramic layers located on the outer surfaces of profile flanges that cover the full span of the beam. The active material is poled through its thickness and equipped with traditional surface electrodes. This is the typical geometry for '3-1' mode operating piezoelectric actuators and sensors.

Further accepted kinematic and structural assumptions for the mathematical formulation of the problem can be found in previous authors papers [5, 10]. The discussion on their significance is also given there.

The rotation of the hub-beam system is excited by an external driving torque $T_{\mathrm{ext,z}}$, that is an algebraic sum of steady-state and periodic components. The structure is controlled through a nonlinear control unit adopting the saturation control strategy in order to reduce beam oscillations.

The general partial differential governing equations for the system under consideration as derived in [8] are as follows:

- for the rigid hub

$$J_{\mathrm{h}}\ddot{\psi}(t) + (B_{22} + B_4 l)\ddot{\psi}(t) + B_4 l\ddot{\vartheta}_y + \int_0^l \left\{ b_1(R_0 + x)\left[2u_0\ddot{\psi}(t) + 2\dot{u}_0\dot{\psi}(t) - \ddot{w}_0\right]\right\} \mathrm{d}x - T_{\mathrm{ext},z}(t) = 0 \tag{7.1}$$

- displacement in lead-lag plane w_0

$$b_1\ddot{w}_0 + 2b_1\dot{u}_0\,\dot{\psi}(t) - b_1 w_0\dot{\psi}^2(t) + b_1(R_0 + x + u_0)\ddot{\psi}(t) - a_{55}\vartheta_y{}' - a_{55}w_0'' - \left(T_x w_0'\right)' = 0 \tag{7.2}$$

with boundary conditions

$$w_0\big|_{x=0} = 0, \qquad \left(\vartheta_y + w_0'\right)\big|_{x=l} = 0$$

- transverse shear ϑ_y

$$B_4\ddot{\vartheta}_y - B_4\vartheta_y\dot{\psi}^2(t) - B_4\ddot{\psi}(t) + a_{55}(\vartheta_y + w_0') - a_{33}\vartheta_y{}'' - a_{37}\varphi'' - a_{3e}E_3' - a_{3b}\left[\mathrm{sgn}(E_3)E_3^2\right]' - a_{3f}\left(E_3^3\right)' = 0 \tag{7.3}$$

with boundary conditions

$$\vartheta_y\big|_{x=0} = 0, \qquad \left[a_{33}\vartheta_y{}' + a_{37}\varphi' + a_{3e}E_3 + a_{3b}\,\mathrm{sgn}(E_3)E_3^2 + a_{3f}E_3^3\right]\big|_{x=l} = 0$$

- profile twist angle φ

$$(B_4 + B_5)\ddot{\varphi} + (B_4 - B_5)\varphi\dot{\psi}^2(t) - a_{37}\vartheta_y{}'' - a_{77}\varphi'' - \left(T_r\varphi'\right)' = 0, \tag{7.4}$$

with boundary conditions

$$\varphi\big|_{x=0} = 0, \qquad \left(a_{37}\vartheta_y{}' + a_{77}\varphi'\right)\big|_{x=l} = 0,$$

- electrostatic equation E_3

$$a_{E3}\vartheta_y{}' - a_{Ee}E_3 - a_{Eb}\,\mathrm{sgn}(E_3)(E_3)^2 - a_{Ef}E_3^3 = 0 \tag{7.5}$$

Terms $T_x(x)$ and $T_r(x)$ present in (7.2) and (7.4) correspond to system stiffening resulting from rotational transportation motion and they are defined as

$$T_x(x) = b_1(l - x)\left[R_0 + \tfrac{1}{2}(l + x)\right]\dot{\psi}^2(t) \qquad T_r(x) = \gamma T_x(x)$$

where $\gamma = \frac{B_4+B_5}{m_0\beta}$ and β is cross-section perimeter.

Term m_0 is an averaged blade mass density per unit length, and b_1, B_4 and B_5 are inertia coefficients as defined in [5]. The coefficient a_{33} corresponds to bending stiffness, a_{55} to transverse shear stiffness, a_{77} is torsional one and a_{37} is bending-torsion coupling stiffness. Coefficients $a_{3e} = a_{E3}$, a_{3b}, a_{3f} and a_{Eb}, a_{Ef} are electromechanical reduced stiffnesses resulting from piezoelectric and electrostatic properties of the actuators, where $(.)_b$ and $(.)_f$ subscripts refer to higher order electric field E_3 terms present in nonlinear constitutive relation of piezoceramics [6, 27, 33]. For their definition please refer to [8].

The derived equations of motion for the rigid hub-thin-walled piezoelectric-composite beam constitute a system of nonlinear coupled partial differential equations. It can be observed the electrical degree of freedom (dof) and individual mechanical ones representing bending and profile twist are coupled through the transverse shear deformation (7.3). Higher order electric field terms are present in this equation, as well as in electrostatic one. These terms naturally result from the discussed nonlinear piezoelectric effect.

7.3 Hub-Beam System Dynamics

The presented in the previous section, the full system of partial differential governing equations, is transformed into ordinary differential ones taking into account the normal modes projection with the associated orthogonality condition. To this aim the Galerkin procedure for the first natural mode is applied. Next, the system is converted to the dimensionless notation. The coupled flexural-torsional mode projection results in the final set of nonlinear ODEs as follows

$$
\begin{aligned}
&(1 + J_{\mathrm{h}} + \alpha_{\mathrm{h}12} q_1^2)\ddot{\psi} + \zeta_{\mathrm{h}}\dot{\psi} + \alpha_{\mathrm{h}11}\ddot{q}_1 + \alpha_{\mathrm{h}13} q_1 \dot{q}_1 \dot{\psi} = \mu \\
&\ddot{q}_1 + \zeta_1 \dot{q}_1 + \alpha_{12}\ddot{\psi} + (\alpha_{11} + \alpha_{13}\dot{\psi}^2) q_1 + \alpha_{14} q_1 \dot{q}_1 \dot{\psi} \\
&\qquad + \alpha_{15}\mathrm{sgn}(q_1) q_1^2 + \alpha_{16} q_1^3 = 0
\end{aligned} \tag{7.6}
$$

where q_1 is the generalized coordinate corresponding to the studied coupled flexural–torsional mode, coefficients $\alpha_{\mathrm{h}1j}$ $(j = 1, 2, 3)$ and α_{1j} $(j = 1, \ldots, 4)$ are obtained from the modes projection; ζ_1, ζ_{h} are the beam and the hub damping coefficients, and J_{h} is the dimensionless mass moment of inertia of the hub. External torque supplied to the hub is expressed as a sum of a constant component μ_0 and a periodic function of time t. Thus

$$
\mu = \mu_0 + \rho \cos \omega t \tag{7.7}
$$

where ρ and ω are the amplitude and the frequency of the excitation, respectively.

As we can notice, (7.6) are nonlinear and mutually coupled. The driving $(7.6)_1$ represents dynamics of the hub and it is nonlinear due to the coupling with the beam motion. The $(7.6)_2$ is nonlinear for two reasons: (a) an existence of centrifugal and Coriolis forces resulting from the hub rotation and (b) the nonlinear electric field of PZT layers. Furthermore, additional couplings of beam and hub motions occur due to inertia terms $\ddot{q}_1$ and $\ddot{\psi}$ each present in both equations.

Dimensionless coefficients α and ζ for the studied structure geometry given in [10] take the following values:

$$
\begin{aligned}
&\alpha_{11} = 10.864, \quad \alpha_{12} = 1.772, \quad \alpha_{13} = 0.349, \quad \alpha_{14} = -1.55, \\
&\alpha_{15} = -2.327, \quad \alpha_{16} = 0.0, \quad \alpha_{\mathrm{h}11} = -0.532, \quad \alpha_{\mathrm{h}12} = -0.404, \\
&\alpha_{\mathrm{h}13} = -0.808, \quad \zeta_{\mathrm{h}} = 0.1, \quad \zeta_{\mathrm{c}} = 0.001, \quad \zeta_1 = 0.01 \times \omega_0, \\
&\omega_0 = \sqrt{\alpha_{11}} \qquad J_{\mathrm{h}} = 1.0
\end{aligned}
$$

In further analysis components of the external torque (i.e. μ_0, ρ and excitation frequency ω) are considered as bifurcation parameters and subject to variation. Dynamics of the system will be investigated around the main resonance zone ω_1, where

$$
\omega_1 = \sqrt{\frac{\alpha_{11} + \alpha_{13}\dot{\psi}^2}{1 - \frac{\alpha_{12}\alpha_{\mathrm{h}1}}{1 + J_{\mathrm{h}}}}} \tag{7.8}
$$

The above expression comes from the set (7.6) after neglecting the nonlinear terms, damping and external excitation, but keeping rotation effect and the mass moment of hub inertia.

7.3.1 Analysis of a Linear Model

Let us start with the simplest case neglecting all beam interactions present in the driving $(7.6)_1$. Thus we get

$$J\ddot{\psi} + \zeta_{\mathrm{h}}\dot{\psi} = \mu_0 + \rho\cos\omega t \tag{7.9}$$

where $J = 1 + J_{\mathrm{h}}$.

This equation can be solved in a closed form. Performing integration and posing initial conditions $\psi(t=0) = \psi_0 = 0$ and $\dot{\psi}(t=0) = \dot{\psi}_0$, we get solutions for the hub angular velocity and angle of rotation (i.e. temporary position of the system)

$$\begin{aligned}
\dot{\psi} =& \frac{1}{\zeta_{\mathrm{h}}^2 + J^2\omega^2}\left(\frac{\mu_0}{\zeta_{\mathrm{h}}} - \rho J\omega\cos\omega t + \rho\zeta_{\mathrm{h}}\sin\omega t\right) + \left(\dot{\psi}_0 - \frac{\mu_0}{\zeta_{\mathrm{h}}} + \rho\frac{J\omega}{\zeta_{\mathrm{h}}^2 + J^2\omega^2}\right)e^{\frac{-\zeta_{\mathrm{h}}}{J}t} \\
\psi =& \frac{1}{\zeta_{\mathrm{h}}}\left(J\dot{\psi}_0 + \frac{\rho}{\omega} - \mu_0\frac{J}{\zeta_{\mathrm{h}}}\right) + \frac{1}{\zeta_{\mathrm{h}}^2 + J^2\omega^2}\left(\frac{\mu_0}{\zeta_{\mathrm{h}}}t - \rho J\sin\omega t - \rho\frac{\zeta_{\mathrm{h}}}{\omega}\cos\omega t\right) \\
& - \frac{J}{\zeta_{\mathrm{h}}}\left(\dot{\psi}_0 - \frac{\mu_0}{\zeta_{\mathrm{h}}} + \rho\frac{J\omega}{\zeta_{\mathrm{h}}^2 + J^2\omega^2}\right)e^{-\frac{\zeta_{\mathrm{h}}}{J}t}
\end{aligned} \tag{7.10}$$

Plots of the hub angular velocity $\dot{\psi}$ and angle of rotation ψ versus time are presented in Fig. 7.2. Since the driving torque is composed of constant and periodic terms, so the angular speed solution tends to a steady state after some transient period. System oscillations are set around an average value $\overline{\Omega}_{\mathrm{h}}$ equal to μ_0/ζ_{h}. For the assumed data $\mu_0 = 0.005$, $\rho = 0.005$, $\omega = 2.715$, $J_{\mathrm{h}} = 1$, we get $\overline{\Omega}_{\mathrm{h}} = 0.05$ which corresponds to 177 rpm in physical units.

In the subsequent simulation the reduced, one DOF model (7.9) is extended to include dynamics of the beam. Higher order nonlinear terms of beam dynamics are neglected. However, the nonlinear term coming from angular velocity that couples hub and beam motions is preserved to capture the centrifugal stiffening effect properly within the linear formulation frame. The resulting system of governing equations is

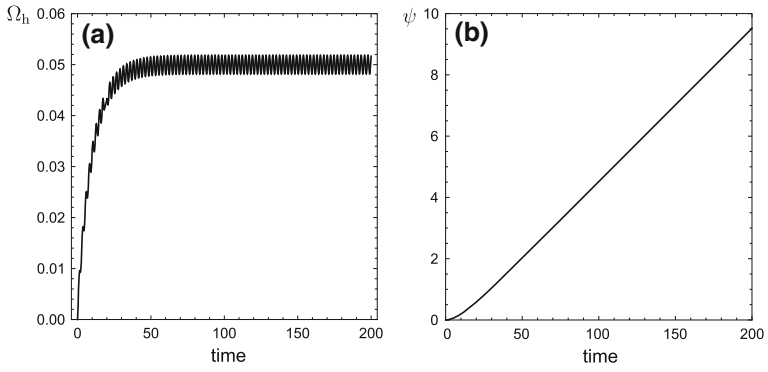

Fig. 7.2 Angular velocity Ω_{h} (**a**) and angle of rotation ψ (**b**) of a simplified linear model forced by torque composed of constant and variable components $\mu = \mu_0 + \rho\cos\omega t$; $\mu_0 = 0.005$, $\rho = 0.005$, $\omega = 2.715$, $J_{\mathrm{h}} = 1$

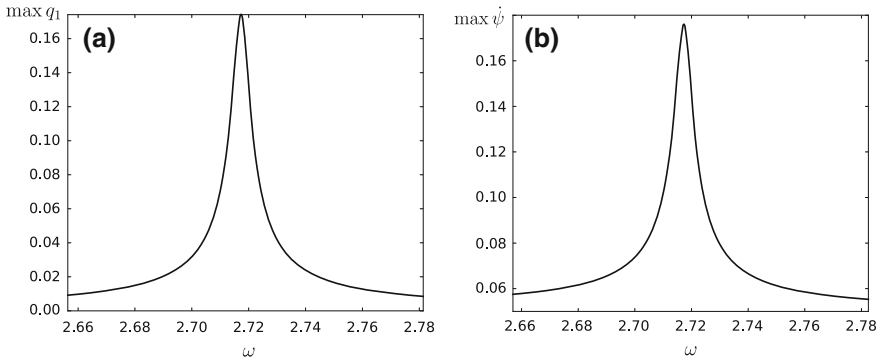

Fig. 7.3 The linear beam model; resonance curves of (**a**) maximal beam displacement and (**b**) hub angular velocity; $\mu_0 = 0.005$, $\rho = 0.005$, $J_\mathrm{h} = 1$

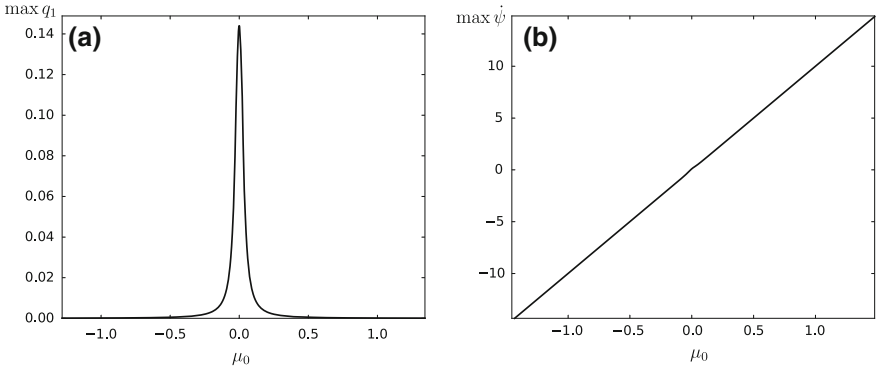

Fig. 7.4 The linear beam model forced by the torque $\mu = \mu_0 + \rho \cos \omega t$—influence of the μ_0 parameter; bifurcation plots for (**a**) maximal beam displacement q_1 and (**b**) hub angular velocity $\dot{\psi}$; $\rho = 0.005$, $\omega = 2.715$, $J_\mathrm{h} = 1$

$$\begin{aligned} (1 + J_h)\ddot{\psi} + \zeta_h \dot{\psi} + \alpha_{\mathrm{h}11}\ddot{q}_1 &= \mu \\ \ddot{q}_1 + \zeta_1 \dot{q}_1 + \alpha_{12}\ddot{\psi} + (\alpha_{11} + \alpha_{13}\dot{\psi}^2) q_1 &= 0 \end{aligned} \tag{7.11}$$

The response of such a system to the external torque supplied to the hub is analysed around first natural frequency of the structure. The curves presented in Fig. 7.3 have classical linear nature. Either beam or hub amplitudes increase around the resonance zone. Note that the hub response curve starts from a non zero value. This comes from the nonzero value of torque constant component μ_0.

The effect of system rotation velocity and expected beam centrifugal stiffening is demonstrated in Fig. 7.4. The analysis has been performed for the fixed excitation frequency and amplitude $\omega = 2.715$, $\rho = 0.005$ and the varied μ_0 component. Studying the plot (b) one observes the increasing μ_0 magnitude results in higher angular hub velocities. The relation is almost linear with just a small perturbation around $\mu_0 = 0$.

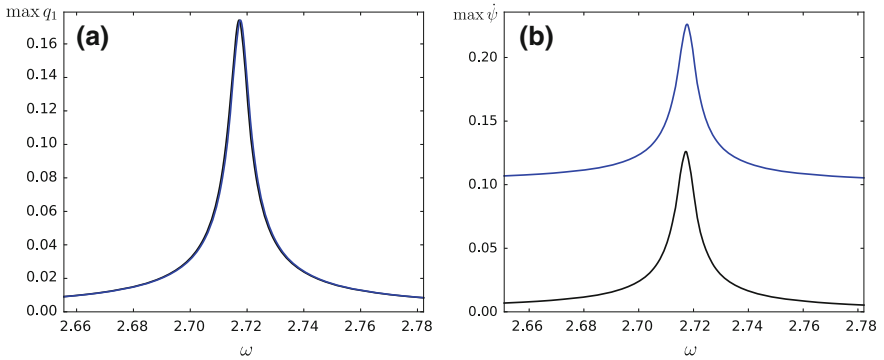

Fig. 7.5 The linear beam model forced by the torque $\mu = \mu_0 + \rho \cos \omega t$; resonance curves of (**a**) maximal beam displacement q_1 and (**b**) hub angular velocity $\dot{\psi}$; $\mu = 0$–*black*, $\mu_0 = 0.01$–*blue*; $\rho = 0.005$, $J_\mathrm{h} = 1$

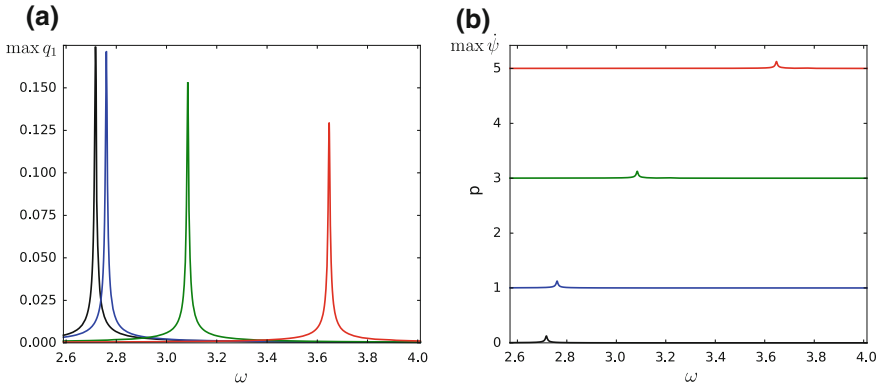

Fig. 7.6 The linear beam model forced by the torque; resonance curves of (**a**) maximal beam displacement q_1 and (**b**) hub angular velocity; $\mu = 0$—*black*, $\mu_0 = 0.1$—*blue*, $\mu_0 = 0.3$—*green*, $\mu_0 = 0.5$—*red*; $\rho = 0.005$, $J_\mathrm{h} = 1$

The increased angular speed makes the beam stiffer therefore the resonance zone is shifted and blade response amplitude is decreased (Fig. 7.4a). For the analysed case beam oscillations are almost fully suppressed if $-0.25 > \mu_0 > 0.25$.

The influence of the μ_0 parameter is demonstrated also in resonance curves (Fig. 7.5) computed for $\mu_0 = 0$ (black curve) and $\mu_0 = 0.01$ (blue one). Although the difference in the beam response amplitude is minor (Fig. 7.5a), the hub angular velocity curves are separated (Fig. 7.5b). The differences are becoming more evident if μ_0 is further increased. The system resonance zone gets shifted towards higher frequencies and amplitudes are substantially reduced due to stronger centrifugal stiffening effect (see Fig. 7.6 for beam response (a) and hub angular velocity (b)).

Results of previous authors research [10] indicated the hub inertia might play an important role when studying the hub-beam system behaviour. In particular, if its

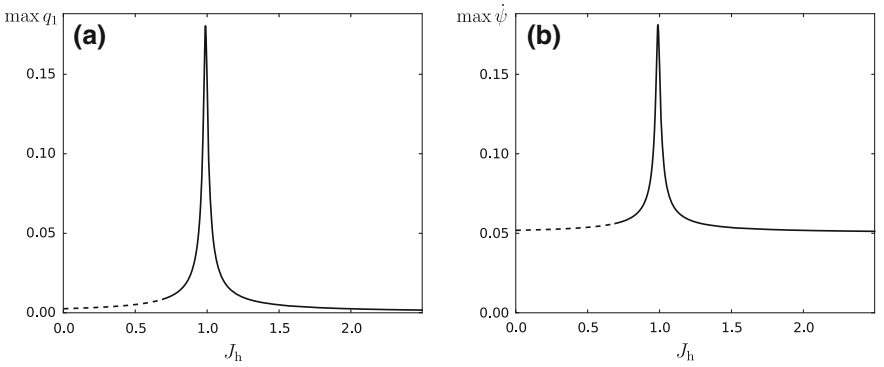

Fig. 7.7 Response of the linear beam model against the J_h parameter; **a** maximal beam displacement and **b** hub angular velocity; $\mu_0 = 0.005$, $\rho = 0.005$, $\omega = 2.715$

ratio to beam inertia is not high, then it has a crucial impact on the natural frequencies of the structure. However, for high hub to beam ratios changes in hub inertia do not affect the system natural frequencies. In the limit case of an infinitely heavy hub the beam dynamics corresponds to a cantilever specimen behaviour in a rotating coordinates frame.

Considering a linear beam model and its coupling with the hub as given in (7.11) we compute periodic solution of the whole hub-beam assembly against J_h, treated as a bifurcation parameter. To this aim external torque parameters are set to $\mu_0 = 0.005$, $\rho = 0.005$, and $\omega = 2.715$ and two μ_0 cases are analysed. The obtained results are shown in Fig. 7.7. One observes the periodic solution becomes unstable below the limit $J_h \approx 0.69$. The unstable solutions presented by dashed branch occurs via torus bifurcation, periodic motion transits into quasi-periodic one.

Time histories for the cases close to the bifurcation point exhibit beating phenomenon (Fig. 7.8). For a point $J_h = 0.7$ on the stable branch, after long transient state, the solution becomes periodic (Fig. 7.8a, b), but for a point on the unstable branch $J_h = 0.65$, beating oscillations increase (Fig. 7.8c).

7.3.2 Analysis of a Nonlinear Model

The dynamics of a full model without control is represented by a set of (7.6) which is nonlinear due to the coupling of the hub and beam motions and due to the nonlinear constitutive characteristic of the PZT element embedded into the plant.

Resonance curves, either for the beam or the hub, exhibit softening effect which arises from both mentioned above factors. In order to demonstrate a separated influence of the nonlinearity resulting from system dynamics resonance curves are plotted imposing linear properties of the PZT element—see Fig. 7.9. To this aim α_{15} and α_{16} coefficients has been set to zero. In fact, a slope of response characteristics becomes

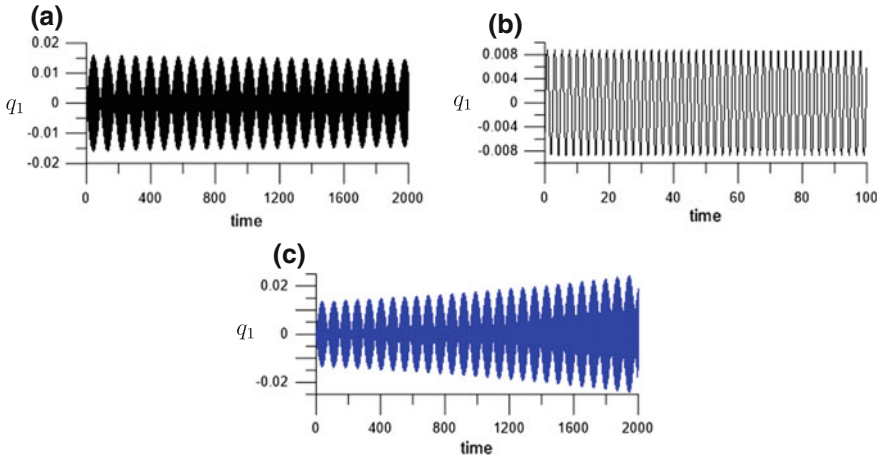

Fig. 7.8 Time histories of beam response for stable $J_h = 0.7$ (**a**, **b**) and unstable $J_h = 0.65$ zones (**c**); the linear beam model; $\mu_0 = 0.005$, $\rho = 0.005$, $\omega = 2.715$

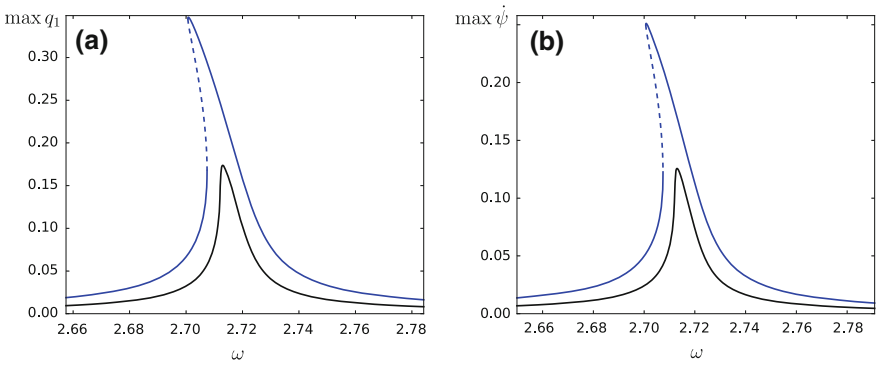

Fig. 7.9 The hub-beam system with the linear PZT element; resonance curves of (**a**) beam displacement and (**b**) hub angular velocity; $\rho_0 = 0.005$—*black*, $\rho_0 = 0.01$—*blue*; $\mu = 0$, $J_h = 1$

evident for large amplitudes; for the beam exceeding even 0.3 of its length (blue line, left plot). For small or average oscillations this effect is almost invisible (black line) but still present.

The impact of the separated nonlinearity of piezoceramics is presented in Fig. 7.10, where resonance curves for the nonlinear PZT element (blue line) and a linear one (black line) are put together. Independently of the piezoceramics model case nonlinearities coming from system dynamics are retained. As we may notice, the nonlinearity of the piezoelectric constitutive model dominates and decisively determines the softening effect. This results from high magnitudes of the electric field corresponding to large oscillations of the beam. The softening effect is also present on

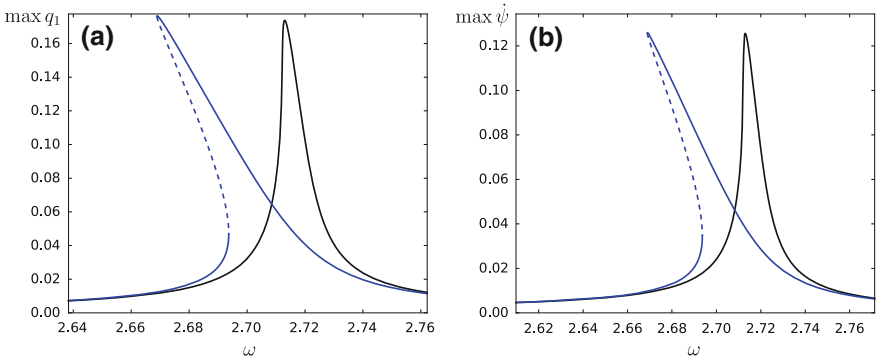

Fig. 7.10 Resonance curves around natural frequency, (**a**) beam and (**b**) hub response, *black line* linear PZT model, *blue line* nonlinear PZT model; $\rho = 0.005$, $J_\mathrm{h} = 1$, $\mu_0 = 0$; system without control

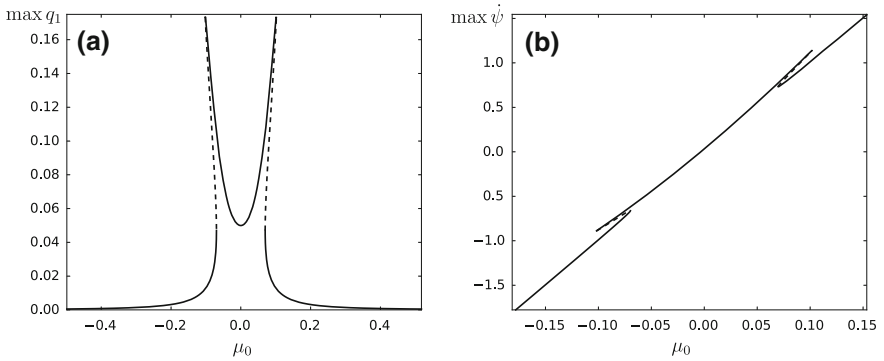

Fig. 7.11 Bifurcation diagram of a hub-beam model with nonlinear PZT element against μ_0 parameter, (**a**) beam displacement and (**b**) hub angular velocity; $\rho = 0.005$, $J_\mathrm{h} = 1$, $\omega = 2.715$

hub characteristic plot. Therefore, one may conclude the constitutive nonlinearity of the piezoceramic has to be taken into account in near resonant conditions.

The influence of both nonlinearities is also clearly visible in bifurcation diagrams of the beam and hub responses versus constant component μ_0 of the driving torque (Fig. 7.11). Comparing this result with linear model presented in Fig. 7.4 we observe double nonlinear resonance peaks with stable and unstable branches on the bifurcation diagram. Nonlinearity is also observed on hub response plot (Fig. 7.11b).

The bifurcation diagram versus hub inertia J_h demonstrates a nonlinearity of a hardening-like effect (Fig. 7.12). There is a saddle-node bifurcation about $J_\mathrm{h} = 1$ but for small values of J_h the system loses stability through a torus bifurcation, in a very similar way to that presented for a linear system—see Fig. 7.7.

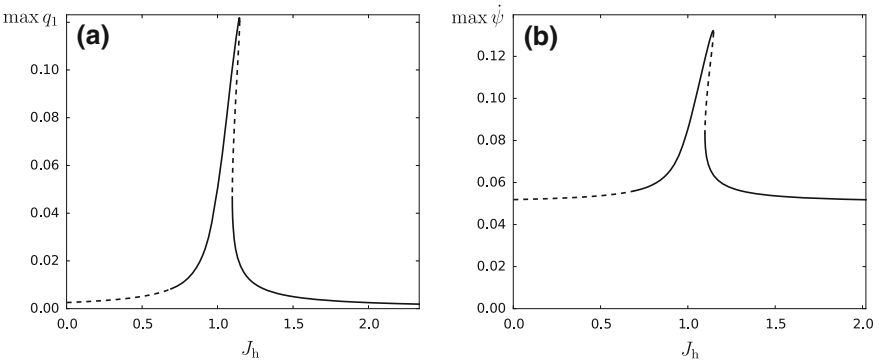

Fig. 7.12 The hub-beam model with nonlinear PZT forced by the torque $\mu = \mu_0 + \rho \cos \omega t$— influence of the J_h parameter; **a** maximal beam displacement q_1 and **b** hub angular velocity $\dot{\psi}$; $\mu_0 = 0.005$, $\rho = 0.005$, $\omega = 2.715$

7.3.3 Nonlinear Model with Control

The applied control method should be effective considering the fully nonlinear system, thus it should take into account complete hub-beam dynamics, as well as discussed nonlinear properties of the PZT element. The controller is expected to work effectively for a periodic motion, so we avoid system parameters leading to torus bifurcation and quasi-periodicity.

The proposed in this research control strategy is based on an additional oscillator $(7.12)_3$ added to the original governing system (7.6) and acting as a controller

$$\begin{aligned}
&(1 + J_h + \alpha_{h12} q_1^2)\ddot{\psi} + \zeta_h \dot{\psi} + \alpha_{h11} \ddot{q}_1 + \alpha_{h13} q_1 \dot{q}_1 \dot{\psi} = \mu \\
&\ddot{q}_1 + \zeta_1 \dot{q}_1 + \alpha_{12} \ddot{\psi} + (\alpha_{11} + \alpha_{13} \dot{\psi}^2) q_1 + \alpha_{14} q_1 \dot{q}_1 \dot{\psi} \\
&\qquad + \alpha_{15} \mathrm{sgn}(q_1) q_1^2 + \alpha_{16} q_1^3 = g_1 q_c^2 \\
&\qquad \ddot{q}_c + \zeta_c \dot{q}_c + \omega_{0c}^2 q_c = g_2 q_c q_1
\end{aligned} \tag{7.12}$$

The control input signal q_c is squared and multiplied by the gain g_1 and added to the right hand side of $(7.6)_2$. On the other hand, the controller equation is coupled with beam oscillations by a product of q_1 and q_c signals multiplied by the gain g_2. To fully exploit the effectiveness of the postulated control method both gains g_1 and g_2 should be properly tuned [2]. Such a control method results in the so called amplitude saturation phenomenon and has been successfully applied for non-rotating systems [14, 15, 30]. It should be noted that the proposed control method introduces additional nonlinearities to the system, and these coexist with nonlinearities of the basic hub-beam system (the plant) presented in Sect. 7.3.2.

The postulated saturation control method is highly effective in a wide range of near resonant frequencies provided the controller is properly tuned to the plant. The requirement is the natural frequency of the controller ω_{0c} has to be set to one-half

of the plant natural frequency ω_1. Since the natural frequency of the separated beam differs from natural frequency of the entire hub-beam system a complete hub-beam assembly has always to be considered while examining the natural frequencies of the plant [10]. Moreover, system rotation that leads to beam stiffening effect due to centrifugal load has to be taken into account.

The rotating beam natural frequency, considered as a rotating cantilever beam (i.e. separated from the hub) is defined as

$$\omega_{\text{beam}} = \sqrt{\alpha_{11} + \alpha_{13}\dot{\psi}^2} \tag{7.13}$$

The frequency of the full hub-beam system ω_1 has to be evaluated from (7.8), where the hub inertia term J_h is present. In the limit case $J_\text{h} \to \infty$ the final result tends to formula (7.13).

To verify the robustness of the postulated saturation strategy for the hub-beam system several numerical simulations are performed. To this aim frequency-response curves are constructed around its first resonance zone. Moreover, controller response curves are plotted to verify the saturation phenomenon for the considered system.

7.3.3.1 Oscillations of the System About Neutral Position

At the first stage we consider the periodic torque μ supplied to the hub with its constant component equal to zero $\mu_0 = 0$—see (7.7). Responses of the uncontrolled and controlled system are presented in Fig. 7.13. One can observe amplitudes of the beam as well as the hub get reduced almost to zero (blue line in Fig. 7.13a, b) around the system natural frequency $\omega_1 = 2.715$. The peak of the nonlinear resonance curve becomes unstable due to the controller activation (Fig. 7.13c). It is worth mentioning that responses of the beam and the hub are harmonic while the controller is sub-harmonic with respect to the frequency of excitation. The most effective vibration suppressing is observed directly around the system natural frequency. Time histories plotted in Fig. 7.13d at $\omega = 2.715$ for the beam without control (black) and for the activated controller case (blue) confirm the results presented in response curves plot Fig. 7.13a.

As reported in other research papers [2, 30] efficiency of the implemented control method depends on gains g_1, g_2 applied for input and output signals. To find the optimal settings for the structure the influence of both gain factors on the controller response is studied in more detail.

Two simulations have been performed for fixed structural parameters, as well as excitation amplitude and frequency. In the first case the control gain g_1 has been varied in the range of $\langle 0, 1\rangle$ while keeping the gain g_2 constant and set to value 1. The obtained controller signal is shown in Fig. 7.14a. Next, the feedback gain g_2 has been varied at gain $g_1 = 0.01$ (Fig. 7.14b). It is evident high amplitudes of the controller may be expected for low values of the gain g_1. Opposite effect is present in the second simulation, where high controller responses occur at higher values of

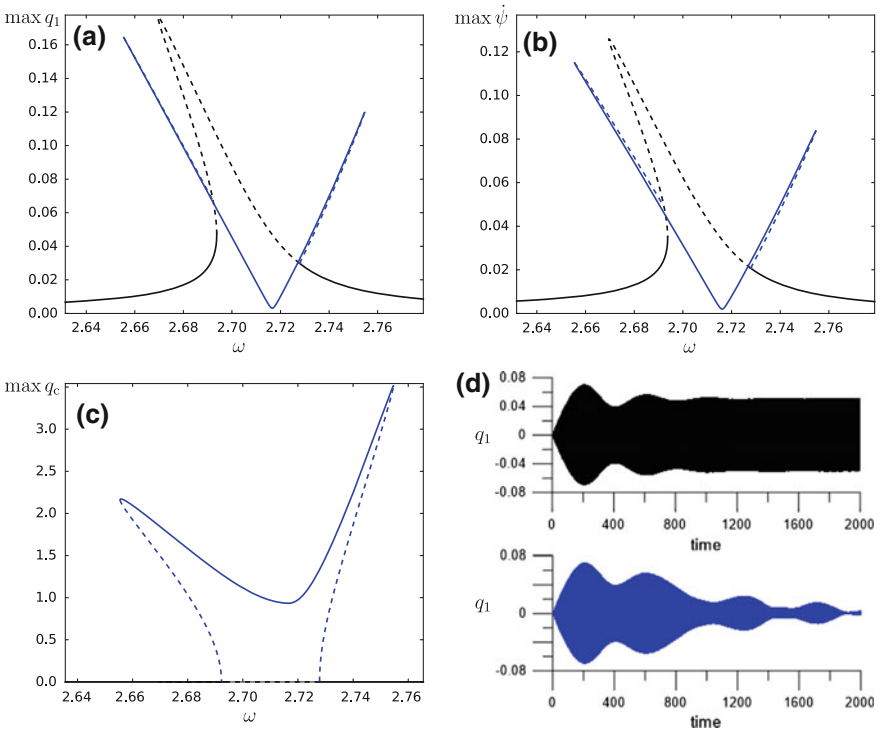

Fig. 7.13 Resonance curves around natural frequency with activated controller, (**a**) beam response, (**b**) hub angular velocity, (**c**) controller response and (**d**) time histories of beam response without control—*black line*, with control—*blue line* for $\omega = 2.715$; $g_1 = 0.01$, $g_2 = 1$, $\rho = 0.005$

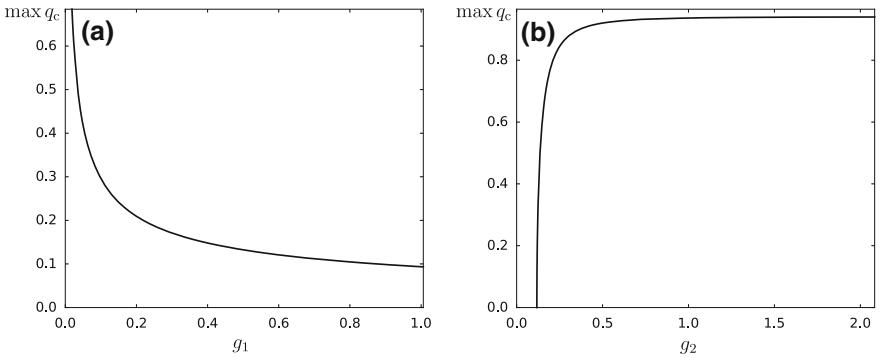

Fig. 7.14 Response of the controller against (**a**) gain g_1 and fixed $g_2 = 1$, (**b**) gain g_2 and fixed $g_1 = 0.01$; $\mu_0 = 0$, $\omega = 2.715$; $\rho = 0.005$, $J_h = 1$

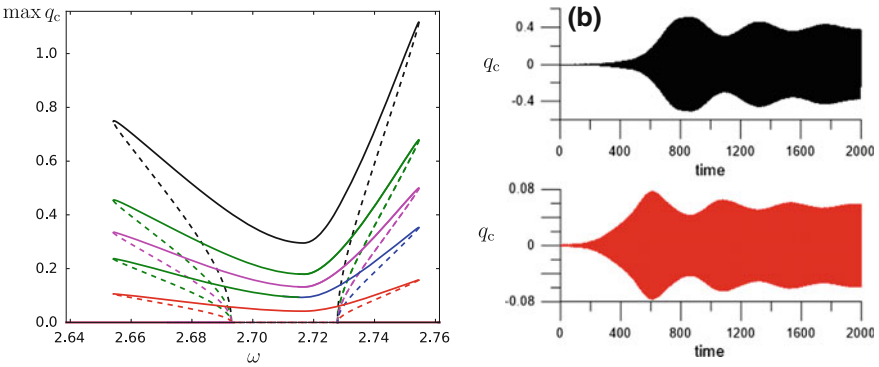

Fig. 7.15 Resonance curves of the controller (**a**) for selected values of gain g_1: $g_1 = 0.1$—*black*, $g_1 = 0.271$—*green*, $g_1 = 0.5$—*pink*, $g_1 = 1$—*blue*, $g_1 = 5$—*red* and (**b**) time histories of controller response $g_1 = 0.1$—*black*, $g_1 = 5$—*red*; $\omega = 2.715$, $g_2 = 1$, $\rho = 0.005$, $\mu_0 = 0$, $J_h = 1$

the feedback gain g_2. Moreover, it is observed the increase of any gains results in the controller response asymptotically approaching a limit value. Thus, above a certain thresholds, gains changes have no effect on the controller response.

To verify these results resonance curves for selected values of gain g_1 and corresponding time histories of the controller response are presented in Fig. 7.15. Based on Figs. 7.14 and 7.15 we may conclude that $g_1 = 0.5$ and $g_2 = 1$ are appropriate values in terms of controller performance. They guarantee effective plant vibration suppression combined with a rational engagement of the controller.

Resonance curves computed for gains $g_1 = 0.5$ and $g_2 = 1$ are presented in Fig. 7.16. In this case vibrations of the beam and the hub are well reduced around system natural frequency (Fig. 7.16a, b) with a relatively small engagement of the controller (Fig. 7.16c). Time histories of the beam and the controller are shown in Fig. 7.16d.

The potential consequences of an incorrect choice of gains g_1 and g_2 are demonstrated in Fig. 7.17. For the case $g_1 = 1$ and $g_2 = 0.12$ the control strategy is basically ineffective. The reason is the activation of the controller in a very narrow range of frequencies that do not cover the part of the characteristic corresponding to peak beam responses—see Fig. 7.17a. Furthermore, the amplitude of the controller is restrained (see Fig. 7.14) thus the plant vibrations are weakly suppressed. Hence it may be concluded that the appropriate selection of control and feedback gains is a key factor in terms of successful vibrations suppression.

7.3.3.2 The Full Rotation Case

To consider the full rotation case we assume the constant torque component μ_0 to be a non-zero value. Then the average angular velocity is different from zero and the system performs the full rotation—see also Fig. 7.2. This results in the beam

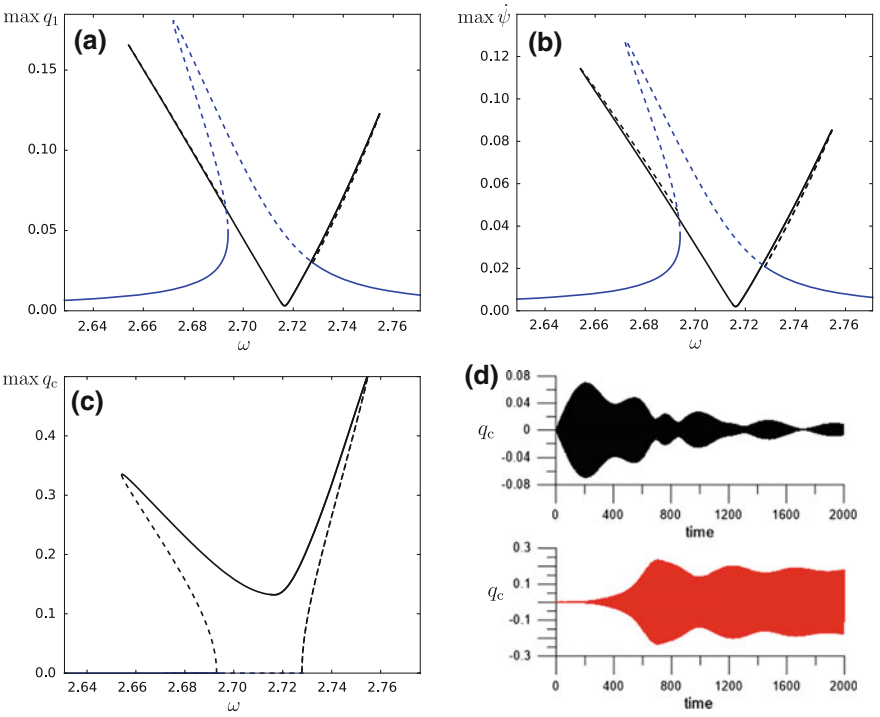

Fig. 7.16 Resonance curves around the first natural frequency with activated NSC for (**a**) the beam, (**b**) the hub, (**c**) the controller, $g_1 = 0.5$, $g_2 = 1$, $\rho = 0.005$, $\mu_0 = 0$, and (**d**) time histories of beam response (*black*) and controller (*red*) $\omega = 2.715$

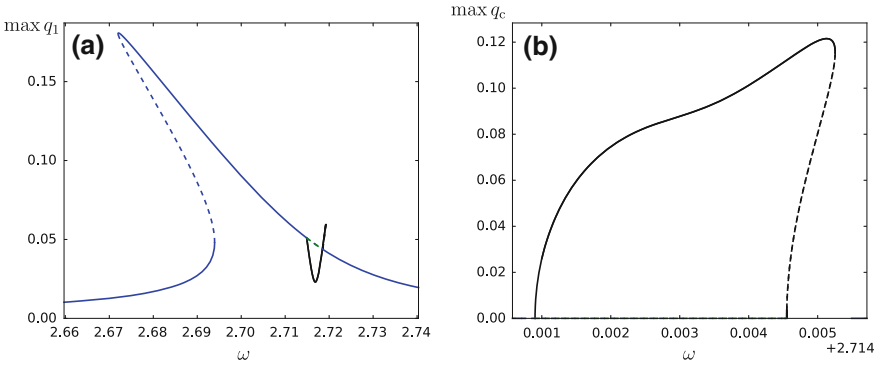

Fig. 7.17 Resonance curves of the beam (**a**) and controller (**b**) for selected values of gain $g_1 = 1$, $g_2 = 0.12$; $\rho = 0.005$, $\mu_0 = 0$, $J_h = 1$

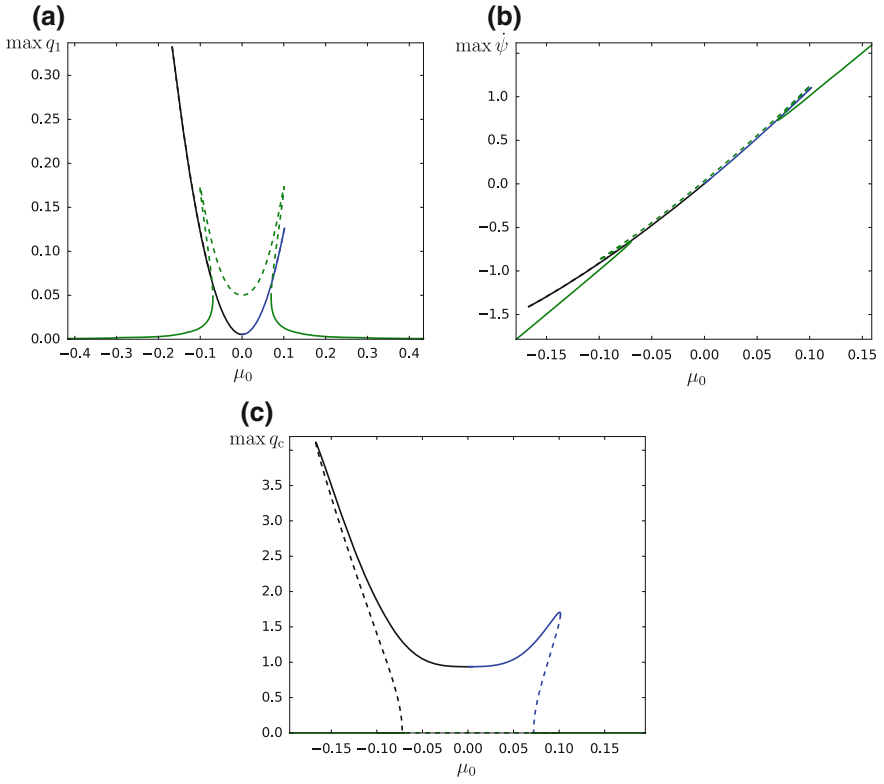

Fig. 7.18 Bifurcation diagram against μ_0 parameter for a nonlinear hub-beam model forced by torque with constant and periodic components, $\mu = \mu_0 + \rho \cos \omega t$, and nonlinear control, (**a**) beam displacement, (**b**) hub angular velocity and (**c**) controller response; $\rho = 0.005$, $J_h = 1$, $\omega = 2.715$, $g_1 = 0.01$, $g_2 = 1$

stiffening due to centrifugal load. Eventually, the system response characteristic is shifted to higher frequency values.

To check the effectiveness of the controller for a fully rotating structure, we keep the already agreed values of controller gains g_1 and g_2 and vary the μ_0 component of the torque. Outcomes of numerical simulations are presented in Fig. 7.18. Studying the beam response curve (plot (a)) one observes the activation of the controller results in the significant reduction of beam vibrations around the $\mu_0 = 0$ value—see also Fig. 7.11a for comparison. For the absolute values of μ_0 close to 0.1 and higher the postulated control strategy is not effective due to the significant stiffening effect and expected de-tuning of the controller with respect to the altered natural frequency of the system. Meanwhile, the hub response is not affected by the control unit, especially around the $\mu_0 = 0$ value (Fig. 7.18b). Interesting observation can be made with respect to the controller signal. In the range of $\mu_0 \in \langle -0.05, 0.05 \rangle$ (corresponds

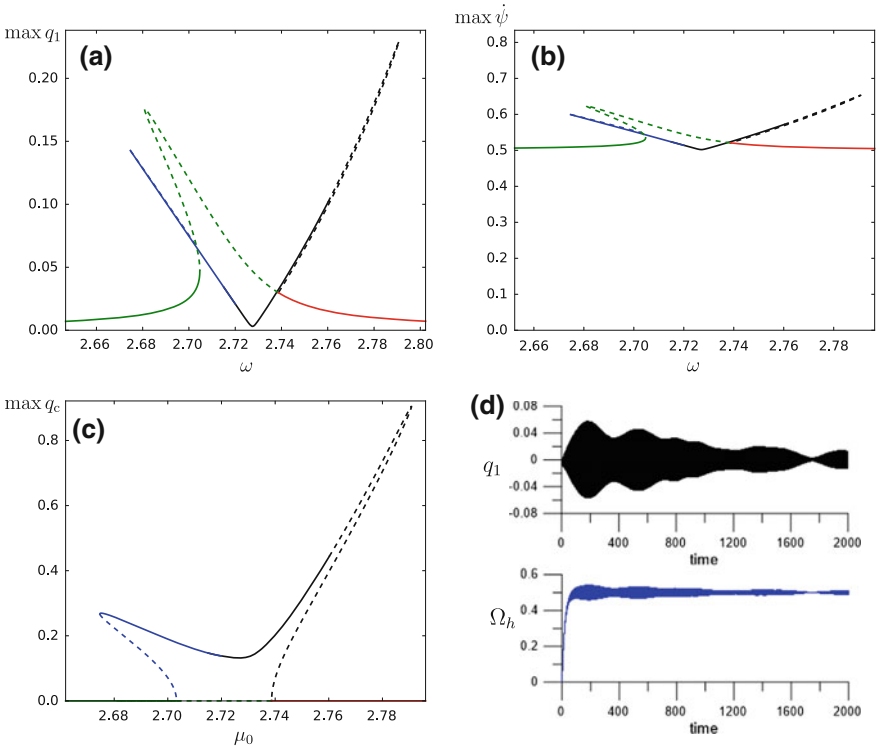

Fig. 7.19 Resonance curves around the first natural frequency with activated NSC for (**a**) the beam, (**b**) the hub, (**c**) the controller, $g_1 = 0.5$, $g_2 = 1$, $\rho = 0.005$, $\mu_0 = 0.05$, and (**d**) time histories of beam response (*black*) and hub response (*blue*) $\omega = 2.73$

to rotational speed varied from -1770 rpm to $+1770$ rpm) its magnitude remains stable and on almost the same level—plateau in Fig. 7.18c.

To confirm the above given outcomes the subsequent simulation is performed for the specific case of $\mu_0 = 0.05$ and keeping the torque amplitude $\rho = 0.005$. These settings make the hub to rotate with instantaneous speed oscillating about an average value of 1770 rpm expressed in physical units. Resonance curves of the hub-beam system are presented in Fig. 7.19. Due to the rotation the natural frequency of the structure is slightly shifted into higher frequencies comparing to the system performing oscillations about neutral position (Fig. 7.16).

Another observation is that a part of the resonance branch of the controller (Fig. 7.19c) and, correspondingly, of the beam and the hub becomes unstable as well (Fig. 7.19a, b). This effect can lead to dangerous phenomena if the controller is not properly tuned or gets out of tune while operating. However, around the resonance zone, oscillations are suppressed very well. Time histories of the beam and the hub response for $\omega = 2.73$ are presented in Fig. 7.19d by black and blue colours, respectively.

Considering the given results we may conclude that the proposed saturation strategy is also effective if the structure performs full rotation. However, special care shall be devoted to precise controller tuning to avoid system operation in unstable zones.

7.4 Conclusions and Final Comments

In this research we consider a nonlinear adaptive control of the rotating hub-beam structure using the saturation phenomenon. The aim of the control is to suppress coupled bending-torsional vibrations of the composite thin-walled beam made of CAS laminate with an embedded piezoceramic material exhibiting nonlinear constitutive relation. The excitation of the structure is provided by the driving torque expressed as a sum of its mean value and a periodic component. A two-to-one internal-resonance condition is maintained between the plant and the controller to fully exploit the effectiveness of the strategy. The mathematical model of the system under consideration has been derived directly from previous authors' papers [8, 10].

The discussed structure has been investigated for possible levels of original system simplifications. In subsequent simulations the following specific cases have been considered: (a) a fully linear model neglecting all beam interactions present in the governing equation, (b) a nonlinear model of the uncontrolled structure with independent analysis of nonlinearities due to the coupling of hub and beam motions and due to nonlinear constitutive characteristics of the PZT element, (c) control of the nonlinear system subjected to periodic zero-mean value driving torque, and (d) control of the nonlinear system performing the full rotation.

Obtained results of numerical simulations prove the applied nonlinear control to be a robust and effective method for beam vibration suppression in near-by resonance zones for a non-rotating as well as rotating structure. It is shown that vibration of the beam can be suppressed to similar levels independently of the model simplification degree presuming the condition of proper controller tuning is preserved. However, significant differences in the width of vibration suppression zones are observed for the studied subcases.

Performed numerical tests allow to conclude the system is sensitive to the feedback gain. In its lower range of magnitude values the response of the controller increases rapidly, while for higher ones the impact is much less pronounced. On the other hand, the control gain is shown to be inversely proportional to the controller output and high amplitudes of the controller may be expected for low values of the gain g_1. Moreover, it is observed the increase of any gains results in the controller response asymptotically approaching a limit value. Thus, above a certain thresholds, gains changes have no effect on the controller response.

While discussing performed tests it is been highlighted that the hub-beam assembly has to be considered as a whole system since the hub mass moment of inertia has an essential impact on natural frequencies of the structure. If the controller is tuned in a classical way, i.e. considering only dynamics of a separated non-rotating cantilever beam, the undesirable results are obtained. The controller is activated

within an improper and extremely narrow zone; moreover an additional resonance with large amplitudes is observed. The above recommendation is referred also to a nonlinear problem that requires an adaptive frequency-tuning mechanism, because of the reported softening characteristic of the system response.

The obtained results prove the possible reduction of complex vibration modes that exhibit strong coupling of torsion and bending deformations resulting from the circumferentially asymmetric stiffness (CAS) lamination scheme just by one active element.

Acknowledgements The work is financially supported by grant DEC–2012/07/B/ST8/03931 from the Polish National Science Centre.

References

1. Arafa, M., Baz, A.: On the nonlinear behavior of piezoelectric actuators. J. Vib. Control **10**(3), 387–398 (2004)
2. Ashour, O.N., Nayfeh, A.H.: Nonlinear control of plate vibrations. In: AIAA/ASME/ASCE/AHS/ASC Structures, Structural Dynamics, and Materials Conference, vol. AIAA-2001–1233, American Institute of Aeronautics and Astronautics, pp. 400–410 (2001)
3. Eissa, M., El-Ganaini, W., Hamed, Y.S.: Saturation, stability and resonance of non-linear systems. Phys. A: Stat. Mech. Appl. **356**(2–4), 341–358 (2005)
4. Gatti, C.D., Ramirez, J.M., Machado, S.P., Febbo, M.: Influence of nonlinear constitutive relations in unimorphs piezoelectric harvesters. J. Phys. Conf. Ser. **773**, 012093 (2016)
5. Georgiades, F., Latalski, J., Warminski, J.: Equations of motion of rotating composite beams with a nonconstant rotation speed and an arbitrary preset angle. Meccanica **49**(8), 1833–1858 (2014)
6. Joshi, S.P.: Non-linear constitutive relations for piezoceramic materials. Smart Mater. Struct. **1**(1), 80–83 (1992)
7. Kapuria, S., Yasin, M.Y.: A nonlinear efficient layerwise finite element model for smart piezolaminated composites under strong applied electric field. Smart Mater. Struct. **22**(5), 055021 (2013)
8. Latalski, J.: Modelling of a rotating active thin-walled composite beam system subjected to high electric fields. In: Naumenko, K., Assmus, M. (eds.) Advanced Methods of Continuum Mechanics for Materials and Structures, vol. 60 of Advanced Structural Materials, pp. 435–456. Springer, Singapore (2016)
9. Latalski, J., Bochenski, M., Warminski, J.: Control of bending-bending coupled vibrations of a rotating thin-walled composite beam. Arch. Acoust. **39**(4), 605–613 (2015)
10. Latalski, J., Warminski, J., Rega, G.: Bending-twisting vibrations of a rotating hub-thin-walled composite beam system. Math. Mech. Solids. doi:10.1177/1081286516629768, on-line March 3rd (2016)
11. Leadenham, S., Erturk, A.: Unified nonlinear electroelastic dynamics of a bimorph piezoelectric cantilever for energy harvesting, sensing, and actuation. Nonlinear Dyn. **79**(3), 1727–1743 (2015)
12. Oates, W.S., Wang, H., Sierakowski, R.L.: Unusual field-coupled nonlinear continuum mechanics of smart materials. J. Intell. Mater. Syst. Struct. **23**(5), 487–504 (2012)
13. Orivuori, J., Zenger, K.: Comparison and performance analysis of some active vibration control algorithms. J. Vib. Control **20**(1), 94–130 (2014)
14. Oueini, S.S., Nayfeh, A.H., Golnaraghi, M.F.: A theoretical and experimental implementation of a control method based on saturation. Nonlinear Dyn. **13**(2), 189–202 (1997)

15. Oueini, S.S., Nayfeh, A.H., Pratt, J.R.: A nonlinear vibration absorber for flexible structures. Nonlinear Dyn. **15**(3), 259–282 (1998)
16. Pai, P.F., Wen, B., Naser, A.S., Schulz, M.J.: Structural vibration control using PZT patches and non-linear phenomena. J. Sound Vib. **215**(2), 273–296 (1998)
17. Parashar, S.K., Wagner, U.V., Hagedorn, P.: Finite element modeling of nonlinear vibration behavior of piezo-integrated structures. Comput. Struct. **119**, 37–47 (2013)
18. Pasquali, M., Gaudenzi, P.: A nonlinear formulation of piezoelectric plates. J. Intell. Mater. Syst. Struct. **23**(15), 1713–1723 (2012)
19. Priya, S., Viehland, D., Carazo, A.V., Ryu, J., Uchino, K.: High-power resonant measurements of piezoelectric materials: Importance of elastic nonlinearities. J. Appl. Phys. **90**(3), 1469 (2001)
20. Reddy, J.N.: On laminated composite plates with integrated sensors and actuators. Eng. Struct. **21**(7), 568–593 (1999)
21. Saaed, T.E., Nikolakopoulos, G., Jonasson, J.E., Hedlund, H.: A state-of-the-art review of structural control systems. J. Vib. Control **21**(5), 919–937 (2015)
22. Saeed, N.A., El-Ganini, W.A., Eissa, M.: Nonlinear time delay saturation-based controller for suppression of nonlinear beam vibrations. Appl. Math. Modell. **37**(20–21), 8846–8864 (2013)
23. Saguranrum, S., Kunz, D.L., Omar, H.M.: Numerical simulations of cantilever beam response with saturation control and full modal coupling. Comput. Struct. **81**(14), 1499–1510 (2003)
24. Silva, L.L., Savi, M.A., Monteiro, P.C. C., Netto, T.A.: On the nonlinear behavior of the piezoelectric coupling on vibration-based energy harvesters. Shock Vib. **2015**, 1–15 (2015)
25. Stanton, S.C., Erturk, A., Mann, B.P., Inman, D.J.: Nonlinear piezoelectricity in electroelastic energy harvesters: modeling and experimental identification. J. Appl. Phys. **108**(7), 074903 (2010)
26. Thakkar, D., Ganguli, R.: Induced shear actuation of helicopter rotor blade for active twist control. Thin-Walled Struct. **45**(1), 111–121 (2007)
27. Tiersten, H.F.: Electroelastic equations for electroded thin plates subject to large driving voltages. J. Appl. Phys. **74**(5), 3389–3393 (1993)
28. Vadiraja, D.N., Sahasrabudhe, A.D.: Vibration analysis and optimal control of rotating pretwisted thin-walled beams using MFC actuators and sensors. Thin-Walled Struct. **47**(5), 555–567 (2009)
29. Wagner, U.v., Hagedorn, P.: Piezo-beam system subjected to weak electric field: experiments and modelling of non-linearities. J. Sound Vib. **256**:5, 861–872 (2002)
30. Warminski, J., Bochenski, M., Jarzyna, W., Filipek, P., Augustyniak, M.: Active suppression of nonlinear composite beam vibrations by selected control algorithms. Commun. Nonlinear Sci. Numer. Simul. **16**(5), 2237–2248 (2011)
31. Warminski, J., Cartmell, M.P., Mitura, A., Bochenski, M.: Active vibration control of a nonlinear beam with self- and external excitations. Shock Vib. **20**(6), 1033–1047 (2013)
32. Warminski, J., Latalski, J.: Saturation control for a rotating thin-walled composite beam structure. Procedia Eng. **144**, 713–720 (2016)
33. Yang, J.-S.: Equations for the extension and flexure of electroelastic plates under strong electric fields. Int. J. Solids Struct. **36**(21), 3171–3192 (1999)
34. Yang, J.-S.: Piezoelectric transformer structural modeling—a review. IEEE Trans. Ultrason. Ferroelectr. Freq. Cont. **54**(6), 1154–1170 (2007)

Chapter 8
Nonlinear Vibrations of a Shallow Arch Subject to Resonant and Low Harmonic Frequency Excitations Under 1:1 Internal Resonance

Abdelbassit Chtouki, Faouzi Lakrad and Mohamed Belhaq

Abstract In the present work the nonlinear dynamics of a two degree of freedom shallow arch model, excited by resonant external harmonic forcing and subject to an imposed slow harmonic motion of its support, are investigated. The case of 1:1 internal resonance between the first and the second bending modes is studied. The charts of behaviors are obtained analytically using the multiple scales method, both in the presence and the absence of the slow excitation, and they are validated numerically. It is shown that the low parametric frequency excitation triggers the existence of periodic bursters in vicinity of the boundaries between the different dynamics of the arch.

8.1 Introduction

Arches are widely used in civil, mechanical and aerospace engineering [1]. They are also used in MEMS switches, actuators, resonators [2], band-pass filters [3] and in energy harversting [4]. Arches are characterized, compared to straight beams, by their initial curvature, strength and the bi-stability behavior or the snap-through phenomenon.

Arches can be classified following their shallowness parameter [5], that is the sag to the span ratio, as shallow or non-shallow. In the present paper only shallow arches, i.e., small shallowness parameter, are considered.

A. Chtouki · F. Lakrad · M. Belhaq (✉)
Laboratory of Renewable Energy and Dynamics of Systems, Faculty of Sciences Ain Chock,
University Hassan II Casablanca, 5366 Maarif, Casablanca, Morocco
e-mail: mbelhaq@yahoo.fr

A. Chtouki
e-mail: Chtouki@gmail.com

F. Lakrad
e-mail: lakrad@hotmail.com

M. Belhaq (ed.), *Recent Trends in Applied Nonlinear Mechanics and Physics*,
Springer Proceedings in Physics 199, https://doi.org/10.1007/978-3-319-63937-6_8

Many authors studied the nonlinear dynamics of shallow arches under various types of loadings and internal resonances. Tien et al. [6, 7] investigated global bifurcations, using a Melnikov method, to determine the chaos occurrence in a two degree-of-freedom (dof) model of a shallow arch subject to a static and a resonant harmonic loading under 1:2 and 1:1 internal resonances.

In the framework of the effect of low frequency excitations on shallow arches, Lakrad and Schiehlen [8] studied the effect of a slowly varying parametric excitation on a single dof shallow arch model. Periodic bursters and chaos were observed and analyzed using a Poincaré map and the Melnikov method. It is worth pointing out that from geometrical point of view periodic bursters can be seen as generalized heteroclinic orbits, see [5] for more mathematical details. It was shown in [9] that a necessary condition for the occurrence of periodic bursters is that the slow excitation is parametric.

Lakrad and coworkers [10, 11] investigated analytically and numerically nonlinear dynamics of a two dof model of a shallow arch with 1:2 internal resonance and subject to a resonant external harmonic forcing and to a very slow harmonic imposed displacement of one of its supports. Periodic bursters are found to exist in the boundaries of the instability regions. Various bursters involving fixed points, quasi-periodic and chaotic solutions are found.

In the present work, we investigate the nonlinear dynamics of the same reduced order model of the shallow arch as [10, 11], in the presence of 1:1 internal resonance and the principal external resonance.

The paper is organized as follows. In the second section the mathematical model of flexural vibrations of the shallow arch is presented. Then, a two dof model is obtained using the Galerkin method through the projection of the equation of motion over the two first bending modes of the arch. In the third section, the effects of the initial rise and the static load on the static equilibria are investigated. In the fourth section, the method of multiple scales is applied around the unbuckled static equilibrium to determine the slowly modulated amplitudes and phases equations. Finally, charts of behaviors are determined, especially the zones of existence of periodic bursters. Analytical approximations of solutions are computed and comparisons to numerical simulations are provided.

8.2 Mathematical Model

We consider a double-hinged shallow arch having an unloaded shape $w_0(x)$, with $x \in [0, L]$, see Fig. 8.1. It is subjected to a lateral sinusoidal loading $P(x, t)$, consisting in a static and a harmonic loadings, and to an imposed horizontal slow harmonic motion of its support $u(L, t)$.

Our mathematical model obeys the following assumptions [5]

- Small change of curvature.
- Large extensional strain.

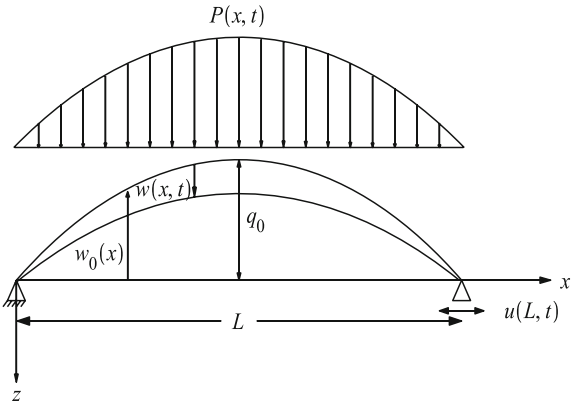

Fig. 8.1 The shallow arch model

- Negligible longitudinal inertia.
- Constant elongation along the axis.

The nonlinear equation of motion governing the inplanar lateral deflection $w(x,t)$ of the shallow arch is given by the following partial differential equation [6]

$$m\ddot{w} + c\dot{w} + EIw'''' - \frac{EA}{L}(w_0'' + w'')\Big[u(L,t) + \frac{1}{2}\int_0^L (w'^2 + 2w_0'w')\mathrm{d}x\Big] = P(x,t) \tag{8.1}$$

where the dot and the prime denote the derivatives with respect to time t and to the variation of the length x, respectively. The material and geometric properties of the arch are labelled as follows

m : the mass per unit length	c : the viscous damping coefficient
A : the cross-sectional area	I : the second moment of the cross-section
E : the Young's modulus	L : the projected length of the arch

The unloaded initial shape of the arch is taken sinusoidal and the excitations are as follows

$$\text{Unloaded shape} \qquad w_0(x) = -q_0 \sin(\frac{\pi x}{L}) \tag{8.2}$$

$$\text{Lateral loading} \qquad P(x,t) = (p_0 + \rho\cos(\nu t))\sin(\frac{\pi x}{L}) \tag{8.3}$$

$$\text{Imposed displacement} \qquad u(L,t) = H\cos(\Omega t) \tag{8.4}$$

where q_0 is the initial rise, p_0 is the static loading, ρ and ν represent amplitude and frequency of the lateral loading, respectively, while H and Ω represent amplitude and frequency of periodic motion of the end point of the arch, respectively. The

arch is doubly-hinged, and consequently it is subjected to the following boundary conditions:

$$w(0,t) = w(L,t) = 0, \qquad w''(0,t) = w''(L,t) = 0 \tag{8.5}$$

The Galerkin method is used to reduce the partial differential equation (8.1) governing the dynamics of the shallow arch to a set of ordinary differential equations. This is done by projecting (8.1) on appropriate shape functions. In our case the linear normal modes of undamped flexural vibrations of simply supported beams are used. Thus, the transverse motion $w(x,t)$ of the arch is approximated by the following expression

$$w(x,t) = \sum_{n=1}^{N} q_n(t) \sin(\frac{n\pi x}{L}) \tag{8.6}$$

For convenience, we introduce the following non-dimensional variables:

The new time scale	$t^* = (\frac{\pi}{L})^2 \sqrt{\frac{EI}{m}} t$
The viscous damping parameter	$\beta = \frac{cL^2}{\pi^2 \sqrt{EIm}}$
The radius of gyration of the cross section	$r = \sqrt{\frac{I}{A}},$
The initial rise parameter	$q_0^* = \frac{q_0}{2r},$
The static loading parameter	$\lambda_0 = \frac{p_0}{2rEI} (\frac{L}{\pi})^4$
The amplitude of the imposed displacement	$h = \frac{HL}{r^2 \pi^2}$
The frequency of the imposed displacement	$\Omega^* = \frac{\Omega L^2}{\pi^2} \sqrt{\frac{m}{EI}}$
The amplitude of the harmonic loading	$\rho^* = \frac{\rho}{2rEI} (\frac{L}{\pi})^4$
The frequency of the harmonic loading	$\nu^* = \frac{\nu L^2}{\pi^2} \sqrt{\frac{m}{EI}}$
Straightened amplitude of the first mode	$Q_1 = \frac{q_1}{2r} - q_0^*$
Amplitude of the nth mode with $n \neq 1$	$Q_n = \frac{q_n}{2r}$
The slow time scale	$\tau = \Omega^* t^*$

To obtain the reduced order model, (8.6) is substituted into (8.1). The outcome is then multiplied by the shape function and is integrated over the arch span.

In what follows the stars will be omitted for simplicity of notations. Therefore, the non-dimensional equations of motion describing the evolution of the amplitudes of the nth mode of the shallow arch, with $n \in \{1, ..., N\}$, can be written as:

$$\ddot{Q}_n + \beta \dot{Q}_n + n^2 Q_n [n^2 - q_0^2 + h\cos(\tau) + \sum_{j=1}^{N} j^2 Q_j^2] = \delta_{n1}(\lambda_0 - q_0 + \rho\cos(\nu t)) \tag{8.7}$$

The low frequency $\Omega = \mathcal{O}(\varepsilon^k)$ with the integer $k \geq 2$ and ε is a bookeeping small parameter, see [10] for more details. Furthermore, δ_{n1} is the Kroneker delta function, with $\delta_{n1} = 1$ if $n = 1$ and vanishes otherwise.

In the set of coupled differential equation (8.7) there exist two kinds of nonlinearities: (i) quadratic nonlinearities that are caused by the static load λ_0 and the initial curvature q_0; (ii) cubic nonlinearities caused by the large extensional strain. Only the mode 1 is directly excited by the external harmonic excitation and all modes have parametric slow harmonic excitation caused by the base motion.

In the present work, the approximated solution (8.6) is truncated to two fundamental normal modes i.e., $N = 2$. Thus, (8.7) gives the following two equations

$$\ddot{Q}_1 + \beta \dot{Q}_1 + (1 + h\cos(\tau))Q_1 + Q_1(Q_1^2 - q_0^2 + 4Q_2^2) + q_0 - \lambda_0 = \rho\cos(\nu t) \tag{8.8}$$

$$\ddot{Q}_2 + \beta \dot{Q}_2 + 4(4 + h\cos(\tau))Q_2 + 4Q_2(Q_1^2 - q_0^2 + 4Q_2^2) = 0 \tag{8.9}$$

The generalized coordinates Q_1 and Q_2 are the amplitudes of the symmetric and the asymmetric modes, respectively.

8.3 Static Analysis

The static equilibria of the arch are computed from (8.8) and (8.9) by dropping the time derivatives and excitations. Two types of solutions are found: the first type corresponds to $Q_2 = 0$ and the second one to $Q_2 \neq 0$. The first type solutions are ruled by the following cubic algebraic equation

$$Q_1^3 + Q_1(1 - q_0^2) + q_0 - \lambda_0 = 0 \tag{8.10}$$

This equation can have either one or three real solutions depending on the parameters of control q_0 and λ_0. In what follows the unbuckled stable static equilibrium will be noted as $Q_1 = \eta_0$. It is obvious that when $q_0 = \lambda_0$, the static equilibria will be ruled by a Pitchfork bifurcation, as was studied in [8].

In Fig. 8.2 are shown the number of static equilibria in the plane (q_0, λ_0). Zones 1 and 2 correspond to $Q_2 = 0$ and to the existence of one stable static solution of

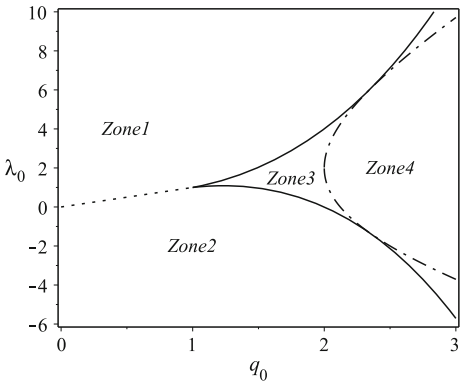

Fig. 8.2 Number of static equilibria in the plane (q_0, λ_0). In zones 1 and 2: existence of one static solution that is stable corresponding to $Q_2 = 0$. This solution corresponds to a buckled configuration in zone 1 and to an unbuckled solution in zone 2. In Zone 3: existence of three solutions with $Q_2 = 0$ with two that are stable. In zone 4: coexistence of equilibria of zone 3 and two unstable static solutions with $Q_2 \neq 0$

(a) $\lambda_0 = -0.8$ (b) $\lambda_0 = 0.5$ (c) $\lambda_0 = 2$

Fig. 8.3 Static configurations for $q_0 = 0.8$ and for various static load λ_0. The *thick* and the *thin lines* correspond to statically deformed arch and undeformed arch, respectively. Figures **a** and **b** belong to zone 2 and Figure **c** belongs to zone 1

(a) $\lambda_0 = -1$ (b) $\lambda_0 = 0.9$ (c) $\lambda_0 = 2$

Fig. 8.4 Static configurations for $q_0 = 1.5$ and for various static load λ_0. *Thin lines* corresponds to the undeformed arch. *Continuous thick* and *dotted lines* correspond to stable and unstable statically deformed arch, respectively. Figures **a** and **b** belong to zone 2 and Figure **c** belongs to zone 3

Q_1. This latter corresponds to a buckled state in zone 1 and to an unbuckled solution in zone 2, see Fig. 8.3 for the deformed configurations of the arch for $q_0 = 0.8$ and various static loading λ_0. It is worth pointing out that increasing initial rise q_0 of the arch increases the critical static loading λ_0 that causes buckling.

The zone 3 corresponds to $Q_2 = 0$ and three static solutions of Q_1. Two of these three equilibria are stable and are the buckled and the unbuckled configurations. In Fig. 8.4 are shown the static equilibria configurations of the arch for $q_0 = 1.5$ and various static loading λ_0. The boundaries of zone 3 with zones 1 and 2 in the plane

(q_0, λ_0) are given by

$$\lambda_0 = q_0 \pm \frac{2}{9}\sqrt{3q_0^6 - 9q_0^4 + 9q_0^2 - 3} \tag{8.11}$$

In zone 4, there is coexistence of the zone 3 static equilibria and two unstable equilibria corresponding to

$$Q_1 = (q_0 - \lambda_0)/3; \;\; Q_2 = \pm\frac{1}{2}\sqrt{q_0^2 - 4 - Q_1^2} = \pm\frac{1}{6}\sqrt{8q_0^2 + 2q_0\lambda_0 - \lambda_0^2 - 36} \tag{8.12}$$

The boundaries of the zone 4 in the plane (q_0, λ_0) are given by

$$\lambda_0 = q_0 \pm \sqrt{9q_0^2 - 36} \tag{8.13}$$

In the rest of this paper, we will work around the unbuckled stable static equilibrium $(Q_1 = \eta_0, Q_2 = 0)$ far from the snap-through bifurcation.

8.4 Perturbation Analysis

We perturb the variables (Q_1, Q_2) in (8.8) and (8.9) around the stable unbuckled static solution $(\eta_0, 0)$. Thus,

$$Q_1(t) = \eta_0 + \varepsilon x_1(t), \qquad Q_2(t) = \varepsilon x_2(t) \tag{8.14}$$

where ε is a small positive parameter. In order to use the multiple scales method [12], parameters of control are scaled as follows: $\rho = \varepsilon^3\tilde{\rho}$, $h = \varepsilon^2\tilde{h}$, $\beta = \varepsilon^2\tilde{\beta}$.
Equations (8.8) and (8.9) up to the order $\mathcal{O}(\varepsilon^3)$ become

$$\begin{aligned}\ddot{x}_1 + \omega_1^2 x_1 &= -\varepsilon(\tilde{h}\eta_0\cos(\tau) + 4\eta_0 x_2^2 + 3\eta_0 x_1^2) \\ &\quad - \varepsilon^2(\tilde{\beta}\dot{x}_1 + \tilde{h}\cos(\tau)x_1 + x_1^3 + 4x_1x_2^2 + \tilde{\rho}\cos(\nu t)) \qquad (8.15)\\ \ddot{x}_2 + \omega_2^2 x_2 &= -\varepsilon(8\eta_0 x_1 x_2) - \varepsilon^2(\tilde{\beta}\dot{x}_2 + 4\tilde{h}\cos(\tau)x_2 + 4x_1^2x_2 + 16x_2^3) \qquad (8.16)\end{aligned}$$

The linearized frequencies ω_1 and ω_2 corresponding to the first and second modes are given by

$$\omega_1 = \sqrt{3\eta_0^2 + 1 - q_0^2} \qquad ; \qquad \omega_2 = \sqrt{4\eta_0^2 + 16 - 4q_0^2} \tag{8.17}$$

The two frequencies depend solely on q_0 and λ_0 since η_0 depends on these two control parameters. In the absence of the static load, i.e., $\lambda_0 = 0$, $\eta_0 = -q_0$ and

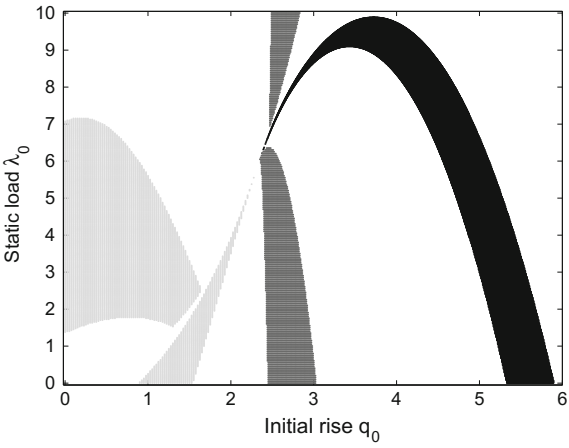

Fig. 8.5 Various internal resonances, relating ω_1 and ω_2, in the plane (q_0, λ_0). The *black zone* corresponds to 2:1 resonance; the strong *grey zone* to 1:1 resonance and the *light grey zone* to 1:2 resonance

$\omega_1 = \sqrt{1 + 2q_0^2}$ and $\omega_2 = 4$. This result is in agreement with [13] where it was shown that, in the case of a double-hinged shallow arch, the only natural frequency that is affected by the initial rise q_0 is the first one. In fact, increasing the initial rise q_0, i.e., tending towards the non-shallow arch case, leads to the increase of the frequency of the first mode, that is asymmetric, till reaching the first overall point where the symmetric mode becomes the fundamental one, see [13] for more details.

Indeed, the initial rise q_0 and the static load parameter λ_0 can be used to tune the natural frequencies ω_1 and ω_2 in order to realize various internal resonances. Figure 8.5 shows various zones of internal resonances in the plane (q_0, λ_0). These regions are computed by setting

$$p - 0.1 \leq \frac{\omega_1}{\omega_2} \leq p + 0.1; \qquad \text{with} \qquad p = \frac{1}{2}, 1, 2. \tag{8.18}$$

In Fig. 8.5, the black zone corresponds to 2:1 internal resonance. The light and strong grey zones correspond to 1:2 and 1:1 internal resonances, respectively. For more results and discussions about internal resonances in mechanical structures see [14].

In what follows, we shall perform the analysis in the strong grey zone i.e., 1:1 internal resonance in the presence of the principal external resonance

$$\omega_1 = \omega_2 + \sigma_1 \qquad ; \qquad \nu = \omega_2 + \sigma_2 \tag{8.19}$$

where $\sigma_i = \varepsilon\tilde{\sigma}_i$, with $i = 1, 2$, are detuning parameters.

Using the multiple scales method [12] one can eliminate the fast time scale dependence. This method ultimately results in the following modulation equations of amplitudes a_1, a_2 and phases of the first and second modes, respectively

$$
\begin{aligned}
\dot{a}_1 &= -\frac{\beta}{2}a_1 - \frac{\rho}{2\omega_1}\sin(\gamma_1) - \frac{k_1}{8\omega_1}a_1a_2^2\sin(2\gamma_1 - 2\gamma_2)\\
a_1\dot{\gamma}_1 &= (\sigma_2 - \sigma_1)a_1 - \frac{\rho}{2\omega_1}\cos(\gamma_1) - \frac{k_2}{8\omega_1}a_1^3 - \frac{k_1}{8\omega_1}a_1a_2^2\cos(2\gamma_1 - 2\gamma_2)\\
&\quad - \frac{k_3}{8\omega_1}a_1a_2^2 - \frac{hX}{2\omega_1}a_1\cos(\tau)\\
\dot{a}_2 &= -\frac{\beta}{2}a_2 + \frac{k_4}{8\omega_2}a_1^2a_2\sin(2\gamma_1 - 2\gamma_2)\\
a_2\dot{\gamma}_2 &= \sigma_2a_2 - \frac{k_4}{8\omega_2}a_1^2a_2\cos(2\gamma_1 - 2\gamma_2) - \frac{k_5}{8\omega_2}a_2^3 - \frac{k_3}{8\omega_2}a_1^2a_2 - \frac{2hY}{\omega_2}a_2\cos(\tau)
\end{aligned}
\tag{8.20}
$$

Here we have considered the slowly varying parametric excitation as constant during the averaging process. In Appendix are listed the parameters X and Y that express the contribution of the low frequency base motion. The Appendix shows also the cubic nonlinearities parameters k_i, with $i = 1..5$.

By setting $u_1 = a_1\cos(\gamma_1)$; $v_1 = a_1\sin(\gamma_1)$; $u_2 = a_2\cos(\gamma_2)$; $v_2 = a_2\sin(\gamma_2)$, equations of modulations (8.20) can be written in Cartesian form as

$$
\begin{aligned}
\dot{u}_1 &= -\frac{\beta}{2}u_1 - (\sigma_2 - \sigma_1)v_1 + \frac{k_1}{4\omega_1}u_1u_2v_2 + \frac{Xh}{2\omega_1}\cos(\tau)v_1\\
&\quad + \frac{1}{8\omega_1}(k_1(v_2^2 - u_2^2) + k_2(u_1^2 + v_1^2) + k_3(u_2^2 + v_2^2))v_1\\
\dot{v}_1 &= -\frac{\beta}{2}v_1 + (\sigma_2 - \sigma_1)u_1 - \frac{k_1}{4\omega_1}v_1u_2v_2 - \frac{Xh}{2\omega_1}\cos(\tau)u_1\\
&\quad - \frac{1}{8\omega_1}(k_1(u_2^2 - v_2^2) + k_2(u_1^2 + v_1^2) + k_3(u_2^2 + v_2^2))u_1 - \frac{\rho}{2\omega_1}\\
\dot{u}_2 &= -\frac{\beta}{2}u_2 - \sigma_2v_2 + \frac{k_4}{4\omega_2}u_1v_1u_2 + \frac{2Yh}{\omega_2}\cos(\tau)v_2\\
&\quad + \frac{1}{8\omega_2}(k_3(u_1^2 + v_1^2) + k_5(u_2^2 + v_2^2) - k_4(u_1^2 - v_1^2))v_2\\
\dot{v}_2 &= -\frac{\beta}{2}v_2 + \sigma_2u_2 - \frac{k_4}{4\omega_2}u_1v_1v_2 - \frac{2Yh}{\omega_2}\cos(\tau)u_2\\
&\quad - \frac{1}{8\omega_2}(k_3(u_1^2 + v_1^2) + k_5(u_2^2 + v_2^2) + k_4(u_1^2 - v_1^2))u_2
\end{aligned}
\tag{8.21}
$$

The Cartesian form of the modulation equations is very useful in the stability analysis, especially in the case of the single mode i.e., $a_2 = 0$. An approximation of the solution of (8.8) and (8.9), up to order $\mathcal{O}(\varepsilon^2)$, is given by

$$Q_1(t) = \eta_0 + a_1\cos(\nu t - \gamma_1) + \frac{c_1}{2}a_2^2\cos(2\nu t - 2\gamma_2) + \frac{c_2}{2}a_1^2\cos(2\nu t - 2\gamma_1) + c_3(\frac{3a_1^2}{2} + 2a_2^2) - \frac{h\eta_0}{\omega_1^2}\cos(\Omega t) \tag{8.22}$$

$$Q_2(t) = a_2\cos(\nu t - \gamma_2) + \frac{d_1}{2}a_1a_2\cos(2\nu t - \gamma_1 - \gamma_2) + \frac{d_2}{2}a_1a_2\cos(\gamma_1 - \gamma_2) \tag{8.23}$$

8.5 Results and Discussions

In this section we will discuss the effects of the low frequency harmonic parametric excitation on the local dynamics of the shallow arch under both principal external and 1:1 internal resonances. Thus, we first present results corresponding to the case of the absence of the low frequency excitation i.e., $h = 0$. Then, the case of $h \neq 0$ will be discussed. In all the numerical applications, $q_0 = 2.52$, $\lambda_0 = 5$ and the damping coefficient $\beta = 0.03$. The unbuckled static position is ($\eta_0 = -2.03$, $Q_2 = 0$), the natural frequncies $\omega_1 = 2.653$ and $\omega_2 = 2.668$.

8.5.1 Absence of the Low Frequency Excitation i.e., $h = 0$

Steady state solutions of the modulation equations (8.20) can be obtained by eliminating all time dependences. In Fig. 8.6, we show the behavior chart of the steady state solutions of the modulation equations (8.20) in the external excitation parameters (ν, ρ) plane, in the absence of the base displacement i.e., $h = 0$. In what follows a single mode refers to ($a_1 \neq 0, a_2 = 0$) and the coupled mode to ($a_1 \neq 0, a_2 \neq 0$).

- The single mode solutions are obtained by solving the following sixth order algebraic equation

$$[(\sigma_2 - \sigma_1)a_1 - \frac{k_2}{8\omega_1}a_1^3]^2 + (\frac{\beta}{2}a_1)^2 - (\frac{\rho}{2\omega_1})^2 = 0 \tag{8.24}$$

- The coupled modes solutions exist when $a_1 \geq 2\omega_2\sqrt{\frac{\beta}{k_4}}$ and are obtained by solving the following two coupled algebraic equations

$$\frac{\beta^2}{4} + \left(\sigma_2 - \frac{k_5a_2^2}{8\omega_2} - \frac{k_3a_1^2}{8\omega_2}\right)^2 - \frac{k_4^2a_1^4}{64\omega_2^2} = 0 \tag{8.25}$$

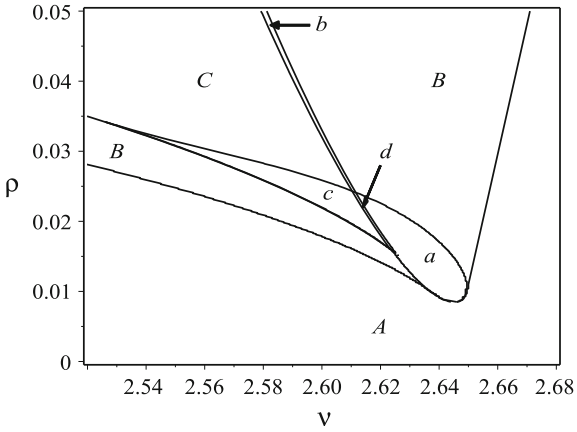

Fig. 8.6 Boundaries of dynamic instability of the modulation equations (8.20) in the external excitation parameters plane (ν, ρ) for $h = 0$. Region A, existence of one stable single mode. Region B, existence of one single and one coupled modes that are stable. Region C, existence of three single modes two among them are stable, and one stable coupled mode. Region a, existence of one unstable single mode and one stable coupled mode. Zones b and c, existence of three single modes with one of them stable, and one stable coupled mode. Region d, contains three unstable solutions of the single mode and one stable coupled mode

$$\left((\sigma_2-\sigma_1)a_1^2-\frac{k_2a_1^4}{8\omega_1}-\frac{k_3a_1^2a_2^2}{8\omega_1}-\frac{k_1\omega_2a_2^2}{k_4\omega_1}(\sigma_2-\frac{k_5a_2^2}{8\omega_2}-\frac{k_3a_1^2}{8\omega_2})\right)^2+\beta^2(\frac{a_1^2}{2}+\frac{k_1\omega_2a_2^2}{2\omega_1k_4})^2=\frac{a_1^2\rho^2}{4\omega_1^2} \tag{8.26}$$

For the considered external loading parameters ρ and ν, simple bifurcations, such as saddle-node and pitchfork bifurcations, are ruling the stability and the existence of various solutions. Eight various zones in the (ν, ρ)-plane summirize and explain bifurcations of steady state solutions of the amplitudes modulation equations (8.20), see Fig. 8.6. The determination of these zones is based mainly on the single modes bifurcations. Large regions are denoted by capital letters and the small regions with lower case letters.

Indeed, single modes exist always, since they are directly excited by the external loading, and at most three of them can coexist. The coupled modes have only one stable solution when they exist. They exist in all regions other than A.

In region A, there is existence of only one stable single mode. In region B, there is coexistence of one stable single mode and coupled modes. In region C coexistence of three single modes solutions with two among them that are stable. Region a corresponds to the existence of one unstable single mode. Zones b and c correspond to the existence of three single mode solutions with one of them stable. The small zone d contains three unstable solutions of the single mode.

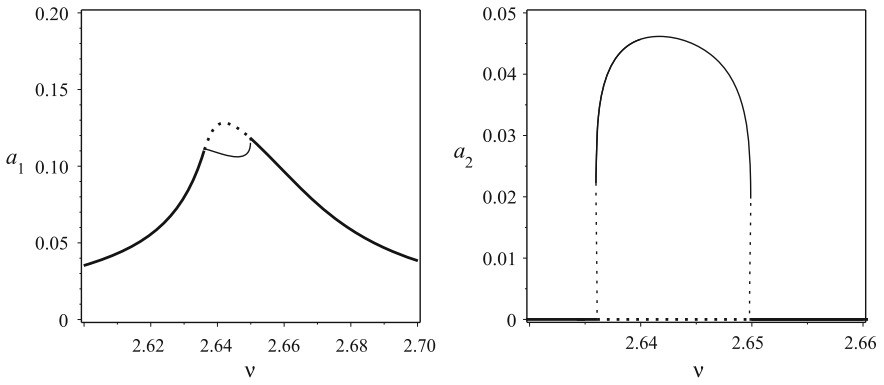

Fig. 8.7 Steady-state amplitudes a_1 (*left*) and a_2 (*right*) versus ν for $\rho = 0.0102$. When increasing ν, the visited regions are regions $A \rightarrow a \rightarrow A$. *Thick lines* correspond to single modes and *thin lines* to coupled modes. The *continuous lines* correspond to stable solutions and the *dashed one* to unstable solutions

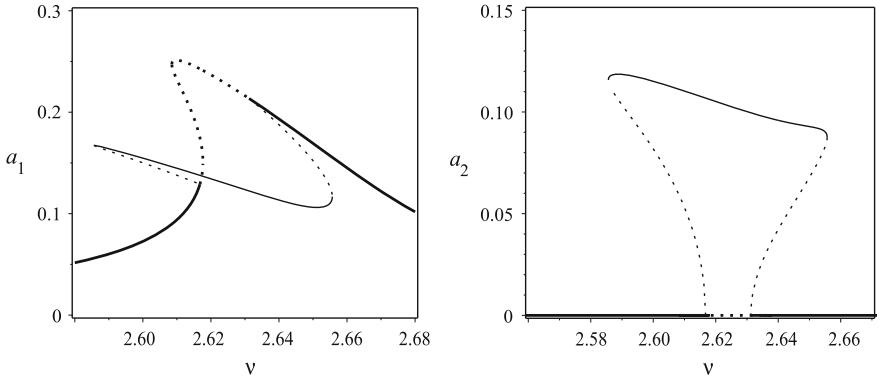

Fig. 8.8 Steady-state amplitudes a_1 (*left*) and a_2 (*right*) versus ν for $\rho = 0.02$. When increasing ν, the visited regions are regions $A \rightarrow B \rightarrow c \rightarrow d \rightarrow a \rightarrow B \rightarrow A$

Figures 8.7, 8.8, 8.9 and 8.10 show steady state amplitudes a_1 and a_2 versus the frequency of the harmonic excitation ν for various values of the amplitude of the harmonic excitation ρ. This latter is chosen such that when varying ν the dynamics will cross various regions that are shown in Fig. 8.6. The amplitudes corresponding to the single mode are plotted in thick lines and those corresponding to the coupled modes in thin lines. Moreover, the continuous and the dashed lines correspond to stable and unstable solutions, respectively. These figures where obtained by solving analytically and numerically (8.24)–(8.26). The bifurcation continuation package Auto [15] was also used. Thus, for instance, in Fig. 8.7, for $\rho = 0.0102$, the dynamics is crossing regions A, a and A. In Fig. 8.8, for $\rho = 0.02$, the dynamics is crossing successivelly in the following order: regions A, B, c, d, a, b and A.

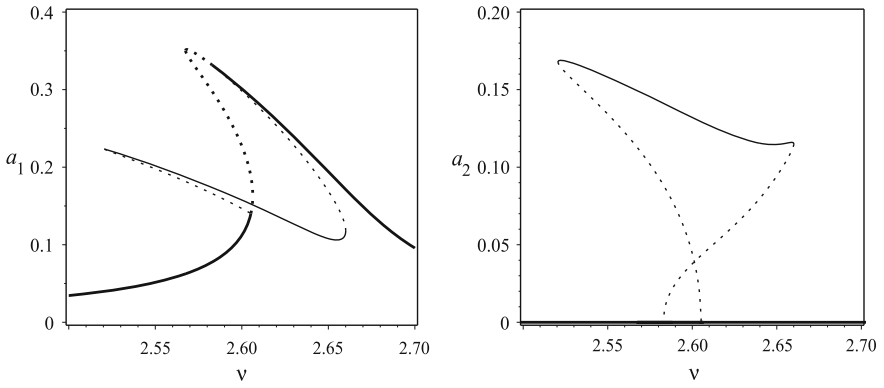

Fig. 8.9 Steady-state amplitudes a_1 (*left*) and a_2 (*right*) versus ν for $\rho = 0.028$. When increasing ν, the visited regions are regions $A \to B \to c \to C \to b \to B \to A$

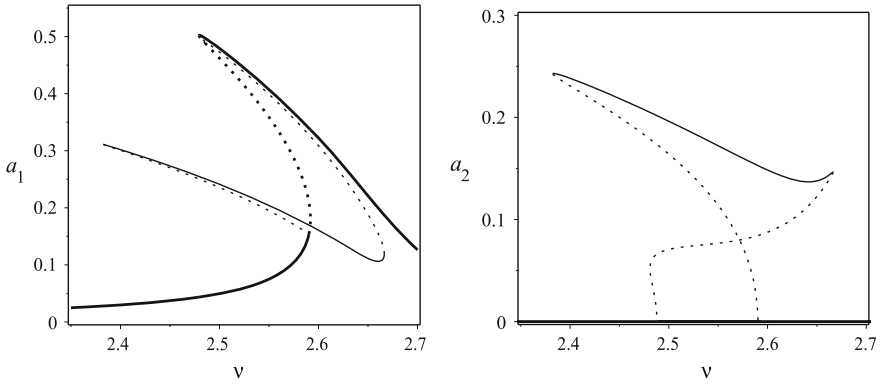

Fig. 8.10 Steady-state amplitudes a_1 (*left*) and a_2 (*right*) versus ν for $\rho = 0.04$. When increasing ν, the visited regions are regions $A \to C \to b \to B \to A$

8.5.2 *Effects of the Low Frequency Excitation*

In the presence of the low frequency parametric harmonic excitation, the equations of modulations (8.20) can be written as a slow-fast system

$$\varepsilon \dot{\mathbf{z}} = \mathbf{f}(\mathbf{z}, \tau); \qquad \dot{\tau} = 1 \tag{8.27}$$

where the state vector $\mathbf{z} = (a_1, \gamma_1, a_2, \gamma_2)$ and the dot is the derivative with respect to the very slow time scale $\tau = \Omega t$, with $\Omega = \mathcal{O}(\varepsilon^2)$. In the limit $\varepsilon \to 0$ one can compute the slow manifold given by $\mathcal{M} = \{(\mathbf{z}, \tau) : \mathbf{f}(\mathbf{z}, \tau) = \mathbf{0}\}$. It is composed of two types of quasi-static solutions:

- The single mode quasi-static solutions given by

$$(\frac{\rho}{2\omega_1})^2 = [(\sigma_2 - \sigma_1 - \frac{hX}{2\omega_1}\cos(\tau))a_1(\tau) - \frac{k_2}{8\omega_1}a_1(\tau)^3]^2 + (\frac{\beta}{2}a_1(\tau))^2 \tag{8.28}$$

$$a_2(\tau) = 0. \tag{8.29}$$

- The coupled modes quasi-static solutions are obtained by solving the following two coupled algebraic equations

$$\frac{\beta^2}{4} + (\sigma_2 - \frac{k_5 a_2^2}{8\omega_2} - \frac{k_3 a_1^2}{8\omega_2} - \frac{2hY\cos(\tau)}{\omega_2})^2 - \frac{k_4^2 a_1^4}{64\omega_2^2} = 0 \tag{8.30}$$

$$\beta^2(\frac{a_1^2}{2} + \frac{k_1\omega_2 a_2^2}{2\omega_1 k_4})^2 + ((\sigma_2 - \sigma_1)a_1^2 + \frac{hXa_1^2}{2\omega_1}\cos(\tau) - \frac{k_2 a_1^4}{8\omega_1} - \frac{k_3 a_1^2 a_2^2}{8\omega_1}$$
$$- \frac{k_1\omega_2 a_2^2}{k_4\omega_1}(\sigma_2 - \frac{k_5 a_2^2}{8\omega_2} - \frac{k_3 a_1^2}{8\omega_2} - \frac{2hY\cos(\tau)}{\omega_2}))^2 = \frac{a_1^2\rho^2}{4\omega_1^2} \tag{8.31}$$

In Fig. 8.11, we show the evolution of the chart behaviors of the modulation equations (8.20) for $h = 0.01$ and $h = 0.02$ in the plane of external excitation parameters (ν, ρ). The behaviors of the solutions in the big zones A, B and C are similar to Fig. 8.6. However, instead of fixed points we deal now with periodic solutions of the modulation equations. Consequently, in regions A, B and C the solutions of the

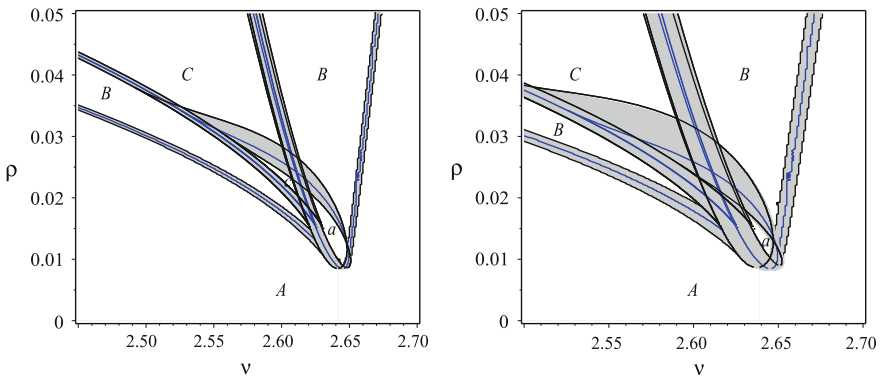

(a) $h = 0.01$ (b) $h = 0.02$

Fig. 8.11 Boundaries of dynamic instability of the modulation equations (8.20) in the external excitation parameters plane (ν, ρ) for **a** $h = 0.01$; and **b** $h = 0.02$. The *blue lines* correspond to the case $h = 0$. The *grey zones* correspond to the presence of periodic bursters. See Fig. 8.6 for the explaination of the *white zones*

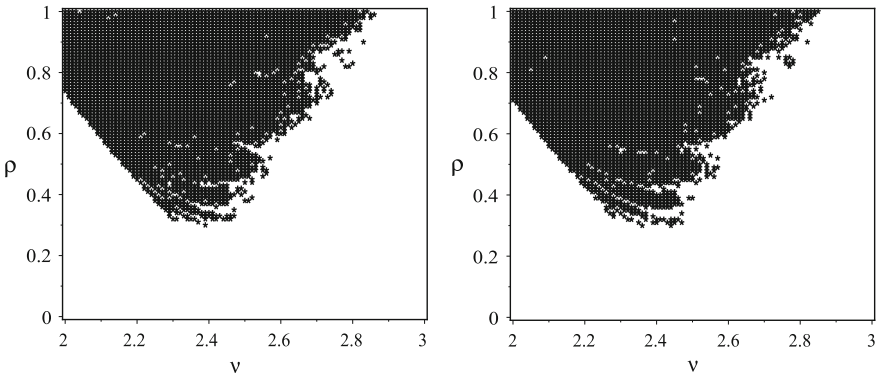

(a) $h = 0$ (b) $h = 0.02$

Fig. 8.12 Snap-through boundaries in the plane of the external forcing parameters (ν, ρ), for $\Omega = 0.0005$ and for $h = 0$ and $h = 0.02$. The *black zone* corresponds to the buckled state and the *white zone* to the unbuckled state

original equations (8.8) and (8.9) are quasi-periodic. In the grey zones these quasi-periodic solutions are changing their nature and/or stability during one period of the slow time scale τ. These zones are where periodic bursters exist. In fact, areas of these zones are increasing with increasing the amplitude of the base motion h. Moreover, the small regions a, b, c and d disappear from the chart of behavior.

It is worth pointing out that all the presented charts of behaviors are based on the study of local dynamics near the stable unbuckled static equilibrium. Consequently, this study is not valid when the snap-through occurs.

In Fig. 8.12 are shown in black the snap-through zone in the plane of the external forcing parameters (ν, ρ), for $h = 0$ and $h = 0.02$. The arch is considered to be undergoing snap-through if the straightened amplitude $Q_1(t) \geq 0$ at any time during the numerical integration of the original equations (8.8) and (8.9). Figure 8.12 shows that the snap-through is occurring for $\rho > 0.2$. Thus, our local analysis is valid since the considered ρ is below the threshold of this escape phenomenon.

In order to validate the perturbation method, Fig. 8.13 shows comparisons, for various h and ρ between the analytical solutions (8.22) and (8.23) and the numerical solutions of (8.8) and (8.9). Figure 8.13a shows a quasi-periodic solution and Fig. 8.13b shows a periodic burster relating a stationary solution and a quasi-periodic solution. It is worth noting that the numerical solution in Fig. 8.13b is delayed with respect to the analytical one, this is due to the metastability phenomenon caused by the low frequency excitation. For more insight about this delay phenomenon see [8]. In Fig. 8.14 are shown two samples of periodic bursters that cross the zones A and a.

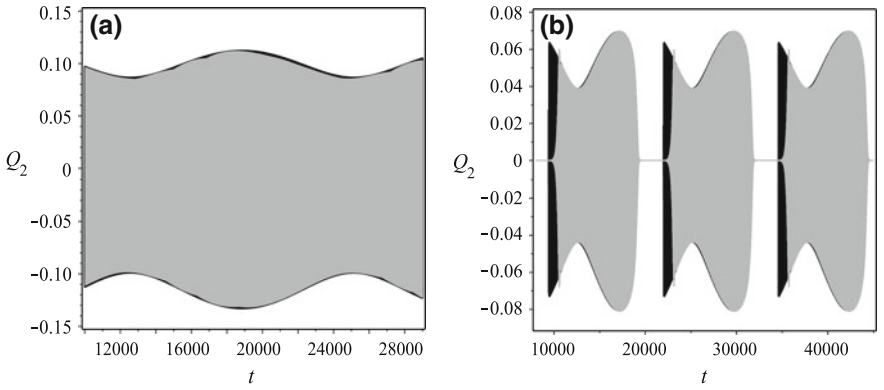

Fig. 8.13 A quasi-periodic and a periodic burster solutions of $Q_2(t)$ for $\nu = 2.64$, $\Omega = 0.0005$. **a** $\rho = 0.025$ and $h = 0.038$, **b** $\rho = 0.013$ and $h = 0.036$. The *black color* for the perturbation method's solution (8.22) and (8.23) and the *grey color* for the numerical solution of (8.8) and (8.9)

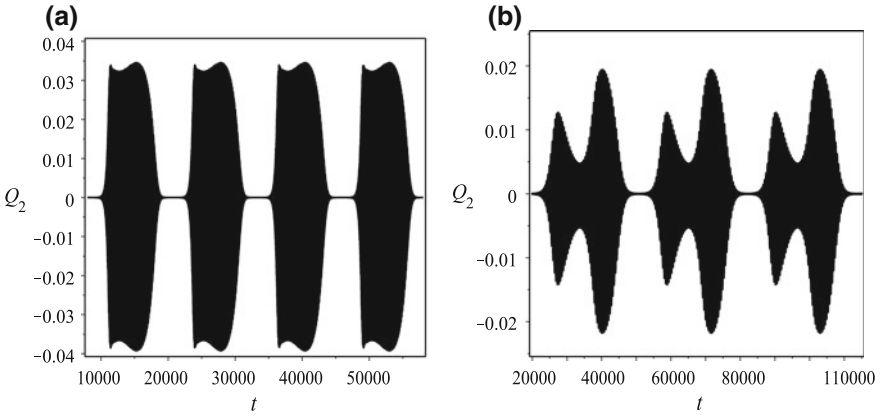

Fig. 8.14 Periodic bursters solution $Q_2(t)$, crossing zones A, a and A, of the original equations (8.8) and (8.9) for $h = 0.01$ **a** $\nu = 2.641$, $\rho = 0.0095$ and $\Omega = 0.0005$, **b** $\nu = 2.645$, $\rho = 0.0087$ and $\Omega = 0.0002$

8.6 Conclusions

In the present work, we have studied the nonlinear dynamics of a two dof model of a shallow arch subject to a resonant and a low frequency harmonic excitations under 1:1 internal resonance and principal external resonance. The low frequency harmonic excitation, that is acting as a parametric forcing, is caused by an imposed displacement of one of the bases of the arch. The role of the initial rise and the dead load in causing various static behaviors and tuning internal resonances is investigated. After the application of the Galerkin method, the multiple scales method is applied

to the reduced order model of the arch. Then, in the absence of the low frequency, the charts of behaviors of the amplitudes modulation equations reveal the existence of two types of solutions: the single and the coupled modes. The first mode involves only the fundamental mode of bending of the arch and the second involves the first and the second modes. The main effect of the low frequency is revealed by the modifications imposed to the charts of behaviors, especially in the boundaries between various dynamics. It is shown that periodic bursters exist in these boundaries. Finally, validations of the analytically approximated solutions and the numerical simulations are shown.

Future investigations will focus on the effect of the low frequency excitation in suppressing an existing chaotic behavior.

Appendix

Parameters of the modulation Eq. (8.20) and the approximated solutions Q_1 and Q_2 given in (8.22) and (8.23) are given by

$$X = 1 - \frac{6{\eta_0}^2}{{\omega_1}^2} \quad ; \quad Y = 1 - \frac{2{\eta_0}^2}{{\omega_1}^2} \quad ; \quad d_1 = -\frac{8\eta_0}{\omega_2^2 - (\omega_1 + \omega_2)^2}$$

$$d_2 = -\frac{8\eta_0}{\omega_2^2 - (\omega_1 - \omega_2)^2} \quad ; \quad k_1 = 8\eta_0 d_2 + 6\eta_0 c_1 + 4 \quad ; \quad k_2 = 3 - \frac{30{\eta_0}^2}{{\omega_1}^2}$$

$$k_3 = 8\eta_0 d_2 + 48\eta_0 c_3 + 8\eta_0 d_1 + 8 \quad ; \quad k_4 = 8\eta_0 c_2 + 8\eta_0 d_2 + 4$$

$$k_5 = 64\eta_0 c_3 + 8\eta_0 c_1 + 48 \quad ; \quad c_1 = -\frac{4\eta_0}{\omega_1^2 - 4\omega_2^2} \quad ; \quad c_2 = \frac{\eta_0}{\omega_1^2} \quad ; \quad c_3 = -\frac{\eta_0}{\omega_1^2}.$$

References

1. Karnovsky, I.A.: Theory of Arched Structures: Strength, Stability, Vibration. Springer, New York (2012)
2. Tajaddodianfar, F., Pishkenari, H.N., Yazdi, M.R.H.: Prediction of chaos in electrostatically actuated arch micro-nano resonators: analytical approach. Commun. Nonlinear Sci. Numer. Simulat. **30**, 182–195 (2016)
3. Ouakad, H.M., Younis, M.I.: On using the dynamic snap-through motion of MEMS initially curved microbeams for filtering applications. J. Sound Vib. **333**, 555–568 (2014)
4. Harne, R.L., Wang, K.W.: A review of the recent research on vibration energy harvesting via bistability systems. Smart Mater. Struct. **22**, 023001 (2013)
5. Golubitsky, M., Josic, K., Kaper, T.J.: An unfolding theory approach to bursting in fast-slow systems. In: Broer, H., Krauskopf, B., Vegter, G. (eds.) Global analysis of dynamical systems. Inst. Phys. Publ. 277–308 (2001)
6. Tien, W-M., Namachchivaya, N.S., Bajaj. A.K.: Nonlinear dynamics of a shallow arch under periodic excitation-I. 1:2 internal resonance. Int. J. Non-linear Mech. **29**(3), 349–366 (1994)

7. Tien, W.M., Sri Namachchivaya, N., Malhotra, N.: Nonlinear dynamics of a shallow arch under periodic excitation-II. 1:1 internal resonance. Int. J. Non-linear Mech. **29**(3), 367–38 (1994)
8. Lakrad, F., Schiehlen, W.: Effects of a low frequency parametric excitation. Chaos Solitons Fractals **22**, 1149–1164 (2004)
9. Lakrad, F., Belhaq, M.: Quasi-periodic solutions and periodic bursters in quasiperiodically driven oscillators. Commun. Nonlinear Sci. Numer. Simulat. **14**, 2426–2433 (2009)
10. Lakrad, F., Belhaq, M.: Solutions of a shallow arch under fast and slow excitations, in IUTAM Symposium on Chaotic Dynamics and Control of Systems and Processes in Mechanics. In: Rega, G., Vestroni, F. (eds.) Solid Mechanics and its Applications, vol. 122, 233–240. Springer (2005)
11. Lakrad, F., Chtouki, A., Belhaq, M.: Nonlinear vibrations of a shallow arch under a low frequency and a resonant harmonic excitations. Meccanica **51**, 2577–2587 (2016)
12. Nayfeh, A.H., Mook, D.T.: Nonlinear Oscillations. Wiley, New York (1979)
13. Lacarbonara, W., Rega, G.: Resonant non-linear normal modes. Part II: activation/orthogonality conditions for shallow structures systems. Int. J. Non-Linear Mech. **38**, 873–887 (2003)
14. Nayfeh, A.H.: Nonlinear Interactions. Wiley, New York (2000)
15. Doedel, E.J., Kernevez, J.P.: Auto: software for continuation problems in ordinary differential equations with applications. Technical Report, California Institute of Technology. Applied Mathematics (1986)

Chapter 9
Extreme Pulse Dynamics in Mode-Locked Lasers

Wonkeun Chang, José M. Soto-Crespo, Peter Vouzas and Nail Akhmediev

Abstract This chapter is devoted to dissipative solitons that produce sharp peaks (spikes) on top of its high amplitude central part. The peak amplitude of these spikes can exceed several times the amplitude of the soliton base. This unusual phenomenon is found for solutions of the complex cubic-quintic Ginzburg-Landau equation (CGLE) in a special region of its free parameters. Depending on them, the spikes can appear chaotically or regularly. Both regimes are discussed in this chapter. The spikes with chaotic appearance can be considered as rogue waves and the probability density function confirms this. The solitons with spikes can also be considered as noise-like pulses that have been discussed in several recent publications without actually revealing the nature of the noise. The wide spectrum of these pulses suggests their application for generation of super-continuum directly out of lasers. The transition from regular to chaotic dynamics can be used in experiments to investigate this new interesting phenomenon.

9.1 Introduction

Mode-locked laser systems generating ultrashort pulses [1] have witnessed a rapid development in the past decade [2–5]. Femtosecond pulses with high average power are useful in numerous applications, including advanced material processing [6, 7], biomedical applications [8, 9], nonlinear frequency conversions [10], frequency comb generation [11, 12] and fundamental science [13, 14]. Until recently, most

W. Chang · P. Vouzas · N. Akhmediev (✉)
Optical Sciences Group, Research School of Physics and Engineering,
The Australian National University, Acton Act 2601, Australia
e-mail: nail.akhmediev@anu.edu.au; nna124@rsphysse.anu.edu.au
W. Chang
e-mail: wonkeun.chang@anu.edu.au
P. Vouzas
e-mail: peter.vouzas@anu.edu.au

J.M. Soto-Crespo
Instituto de Óptica, C.S.I.C., Serrano 121, 28006 Madrid, Spain
e-mail: j.soto@csic.es

M. Belhaq (ed.), *Recent Trends in Applied Nonlinear Mechanics and Physics*,
Springer Proceedings in Physics 199, https://doi.org/10.1007/978-3-319-63937-6_9

of the research focus has been placed on conventional stationary regimes of mode-locked lasers. Far less study has been carried out on non-stationary regimes. However, a swift research progress in this field is pushing the limits of our knowledge, requiring us to get a comprehensive understanding of various other operation regimes.

There is a very large variety of operation regimes of mode-locked lasers that has been reported in the literature so far. These include stationary regimes, as well as many other regimes of non-stationary nature where consecutive pulses are different, such as pulsating regimes and a multiplicity of chaotic regimes [15]. Particular examples include noise-like pulses with a broadband spectrum [16, 17] or "broadband quasi-stationary pulses" [18]. The number of publications on this subject is continuously growing [19, 20]. Many studies have shown that these non-stationary regimes appear at the boundaries of the region of existence of stable stationary pulse regimes [15]. Various types of chaotic pulses have been observed experimentally [21–26]. Finding, characterizing and understanding this large variety of mode-locked laser operation regimes constitute important contributions to the research progress in this direction.

The concept of dissipative soliton laser provides an excellent framework to study various mode-locked laser configurations [2]. It is based on the notion of dissipative soliton, which refers to the formation of a localized structure in a nonlinear dissipative system due to mechanisms of self-organization [27]. The concept can be used to describe complex phenomena observed in many different disciplines, such as pattern formation in reaction-diffusion systems [28], vegetation clustering in arid lands [29, 30], and ultrashort pulse generation in mode-locked laser systems [31]. Even though these systems are physically different and therefore require different sets of equations to describe them, they have basic common ingredients that enable us to consider them from a single perspective, i.e. the energy/matter gain and loss through the soliton interactions with its surroundings, and the effects of dispersion and nonlinearity which redistribute the energy/matter within the soliton.

A dissipative soliton is the result of the complex balance between dispersion, nonlinearity, gain and loss [32]. In a mode-locked laser, the gain is provided by the active medium in the cavity, and losses are present in the cavity as well as in the mode-locking device. The dispersion and nonlinearity are also present in the optical components comprising the cavity. A mode-locked laser operates in a stationary pulse regime when the balance between these four ingredients is maintained throughout the laser operation. If the balance forms a limit-cycle, it operates in a pulsating regime [15]. Chaotic pulses may be also formed in the laser when we have a complex balance dynamics.

In particular, the noise-like pulse regime [16, 17, 19, 20] is characterized by its output that has: (1) a very broad and smooth spectrum; (2) a temporal autocorrelation trace with a narrow peak standing on a wide pedestal; and (3) low temporal coherence. These output features indicate that a noise-like pulse has a fine inner structure of ultrashort intense peaks whose duration, amplitude and phase change chaotically. Its first experimental observation was reported by Horowitz and his co-workers in an erbium-doped fiber laser [16] and many other reports followed thereafter in other mode-locked laser configurations [33–35].

Optical rogue waves are table-top counterparts of destructive giant waves that appear in the deep ocean [36–38]. There is currently a large research activity on them, as they provide a convenient way to understand oceanic rogue waves, and possibly other extreme events, in a controlled laboratory environment. Investigations have shown that some, but not all, chaotic regimes exhibit optical rogue waves, and the likelihood of rogue wave appearance is determined by the system parameters. Rogue waves can appear in both conservative and dissipative systems.

Optical rogue waves were first observed in the super-continuum radiation generated in an optical fiber by Solli et al. in 2007 [39]. The idea quickly spread into other fields of physics [40]. Rogue waves have been predicted to exist in plasmas, Bose-Einstein condensates [41] and even in the financial world [42]. From a mathematical point of view, a rogue wave could be defined as a solution of an evolution equation, localized both in space and time [43, 44]. For a conservative system such as the NLSE, the simplest form of a rogue wave is the Peregrine soliton [45]. Higher-order solutions localized in time and in space consist of several of them [43]. The Peregrine soliton has been experimentally observed in optics [46] and for water waves [47] thus proving the idea of being the prototype of a rogue wave [44]. Higher-order rogue wave solutions have also been observed [48, 49]. Solutions in the form of rogue waves can appear in a turbulent wave field [50, 51]. More generally, rogue waves can be caused by the interaction and cross-interaction of solitons and breathers [52, 53]. In optical fibers, in the presence of energy exchange between solitons, rogue waves appear as solitons with the highest amplitude generated as a result of their interactions [54–56].

Extreme optical peaks have been also observed in two dimensions [57–59]. Both linear [58] and nonlinear [57] phenomena can lead to a non-Gaussian statistics which is a signature of extreme waves in the system. Mathematically, 2D rogue waves can be modeled using exact solutions of a higher-dimensional NLS equation [60] or the Kadomtsev-Petviashvili equation [61]. Reviews of mechanisms for rogue wave formation can be found in [40, 62–64].

For dissipative systems, the equations governing nonlinear waves are different. One of them is a generalization of the NLSE, known as the complex cubic-quintic Ginzburg-Landau equation, widely used to model passively-mode-locked lasers. In these cases, exact solutions for rogue waves are not known. They can be found using numerical simulations. The natural name for these objects would be dissipative rogue waves [65]. Their properties are different from those of rogue waves in conservative systems. There are many types of such solutions [66–70], and the list is still very far from being completed.

The progress in the theory of rogue waves goes hand in hand with the progress in experimental techniques to measure them. As each rogue wave is unique and different from others, traditional accumulation techniques used to work with trains of identical pulses are not suitable for this purpose. New methods capable of dealing with individual pulses have been developed in optics [71]. They include time stretching analog-to-digital conversions [72, 73], time microscopy [74] and time lens magnifiers [75]. The main idea of these techniques is to lock the pulse in a given time window and to stretch it in time to the extent that electronic devices can measure its profile

with sufficient resolution. These experimental techniques open a new era in optics making it possible real time measurements of individual pulses rather than averages over many pulses.

Dissipative systems offer infinite possibilities in generating pulses with unexpected features. In addition to those listed above, we can mention spiny solitons [76] and other formations with extreme spikes on top of existing stationary structures [77, 78]. Finding these solutions require massive numerical simulations on a trial-and-error basis. So far, we did not find a systematic way to predict the properties of the pulses obtained for a given set of the system parameters. This can hardly be done because of the multiplicity of bifurcations that the solutions experience when changing parameters [79]. Predictions of simple stationary or pulsating solitons can be done using trial functions and method of moments [80] or Lagrangian techniques [81]. However, pulses with chaotically changing parameters do not allow such approximations. The pulse profile in this case changes on propagation and modeling it is a difficult task.

In this chapter, we present several non-stationary regimes of mode-locked lasers that exhibit extreme pulse dynamics. They have been discovered numerically in [76–78] by solving the master equation for mode-locked lasers. These solutions are found in the case of normal cavity dispersion, although the results might be extended to the anomalous dispersion case as well.

9.2 Modeling Passively Mode-Locked Lasers

One of the main techniques used in the modeling of passively mode-locked lasers is the so-called master equation approach [82]. This approach was first suggested by Haus [83, 84], and later developed into a cubic-quintic Ginzburg-Landau equation (CGLE), as the equation of minimal complexity [85] that admits stable soliton solutions, thus allowing us to describe pulse generation phenomena by optical oscillators. The presence of several parameters in the CGLE makes the dynamical system highly complicated [15]. Each equation parameter can be related to an actual parameter of a particular laser system [86] although the relation depends on the specific laser and varies significantly from one type to another.

The CGLE in its standard form is given by [2]:

$$i\psi_z + \frac{D}{2}\psi_{tt} + |\psi|^2\psi + \nu|\psi|^4\psi = i\delta\psi + i\beta\psi_{tt} + i\varepsilon|\psi|^2\psi + i\mu|\psi|^4\psi \ , \quad (9.1)$$

where for mode-locked lasers, t is the normalized time in a reference frame that moves with the pulse in the cavity and z is related to the cavity round-trip number. ψ is the complex envelope of the optical field. Reactive terms are given on the left-hand side; D is the average cavity dispersion: $D > 0$ for anomalous dispersion and $D < 0$ for normal dispersion, and ν, which can be either positive or negative, describes the quintic refractive index. Dissipative terms are presented on the right-hand side; δ (<0)

represents linear loss; the term containing β (>0) describes parabolic gain dispersion; ε (>0) and μ (<0) are the nonlinear gain and gain saturation coefficients, respectively. Despite (9.1) being an approximate general model for describing systems far from equilibrium, most of the complex pulse dynamics reported in passively mode-locked lasers have been found as solutions of this equation. Hence, it is a powerful equation that can provide a universal approach to study various mode-locked laser systems.

Although dealing with a single equation facilitates the finding, to some extent, of analytical exact or approximate solutions, in general, we need to rely on numerical methods to solve (9.1). We use a split-step Fourier technique. One of the most important issues in dealing with extreme pulse dynamics is that the numerical grid has to be sufficiently wide, in both time and frequency domains, to have practically zero values at the edges of the grids, while conveniently sampling all the features happening in different time- or z- scales. We used up to 524,228 mesh points in the transverse window to sample a t-interval of up to $[-200, 200]$, which ensured that the localized solutions are contained well within the boundaries of the grids, and at the same time that a sufficient number of grid points described extreme aspects of the solution. Moreover, we used an adaptive step-size control in the propagation direction to optimize the computational efficiency, while minimizing the numerical errors.

There are six system parameters that can be varied in (9.1). In order to obtain meaningful localized solutions, each one of the system parameters has to be chosen within a narrow interval. Without any prior knowledge of the solutions nearby, this can be a very exhaustive task. However, this is a crucial part of discovering new dynamics in mode-locked laser systems that may have very important implications.

9.3 Formation of Extreme Amplitude Spikes

Our search resulted in finding quite unusual pulsations of a single pulse, when $D = -2.5$, $\nu = -0.002$, $\delta = -0.08$, $\beta = 0.18$, $\varepsilon = 0.04$ and $\mu = -0.000025$. As shown in Fig. 9.1, these pulsations are characterized by a sharp growth of the amplitude of the pulse followed by an even sharper drop. This spike appears and disappears within a very short propagation interval. The lifetime of the spike is significantly shorter than the period of pulsation. The peak amplitude of the spike is also much higher than the amplitude of the low-lying pulse, which is around 15. A second spike, slightly different, immediately follows the first one, while the situation remains basically stationary in the rest of the period. For the above set of equation parameters, the spikes appear as asymmetric pairs as shown in Fig. 9.1.

The sharp growth can be considered as unexpected, as during most of the period, the pulse amplitude slightly varies, remaining near 15. We can refer to this part of the pulse as *pedestal*. The width of the extreme pulse is much narrower than the width of the pedestal. The same data are presented in a false color plot in Fig. 9.2. The two red spots in this figure represent the two extreme pulses forming the pair. After the sharp growth up to the maximal value, the central amplitude sharply drops to a

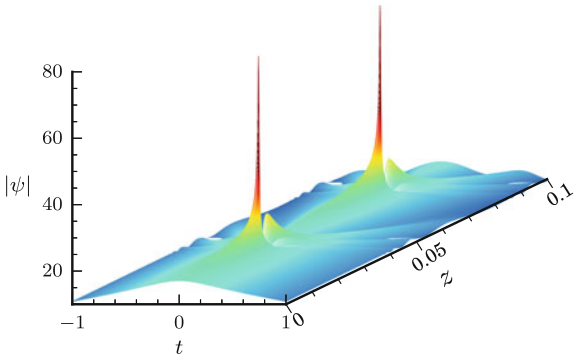

Fig. 9.1 Extreme pulses found for the following set of (9.1) parameters: $D = -2.5$, $\nu = -0.002$, $\delta = -0.08$, $\beta = 0.18$, $\varepsilon = 0.04$ and $\mu = -0.000025$. Extreme pulses are located on *top* of a wider pulse which acts as its pedestal. Only the central part of the pulse is shown here: note that the vertical scale starts from 10

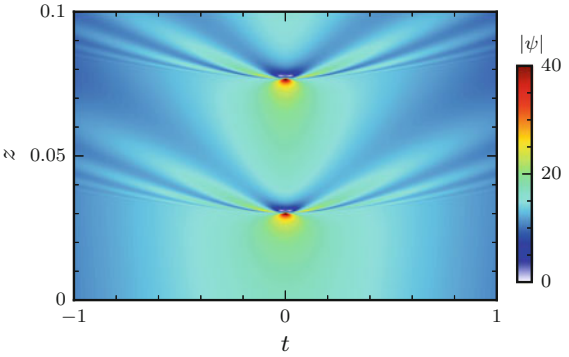

Fig. 9.2 Same data as in Fig. 9.1 in *false color*. The *color scale* is saturated at 40 to show the spikes, which otherwise would not be visible

value ≈2 which is much lower than the average amplitude of the pedestal. It is even more surprising that the extreme pulse generation is repeated after a short interval following the first peak.

The whole evolution is periodic with two extreme maxima in each period. Figure 9.3 shows the evolution of the field amplitude at its center (red solid-line), i.e. at the point $t = 0$, and the total pulse energy $Q(z)$ which is $\int_{-\infty}^{\infty} |\psi(z,t)|^2 dt$ (black dashed-line). The amplitudes of the two extreme peaks are similar but not exactly the same. The first peak is slightly higher than the second one. Accordingly, the total energy when the second peak appears is lower than that of the first one. The major fraction of the energy is contained within the pedestal. The increase of energy when the first extreme pulse appears is around 30% of the average energy of the pulse. The pulse energy increases gradually well before the appearance of the first spike as shown in Fig. 9.3. The period of pulsations is much longer than the lifetime of each peak. The pair generation is repeated indefinitely.

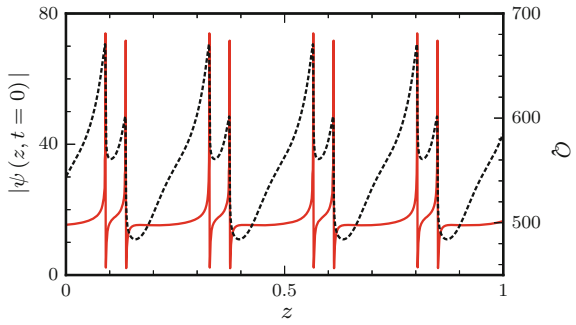

Fig. 9.3 Evolution of the pulse amplitude at its center $|\psi\,(z, t = 0)|$ (*red solid-line*) and the pulse energy $Q\,(z)$ (*black dashed-line*) for the same parameters as in Fig. 9.1

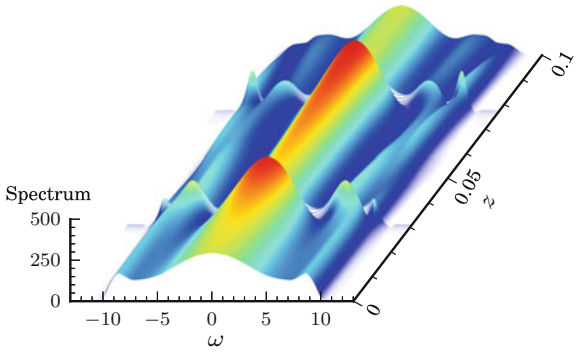

Fig. 9.4 Evolution of the spectrum of the pulse shown in Fig. 9.4

Another observation from Fig. 9.3 is that the amplitude of the extreme peaks in the solution are approximately five times higher than the amplitude of the pedestal. This means that the intensity amplification factor of the peak is around 25. This creates interesting possibilities for practical applications of this effect. A single laser oscillator can be used for generating high amplitude ultrashort pulses without additional compressors provided that the correct parameters of the system are found and carefully tuned to match the period of the evolution with the cavity length. According to these simulations, this can be done in lasers with normal average cavity dispersion.

The evolution of the pulse spectrum is shown in Fig. 9.4. The z-interval of this plot is the same as in Fig. 9.1. It includes the two extreme peaks of the pair. The extreme peaks cause the widening of the spectrum. Two sidebands are clearly seen on each side of the main spectral peak. They vary in size from the first peak to the second one. These sidebands are not related to the periodicity of the overall evolution. They quickly vanish when the high peaks disappear.

9.4 Bifurcation Diagram

The regime of pulse generation presented in Sect. 9.3 is periodic with high accuracy. The existence of two different spikes within each spatial period is an unusual feature of this periodic solution. As in other dissipative systems, periodic motion here should be considered as relaxation oscillations. These are usually sensitive to the parameters of the system. Changing any of them leads to drastic changes of the oscillation dynamics. Figure 9.5 shows the bifurcation diagram of the peak amplitude of the spikes when the dispersion parameter D is changed from -2.49 to -2.67. Let us recall that previous figures correspond to the value $D = -2.5$. At this point, we have two maximal amplitudes that are shown by two dots one above the other on this diagram. Reducing the parameter D, i.e. moving towards the left, we observe a smooth increase of the two amplitudes.

The two spikes can be observed up to the point $D \approx -2.64$. At this point, a bifurcation causes the merging of the two spikes into one. In the interval $-2.662 < D < -2.64$ the soliton has only one spike in each period. Thus we have a single curve on the bifurcation diagram. An example of the pulse amplitude evolution at one point of this interval is shown in Fig. 9.6. The point $D \approx -2.664$ represents the transition to a chaotic state where the spikes appear randomly. Every point on the vertical lines in this region represents a given realization of the spike amplitude. As the plot shows, the amplitudes here can take even higher values than in the region of regularly pulsating evolution. Thus, the region of the dispersion parameter lower than $D = -2.662$, would be the one where we can look for optical rogue waves [66, 87–89].

We have chosen D to be variable for the bifurcation diagram as the dispersion is the parameter of a laser system that can be changed with a relative ease. Similar bifurcation diagrams can be obtained when changing other parameters of the system. An important point is that the peak amplitude of the spikes remain extremely high relative to the peak amplitude of the pedestal in the whole interval of D presented in Fig. 9.5. They also remain high when we change other parameters. For example,

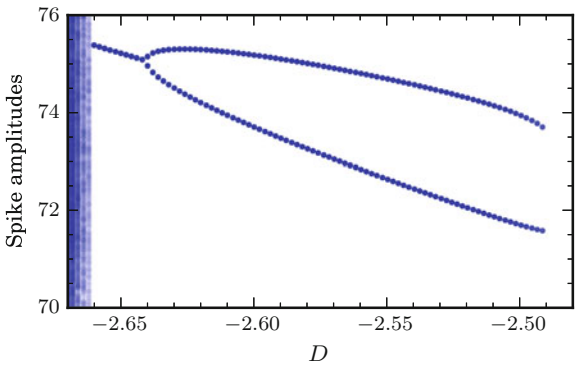

Fig. 9.5 Bifurcation diagram: spike amplitudes versus dispersion parameter D. Pairs merge into a single high peak at $D \approx -2.64$. The soliton becomes unstable and disappears at $D > -2.49$. The soliton enters a chaotic regime of evolution at $D < -2.662$

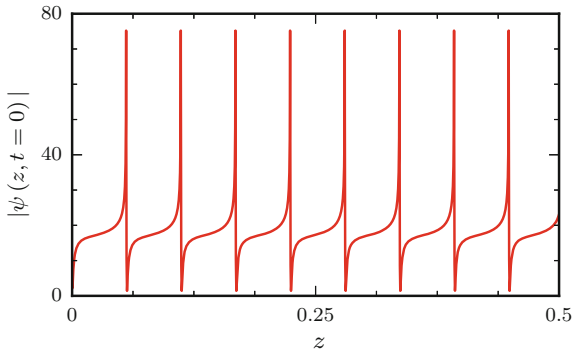

Fig. 9.6 Equally separated spikes on top of a soliton when $D = -2.65$. All spikes are now located at the center ($t = 0$) of the pulsating soliton

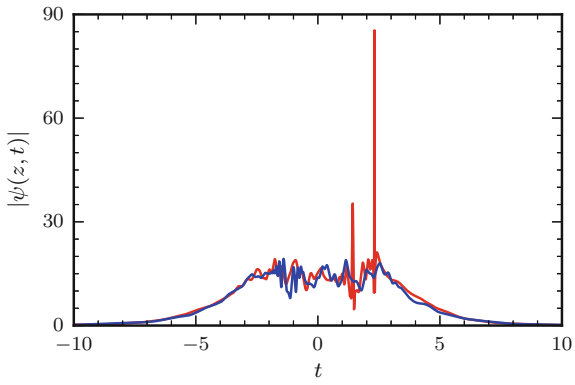

Fig. 9.7 Spiny soliton obtained for $D = -2.67$. The rest of parameters are the same as in Fig. 9.1. The *blue* and *red curves* correspond to two different z. The *red curve* has an exceptionally high amplitude spike

increasing the parameter ε from 0.04 to 0.042 while leaving other parameters fixed also results in the merging of the pair of peaks within a period into a single one. Still, the motion remains periodic in z although the period changes approximately from 0.27 to 0.045, i.e. it is reduced approximately six times. Further increase of ε up to $\varepsilon = 0.0423$ leads to a chaotic pulse evolution while a small decrease of ε from 0.04 to 0.039, results in pulse decay and its subsequent disappearance.

9.5 Spiny Solitons

As shown in Fig. 9.5, the system enters a chaotic regime when $D < -2.662$. We now look at the details of the chaotic operation regime in this region. Examples of the chaotic solutions at $D = -2.67$ for two different values of z are shown in Fig. 9.7. The upper part of the pulse evolves chaotically while the whole pulse stays localized having well defined exponentially decaying tails. It exhibits many features of the noise-like pulses, except that chaotically varying ultrashort structures are present on

top of a long pulse rather than from the zero background as in typical noise-like pulses. Hence, we name the solutions shown in Fig. 9.7, "spiny solitons".

Similar to the solutions studied in Sect. 9.3, the spiny solitons also have a localized pedestal with short-lived spikes that appear and disappear on top of it. However, in drastic contrast to the regular pulsating pattern observed before, the appearance of the spikes are random, both in t and z directions. The peak amplitudes also vary chaotically, and may reach very high values. For example, one spike shown in Fig. 9.7 has a particularly high amplitude ≈80. Only the tails of the solution have a regular exponential decay.

The appearance of these chaotic spikes is the most prominent feature of the solution for a given set of (9.1) parameters. In order to see this more clearly, we present in Fig. 9.8 the false color plot of the field amplitude evolution $|\psi|$ in the (t,z)-plane. Several spikes, chaotically appearing and quickly disappearing across the soliton, are shown in the figure. The points with the highest amplitudes of these spikes can be seen as red spots. These spots are very small in comparison to the width of the soliton. They are exceptionally narrow both in z and in t directions. However, their

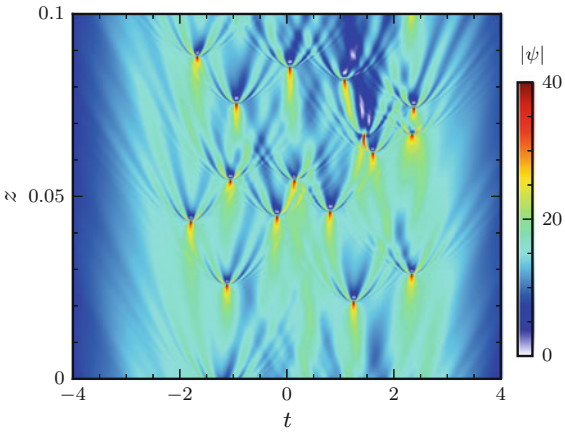

Fig. 9.8 *False color plot* of the field amplitude of the spiny soliton on the (t,z)-plane. Narrow high-amplitude (>40) spikes randomly appear on top of the soliton. The horizontal scale here is zoomed in comparison to Fig. 9.7, allowing us to see more clearly the central part of the soliton

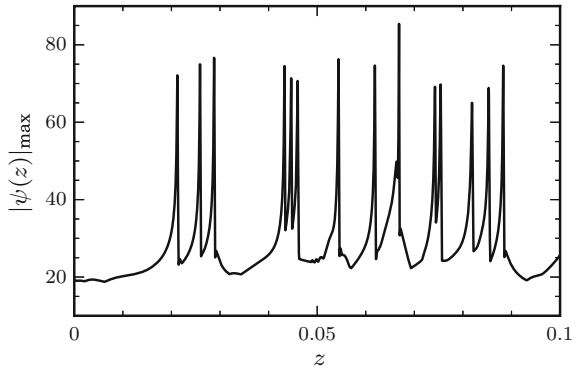

Fig. 9.9 Absolute maximum field amplitude for all t at each z, for the same data as in Fig. 9.8. Spikes have similar profiles but different amplitudes

amplitude exceeds the highest red level in the color scale shown on the right hand side of this plot, that for the sake of clarity of the whole pattern has been set to 40.

In order to see the real values of the amplitudes of these peaks, we selected the absolute maximum of each field amplitude profile $|\psi\ (t)|$ and plotted this value against z. Figure 9.9 represents these data for the same z-interval as in Fig. 9.8. As we can see, these peaks are generated with randomly changing amplitudes, but the height of most of them is above the level of 70.

9.6 Probability Density Functions and Optical Rogue Waves

The chaotically appearing spikes with extreme amplitudes may represent optical rogue waves. We find this out by calculating the probability density function (PDF) for the peak maxima in the region where chaotic behavior is observed. First, we have found that consecutive profiles separated by a z-interval of 0.02 appear completely uncorrelated, thus confirming that the field profiles are truly chaotic. As a second step, we counted all local maxima appearing on top of each soliton profile $|\psi\ (t)|$ separated by $\Delta z = 0.02$ for 50 different realizations. We considered various separations larger than 0.02, but did not observe perceptible differences when increasing Δz. Counting millions of local maxima this way we calculated the density of probability for each amplitude. The amplitude slots have been chosen sufficiently small for curves to be smooth enough, but sufficiently large to have adequate number of data within each slot.

The PDFs for the data exemplified by Fig. 9.8 are shown in Fig. 9.10. Probability is plotted in logarithmic scale. The probability curves are calculated for four different values of D. The curves do not change much when D is varied. They show the maximum of probability around the amplitude of the pedestal and decrease at each side of this maximum. The data with very small amplitudes have been removed, and

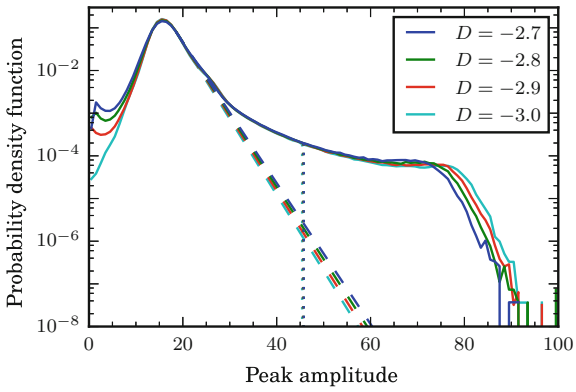

Fig. 9.10 Probability density functions calculated for several values of D. The rest of the parameters are the same as in Fig. 9.1. The *dashed lines* represent the best fit for the exponential tails of each probability density function curve. The *vertical dotted lines* correspond to rogue wave thresholds

Table 9.1 The total number of wave maxima counted in simulations, the calculated significant wave-height (SWH), the rogue wave amplitude (2.2 × SWH) and the total probability of a rogue event for four different values of D

D	Number of maxima	SWH	Rogue wave amplitude	Rogue wave probability
−2.7	27,041,311	20.80	>45.77	0.003
−2.8	27,310,749	20.78	>45.71	0.003
−2.9	31,313,312	20.73	>45.61	0.003
−3.0	27,460,729	20.65	>45.42	0.003

the significant wave height (SWH) is calculated using its standard definition, which is the mean wave height of the highest third of the waves. The values of the SWH for each case are given in Table 9.1. Rogue waves are defined as the waves that have an amplitude exceeding 2.2 times the SWH. The rogue wave threshold for each D is also presented in Table 9.1.

From Fig. 9.10, we can clearly see the elevated tail of the PDF at the region of spikes, i.e. at the amplitudes around 70–80. The probability in this region is several orders of magnitude higher than expected from a simple exponential approximation of the main part of the curve. Hence, these spikes indeed represent optical rogue waves. The total probability of the appearance of rogue waves is calculated as an integral of the area below the PDF curve above the rogue wave threshold. This probability is found to be 0.003 for all four cases as can be seen from Table 9.1.

9.7 Measurement Techniques

It may not be possible to register the short spikes in optical experiments. A complete characterization of the chaotic spikes through shot-to-shot measurements often requires highly-sensitive ultrafast diagnostic tools that may not be readily available. What could be possible to measure is the average profile of the pulses. An example of average profile is shown in Fig. 9.11a. The curve is calculated as the average of profiles taken at 10,000 equidistantly located values of z along the direction of propagation. The spikes are then averaged out and the resulting soliton has a flat top.

The fine structure of a pulse can be studied experimentally through its autocorrelation function. In particular, noise-like pulses have been characterized from these measurements [16, 90]. The standard way of measuring the intensity autocorrelation function uses the second harmonic generation (SHG) technique with a nonlinear crystal where two beams cross each other with a time delay τ. The autocorrelation function $C(\tau)$ obtained from the SHG data can be calculated as:

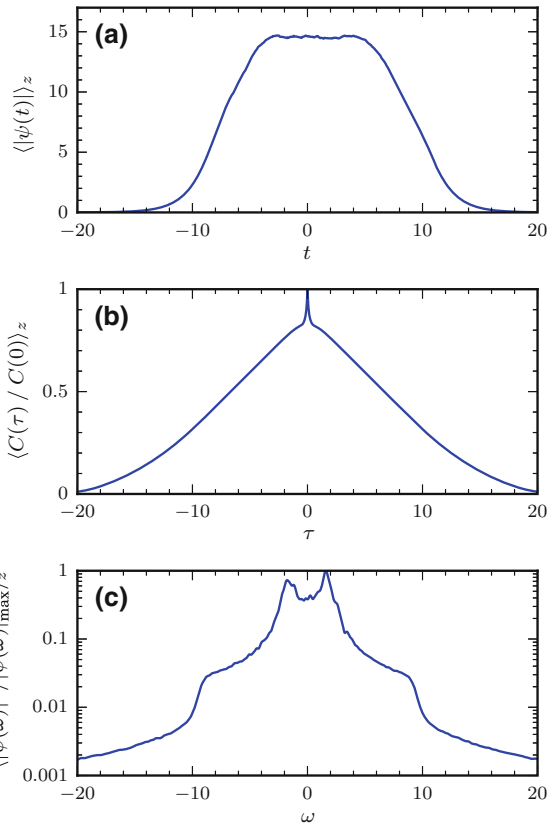

Fig. 9.11 **a** The average profile of the chaotic soliton at $D = -2.67$. The spikes are averaged out and the soliton has a *flat top*. **b** Average autocorrelation function for the same data as in (**a**). **c** Corresponding average spectrum for the same data. The rest of the parameters are the same as in Fig. 9.1

$$C(\tau) = \frac{1}{N}\sum_{i=1}^{N}\int_{-\infty}^{\infty} I_i(t)\, I_i(t-\tau)\, dt\ , \tag{9.2}$$

where $I(t) = |\psi(t)|^2$ and the sum signifies averaging on N data set chosen to be equally spaced along z. We set N to be large enough (10,000) to make sure that many rogue wave events occur within the interval. In order to have a convenient normalization, this function is divided by its maximum value $C(0)$. The autocorrelation function defined this way is shown in Fig. 9.11b for the same data as in Fig. 9.11a. The base of the autocorrelation function naturally depends on the soliton width. Here, the peak height relative to the base indicates that there is a strong background of dissipative soliton that results in the base. On the other hand, the width of the autocorrelation peak is not necessarily defined by the widths of spikes on top of the pulse. The coherence length across the chaotic profile is actually wider than the size of the spikes. Comparing our results with the data available in the literature, we have found that the shape of the autocorrelation function in Fig. 9.11b is close to the one obtained in [90, 91] rather than the one in [16].

We have also calculated the average spectrum using the same number of data (10,000). It is shown in Fig. 9.11c. Although, we used a relatively large amount of data for averaging, the spectrum still shows a chaotic component in its central part. The slight asymmetry of the spectrum is also related to the insufficient number of data taken for the averaging. The specific shape of this spectrum may potentially be used in experiments for identification of this type of dissipative solitons. Indeed, the spectrum has a unique shape with characteristic shoulders and horns. It is different from the smooth narrow [16, 19] or wide [33] spectra observed in experimental studies of noise-like pulses. It is also different from the complicated multi-peak spectra observed in [92]. However, there are common features of our spectrum with those observed in [18]. Although, we cannot compare the autocorrelation functions in this case. Generally, it is very likely that the solitons observed in our present numerical simulations comprise a new class of dissipative solitons, yet to be observed experimentally.

Modern experimental techniques allow us to measure short pulses simultaneously in frequency and in time domains. One of these powerful techniques is known as cross-correlation frequency-resolved optical gating (XFROG) [93]. The technique is especially useful when dealing with pulses having a rich structure. In order to give an idea of how the XFROG diagram may look like in the case of spiny solitons, we have calculated one example which is shown in Fig. 9.12. For these calculations, we used the gate pulse in the form of a Gaussian with full-width at half maximum of 0.1. In order to obtain the XFROG diagram, we used one profile $\psi\,(t, z_0)$ of the data shown in Fig. 9.8. We have chosen the profile at $z_0 = 0.0259$, which simultaneously contains one spike and a peak growing into a spike. These two points are separated in τ. The spike corresponds to the white spot in Fig. 9.12 at $\tau \approx -1.1$ while the growing peak corresponds to the red spot at $\tau \approx 2.3$.

These two parts of the spectrogram show the two stages of the spike evolution in time. The trace of earlier stage at $\tau \approx 2.3$ is tilted demonstrating that the spike is in the stage of compression. The tilt would be better seen if the diagram is zoomed along the τ-axis. The stage at $\tau \approx -1.1$ corresponds to completely compressed

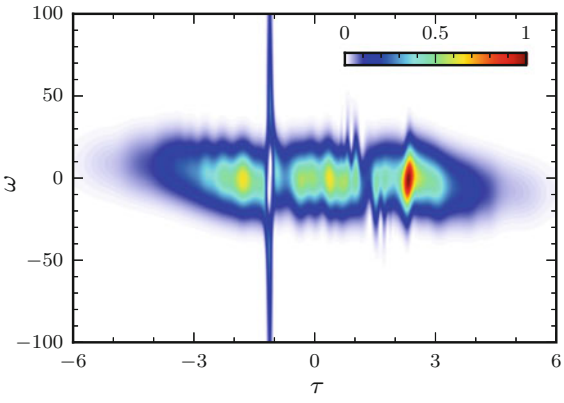

Fig. 9.12 Cross-correlation frequency-resolved optical gating diagram calculated with the same data as in Fig. 9.8 at $z = 0.0259$

spike. Consequently, it does not have a tilt. The spectrum in most part of the XFROG pattern is relatively narrow. However, at $\tau \approx -1.1$, it significantly widens and extends beyond the frame of the plot from -100 to $+100$.

9.8 Conclusions

In conclusion, we have presented numerical results demonstrating the existence of solitons with short-life narrow spikes on top of its wide base, i.e. the spikes are localized both in space and time in contrast to the base soliton that is localized only in transverse direction. The spikes may appear periodically following a strict cycle or chaotically in both space and time. We named the chaotic objects "spiny solitons". Spiny solitons may appear in different forms depending on the parameters of the equation that governs the dynamics. We dealt with the complex cubic-quintic Ginzburg-Landau equation (CGLE) that models many phenomena in physics including the generation of short pulses in passively mode-locked lasers. Our results are discussed in terms of optical pulses but the versatility of the CGLE suggests that periodic spikes and spiny solitons may appear in a variety of settings. Spiny solitons can appear in the form of rogue waves or noise-like pulses. Their width is narrower than the base soliton thus providing the way for generating ultra-short pulses. Their amplitude is higher than the amplitude of its base suggesting that these pulses can carry significant amount of energy. The controlled transition from regular to chaotic generation of spikes is another practical way of dealing with these pulses. They can be generated in the form of rogue waves as well as in the form of periodic train of pulses. The width of their spectrum can also be controlled by the external parameters. This provides us with a new way of generating super-continuum in optics. Hence the periodic spike formations and the spiny solitons have a number of interesting properties that can be used in various applications. The region of parameters of the CGLE that we gave in this chapter is not the only one that produces these solitons. Further studies may produce even more interesting solutions that will enrich our knowledge of dissipative solitons and their applications.

Acknowledgements The authors acknowledge the support of the Australian Research Council (DE130101432, DP140100265 and DP15102057). The work of JMSC was supported by MINECO under contract TEC2015-71127-C2-1-R, and by C.A.M. under contract S2013/MIT-2790. JMSC and NA acknowledge the support of the Volkswagen Foundation.

References

1. Smith, P.W.: Mode-locking of lasers. Proc. IEEE **58**(9), 1342 (1970)
2. Grelu, P., Akhmediev, N.: Dissipative solitons for mode-locked lasers. Nat. Photon. **6**, 84 (2012)
3. Kutz, J.N.: Mode-locked soliton lasers. SIAM Rev. **48**(4), 629–678 (2006)
4. Fermann, M.E., Hartl, I.: Ultrafast fibre lasers. Nat. Photon. **7**, 868 (2013)

5. Brida, D., Krauss, G., Sell, A., Leitenstorfer, A.: Ultrabroadband Er: fiber lasers. Laser Photonics Rev. **8**(3), 409–428 (2014)
6. Sugioka, K., Cheng, Y.: Ultrafast lasers—reliable tools for advanced materials processing. Light Sci. Appl. **3**, e149 (2014)
7. Gattass, R.R., Mazur, E.: Femtosecond laser micromachining in transparent materials. Nature Photon. **2**, 219 (2008)
8. Chung, S.H., Mazur, E., Biophoton, J.: Surgical applications of femtosecond lasers **2**, 557 (2009)
9. Neutze, R., Wouts, R., van der Spoel, D., Weckert, E., Hajdu, J.: Potential for biomolecular imaging with femtosecond X-ray pulses. Nature **406**, 752 (2000)
10. Fejer, M.M.: Nonlinear optical frequency conversion. Phys. Today **47**, 25 (1994)
11. Kippenberg, T.J., Holzwarth, R.L., Diddams, S.A.: Microresonator based optical frequency combs. Science **332**, 555 (2011)
12. Papp, S.B., Beha, K., Del'Haye, P., Quinlan, F., Lee, H., Vahala, K.J., Diddams, S.A.: Microresonator frequency comb optical clock. Optica **1**, 10 (2014)
13. Kim, I.J., Pae, K.H., Kim, C.M., Kim, H.T., Sung, J.H., Lee, S.K., Yu, T.J., Choi, I.W., Lee, C.L., Nam, K., Nickles, P.V., Jeong, T.M., Lee, J.: Transition of proton energy scaling using an ultrathin target irradiated by linearly polarized femtosecond laser pulses. Phys. Rev. Lett. **111**, 165003 (2013)
14. Muller, H.G.: Reconstruction of attosecond harmonic beating by interference of two-photon transitions. Appl. Phys. B **74**, s17 (2002)
15. Akhmediev, N., Soto-Crespo, J.M., Town, G.: Pulsating solitons, chaotic solitons, period doubling, and pulse coexistence in mode-locked lasers: CGLE approach. Phys. Rev. E **63**, 056602 (2001)
16. Horowitz, M., Barad, Y., Silberberg, Y.: Noiselike pulses with a broadband spectrum generated from an erbium-doped fibre laser. Opt. Lett. **22**, 799 (1997)
17. Zhao, L.M., Tang, D.Y., Cheng, T.H., Tam, H.Y., Lu, C.: 120 nm bandwidth noise-like pulse generation in an erbium-doped fiber laser. Opt. Commun. **281**, 157–161 (2008)
18. Kang, J.U.: Broadband quasi-stationary pulses in mode-locked fiber ring laser. Opt. Commun. **182**, 433–436 (2000)
19. Pottiez, O., Grajales-Coutino, R., Ibarra-Escamilla, B., Kuzin, E.A., Herndez-Garca, J.C.: Adjustable noiselike pulses from a figure-eight fiber laser. Appl. Opt. **50**(25), E24–E31 (2011)
20. Horowitz, M., Silberberg, Y.: Control of noiselike pulse generation in erbium-doped fiber lasers. IEEE Photonics Technol. Lett. **10**(10), 1389 (1998)
21. Lei, D., Yang, H., Dong, H., Wen, S., Xu, H., Zhang, J.: Effect of birefringence on the bandwidth of noise-like pulse in an erbium-doped fiber laser. J. Mod. Opt. **56**(4), 572–576 (2009)
22. Hernandez-Garcia, J.C., Pottiez, O., Estudillo-Ayala, J.M.: Supercontinuum generation in a standard fiber pumped by noise-like pulses from a figure-eight fiber laser. Laser Phys. **22**(1), 221–226 (2012)
23. Tang, D.Y., Zhao, L.M., Zhao, B.: Soliton collapse and bunched noise-like pulse generation in a passively mode-locked fiber ring laser. Opt. Express **13**(7), 2289–2294 (2005)
24. Takushima, Y., Yasunaka, K., Ozeki, Y., Kikuchi, K.: 87 nm bandwidth noise-like pulse generation from erbium-doped fibre laser. Electron. Lett. **41**(7), 399–400 (2005)
25. Zaytsev, A., Lin, C.-H., You, Y.-J., Chung, C.-C., Wang, C.-L., Pan, C.-L.: Supercontinuum generation by noise-like pulses transmitted through normally dispersive standard single-mode fibers. Opt. Express **21**(13), 16056–16062 (2013)
26. Schreiber, T., Ortaç, B., Limpert, J., Tünnermann, A.: On the study of pulse evolution in ultrashort pulse mode-locked fiber lasers by numerical simulations. Opt. Express **13**, 8252 (2007)
27. Akhmediev, N., Ankiewicz, A.: Dissipative Solitons. Lecture Notes in Physics, Springer, Berlin (2005)
28. Descalzi, O., Akhmediev, N., Brand, H.R.: Exploding dissipative solitons in reaction-diffusion systems. Phys. Rev. E **88**, 042911 (2013)
29. Tlidi, M., Lefever, R., Vladimirov, A.: On Vegetation Clustering, Localized Bare Soil Spots and Fairy Circles, Chapter in the book [31], pp. 381

30. Bordeu, I., Clerc, M.G., Couteron, P., Lefever, R., Tlidi, M.: Self-replication of localized vegetation patches in scarce environments. Sci. Rep. **6**, 33703 (2016)
31. Akhmediev, N., Ankiewicz, A.: Dissipative Solitons: From Optics to Biology and Medicine, Lecture Notes in Physics. Springer, Berlin (2008)
32. Akhmediev, N.: General theory of solitons. In: Boardman, A.D., Sukhorukov, A.P. (eds.) Soliton-Driven Photonics, pp. 371–395. Kluver Academic Publishers, Netherlands (2001)
33. Vázquez-Zuniga, L.A., Jeong, Y.: Super-broadband noise-like pulse erbium-doped fiber ring laser with a highly nonlinear fiber for Raman gain enhancement. IEEE Photon. Technol. Lett. **24**, 1549 (2012)
34. Sobon, G., Sotor, J., Martynkien, T., Abramski, K.M.: Ultra-broadband dissipative soliton and noise-like pulse generation from a normal dispersion mode-locked Tm-doped all-fiber laser. Opt. Express **24**, 6156 (2016)
35. Chen, Y., Wu, M., Tang, P., Chen, S., Du, J., Jiang, G., Li, Y., Zhao, C., Zhang, H., Wen, S.: The formation of various multi-soliton patterns and noise-like pulse in a fiber laser passively mode-locked by a topological insulator based saturable absorber. Laser Phys. Lett. **11**, 055101 (2014)
36. Osborne, A.: Nonlinear ocean waves and the inverse scattering transform. Elsevier, Amsterdam (2010)
37. Yuen, H.C., Lake, B.M.: Nonlinear deep water waves: theory and experiment. Phys. Fluids **18**, 956–960 (1975)
38. Onorato, M., Osborne, A.R., Serio, M., Bertone, S.: Freak waves in random oceanic sea states. Phys. Rev. Lett. **86**, 5831–5834 (2001)
39. Solli, D.R., Ropers, C., Koonath, P., Jalali, B.: Optical rogue waves. Nature **450**, 1054 (2007)
40. Akhmediev, N., Pelinovsky, E. (eds.): "Rogue waves—towards a unifying concept?: Discussions and debates", Eur. Phys. J. Spec. Top. **185**, 266 (2010)
41. Bludov, Y.V., Konotop, V.V., Akhmediev, N.: Matter rogue waves. Phys. Rev. A **80**, 033610 (2009)
42. Zhen-Ya, Y.: Financial rogue waves. Commun. Theor. Phys. **54**(5), 947–949 (2010)
43. Akhmediev, N., Ankiewicz, A., Taki, M.: Waves that appear from nowhere and disappear without a trace. Phys. Lett. A **373**, 675–678 (2009)
44. Shrira, V.I., Geogjaev, V.V.: What makes the Peregrine soliton so special as a prototype of freak waves? J. Eng. Math. **67**, 11–22 (2010)
45. Peregrine, D.H.: Water waves, nonlinear Schrödinger equations and their solutions. J. Aust. Math. Soc. Ser. B **25**, 16–43 (1983)
46. Kibler, B., Fatome, J., Finot, C., Millot, G., Dias, F., Genty, G., Akhmediev, N., Dudley, J.M.: The Peregrine soliton in nonlinear fibre optics. Nat. Phys. **6**(10), 790–795 (2010)
47. Chabchoub, A., Hoffmann, N.P., Akhmediev, N.: Rogue wave observation in a water wave tank. Phys. Rev. Lett. **106**, 204502 (2011)
48. Chabchoub, A., Hoffmann, N.P., Onorato, M., Akhmediev, N.: Super rogue waves: observation of a higher-order breather in water waves. Phys. Rev. X **2**, 011015 (2012)
49. Chabchoub, A., Hoffmann, N., Onorato, M., Slunyaev, A., Sergeeva, A., Pelinovsky, E., Akhmediev, N.: Observation of a hierarchy of up to fifth-order rogue waves in a water tank. Phys. Rev. E **86**, 056601 (2012)
50. Akhmediev, N., Soto-Crespo, J.M., Ankiewicz, A., Devine, N.: Early detection of rogue waves in a chaotic wave field. Phys. Lett. A **375**, 2999–3001 (2011)
51. Soto-Crespo, J.M., Devine, N., Hoffmann, N.P., Akhmediev, N.: Rogue waves of the Sasa-Satsuma equation in a chaotic wave field. Phys. Rev. E **90**, 032902 (2014)
52. Soto-Crespo, J.M., Devine, N., Akhmediev, N.: Integrable turbulence and rogue waves: breathers or solitons? Phys. Rev. Lett. **116**, 103901 (2016)
53. Akhmediev, N., Soto-Crespo, J.M., Devine, N.: Breather turbulence versus soliton turbulence: rogue waves, probability density functions, and spectral features. Phys. Rev. E **94**, 022212 (2016)
54. Taki, M., Mussot, A., Kudlinski, A., Louvergneaux, E., Kolobov, M., Douay, M.: Third-order dispersion for generating optical rogue solitons. Phys. Lett. A **374**(4), 691–695 (2010)

55. Genty, G., DeSterke, C.M., Bang, O., Dias, F., Akhmediev, N., Dudley, J.M.: Collisions and turbulence in optical rogue wave formation. Phys. Lett. A **373**, 989–996 (2010)
56. Akhmediev, N., Soto-Crespo, J.M., Ankiewicz, A.: Could rogue waves be used as efficient weapons against enemy ships? Eur. Phy. J. Spec. Top. **185**, 259–266 (2010)
57. Montina, A., Bortolozzo, U., Residori, S., Arecchi, F.T.: Non-Gaussian statistics and extreme waves in a nonlinear optical cavity phys. Phys. Rev. Lett. **103**, 173901 (2009)
58. Arecchi, F.T., Bortolozzo, U., Montina, A., Residori, S.: Granularity and inhomogeneity are the joint generators of optical rogue waves. Phys. Rev. Lett. **106**, 153901 (2011)
59. Yang, Z.P., Zhong, W.-P., Belić, M.: 2D optical rogue waves in self-focusing Kerr-type media with spatially modulated coefficients. Laser Phys. **258**, 085402 (2015)
60. Kundu, A., Mukherjee, A., Naskar, T.: Modelling rogue waves through exact dynamical lump soliton controlled by ocean currents. Proc. R. Soc. A **470**, 20130576 (2014)
61. Dubard, P., Matveev, V.B.: Multi-rogue waves solutions: from the NLS to the KP-I equation, Nonlinearity **26**(12), R93 (2013)
62. Onorato, M., Residori, S., Bortolozzo, U., Arecchi, T.: Rogue waves and their generating mechanisms in different physical contexts. Phys. Rep. **528**(2), 47–89 (2013)
63. Akhmediev, N., Dudley, J.M., Solli, D.R., Turitsyn, S.K.: Recent progress in investigating optical rogue waves. J. Opt. **15**, 060201 (2013)
64. Akhmediev, N., Kibler, B., Baronio, F., Belić, M., Zhong, W.-P., Zhang, Y., Chang, W., Soto-Crespo, J.M., Vouzas, P., Grelu, P., Lecaplain, C., Hammani, K., Rica, S., Picozzi, A., Tlidi, M., Panajotov, K., Mussot, A., Bendahmane, A., Szriftgiser, P., Genty, G., Dudley, J., Kudlinski, A., Demircan, A., Morgner, U., Amiraranashvili, S., Bree, C., Steinmeyer, G., Masoller, C., Broderick, N.G.R., Runge, A.F.J., Erkintalo, M., Residori, S., Bortolozzo, U., Arecchi, F.T., Wabnitz, S., Tiofack, C.G., Coulibaly, S., Taki, M.: Roadmap on optical rogue waves and extreme events. J. Opt. **18**, 063001 (2016)
65. Soto-Crespo, J.M., Grelu, P., Akhmediev, N.: Dissipative rogue waves: extreme pulses generated by passively mode-locked lasers. Phys. Rev. E **84**, 016604 (2011)
66. Zaviyalov, A., Egorov, O., Iliew, R., Lederer, F.: Rogue waves in mode-locked fiber lasers. Phys. Rev. A **85**, 013828 (2012)
67. Lecaplain, C., Grelu, P., Soto-Crespo, J.M., Akhmediev, N.: Dissipative rogue waves generated by chaotic pulse bunching in a mode-locked laser. Phys. Rev. Lett. **108**, 233901 (2012)
68. Lecaplain, C., Grelu, P., Soto-Crespo, J.M., Akhmediev, N.: Dissipative rogue wave generation in multiple-pulsing mode-locked fiber laser. J. Optics **15**, 064005 (2013)
69. Chang, W., Akhmediev, N.: Exploding solitons and rogue waves in optical cavities. In: Grelu, Ph. (ed.) Nonlinear Optical Cavity Dynamics: From Microresonators to Fiber Lasers. Wiley-VCH (2016)
70. Peng, J., Tarasov, N., Sugavanam, S., Churkin, D.: Rogue waves generation via nonlinear soliton collision in multiple-soliton state of a mode-locked fiber laser. Opt. Express, **24**(19), 24256 (2016)
71. Jalali, B., Solli, D., Goda, K., Tsia, K., Ropers, C.: Real-time measurements, rare events and photon economics. Eur. Phys. J. Spec. Top. **185**, 145–157 (2010)
72. Bhushan, A., Coppinger, F., Jalali, B.: Time-stretched analogue-to-digital conversion. Electron. Lett. **34**, 1081–1082 (1998)
73. Coppinger, F., Bhushan, A., Jalali, B.: Photonic time stretch and its application to analog-to-digital conversion. IEEE Trans. Microw. Theory Tech. **47**, 1309–1314 (1999)
74. Suret, P., El Koussaifi, R., Tikan, A., Evain, C., Randoux, S., Szwaj, C., Bielawski, S.: Single-shot observation of optical rogue waves in integrable turbulence using time microscopy. Nat. Commun. **7**, 13136 (2016)
75. Närhi, M., Wetzel, B., Billet, C., Toenger, S., Sylvestre, T., Merolla, J.-M., Morandotti, R., Dias, F., Genty, G., Dudley, J.M.: Real-time measurements of spontaneous breathers and rogue wave events in optical fibre modulation instability. Nat. Commun. (2016). https://doi.org/10.1038/ncomms13675
76. Chang, W., Soto-Crespo, J.M., Vouzas, P., Akhmediev, N.: Spiny solitons and noise-like pulses. J. Opt. Soc. Am. **32**, 1377–1383 (2015)

77. Chang, W., Soto-Crespo, J.M., Vouzas, P., Akhmediev, N.: Extreme amplitude spikes in a laser model described by the complex Ginzburg-Landau equation. Opt. Lett. **40**, 1377–1383 (2015)
78. Chang, W., Soto-Crespo, J.M., Vouzas, P., Akhmediev, N.: Extreme soliton pulsations in dissipative systems. Phys. Rev. E **92**, 022926 (2015)
79. Tsoy, E., Akhmediev, N.: Bifurcations from stationary to pulsating solitons in the cubic–quintic complex Ginzburg-Landau equation. Phys. Lett. A **343**, 417–422 (2005)
80. Tsoy, E., Ankiewicz, A., Akhmediev, N.: Dynamical models for dissipative localized waves of the complex Ginzburg-Landau equation. Phys. Rev. E **73**, 036621 (1–10) (2006)
81. Ankiewicz, A., Akhmediev, N.: Comparison of Lagrangian approach and method of moments for reducing dimensionality of soliton dynamical systems. Chaos **18**, 033129 (2008)
82. Kärtner, F.X.: Few-Cycle Laser Pulse Generation and Its Applications. Springer, Berlin-Heidelberg (2004)
83. Haus, H.A.: Theory of mode locking with a fast saturable absorber. J. Appl. Phys. **46**, 3049 (1975)
84. Haus, H.A.: Mode-locking of lasers. IEEE J. Sel. Top. Quantum Electron. **6**, 1173 (2000)
85. Moores, J.D.: On the Ginzburg-Landau laser mode-locking model with fifth-oder saturable absorber term. Opt. Commun. **96**, 65 (1993)
86. Korytin, A.I., Kryachko, A.Y., Sergeev, A.M.: Dissipative solitons in the complex Ginzburg-Landau equation for femtosecond lasers. Radiophys. Quantum Electron. **44**, 428 (2001)
87. Kovalsky, M.G., Hnilo, A.A., Tredicce, J.R.: Extreme events in the Ti:sapphire laser. Opt. Lett. **36**, 4449–4451 (2011)
88. Runge, A.F.J., Aguergaray, C., Broderick, N.G.R., Erkintalo, M.: Raman rogue waves in a partially mode-locked fiber laser. Opt. Lett. **39**, 319 (2014)
89. Dudley, J.M., Dias, F., Erkintalo, M., Genty, G.: Instabilities, breathers and rogue waves in optics. Nat. Photon. **8**, 755 (2014)
90. Kobtsev, S., Kukarin, S., Smirnov, S., Turitsyn, S., Latkin, A.: Generation of double-scale femto/pico-second optical lumps in mode-locked fiber lasers. Opt. Express **17**, 20707 (2009)
91. Smirnov, S., Kobtsev, S., Kukarin, S., Ivanenko, A.: Three key regimes of single pulse generation per round trip of all-normal-dispersion fiber lasers mode-locked with nonlinear polarization rotation. Opt. Express **20**, 27447 (2012)
92. Wang, Q., Chen, T., Zhang, B., Heberle, A.P., Chen, K.P.: All-fiber passively mode-locked thulium-doped fiber ring oscillator operated at solitary and noiselike modes. Opt. Lett. **36**, 3750 (2011)
93. Linden, S., Giessen, H., Kuhl, J.: XFROG—a new method for amplitude and phase characterization of weak ultrashort pulses. Phys. Stat. Sol. B **206**, 119–124 (1998)

Chapter 10
Periodic and Localized Structures in a Photonic Crystal Fiber Resonator

L. Bahloul, L. Cherbi, A. Hariz, A. Makhoute, E. Averlant and M. Tlidi

Abstract We consider a photonic crystal fiber resonator, driven by a coherent beam. The threshold for appearance of dark localized structures is estimated analytically and numerically by using a weakly nonlinear analysis in the vicinity of the modulational instability threshold. The nonlinear analysis allows to determine the parameter regime where the transition from supercritical to subcritical modulational instability takes place. This transition determines the threshold associated with the formation of dark cavity solitons. Numerical simulations of the governing model equation are in good agreement with the analytical results.

10.1 Introduction

Localized structures (LS's) often called cavity solitons belong to the class of dissipative structures found far from equilibrium. They can be localized in space and consist of bright or dark pulses. Typically, LS's are generated in a sub-critical domain where a uniform solution and a periodic structure coexist. They exhibit a high degree of multistability in a finite range of parameters called a pinning region. Spatial confinement is a universal phenomenon observed in a wide variety of nonlinear systems such as biology, plant ecology, chemistry, fluid mechanics, nonlinear optics and laser physics.

L. Bahloul · L. Cherbi · A. Hariz
Laboratoire of Instrumentation, University of Sciences and Technology Houari Boumediene (USTHB), Bab Ezzouar, Algeria

A. Makhoute
Physique du Rayonnement et des Interactions Laser-Matière, Faculté des Sciences, Université Moulay Ismail, B.P. 11201, Zitoune, Meknès, Morocco

E. Averlant · M. Tlidi (✉)
Département de Physique, Faculté des Sciences, Université Libre de Bruxelles (U.L.B.), CP 231, Campus Plaine, 1050 Bruxelles, Belgium
e-mail: mtlidi@ulb.ac.be

E. Averlant
Brussels Photonics Team, Department of Applied Physics and Photonics (B-PHOT TONA), Vrije Universiteit Brussels, Pleinlaan 2, 1050 Brussels, Belgium

M. Belhaq (ed.), *Recent Trends in Applied Nonlinear Mechanics and Physics*,
Springer Proceedings in Physics 199, https://doi.org/10.1007/978-3-319-63937-6_10

The emergence of LS's is a well-documented issue (see latest overviews on this issue [1–5]). For broad area optical cavities, LSs were fist predicted in [6, 7] and found experimentally in optical bistable systems. They appear when a single homogeneous steady state coexists with periodic structures such as hexagons and stripes [8]. When they are sufficiently separated from each other, bright or dark peaks are independent and randomly distributed in space. However, when the distance between peaks or dips decreases they start to interact via their oscillating, exponentially decaying tails. This interaction then leads to the formation of clusters [9–12].

In fiber cavities, the coupling between chromatic dispersion and nonlinearity may be the source of a temporal modulational instability [13]. The theoretical description of all-fiber resonators is well described by the well known Lugiato and Lefever model (LL model, [14]). As in the case of spatial cavities, LS's are nonlinear bright peaks that have been theoretically predicted [15] and experimentally observed [16] in all fiber cavity driven by a coherent injected signal. This simple and robust device has attracted growing interest in fiber optics due to potential applications for all-optical control of light. All fiber resonators could allow for either the conception of all-optic systems for generation of signals with high repetition rate or to operate as all-optical memories with a bitrate that can reach 25 Gbits/s [16]. Temporal LS's are generated in the pinning range of parameters where the system exhibits a coexistence between two states: the uniform background and the train of pulses of light that emerges from subcritical modulational instability [17]. It has been shown that temporal LSs exhibits a homoclic snaking type of bifurcation [17].

When all fiber cavities are operating close to the zero dispersion regime, it is necessary to take into account high-order chromatic dispersion effects. These effects may play an important role in the dynamics of photonic crystal fibers (PCF's) [18–20]. PCF's allow a high control of the dispersion curve and permit exploring previously inaccessible parameter regimes [21–24]. The inclusion of the fourth order dispersion allows the modulational instability to have a finite domain of existence delimited by two pump power values [25]. Fourth order dispersion has also been predicted to stabilize dark temporal cavity solitons in PCF resonators [17]. Together with this effect, the third order dispersion causes a spontaneous broken reflection symmetry and allows a motion of both periodic and localized structures [26]. The influence of higher order dispersion on the nonlinear dynamical properties of bright temporal LS's in all photonic crystal fiber cavities has been investigated in [27]. Temporal soliton families and resonant radiation near zero group-velocity dispersion have been also reported [28].

The paper is organised as follows. After an introduction, we describe a photonic crystal cavity in Sect. 10.1. We provide a detailed weakly nonlinear analysis near the second threshold associated with the modulational instability in Sect. 10.3. The stationary and drifting LS's are presented in in Sect. 10.4. We conclude in Sect. 10.5.

10.2 Mean Field Model for Photonic Crystal Fiber Cavities

We consider an optical system in which a continuous wave (CW) of power S^2 is launched into a single mode photonic crystal fiber resonator by means of a beam splitter, as shown in Fig. 10.1. The free propagation of light along the fiber is described by a generalized nonlinear Schrödinger equation (NLS) [29] where the propagation constant is expanded to the fourth order of dispersion in Taylor series. The NLS combined with appropriate cavity boundary conditions leads to the model equation [25]:

$$t_r \frac{\partial E(t,\tau)}{\partial t} = (-\alpha - i\delta_0 + i\gamma L|E|^2 - i\beta_2 \frac{L}{2}\frac{\partial^2}{\partial \tau^2} + \beta_3 \frac{L}{6}\frac{\partial^3}{\partial \tau^3} + i\beta_4 \frac{L}{24}\frac{\partial^4}{\partial \tau^4})E(t,\tau) + \sqrt{T}S, \tag{10.1}$$

where $E(t,\tau)$ is the slowly varying envelope of the electric field, t_r is the time of one cavity round trip, t is the slow time scale that describes the evolution of the field envelope from one cavity round trip to the other, and τ is the fast time in the reference frame moving with the group velocity of the light, δ_0 is the detuning between the input beam frequency, and the closest cavity resonance. The coefficients $\beta_{2,3,4}$ account for the second, third and fourth order chromatic dispersion, respectively, γ is nonlinear parameter, α represents the linear dissipation and T is the transmission coefficient of the beam splitter. In addition, we have neglected nonlinear phenomena such as two-photon absorption and Raman scattering, since we deal with pulses width larger than 1 ps [17].

Equation (10.1) is valid when the cavity finesse is high, and when the nonlinear phase shift and losses are much smaller than unity. We furthermore assume that the optical field maintains its polarization as it propagates along the fiber. The (10.1) can be further simplified to obtain a generalized Lugiato-Lefever model in an adimensional form [25]

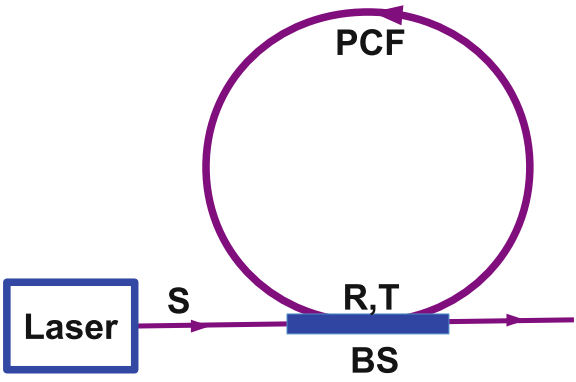

Fig. 10.1 Schematic setup of PCF cavity. The transmission and the reflexion coefficients of the beam spitter (*BS*) are denoted by R and T, respectively. The slowly varying envelope of the electric field circulation inside the cavity is represented by E, and S is the injected field amplitude

$$\frac{\partial E}{\partial t} = S - (1 + i\Delta)E + i\,|E|^2\,E - i\,B_2\frac{\partial^2 E}{\partial \tau^2} + B_3\frac{\partial^3 E}{\partial \tau^3} + i\,B_4\frac{\partial^4 E}{\partial \tau^4}. \tag{10.2}$$

The link between the adimensional variables and parameters and the physical ones are defined in [25]. The homogeneous steady states (HSS) of (10.2) satisfy $S = [1 + i(\Delta - |E_s|^2)]E_s$. We perform a linear stability analysis of the HSS with respect to finite frequency perturbations of the form $\exp(\lambda t + i\Omega\tau)$. This analysis yields the eigenvalues

$$\lambda = -1 + i\,B_3\Omega^3 \pm \sqrt{I_s^2 - (-\Delta + 2I_s + B_2\Omega^2 + B_4\Omega^4)^2} \tag{10.3}$$

where $I_s = |E_s|^2$ corresponds to the uniform intensity background of light.

The system becomes unstable when one of these two eigenvalues becomes zero with a finite frequency. The system exhibits a modulational instability between the first threshold $I_{c1} = 1$, and the second threshold $I_{c2} = [2\kappa + \sqrt{\kappa^2 - 3}]/3$ with $\kappa = B_2^2/(4B_4) + \Delta$. It has been shown in [25, 27] that the fourth-order dispersion limits the region of modulation instability between these two intensity levels. Indeed, when $B_4 = 0$, the second threshold does not exist. We note also frequency degeneracy Ω_l^2 and Ω_u^2 at the first instability threshold where $\Omega_{l,u}^2 = [-B_2 \pm \sqrt{B_2^2 + 4B_4(\Delta - 2)}]/(2B_4)$. At the second threshold I_{c2}, a new critical frequency appears $\Omega^2 = -B_2/2B_4$.

In what follows, we remove the frequency degeneracy for the first threshold by choosing B_2, B_4 and Δ such as $B_2^2 + 4(\Delta - 2)B_4 = 0$. In this case, the MI zone is limited between two thresholds, the first at $I_{1c} = 1$ and the second will be at $I_{2c} = 5/3$, while the destabilized frequencies in both thresholds will be equal to $\Omega_c^2 = \Omega_l^2 = \Omega_u^2 = -B_2/(2B_4)$.

10.3 Weakly Nonlinear Analysis

We shall describe the nonlinear evolution of the system in the vicinity of the second instability point $I_{2c} = 5/3$. The small-amplitude inhomogeneous stationary solutions, i.e., solutions that are independent of slow t and fast τ times can be calculated analytically by employing the standard theory [30, 31]. For this purpose, we first decompose the electric field into its real and imaginary parts: $E = x_1 + i\,x_2$ and introduce the excess variables as $(x_1(t,\tau), x_2(t,\tau)) = (x_{1s}, x_{2s}) - (U(t,\tau), V(t,\tau))$ with x_{1s} and x_{2s} are, respectively, the real and the imaginary parts of the homogeneous solutions independent of t and τ. The homogeneous solutions of (10.2) obey to

$$-x_{1s} + S - x_{2s}(x_{1s}^2 + x_{2s}^2 - \Delta) = 0\,, \tag{10.4}$$

$$-x_{2s} + x_{1s}(x_{1s}^2 + x_{2s}^2 - \Delta) = 0\,. \tag{10.5}$$

Next, we introduce a small parameter $\epsilon \ll 1$ which measures the distance from the critical modulational point. We expand all variables around their critical values at the bifurcation point.

$$S = S_{2c} + \epsilon\mu_1 + \epsilon^2\mu_2 + \cdots \tag{10.6}$$

$$(U, V) = \epsilon(U_0, V_0) + \epsilon^2(U_1, V_1) + \epsilon^3(U_2, V_2) + \cdots \tag{10.7}$$

$$(x_{1s}, x_{2s}) = (a_0, b_0) + \epsilon(a_1, b_1) + \epsilon^2(a_2, b_2) + \cdots \tag{10.8}$$

We expand the time as

$$\frac{\partial}{\partial t} = \frac{\partial}{\partial T_0} + \epsilon\frac{\partial}{\partial T_1} + \epsilon^2\frac{\partial}{\partial T_2} + \cdots \tag{10.9}$$

At the leading order in ϵ we find that $a_0 = b_0 = \mu_1 = 0$. At this order, near the critical point we can approximate soltuions by a linear superposition of the corresponding critical frequencies Ω_c and Q_c

$$(U_0, V_0) = \left(1, \frac{\rho + 3}{1 - 3\rho}\right)\tilde{W}\exp i(Q_c T_0 + \Omega_c \tau) + c.c. \tag{10.10}$$

where $c.c.$ denotes the complex conjugate and $\rho = 5/3 - \Delta$. The complex amplitude $\tilde{W}$ associated with the frequancy Ω_c does not depend on the time τ, it depends only on the time T_0. The quantities a_i, b_i, U_i, and V_i can be calculated by inserting (10.6–10.9) into (10.2, 10.4, 10.5) and equating terms with the same powers of ϵ. At order ϵ^2, the solvavility condition imposes that $a_1 = b_1 = \mu_1 = 0$. The application of the solvability condition to the order ϵ^3 brings an amplitude equation for the unstable mode. In terms of the unscaled amplitudes (W $= \epsilon\ \tilde{W} + \cdots$), we obtain

$$\frac{\partial W}{\partial t} = \mu W + (f_r + i f_i)W|W|^2 \tag{10.11}$$

in which

$$\mu = \frac{S - S_{2c}}{(3\rho + 1))(\rho + 3)S_c} \text{ with } S_{2c} = \sqrt{\frac{5}{3}}\sqrt{1 + \rho^2} \tag{10.12}$$

$$f_r = \frac{ac + bd}{c^2 + d^2} \text{ and } f_i = \frac{bc - ad}{c^2 + d^2} \tag{10.13}$$

where the coefficients a, b, c and d are expressed in term of the detuning parameter $\Delta = 5/3 - \rho$ as

$$
\begin{aligned}
a &= -4(\Delta-2)(\alpha_1+\alpha_2)+\alpha_3\\
\alpha_1 &= 59049\Delta^7 - 798255\Delta^6 + 4417983\Delta^5 - 13345641\Delta^4\\
\alpha_2 &= 24735807\Delta^3 - 29605896\Delta^2 + 21969258\Delta - 7708940\\
\alpha_3 &= 600(486\Delta^6 - 5508\Delta^5 + 24435\Delta^4 - 57654\Delta^3 + 82686\Delta^2 - 73156\Delta + 30792)B_3\Omega^3\\
b &= -60(3\Delta-4)(243\Delta^5 - 2268\Delta^4 + 7398\Delta^3 - 11412\Delta^2 + 11040\Delta - 7304)B_3\Omega^3\\
c &= 3(3\Delta^2 - 20\Delta + 28)(3\Delta-4)^2 c_1\\
c_1 &= (9\Delta^2 - 30\Delta + 34)^2(100(B_3\Omega^3)^2 - 81\Delta^2 + 348\Delta - 372)\\
d &= -60(\Delta-2)(3\Delta-14)(3\Delta-4)^2(9\Delta^2 - 30\Delta + 34)^2 B_3\Omega^3
\end{aligned}
$$

When $f_r(\Delta) < 0$, the modulational instability is subcritical. In this case, it is necessary to retain the fifth order in ϵ, since (10.11) loses its meaning. Thus, if $f_r(\Delta) > 0$, the modulational instability is supercritical, leading to stable small amplitude temporal structures. The parameter regime where the bifurcation is supercritical is plotted in Fig. 10.2a. The transition from super- to sub-critical modulationnal instability is explicitly given by $f_r = 0$. This condition corresponds to the threshold of the emergence of temporal cavity solitons that we shall discuss is the next section. The dependence of the threshold as a function of the third order dispersion coefficient and of the detuning parameter is shown in Fig. 10.2b. Note, however, that the third order dispersion affects the threshold of the modulational instability as well. In the supercritical case where $f_r(\Delta) > 0$, we seek for solutions of (10.11) in the form of $W = A\exp(iRt)$. Inserting this ansatz in (10.11), the stationary solutions are

$$A_s = 0,\ A_s = \pm\sqrt{\frac{-\mu}{f_r}} \text{ and } R = \frac{\mu f_i}{f_r} \tag{10.14}$$

The third order dispersion breaks the symmetry $(\tau, -\tau)$. This breaking symmetry induces a motion of temporal structures and the linear and nonlinear correction to their velocity is

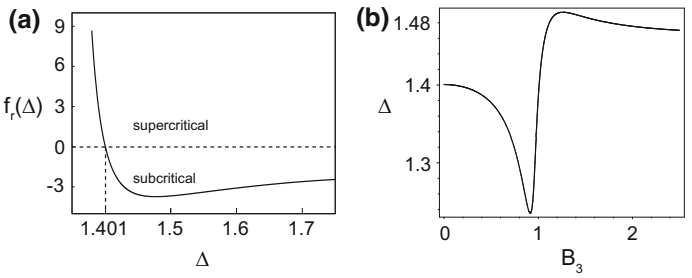

Fig. 10.2 The threshold associated with the transition from super- to sub-critical modulational instability is plotted **a** as a function of the detuning parameter Δ for $B_3 = 0$; **b** in the plane (B_3, Δ). Others parameters are $B_4 = 0.5$, and $B_2 = \sqrt{4B_4(2-\Delta)}$

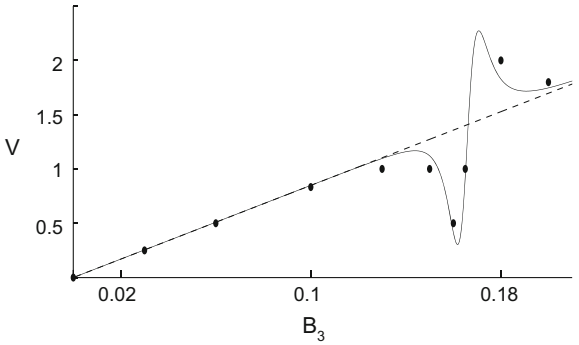

Fig. 10.3 Linear velocity of the periodic structure and its nonlinear correction with respect to B_3. *Dashed curve* denotes the linear velocity. The velocity with its nonlinear correction (10.15) is plotted by a *solid line*. The velocity obtained from direct numerical simulations of (10.2) are indicated by circles. Parameters are $S = 1.4307$, $\epsilon^2 = 0.006$, $\Delta = 1.2$, $B_4 = 0.1$, and $B_2 = -0.5657$

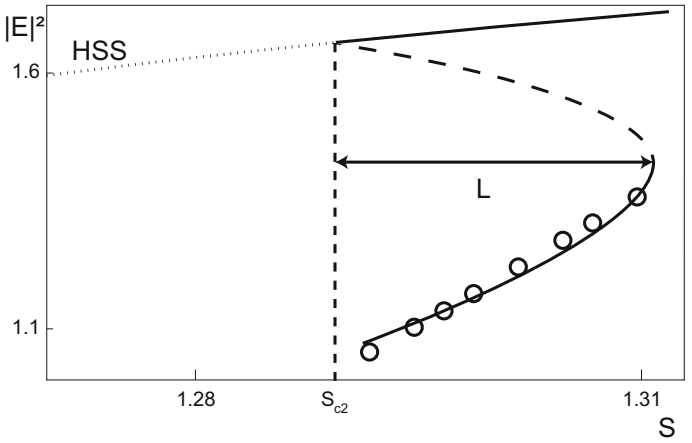

Fig. 10.4 Bifurcation diagram associated with the temporal train of periodic pulses that emerges from subcritical modulational instability. Parameter are $B_4 = 0.1$, $B_2 = -0.3347$, $B_3 = 0$, $\Delta = 1.72$, The *full* (*dashed*) *curve* indicates stable (unstable) solutions. The *open circles* represent the numerical values of the minimum intensity of the temporal train of periodic pulses

$$v = v_l + v_{nl} \text{ with } v_l = \frac{\partial \lambda_i}{\partial \Omega} \text{ and } v_{nl} = \frac{\partial R}{\partial \Omega} \tag{10.15}$$

In terms of the dynamical parameters the linear and the nonlinear velocities are

$$v_l = 3B_3\Omega^2 \text{ and } v_{nl} = \frac{\mu}{f_r}\frac{\partial f_i}{\partial \Omega} \tag{10.16}$$

The velocity as a function of the third order dispersion coefficient (10.16) is plotted in Fig. 10.3. The velocity of moving temporal structures calculated through numerical simulations of the model, (10.2), is in good agreement with the one estimated from the above analysis.

10.4 Moving Localized Structures

In this section, we are interested in the situation where the bifurcation towards modulational instability appears subcritically. In the absence of the third order dispersion, the typical bifurcation diagram is shown in Fig. 10.4. In the domain, denoted by L, the system exhibits a coexistence between two stable solutions: the homogeneous

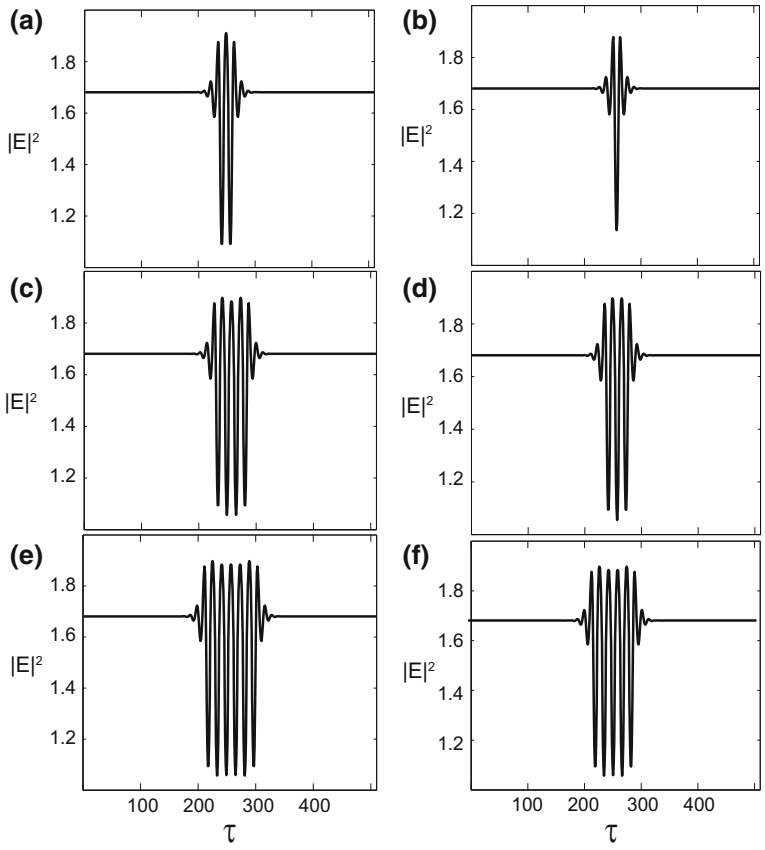

Fig. 10.5 Stationary temporal *dark cavity* solitons with up to 6 dips. **a**-**f** corresponding to 1–6 dips or holes in the insensity profiles, respectively. Parameters are the same as Fig. 10.3 with $B_3 = 0$

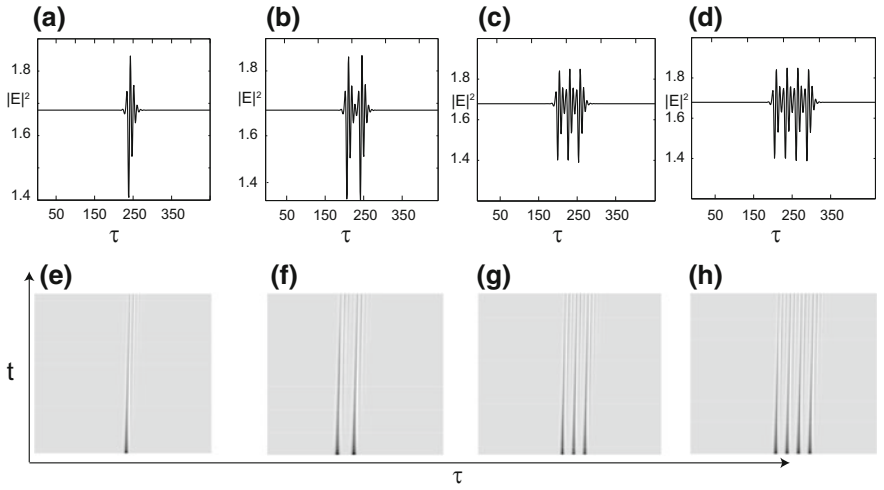

Fig. 10.6 Moving temporal *dark cavity* solitons with up to 4 dips. **a**-**f** are the intensity profiles in the PCF cavity at $t = 0$, whereas **e**-**h** are space-time maps in the (t,τ) plane. Parameters are the same as Fig. 10.3 with $B_3 = 0.1$

steady state (uniform background) and the temporal train of periodic pulses that emerges from subcritical modulational instability. Temporal dark cavity solitons, connecting the HSS and a branch of periodic solutions, are found in a well-defined region of parameters called a pinning zone denoted L in Fig. 10.4. It has been shown that temporal cavity solitons exhibit a homoclinic snaking type of bifurcation [17]. Depending on the initial condition used, a single dip, or multiple ones in the intensity profile can be generated in direct numerical simulations of (10.2). Examples of stationary temporal dark cavity solitons involving one to six dips as shown in Fig. 10.5. They are obtained from the same values of parameters and they are characterized by an oscillating exponentially decaying tails.

Let us now investigate the effect of third order dispersion on the dark cavity solitons. As we have already mentioned, this effect breaks the reflexion symmetry ($\tau \rightarrow -\tau$) of temporal cavity solitons emerging from subcritical bifurcation point. This symmetry breaking induces a drift of the temporal cavity solitons with a constant velocity. Examples of drifiting temporal dark cavity solitons are shown in τ-t maps of the Fig. 10.6.

10.5 Conclusions

In this paper, we have investigated the weakly nonlinear dynamics of all fiber cavities with both fourth and third order dispersions in the neighborhood of the second modulational instability point. We have estimated the velocity of moving temporal

train of periodic pulses that emerge from supercritical modulational instability point. The drift is a consequence of the third order dispersion that breaks the reflexion symmetry ($\tau \rightarrow -\tau$). When the modulational instability appears subcritically, we found moving temporal dark solitons that can be either isolated or self-organized.

Acknowledgements M.T. received support from the Fonds National de la Recherche Scientifique (Belgium). M.T acknowledges the financial support of the Interuniversity Attraction Poles program of the Belgian Science Policy Office, under grant IAP 7–35 *photonics@be*.

References

1. Leblond, H., Mihalache, D.: Models of few optical cycle solitons beyond the slowly varying envelope approximation. Phys. Rep. **523**(2), 61–126 (2013)
2. Tlidi, M., Staliunas, K., Panajotov, K., Vladimirov, A.G., Clerc, M.G.: Localized structures in dissipative media: from optics to plant ecology. Philos. Trans. R. Soc. Lond. A: Math. Phys. Eng. Sci. **372**, 20140101 (2014)
3. Lapine, M., Shadrivov, I.V., Kivshar, Y.S.: Colloquium: nonlinear metamaterials. Rev. Mod. Phys. **86** (2014) 1093–1123. http://dx.doi.org/10.1103/RevModPhys.86.1093. http://link.aps.org/doi/10.1103/RevModPhys.86.1093
4. Knobloch, E.: Spatial localization in dissipative systems. Ann. Rev. Condens. Matter Phys. **6**(1), 325–359 (2015). https://doi.org/10.1146/annurev-conmatphys-031214-014514
5. Lugiato, L., Prati, F., Brambilla, M.: Nonlinear Optical Systems. Cambridge University Press (2015)
6. McLaughlin, D.W., Moloney, J.V., Newell, A.C.: Solitary waves as fixed points of infinite-dimensional maps in an optical bistable ring cavity. Phys. Rev. Lett. **51**, 75 (1983). http://dx.doi.org/10.1103/PhysRevLett.51.75. http://link.aps.org/doi/10.1103/PhysRevLett.51.75
7. Rosanov, N.N., Khodova, G.V.: Autosolitons in bistable interferometers. Opt. Spectrosc. **65**, 449–450 (1988)
8. Tlidi, M., Mandel, P., Lefever, R.: Localized structures and localized patterns in optical bistability. Phys. Rev. Lett. **73**, 640–643 (1994). http://dx.doi.org/10.1103/PhysRevLett.73.640. http://link.aps.org/doi/10.1103/PhysRevLett.73.640
9. Vladimirov, A., McSloy, J., Skryabin, D., Firth, W.: Two-dimensional clusters of solitary structures in driven optical cavities. Phys. Rev. E **65**, 046606 (2002). http://dx.doi.org/10.1103/PhysRevE.65.046606. http://link.aps.org/doi/10.1103/PhysRevE.65.046606
10. Tlidi, M., Vladimirov, A.G., Mandel, P.: Interaction and stability of periodic and localized structures in optical bistable systems. IEEE J. Quantum Electron. **39**(2), 216–226 (2003). http://dx.doi.org/10.1109/JQE.2002.807193
11. Tlidi, M., Lefever, R., Vladimirov, A.: On vegetation clustering, localized bare soil spots and fairy circles. Lect. Notes Phys. **751**, 381 (2008)
12. Vladimirov, A.G., Lefever, R., Tlidi, M.: Relative stability of multipeak localized patterns of cavity solitons. Phys. Rev. A **84**, 043848 (2011). http://dx.doi.org/10.1103/PhysRevA.84.043848. http://link.aps.org/doi/10.1103/PhysRevA.84.043848
13. Haelterman, M., Trillo, S., Wabnitz, S.: Additive-modulation-instability ring laser in the normal dispersion regime of a fiber. Opt. Lett. **17**(10), 745–747 (1992). http://dx.doi.org/10.1364/OL.17.000745. http://ol.osa.org/abstract.cfm?URI=ol-17-10-745
14. Lugiato, L.A., Lefever, R.: Spatial dissipative structures in passive optical systems. Phys. Rev. Lett. **58**, 2209–2211 (1987). http://dx.doi.org/10.1103/PhysRevLett.58.2209. http://link.aps.org/doi/10.1103/PhysRevLett.58.2209
15. Scroggie, A.J., Firth, W.J., McDonald, G.S., Tlidi, M., Lefever, R., Lugiato, L.A.: Pattern formation in a passive kerr cavity, Chaos, Solitons Fractals **4**(8), 1323 (1994). https://doi.org/10.1016/0960-0779(94)90084-1

16. Leo, F., Coen, S., Kockaert, P., Gorza, S.-P., Emplit, P., Haelterman, M.: Temporal cavity solitons in one-dimensional kerr media as bits in an all-optical buffer. Nat. Photon. **4**, 471 (2010). http://dx.doi.org/10.1038/nphoton.2010.120
17. Tlidi, M., Gelens, L.: High-order dispersion stabilizes dark dissipative solitons in all-fiber cavities. Opt. Lett. **35**(3), 306–308 (2010). http://dx.doi.org/10.1364/OL.35.000306. http://ol.osa.org/abstract.cfm?URI=ol-35-3-306
18. Cavalcanti, S.B., Cressoni, J.C., da Cruz, H.R., Gouveia-Neto, A.S.: Modulation instability in the region of minimum group-velocity dispersion of single-mode optical fibers via an extended nonlinear Schrödinger equation. Phys. Rev. A **43**, 6162–6165 (1991). http://dx.doi.org/10.1103/PhysRevA.43.6162. http://link.aps.org/doi/10.1103/PhysRevA.43.6162
19. Pitois, S., Millot, G.: Experimental observation of a new modulational instability spectral window induced by fourth-order dispersion in a normally dispersive single-mode optical fiber. Opt. Commun. **226**(16), 415–422 (2003). https://doi.org/10.1016/j.optcom.2003.09.001. http://www.sciencedirect.com/science/article/pii/S0030401803019217
20. Harvey, J.D., Leonhardt, R., Coen, S., Wong, G.K.L., Knight, J., Wadsworth, W.J., Russell, P.S.: Scalar modulation instability in the normal dispersion regime by use of a photonic crystal fiber. Opt. Lett. **28**(22), 2225–2227 (2003). http://dx.doi.org/10.1364/OL.28.002225http://ol.osa.org/abstract.cfm?URI=ol-28-22-2225
21. Joly, N.Y., Omenetto, F.G., Efimov, A., Taylor, A.J., Knight, J.C., Russell, P.S.J.: Competition between spectral splitting and raman frequency shift in negative-dispersion slope photonic crystal fiber, Opt. Commun. **248**(13), 281–285 (2005). https://doi.org/10.1016/j.optcom.2004.11.091. http://www.sciencedirect.com/science/article/pii/S0030401804012477
22. Yulin, A.V., Skryabin, D.V., Russell, P.S.J.: Four-wave mixing of linear waves and solitons in fibers with higher-order dispersion. Opt. Lett. **29**(20), 2411–2413 (2004). http://dx.doi.org/10.1364/OL.29.002411. http://ol.osa.org/abstract.cfm?URI=ol-29-20-2411
23. Wadsworth, W.J., Joly, N., Knight, J.C., Birks, T.A., Biancalana, F., Russell, P.S.J.: Supercontinuum and four-wave mixing with q-switched pulses in endlessly single-mode photonic crystal fibres. Opt. Express **12**(2), 299–309 (2004). http://dx.doi.org/10.1364/OPEX.12.000299. http://www.opticsexpress.org/abstract.cfm?URI=oe-12-2-299
24. Demircan, A., Bandelow, U.: Supercontinuum generation by the modulation instability. Opt. Commun. **244**(16), 181–185 (2005). https://doi.org/10.1016/j.optcom.2004.09.049. http://www.sciencedirect.com/science/article/pii/S0030401804009526
25. Tlidi, M., Mussot, A., Louvergneaux, E., Kozyreff, G., Vladimirov, A.G., Taki, M.: Control and removal of modulational instabilities in low-dispersion photonic crystal fiber cavities. Opt. Lett. **32**(6), 662–664 (2007). http://dx.doi.org/10.1364/OL.32.000662. http://ol.osa.org/abstract.cfm?URI=ol-32-6-662
26. Tlidi, M., Bahloul, L., Cherbi, L., Hariz, A., Coulibaly, S.: Drift of dark cavity solitons in a photonic-crystal fiber resonator. Phys. Rev. A **88**, 035802 (2013). http://dx.doi.org/10.1103/PhysRevA.88.035802. http://link.aps.org/doi/10.1103/PhysRevA.88.035802
27. Bahloul, L., Cherbi, L., Hariz, A., Tlidi, M.: Temporal localized structures in photonic crystal fibre resonators and their spontaneous symmetry-breaking instability. Philos. Trans. R. Soc. Lond. A: Math. Phys. Eng. Sci. **372**(2027) (2014). http://dx.doi.org/10.1098/rsta.2014.0020
28. Milián, C., Skryabin, D.: Soliton families and resonant radiation in a micro-ring resonator near zero group-velocity dispersion. Opt. Express **22**(3), 3732–3739 (2014). https://doi.org/10.1364/OE.22.003732. http://www.opticsexpress.org/abstract.cfm?URI=oe-22-3-3732
29. Agrawal, G.P.: Nonlinear Fiber Optics, 5th edn, Academic Press (2012)
30. Manneville, P.: Dissipative Structures and Weak Turbulence. Academic Press (1990)
31. Tlidi, M., Lefever, R., Mandel, P.: Pattern selection in optical bistability. Quantum Semiclassical Opt. J. Eur. Opt. Soc. Part B **8**(4), 931 (1996). http://stacks.iop.org/1355-5111/8/i=4/a=014

Chapter 11
Exploring the Nonlinear Stochastic Dynamics of an Orchard Sprayer Tower Moving Through an Irregular Terrain

Americo Cunha Jr, Jorge Luis Palacios Felix and José Manoel Balthazar

Abstract In agricultural industry, the process of orchards spraying is of extreme importance to avoid losses and reduction of quality in the products. In orchards spraying process an equipment called sprayer tower is used. It consists of a reservoir and fans mounted over an articulated tower, which is supported by a vehicle suspension. Due to soil irregularities this equipment is subject to random loads, which may hamper the proper dispersion of the spraying fluid. This work presents the construction of a consistent stochastic model of uncertainties to describe the non-linear dynamics of an orchard sprayer tower. In this model, the mechanical system is described by as a multi-body with three degrees of freedom, and random loadings as a harmonic random process. Uncertainties are taken into account through a parametric probabilistic approach, where maximum entropy principle is used to specify random parameters distributions. The propagation of uncertainties through the model is computed via Monte Carlo method.

11.1 Introduction

The spraying process of orchards has extreme importance in fruit growing, not only to prevent the economic damages associated with the loss of a production, but also to ensure the quality of the fruit that will arrive the final consumer. This process uses an equipment, called *sprayer tower*, which is illustrated in Fig. 11.1. This equipment is composed by a vehicle suspension and a support tower, equipped with several fans, and in a typical operating condition it vibrates nonlinearly [2, 8].

A. Cunha Jr (✉)
Universidade do Estado do Rio de Janeiro, Rio de Janeiro, Brazil
e-mail: americo@ime.uerj.br

J.L.P. Felix
Universidade Federal da Fronteira Sul, Chapecó, Brazil
e-mail: jorge.felix@uffs.edu.br

J.M. Balthazar
Instituto Tecnológico de Aeronáutica, São José dos Campos, Brazil
e-mail: jmbaltha@ita.br

M. Belhaq (ed.), *Recent Trends in Applied Nonlinear Mechanics and Physics*,
Springer Proceedings in Physics 199, https://doi.org/10.1007/978-3-319-63937-6_11

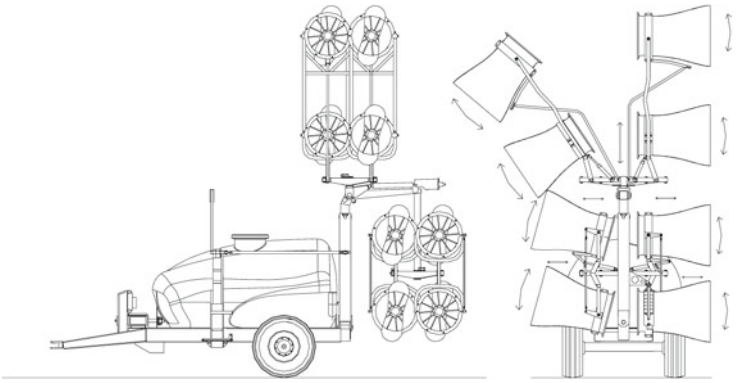

Fig. 11.1 Sketch of the orchard sprayer tower (courtesy of Máquinas Agrícolas Jacto S/A)

Understanding the dynamics of this equipment is essential to its design and also to discover operating conditions that may be harmful to the spraying process. In this sense, this work aims to model the nonlinear dynamics of the sprayer tower, taking into account the deterministic and stochastic aspects. In particular, it is of great interest to predict the maximum amplitude of the lateral vibration of the structure, and verify if the uncertainties in the soil-induced loadings are capable of generating undesirable levels of oscillations.

The rest of this chapter is organized as follows. In Sect. 11.2 it is presented the deterministic model and analysis for the mechanical system. A stochastic model to take into account the uncertainties associated to the model parameters, and the corresponding stochastic simulations are shown in Sect. 11.3. Finally, in Sect. 11.4, final remarks are highlighted.

11.2 Deterministic Analysis

In the modeling process developed here, the mechanical system is considered as the multibody system illustrated in Fig. 11.2. The masses of the chassis and the tank are assumed to be concentrated at the bottom of the double pendulum, as a point mass denoted by m_1. On the other hand, the point mass m_2, at the top of the double pendulum, takes into account the masses of the fans. The point of articulation between the moving suspension and the tower is denoted by P and its distance to the suspension center of gravity is L_1. The junction P has torsional stiffness k_T, and damping torsional coefficient c_T. The tower has length L_2, and is considered to be massless. The left wheel of the vehicle suspension is represented by a pair spring/damper with constant respectively given by k_1 and c_1 located at a distance B_1 from suspension center line, and it is subject to a vertical displacement y_{e1}. Similarly, the right wheel is represented by a pair spring/damper characterized by k_2 and c_2, it

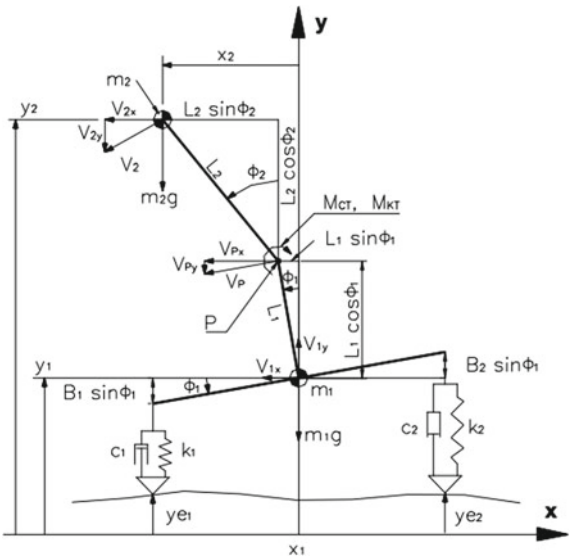

Fig. 11.2 Schematic representation of the mechanical-mathematical model: an inverted double pendulum, mounted on a moving suspension

is B_2 away from suspension center line, and displaces vertically y_{e2}. The moments of inertia of the suspension and of the tower, with respect to their centers of gravity, are respectively denoted by I_1 and I_2. The acceleration of gravity is denoted by g. Finally, introducing the inertial frame of reference XY, the vertical displacement of the suspension is measured by y_1, while its rotation is computed by ϕ_1, and the rotation of the tower is denoted by ϕ_2. Therefore, this model, which was developed by [7, 8], has three degrees of freedom: y_1, ϕ_1 and ϕ_2.

It can be deduced from the geometry of Fig. 11.2 that tower horizontal (lateral) displacement is given by

$$x_2 = -L_1 \sin\phi_1 - L_2 \sin\phi_2. \tag{11.1}$$

Typically, the sprayer tower moves on an irregular terrain during its operation, which induces oscillatory displacements (loads) in the tires. In order to reproduce a typical load (induced by soil) the left and right tires displacements are respectively assumed to be periodic functions in time, out of phase, with the same amplitude, and a single frequencial component,

$$y_{e1}(t) = A \sin(\omega t), \quad \text{and} \quad y_{e2}(t) = A \sin(\omega t + \rho), \tag{11.2}$$

where A and ω respectively denotes the amplitude and frequency of the tires displacements, and ρ is the phase shift between the two tires.

Employing a Lagrangian formalism to obtain the nonlinear dynamical system associated to the mechanical system, the following set of ordinary differential equations is obtained

$$[M]\begin{pmatrix}\ddot{y}_1\\ \ddot{\phi}_1\\ \ddot{\phi}_2\end{pmatrix}+[N]\begin{pmatrix}\dot{y}_1^2\\ \dot{\phi}_1^2\\ \dot{\phi}_2^2\end{pmatrix}+[C]\begin{pmatrix}\dot{y}_1\\ \dot{\phi}_1\\ \dot{\phi}_2\end{pmatrix}+[K]\begin{pmatrix}y_1\\ \phi_1\\ \phi_2\end{pmatrix}=\mathbf{g}-\mathbf{h}, \quad (11.3)$$

where $[M]$, $[N]$, $[C]$ and $[N]$ are 3×3 (configuration dependent) real matrices, respectively, defined by

$$[M]=\begin{bmatrix} m_1+m_2 & -m_2\,L_1\,\sin\phi_1 & -m_2\,L_2\,\sin\phi_1\\ -m_2\,L_1\,\sin\phi_1 & I_1+m_2\,L_1^2 & m_2\,L_1\,L_2\,\cos(\phi_2-\phi_1)\\ -m_2\,L_2\,\sin\phi_1 & m_2\,L_1\,L_2\,\cos(\phi_2-\phi_1) & I_2+m_2\,L_2^2\end{bmatrix}, \quad (11.4)$$

$$[N]=\begin{bmatrix} 0 & -m_2\,L_1\,\cos\phi_1 & -m_2\,L_2\,\cos\phi_2\\ 0 & 0 & -m_2\,L_1\,L_2\,\sin(\phi_2-\phi_1)\\ 0 & -m_2\,L_1\,L_2\,\sin(\phi_2-\phi_1) & 0\end{bmatrix}, \quad (11.5)$$

$$[C]=\begin{bmatrix} c_1+c_2 & (c_2\,B_2-c_1\,B_1)\cos\phi_1 & 0\\ (c_2\,B_2-c_1\,B1)\cos\phi_1 & c_T+(c_1\,B_1^2+c_2\,B_2^2)\cos^2\phi_1 & -c_T\\ 0 & -c_T & c_T\end{bmatrix}, \quad (11.6)$$

$$[K]=\begin{bmatrix} k_1+k_2 & 0 & 0\\ (k_2\,B_2-k_1\,B1)\cos\phi_1 & k_T & -k_T\\ 0 & -k_T & k_T\end{bmatrix}, \quad (11.7)$$

and let $\mathbf{g}$, and $\mathbf{h}$ be (configuration dependent) vectors in $\mathbb{R}^3$, respectively, defined by

$$\mathbf{g}=\begin{pmatrix}(k_2\,B_2-k_1\,B_1)\sin\phi_1+(m_1+m_2)g\\ (k_1\,B_1^2+k_2\,B_2^2)\sin\phi_1\,\cos\phi_1-m_2\,g\,L_1\,\sin\phi_1\\ -m_2\,g\,L_2\,\sin\phi_2\end{pmatrix}, \quad (11.8)$$

and

$$\mathbf{h}=\begin{pmatrix}k_1\,y_{e1}+k_2\,y_{e2}+c_1\,\dot{y}_{e1}+c_2\,\dot{y}_{e2}\\ -B_1\,\cos\phi_1\,(k_1\,y_{e1}+c_1\,\dot{y}_{e1})+B_2\,\cos\phi_1\,(k_2\,y_{e2}+c_2\,\dot{y}_{e2})\\ 0\end{pmatrix}. \quad (11.9)$$

Considering the static equilibrium configuration as initial condition, the resulting nonlinear initial value problem is integrated using a Runge-Kutta method [1].

Table 11.1 Nominal parameters used in the simulations of the mechanical system

Parameter	Value	Unit
m_1	6500	kg
m_2	800	kg
L_1	0.2	m
L_2	2.4	m
I_1	6850	kg m^2
I_2	6250	kg m^2
k_1	465×10^3	N/m
k_2	465×10^3	N/m
c_1	5.6×10^3	N/m/s
c_2	5.6×10^3	N/m/s
B_1	0.85	m
B_2	0.85	m
k_T	45×10^3	N/rad
c_T	50×10^3	N m/rad/s
A	0.15	m
w	2π	rad/s
ρ	$\pi/4$	rad

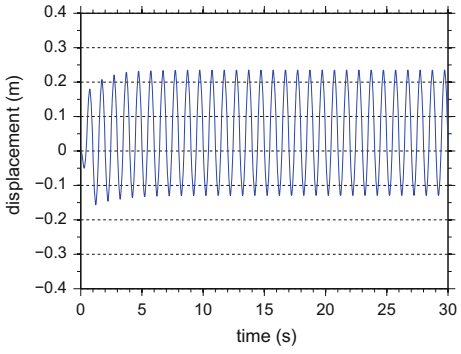

Fig. 11.3 Time series of tower horizontal dynamics: x_2

The evolution of this nonlinear dynamic system is investigated in the interval $[t_0, t_f] = [0,30]s$, adopting for the physical and geometrical parameters the nominal (deterministic) values shown in Table 11.1.

The time series corresponding to the tower horizontal (lateral) dynamics x_2 can be seen in Fig. 11.3, while the corresponding phase space trajectories projections (in $\mathbb{R}^3$ and $\mathbb{R}^2$) are presented in Fig. 11.4.

From a qualitative point of view, the simulation results shown in Figs. 11.3 and 11.4 allow one to see that, after a transient regime of approximately 5 s, the sprayer tower dynamics accumulate into a limit cycle. Hence, for any practical purpose,

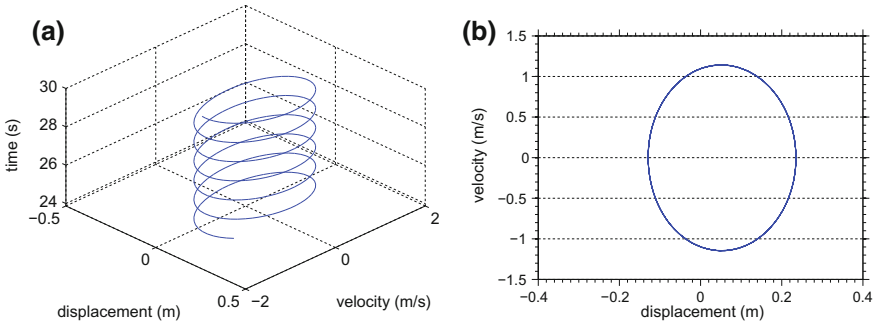

Fig. 11.4 Projections of horizontal dynamics phase space trajectory. **a** x_2 atractor in $\mathbb{R}^3$; **b** x_2 atractor in $\mathbb{R}^2$

the permanent behavior is periodic. In addition, from the quantitative point of view, these same results show that the tower can oscillate with amplitude bigger then 0.2 m, which is the value of B_1 and B_2. This shows that the sprayer tower can reach a critical level of horizontal (lateral) vibration, which can be harmful to the spraying process.

This analysis used a deterministic model for dynamics, where amplitude and frequency of external loading are assumed to be known. However, in practice, amplitude and frequency of external excitation are not known with precision, which induces uncertainties to the dynamic response of the structure. Taking into account the effect of these uncertainties on the model response is essential for a robust design, being the purpose of the next section.

11.3 Stochastic Analysis

Consider a probability space $(\Theta, \Sigma, \mathbb{P})$, where Θ is a sample space, Σ is a σ-field over Θ, and $\mathbb{P} : \Sigma \to [0,1]$ is a probability measure. In this probabilistic space, the amplitude A and the frequency ω are respectively modeled by the independent random variables $\mathbb{A} : \Sigma \to \mathbb{R}$ and $\mathbb{\omega} : \Sigma \to \mathbb{R}$.

To specify the distribution of these random parameters, based only on theoretical information known about them, the maximum entropy principle is employed [5, 10]. For $\mathbb{A}$, which is a positive parameter, it is assumed that: (i) the support of the probability density function (PDF) is the positive real line, i.e., $\mathtt{Supp}\ p_{\mathbb{A}} = (0, +\infty)$; (ii) the mean value is known, i.e. $\mathbb{E}\{\mathbb{A}\} = \mu_{\mathbb{A}} \in (0, +\infty)$; and (iii) $\mathbb{A}^{-1}$ is a second order random variable, so that $\mathbb{E}\{\ln \mathbb{A}\} = q,\ |q| < +\infty$. Besides that, for $\mathbb{\omega}$, that is also a positive parameter, the only known information is assumed to be the support $\mathtt{Supp}\ p_{\mathbb{\omega}} = [\omega_1, \omega_2] \subset (0, +\infty)$.

Consequently, the distributions which maximize the entropy have the following PDFs

$$p_{\mathbb{A}}(a) = \mathbb{1}_{(0,+\infty)}(a)\,\frac{1}{\mu_{\mathbb{A}}}\left(\frac{1}{\delta_{\mathbb{A}}^2}\right)^{\left(\frac{1}{\delta_{\mathbb{A}}^2}\right)}\frac{1}{\Gamma(1/\delta_{\mathbb{A}}^2)}\left(\frac{a}{\mu_{\mathbb{A}}}\right)^{\left(\frac{1}{\delta_{\mathbb{A}}^2}-1\right)}\exp\left(-\frac{a}{\delta_{\mathbb{A}}^2\mu_{\mathbb{A}}}\right), \tag{11.10}$$

and

$$p_{\mathbb{\omega}}(\omega) = \mathbb{1}_{[\omega_1,\omega_2]}(\omega)\,\frac{1}{\omega_2-\omega_1}, \tag{11.11}$$

which correspond, respectively, to the gamma and uniform distributions. In the above equations $\mathbb{1}_X(x)$ denotes the indicator function of the set X, and $0 \leq \delta_{\mathbb{A}} = \sigma_{\mathbb{A}}/\mu_{\mathbb{A}} < 1/\sqrt{2}$ is a dispersion parameter, being $\sigma_{\mathbb{A}}$ the standard deviation of $\mathbb{A}$.

The stochastic simulations reported here adopted, for the random variables $\mathbb{A}$ and $\mathbb{\omega}$, the following parameters $\mu_{\mathbb{A}} = 0.15\,m$, $\sigma_{\mathbb{A}} = 0.2 \times \mu_{\mathbb{A}}$, and $[\omega_1, \omega_2] = [0, 2] \times 2\pi\ rad/s$.

Due to the randomness of $\mathbb{A}$ and $\mathbb{\omega}$, the tire displacements are now described by the following random processes

$$\mathbb{y}_{e1}(t) = \mathbb{A}\,\sin(\mathbb{\omega}\,t)\,, \quad \text{and} \quad \mathbb{y}_{e2}(t) = \mathbb{A}\,\sin(\mathbb{\omega}\,t+\rho)\,. \tag{11.12}$$

Therefore, the dynamics of the mechanical system evolves (almost sure) according to the following system of stochastic differential equations

$$[\mathbb{M}]\begin{pmatrix}\ddot{\mathbb{y}}_1\\ \ddot{\mathbb{\phi}}_1\\ \ddot{\mathbb{\phi}}_2\end{pmatrix} + [\mathbb{N}]\begin{pmatrix}\dot{\mathbb{y}}_1^2\\ \dot{\mathbb{\phi}}_1^2\\ \dot{\mathbb{\phi}}_2^2\end{pmatrix} + [\mathbb{C}]\begin{pmatrix}\dot{\mathbb{y}}_1\\ \dot{\mathbb{\phi}}_1\\ \dot{\mathbb{\phi}}_2\end{pmatrix} + [\mathbb{K}]\begin{pmatrix}\mathbb{y}_1\\ \mathbb{\phi}_1\\ \mathbb{\phi}_2\end{pmatrix} = \mathbb{g} - \mathbb{h},\ \ a.s. \tag{11.13}$$

where the real-valued random matrices/vectors $[\mathbb{M}]$, $[\mathbb{N}]$, $[\mathbb{C}]$, $[\mathbb{K}]$, $\mathbb{g}$ and $\mathbb{h}$ are stochastic versions of the matrices/vectors $[M]$, $[N]$, $[C]$, $[K]$, $\mathbf{g}$ and $\mathbf{h}$.

Monte Carlo (MC) method [4, 6] is employed to compute the propagation of uncertainties of the random parameters through the nonlinear dynamics. In this method, realizations of the random parameters are generated. Each one defines a new deterministic nonlinear dynamical system, which is integrated using the procedure described in Sect. 11.2. Then, statistics of the generated data is calculated to access the stochastic nonlinear dynamics.

The map $n_s \in \mathbb{N} \mapsto \texttt{conv}(n_s) \in \mathbb{R}$, used to evaluate the convergence of MC simulation, is defined by

$$\texttt{conv}(n_s) = \left(\frac{1}{n_s}\sum_{n=1}^{n_s}\int_{t=t_0}^{t_f}\left(\mathbb{y}_1(t,\theta_n)^2 + \mathbb{\phi}_1(t,\theta_n)^2 + \mathbb{\phi}_2(t,\theta_n)^2\right)\,dt\right)^{1/2}, \tag{11.14}$$

where n_s is the number of MC realizations. See [9] for further details.

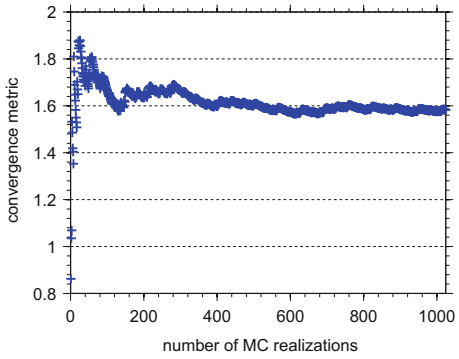

Fig. 11.5 Illustration of MC convergence metric as function of the number of realizations

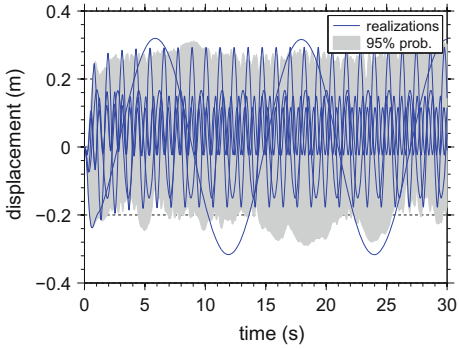

Fig. 11.6 Confidence envelope and some realizations for tower horizontal displacement

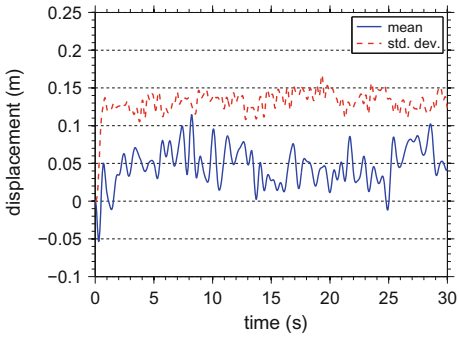

Fig. 11.7 Sample mean/standard deviation for tower horizontal displacement

As can be seen in Fig. 11.5, which shows the evolution of $\texttt{conv}(n_s)$ as a function of n_s, for $n_s = 1024$ the metric value is stationary. So, all MC simulations reported in this work use $n_s = 1024$ to address the stochastic dynamics.

Realizations of tower horizontal (lateral) dynamics x_2 time series can be seen in Fig. 11.6, as well as the corresponding 95% of probability confidence band. A wide variability in x_2 can be observed (Fig. 11.6). This fact may also be noted in Fig. 11.7, which shows the evolution of the sample mean and standard deviation of x_2. Note

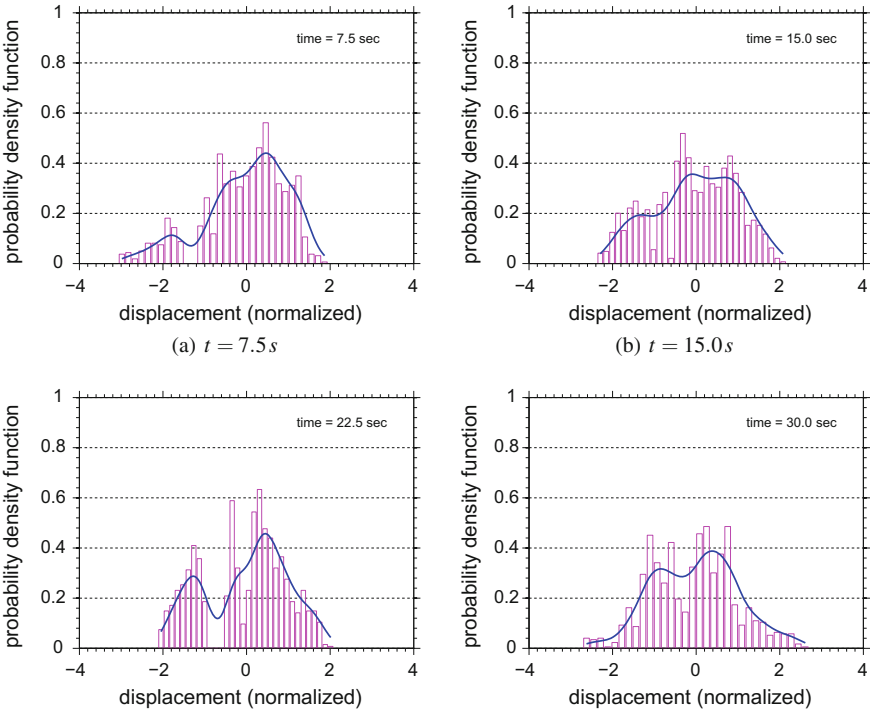

Fig. 11.8 Probability density function of tower horizontal dynamics (at different instants)

that, in all the interval of analysis, the standard deviation is bigger than the mean value, which indicates a significant spreading of the realizations with respect to the mean.

In Fig. 11.8 are presented estimations of the (normalized[1]) probability density function (PDF) of the tower horizontal vibration, for different instants of time. In all cases it is possible to observe asymmetries with respect to mean and multimodal behavior. In Fig. 11.9 the reader finds the time average of the tower horizontal dynamics PDF, which reflects the multimodal characteristic observed in the instants of time analyzed in Fig. 11.8.

By way of reference, a lateral vibration with an amplitude level greater than 10% of the B_1 value will be considered high, i.e.,

$$\text{large vibration} = \{\aleph_2(t) > 10\% \text{ of } B_1\}\,. \tag{11.15}$$

[1] In this context, the meaning of normalized is zero mean and unity standard deviation.

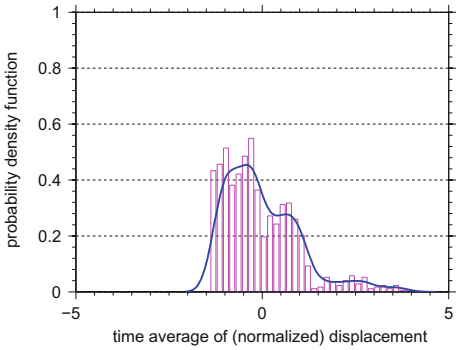

Fig. 11.9 Time average of tower horizontal dynamics probability density function

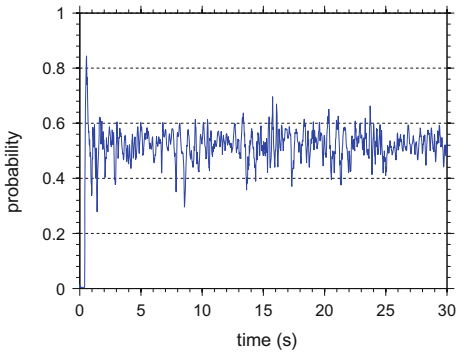

Fig. 11.10 Evolution of the probability of large horizontal vibrations

For any instant t, it is of interest to determine the value of

$$\mathbb{P}\left\{\aleph_2(t) > 10\% \text{ of } B_1\right\} = 1 - \mathbb{P}\left\{\aleph_2(t) \leq 10\% \text{ of } B_1\right\}, \tag{11.16}$$

where

$$\mathbb{P}\left\{\aleph_2(t) \leq 10\% \text{ of } B_1\right\} = \int_{-\infty}^{B_1/10} dF_{\aleph_2(t)}(x_2). \tag{11.17}$$

In Fig. 11.10 the reader can see the value of $\mathbb{P}\left\{\aleph_2(t) > 10\% \text{ of } B_1\right\}$ as function of time. Note that, for almost all the instants, the probability of an unwanted level of vibration may be significative values, being this value almost always greater than 40%.

11.4 Final Remarks

This work presented the study of the nonlinear dynamics of an orchard tower sprayer subjected to random excitations due to soil irregularities. Random loadings were taken into account through a parametric probabilistic approach, where the external

loading was modeled as a harmonic random process, with random parameters distributions specified by maximum entropy principle. Monte Carlo simulations of the stochastic dynamics reveal a wide range of possible responses for the mechanical system, and show the possibility of large lateral vibrations being developed during the sprayer operation.

Preliminary results of this work were presented in [3], and deeper analysis of this problem, including a more complex stochastic loading, can be found in [2].

Acknowledgements The authors are indebted to Brazilian agencies CNPq, CAPES, FAPESP, and FAPERJ for the financial support given to this research. They are also grateful to Máquinas Agrícolas Jacto S/A for the important data supplied.

References

1. Ascher, U., Greif, C.: A First Course in Numerical Methods. SIAM, Philadelphia (2011)
2. Cunha Jr, A., Felix, J.L.P., Balthazar, J.M.: Quantification of parametric uncertainties induced by irregular soil loading in orchard tower sprayer nonlinear dynamics. J. Sound Vib. **408**, 252–269 (2017). https://doi.org/10.1016/j.jsv.2017.07.023
3. Cunha Jr, A., Felix, J.L.P., Balthazar, J.M.: Exploring the nonlinear stochastic dynamics of an orchard sprayer tower moving through an irregular terrain. In: CSNDD'2016 Booklet of Abstracts. Marrakech, Morocco (2016)
4. Cunha Jr., A., Nasser, R., Sampaio, R., Lopes, H., Breitman, K.: Uncertainty quantification through Monte Carlo method in a cloud computing setting. Comput. Phys. Commun. **185**, 1355–1363 (2014). https://doi.org/10.1016/j.cpc.2014.01.006
5. Jaynes, E.T.: Information theory and statistical mechanics. Phys. Rev. Ser. **II**(106), 620–630 (1957). https://doi.org/10.1103/PhysRev.106.620
6. Kroese, D.P., Taimre, T., Botev, Z.I.: Handbook of Monte Carlo Methods. Wiley, New Jersey (2011)
7. Sartori Junior, S.: Mathematical modeling and dynamic analysis of a orchards spray tower. M.Sc. Dissertation, Universidade Estadual Paulista Julio de Mesquita Filho, Bauru (2008). (in portuguese)
8. Sartori Junior, S., Balthazar, J.M., Pontes Junior, B.R.: Non-linear dynamics of a tower orchard sprayer based on an inverted pendulum model. Biosyst. Eng. **103**, 417–426 (2009). https://doi.org/10.1016/j.biosystemseng.2008.09.003
9. Soize, C.: A comprehensive overview of a non-parametric probabilistic approach of model uncertainties for predictive models in structural dynamics. J. Sound Vib. **288**, 623–652 (2005). https://doi.org/10.1016/j.jsv.2005.07.009
10. Soize, C.: Stochastic modeling of uncertainties in computational structural dynamics-recent theoretical advances. J. Sound Vib. **332**, 2379–2395 (2013). https://doi.org/10.1016/j.jsv.2011.10.010

Chapter 12
Linearization of Nonlinear Resonances Through the Addition of Intentional Nonlinearities

Giuseppe Habib and Gaetan Kerschen

Abstract Important properties of linear systems, such as force-displacement proportionality and invariance of the resonant frequency, are not satisfied by nonlinear systems. The objective of this paper is to demonstrate that the intentional addition of properly tuned nonlinearities to a nonlinear system allows to retrieve those linear properties, enlarging the range over which a nonlinear system behaves linearly. Analytical findings are validated by numerical simulations.

12.1 Introduction

Devices used for sensing, imaging and detection are usually required to exhibit linear behavior in their dynamic range. However, nonlinearity is a frequent occurrence in engineering applications. Nano- and microresonators experience nonlinear behavior already at low amplitudes compared to noise floor [1, 8], strongly limiting the dynamic range of devises used, for instance, for ultrasensitive force and mass sensing [4], radio-frequency signal processing [13], narrow band filtering [14], time keeping [15] and nanoscale imaging [2].

Feedback linearization [3, 12] is a well-established approach for enforcing linear behavior, which uses feedback control to cancel the undesired nonlinearities. However, it requires an accurate and rapid monitoring of the system's states, an actuator and an external source of energy, which complicates its practical realization.

Several passive techniques, for enforcing linear properties in nonlinear systems, have been proposed in the literature. Kozinsky et al. [10] experimentally showed that an electrostatic mechanism can be implemented to tune the nonlinearity of a nanomechanical resonator: the softening effect provided by the electrostatic force

G. Habib (✉)
Budapest University of Technology and Economics, Műegyetem rkp. 3,
1111 Budapest, Hungary
e-mail: habib@mm.me.hu

G. Kerschen
University of Liege, 1, Chemin des Chevreuils, B-4000 Liege, Belgium
e-mail: g.kerschen@ulg.ac.be

M. Belhaq (ed.), *Recent Trends in Applied Nonlinear Mechanics and Physics*,
Springer Proceedings in Physics 199, https://doi.org/10.1007/978-3-319-63937-6_12

can compensate the hardening due to the geometry of a doubly-clamped beam. Mayet and Ulbrich [11] developed an isochronic bifilar pendulum, where isochronicity is obtained through a specific pendulum displacement path, for vibration absorption purposes. Kovacic and Rand [9] identified a class of conservative nonlinear systems having amplitude-independent frequency, i.e. isochronicity of the resonant frequency. Dou et al. [5] exploited a topology optimization technique to retrieve hardening, softening or isochronous behavior in nonlinear structures.

Recently, Habib et al. [6] proposed a linearization approach based on the intentional addition of nonlinearities into a system, in order to compensate the existing ones. Unlike previous attempts concerned with passive linearization, their approach relied on a principle of similarity [7], which states that the added nonlinearity should possess the same mathematical form as that of the original nonlinear system, allowing to extend the linear regime of motion. In [6], besides the invariance of the resonant frequency, attention is paid to the enforcement of force-displacement proportionality, typical characteristic of linear systems, not satisfied in nonlinear ones. The approach proposed in [6] exploits nonlinear normal modes (NNMs) and the energy balance criterion to identify the resonant peaks. Although this approach proved to be effective both numerically and experimentally, it might fail if two modes are too close to each other or if damping is large, due to the significant deviation of a resonant peak form the NNM.

The present paper proposes an approach similar to the one presented in [6], with the difference that resonant peaks are directly identified from the frequency response function, without exploitation of the NNMs. Properly-tuned nonlinearities are introduced in the nonlinear system to increase the range over which a specific resonance responds linearly. Specifically, we seek to enforce two important properties of linear systems, namely the force-displacement proportionality and the invariance of resonance frequencies. The developed analytical procedure is validated numerically through two different mathematical models.

12.2 Mathematical Model and Analytical Procedure

We consider a general n-degree-of-freedom (DoF) nonlinear mechanical system, harmonically excited, described by the system of differential equations

$$\mathbf{M}\ddot{\mathbf{x}} + \mathbf{C}\dot{\mathbf{x}} + \mathbf{K}\mathbf{x} + \tilde{\alpha}_3\mathbf{b}_{nl} = f_0\cos(\omega t)\mathbf{f}, \tag{12.1}$$

where $\mathbf{M}$, $\mathbf{C}$ and $\mathbf{K}$ are the mass, damping and stiffness matrices, respectively, $\mathbf{b}_{nl}$ includes the nonlinear terms, assumed purely cubic for simplicity, f_0 is the forcing amplitude, ω is the excitation frequency, t is time, $\mathbf{f}$ is a constant vector that locates the applied force and $\tilde{\alpha}_3$ is a real number.

A nonlinear spring, having the same order as the nonlinearity of the primary system is then added to the mechanical structure. The complete system can therefore be formulated as

$$\mathbf{M}\ddot{\mathbf{x}} + \mathbf{C}\dot{\mathbf{x}} + \mathbf{K}\mathbf{x} + \tilde{\alpha}_3\mathbf{b}_{nl} + \beta_3\mathbf{b}_{\beta 3} = f_0\cos(\omega t)\mathbf{f}, \tag{12.2}$$

where $\beta_3 = b_3\tilde{\alpha}_3$. Normalizing the system according to $\mathbf{y} = \mathbf{x}/f_0$, it becomes

$$\mathbf{M}\ddot{\mathbf{y}} + \mathbf{C}\dot{\mathbf{y}} + \mathbf{K}\mathbf{y} + \alpha_3\left(\mathbf{b}_{nl} + b_3\mathbf{b}_{\beta 3}\right) = \cos(\omega t)\mathbf{f}, \tag{12.3}$$

where the forcing amplitude and the nonlinearity are expressed by the unique parameter $\alpha_3 = \tilde{\alpha}_3 f_0^2$. The forcing amplitude appears only in the expression of the nonlinear coefficients, which means that it is equivalent to consider a strongly nonlinear system or a system with a large forcing amplitude.

We then apply the harmonic balance procedure, i.e. we approximate the solution of the system to its first harmonic content. Imposing $\mathbf{y}(1) = \mathbf{q}(1)\cos(\omega t) + \mathbf{q}(2)\sin(\omega t)$ and so on for the other system coordinates, we obtain

$$\mathbf{W}\mathbf{q} + \alpha_3\left(\mathbf{d}_{10}(\mathbf{q}) + b_3\mathbf{d}_{13}(\mathbf{q})\right) = \mathbf{c}, \tag{12.4}$$

where $\mathbf{W}$ includes linear terms, $\mathbf{d}_{10}(\mathbf{q})$ and $\mathbf{d}_{13}(\mathbf{q})$ contains third order terms (which are proportional to α_3) and $\mathbf{c}$ refers to the excitation and it is directly obtained from $\mathbf{f}$. The advantage of this formulation is that the solution of the system of nonlinear differential equations is reduced to a system of nonlinear algebraic equations.

In order to find an explicit (but approximate) solution of (12.4), we expand $\mathbf{q}$ in series with respect to α_3, such that $\mathbf{q} \approx \mathbf{q}_0 + \alpha_3\mathbf{q}_1 + \alpha_3^2\mathbf{q}_2 + O\left(\alpha_3^3\right)$. Inserting the approximate solution into (12.4) and collecting terms with different order of α_3 we have

$$\begin{aligned} &\left(\alpha_3^0\right) \quad \mathbf{W}\mathbf{q}_0 = \mathbf{c} \\ &\left(\alpha_3^1\right) \quad \mathbf{W}\mathbf{q}_1 + \mathbf{d}_{10}(\mathbf{q}_0) + b_3\mathbf{d}_{13}(\mathbf{q}_0), \end{aligned} \tag{12.5}$$

whose solution in explicit form is

$$\begin{aligned} \mathbf{q}_0 &= \mathbf{W}^{-1}\mathbf{c} \\ \mathbf{q}_1 &= -\mathbf{W}^{-1}\mathbf{d}_{10}(\mathbf{q}_0) + b_3\left(-\mathbf{W}^{-1}\mathbf{d}_{13}(\mathbf{q}_0)\right) = \mathbf{q}_{10} + b_3\mathbf{q}_{13}. \end{aligned} \tag{12.6}$$

We look for the frequency response of a specific DoF. Without loss of generality we focus on the first one, whose square is given by

$$\begin{aligned} H = \mathbf{q}(1)^2 + \mathbf{q}(2)^2 &\approx \mathbf{q}_0(1)^2 + \mathbf{q}_0(2)^2 + \alpha_3\left(2\mathbf{q}_0(1)\mathbf{q}_{10}(1) + 2\mathbf{q}_0(2)\mathbf{q}_{10}(2)\right) \\ &+ \alpha_3 b_3\left(2\mathbf{q}_0(1)\mathbf{q}_{13}(1) + 2\mathbf{q}_0(2)\mathbf{q}_{13}(2)\right) = H_0 + \alpha_3\left(H_{10} + b_3 H_{13}\right). \end{aligned} \tag{12.7}$$

Summarizing, the procedure developed so far consists in a simple harmonic balance reduction and to a straightforward expansion, such that an approximate form of the frequency response function can be expressed explicitly, keeping the contribution of the linear part of the system and that due to the nonlinear terms separated.

12.2.1 Identification of the Nonlinear Resonant Peak

The resonant frequencies $\omega_{1\ldots n}$ of the nonlinear system (understood as the local maxima of the resonant frequency) are given by the solution of the equation $\partial_\omega H = 0$, where ∂_ω indicates the partial derivative with respect to ω. However, since α_3 is assumed small, they can be considered as small variations of their linear counterparts $\hat{\omega}_{1\ldots n}$. Linear resonant frequencies $\hat{\omega}_{1\ldots n}$ can be easily identified with basic numerical tools and are invariant with respect to the forcing amplitude.

We linearize $\partial_\omega H$ around the target linear resonant frequency $\hat{\omega}_i$, we thus have

$$\partial_\omega H \approx \partial_\omega H|_{\omega=\hat{\omega}_i} + \partial_\omega^2 H|_{\omega=\hat{\omega}_i} \left(\omega - \hat{\omega}_i\right), \tag{12.8}$$

where

$$\partial_\omega H|_{\omega=\hat{\omega}_i} = \partial_\omega H_0|_{\omega=\hat{\omega}_i} + \alpha_3 \left(\partial_\omega H_{10}|_{\omega=\hat{\omega}_i} + b_3 \partial_\omega H_{13}|_{\omega=\hat{\omega}_i}\right) \tag{12.9}$$

and

$$\partial_\omega^2 H|_{\omega=\hat{\omega}_i} = \partial_\omega^2 H_0|_{\omega=\hat{\omega}_i} + \alpha_3 \left(\partial_\omega^2 H_{10}|_{\omega=\hat{\omega}_i} + b_3 \partial_\omega^2 H_{13}|_{\omega=\hat{\omega}_i}\right). \tag{12.10}$$

Imposing $\partial_\omega H = 0$, we have that the variation of the resonant frequency due to the nonlinear contribution, in first approximation is

$$\delta_i = \omega_i - \hat{\omega}_i \approx -\left.\frac{\partial_\omega H}{\partial_\omega^2 H}\right|_{\omega=\hat{\omega}_i}. \tag{12.11}$$

Linearizing δ_i with respect to α_3 (and recalling that $\partial_\omega H_0|_{\omega=\hat{\omega}_i} = 0$) we have

$$\delta_i \approx -\left.\frac{\partial_\omega H_{10} + b_3 \partial_\omega H_{13}}{\partial_\omega^2 H_0}\right|_{\omega=\hat{\omega}_i} \alpha_3 \tag{12.12}$$

which can be obtained explicitly.

12.2.2 Objective Functions

Two different properties typical of linear systems are considered, namely the force-displacement proportionality of the resonant peaks and the invariance of the resonant frequency. In the first case, the objective of the procedure is to identify b_3 such that the amplitude of the target resonant peak is invariant with respect to variations of the forcing amplitude, i.e. α_3. This is expressed by the objective function

$$F_1 = -H_0|_{\omega=\hat{\omega}_i} + H|_{\omega=\omega_i} = 0. \tag{12.13}$$

In order to solve (12.13) with respect to b_3, we expand H in Taylor series around $\hat{\omega}_i$. F_1 thus becomes

$$\begin{aligned} F_1 = &- H_0|_{\omega=\hat{\omega}_i} + H|_{\omega=\hat{\omega}_i} + \partial_\omega H|_{\omega=\hat{\omega}_i}\delta_i + O(\alpha_3^2) \approx \\ &\alpha_3 \left(H_{10}|_{\omega=\hat{\omega}_i} + b_3 H_{13}|_{\omega=\hat{\omega}_i}\right), \end{aligned} \tag{12.14}$$

if higher order of α_3 are neglected. Imposing $F_1 = 0$, we obtain the condition

$$b_3 = -\left.\frac{H_{10}}{H_{13}}\right|_{\omega=\hat{\omega}_i}. \tag{12.15}$$

If we aim at enforcing invariance of the resonant frequency, the objective function to be satisfied is

$$F_2 = \delta_i = \omega_i - \hat{\omega}_i = 0. \tag{12.16}$$

$F_2 = 0$ is approximately satisfied for

$$b_3 = -\left.\frac{\partial_\omega H_{10}}{\partial_\omega H_{13}}\right|_{\omega=\hat{\omega}_i}. \tag{12.17}$$

If more than one free parameter is available, it is also possible to satisfy more than one objective function at the same time. For example, it is possible to impose force displacement proportionality to two different resonant peaks, or either impose force displacement proportionality and invariant of the resonant frequency to the same resonant peak.

We consider the case of two added cubic springs to the system, having coefficients $b_{3a}\tilde{\alpha}_3$ and $b_{3b}\tilde{\alpha}_3$, respectively, such that we have

$$H \approx H_0 + \alpha_3 \left(H_{10} + b_{3a} H_{13a} + b_{3b} H_{13b}\right). \tag{12.18}$$

With the objective of imposing both force-displacement proportionality and invariance of the resonant frequency to a single resonant peak, the two objective functions F_1 and F_2 are reduced to

$$\begin{aligned} F_1 &\approx \alpha_3 \left(H_{10} + b_{3a} H_{13a} + b_{3b} H_{13b}\right)|_{\omega=\hat{\omega}_i} = 0 \\ F_2 &\approx \alpha_3 \left(\partial_\omega H_{10} + b_{3a}\partial_\omega H_{13a} + b_{3b}\partial_\omega H_{13b}\right)|_{\omega=\hat{\omega}_i} = 0 \end{aligned} \tag{12.19}$$

and are both satisfied for

$$b_{3a} = \left.\frac{\partial H_{10} H_{13b} - \partial H_{13b} H_{10}}{\partial H_{13b} H_{13a} - \partial H_{13a} H_{13b}}\right|_{\omega=\hat{\omega}_i} \quad \text{and} \quad b_{3b} = \left.\frac{\partial H_{10} H_{13a} - \partial H_{13a} H_{10}}{\partial H_{13a} H_{13b} - \partial H_{13b} H_{13a}}\right|_{\omega=\hat{\omega}_i}. \tag{12.20}$$

Instead, aiming at simultaneously imposing force displacement proportionality to two different resonant peaks, ω_i and ω_j, we have

$$\begin{aligned} F_{1i} &\approx \alpha_3 \left(H_{10} + b_{3a} H_{13a} + b_{3b} H_{13b}\right)|_{\omega=\hat{\omega}_i} = 0 \\ F_{1j} &\approx \alpha_3 \left(H_{10} + b_{3a} H_{13a} + b_{3b} H_{13b}\right)|_{\omega=\hat{\omega}_j} = 0, \end{aligned} \tag{12.21}$$

which are both satisfied for

$$b_{3a} = \frac{H_{10}|_{\omega=\hat{\omega}_i} H_{13b}|_{\omega=\hat{\omega}_j} - H_{10}|_{\omega=\hat{\omega}_j} H_{13b}|_{\omega=\hat{\omega}_i}}{H_{13a}|_{\omega=\hat{\omega}_j} H_{13b}|_{\omega=\hat{\omega}_i} - H_{13a}|_{\omega=\hat{\omega}_i} H_{13b}|_{\omega=\hat{\omega}_j}} \tag{12.22}$$

and

$$b_{3b} = \frac{H_{10}|_{\omega=\hat{\omega}_j} H_{13a}|_{\omega=\hat{\omega}_i} - H_{10}|_{\omega=\hat{\omega}_i} H_{13a}|_{\omega=\hat{\omega}_j}}{H_{13a}|_{\omega=\hat{\omega}_j} H_{13b}|_{\omega=\hat{\omega}_i} - H_{13a}|_{\omega=\hat{\omega}_i} H_{13b}|_{\omega=\hat{\omega}_j}}. \tag{12.23}$$

During the developed procedure, several approximation have been performed, limiting the effect of the nonlinear terms to their first order, which might appear a relatively tight limitation. However, since we considered only one free parameter, such an approximation is sufficient to identify the optimal b_3 for moderate α_3 values (either small forcing amplitude or small nonlinearity). Furthermore, according to the adopted principle of similarity [7], in order to compensate a nonlinearity of order n, the most effective nonlinearity to compensate its effect is the one with the same order. Nevertheless, if we consider an additional nonlinear component encompassing also higher order terms, the presented procedure should be extended to higher order, as well, which can improve the attempted linearization, as illustrated in the following section.

12.3 Numerical Validation

12.3.1 Force-Displacement Proportionality

We consider a simple 2-DoF system, whose dynamics is governed by the following system of differential equations

$$\begin{aligned} &m_1\ddot{x}_1 + c_1\dot{x}_1 + c_{12}\left(\dot{x}_1 - \dot{x}_2\right) + k_1 x_1 + k_{12}\left(x_1 - x_2\right) + x_1^3 + k_{3a}\left(x_1 - x_2\right)^3 = f_0 \cos \omega t \\ &m_2\ddot{x}_2 + c_2\dot{x}_2 + c_{12}\left(\dot{x}_2 - \dot{x}_1\right) + k_2 x_2 + k_{12}\left(x_2 - x_1\right) + k_{3b} x_2^3 + k_{3a}\left(x_2 - x_1\right)^3 = 0, \end{aligned} \tag{12.24}$$

where $m_1 = 1, m_2 = 0.1, c_1 = c_2 = c_{12} = 0.01, k_1 = 1, k_2 = 0.015$ and $k_{12} = 0.08$. The coefficients k_{3a} and k_{3b} are related to nonlinear terms not presented in the original system, but included in order to retrieve the target linear property.

Figure 12.1a, illustrates the frequency response of the original system ($k_{3a} = k_{3b} = 0$). For increasing values of the forcing amplitude, the normalized amplitude of the first resonant peak decreases, while the second peak undergoes a large growth

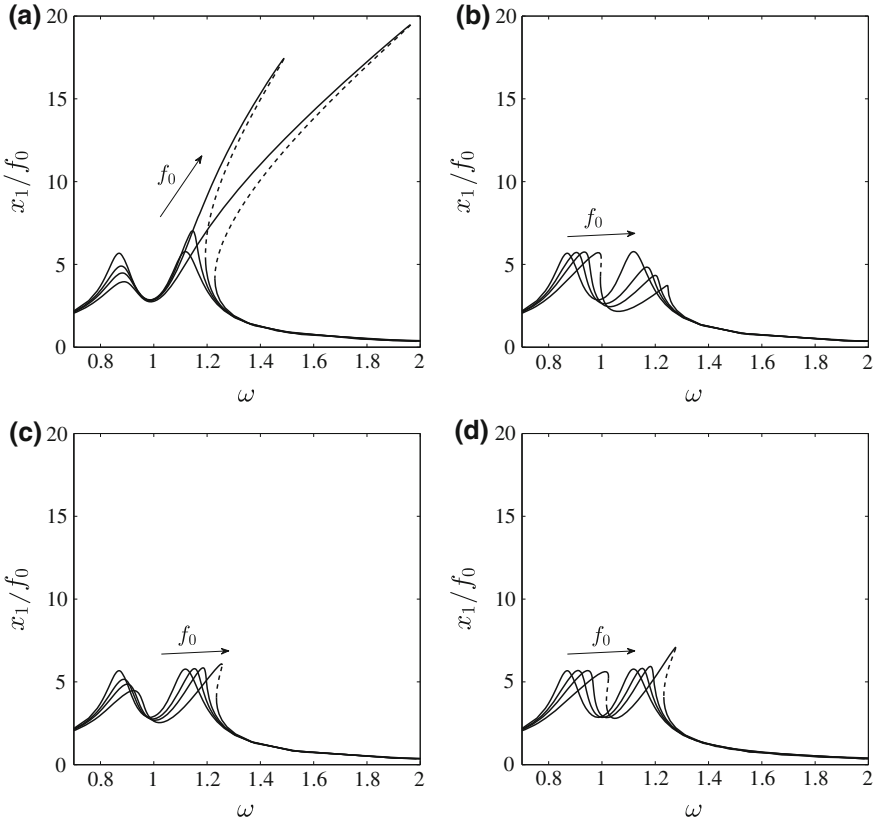

Fig. 12.1 Normalized frequency response function of the system in (12.24) for $f_0 = 0$, 0.05, 0.07 and 0.1. **a** $k_{3a} = k_{3b} = 0$ (original system), **b** $k_{3a} = 0.02197$, $k_{3b} = 0$ (force-displacement proportionality first peak), **c** $k_{3a} = 0.008023$, $k_{3b} = 0$ (force-displacement proportionality second peak) and **d** $k_{3a} = 0.004108$, $k_{3b} = 0.009501$ (force-displacement proportionality both peaks)

in its amplitude and an increase of its resonant frequency. Adopting the analytical procedure outlined in the previous section and with the objective of imposing force-displacement proportionality to the first resonant peak, we tune one of the additional nonlinearity, such that (12.14) is satisfied, obtaining $k_{3a} = 0.02197$. The relative frequency response is depicted in Fig. 12.1b. It is noted that the first peak amplitude is invariant with respect to the forcing amplitude, which means that the force-displacement proportionality is now verified. The same procedure is repeated for the second resonant peak, resulting in $k_{3a} = 0.008023$; the relative frequency response is illustrated in Fig. 12.1c. Finally, if two additional cubic terms are included, it is possible to satisfy force-displacement proportionality for both resonant peaks simultaneously. This is shown in Fig. 12.1d for $k_{3a} = 0.004108$ and $k_{3b} = 0.009501$.

The effectiveness of the procedure can be better understood from the envelopes of the resonant peaks for the four cases, depicted in Fig. 12.2. The dashed lines refer to

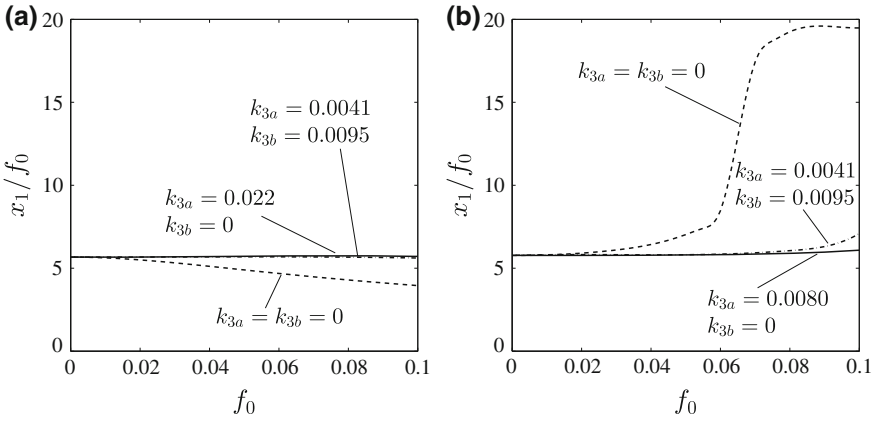

Fig. 12.2 Envelopes of the resonant peaks illustrated in Fig. 12.1. **a** First peak, **b** second peak

the original system, for which the oscillation amplitude does not depend linearly on the forcing amplitude. Solid lines refer to the system with force-displacement proportionality enforced on one of the resonant peaks; in this case the line is practically horizontal for both peaks. Dash-dotted lines refer to the system with force-displacement proportionality enforced on both resonant peaks at the same time. While the procedure works perfectly for the first peak, for the second peak it is valid only for $f_0 < 0.08$; for $f_0 > 0.08$ the second peak starts growing not linearly with respect to the forcing amplitude.

12.3.2 Invariance of the Resonant Frequency

Considering the same primary system, with different parameter values, we now aim at enforcing invariance of the second resonant frequency. The parameter values adopted are $m_1 = m_2 = 1, c_1 = c_2 = c_{12} = 0.01, k_1 = 1$ and $k_2 = k_{12} = 0.333$. Figure 12.3a depicts the frequency resoponse (not normalized) of the original system, i.e. without additional nonlinearities, around the second resonant peak. The system undergoes a strong hardening which bends the resonant peak to the right.

Adopting the outlined analytical procedure, we add a nonlinear term with coefficient $k_{3a} = -0.2434$ to the system. The resultant frequency response, illustrated in Fig. 12.3b, presents a backbone less banded than the one of the original system, however, for relatively large values of the forcing amplitude, the system still undergoes hardening. In order to improve the invariance of the resonant frequency, we extend the analytical procedure to higher order terms, including in the system a fifth order nonlinear term (working in parallel to k_{a3}). The coefficient of the additional fifth order term is $k_{a5} = -0.5084$ and the relative frequency response is depicted in Fig. 12.3c. A comparison between Fig. 12.3b, c discloses the effec-

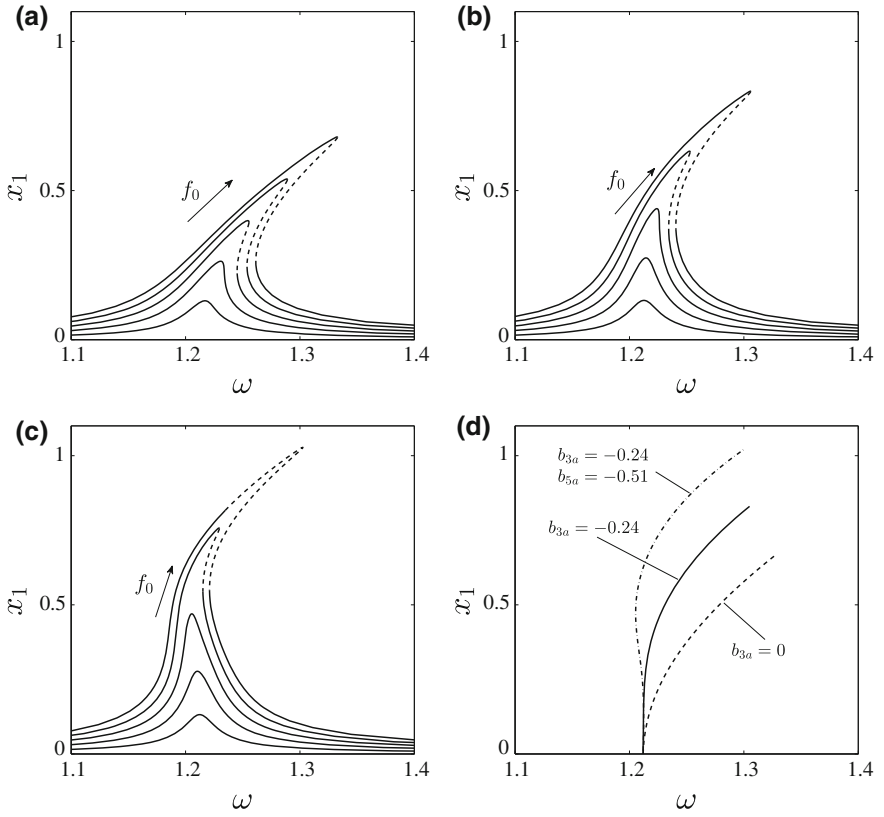

Fig. 12.3 Frequency response function (not normalized) of the system in (12.24) for f_0 ranging from 0 to 0.025, around its second resonant peak. **a** $k_{3a} = k_{3b} = 0$ (original system), **b** $k_{3a} = -0.2434$, $k_{3b} = 0$ (enforced isochronicity), **c** $k_{3a} = -0.2434$, $k_{3b} = 0$, $k_{5a} = -0.5084$ (enforced isochronicity with additional fifth order term). **d** Frequency backbones of resonances in (**a–c**)

tiveness of introducing a higher order nonlinearity, to correct the frequency backbone at large amplitude. However, it should be noticed that an excessively softening restoring force might generate instabilities (see the dashed line around the highest peak in Fig. 12.3c). The effectiveness of the procedure can be better understood from Fig. 12.3d, where the frequency backbone of the three cases are plotted. The dashed line, referring to the original system, is the most bended one, while the dash-dotted one, referring to the system with additional third and fifth order terms, is the straightest.

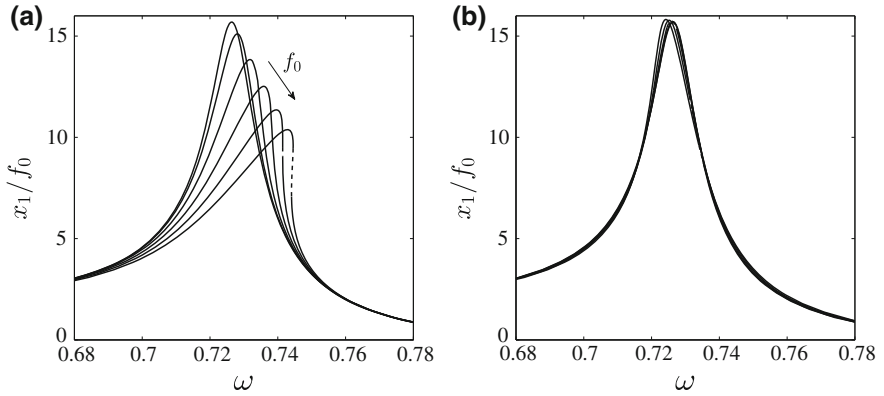

Fig. 12.4 Normalized frequency response function of the system in (12.24) for f_0 ranging from 0 to 0.05, around its first resonant peak. **a** $k_{3a} = k_{3b} = 0$ (original system), **b** $k_{3a} = 0.3680$, $k_{3b} = -0.07449$ (enforced force-displacement proportionality and isochronicity)

12.3.3 Force Displacement Proportionality and Invariance of the Resonant Frequency

Considering the same system as in Sect. 12.3.2, we now aim at enforcing simultaneously force-displacement proportionality and invariance of the first resonant frequency. The first resonant peak of the original system undergoes a slight hardening and a reduction of the normalized oscillation amplitude at the peak for increasing forcing amplitude (Fig. 12.4a). Including in the system two additional nonlinearities, (12.19) is satisfied for $k_{3a} = 0.3680$ and $k_{3b} = -0.07449$, which should guarantee isochronicity and force-displacement proportionality. The resultant frequency response is illustrated in Fig. 12.4b, for f_0 ranging from 0 to 0.05. Similarly to a linear system, the frequency response is almost invariant with respect to the forcing amplitude and all the curves are almost perfectly overlapping each other, which proves the efficacy of the procedure.

12.4 Conclusions

In this paper, we demonstrated that it is possible to linearize a specific resonance of a nonlinear system through the addition of intentional nonlinearities. The proposed methodology relays on a principle of similarity between the original nonlinearity of the system and the additional one. The adopted algorithm is based on a harmonic balance procedure, combined with a straightforward expansion for the estimation of the frequency response function. Its implementation is relatively easy, since it is almost

fully explicit. The effectiveness of the procedure was successfully demonstrated on two different numerical systems, for the enforcement of force-displacement proportionality, isochronicity and both of them simultaneously.

Acknowledgements The authors would like to acknowledge the financial support of the European Union (ERC Starting Grant No. Vib 307265).

References

1. Antonio, D., Zanette, D.H., López, D.: Frequency stabilization in nonlinear micromechanical oscillators. Nat. Commun. **3**, 806 (2012)
2. Binnig, G., Quate, C.F., Gerber, C.: Atomic force microscope. Phys. Rev. Lett. **56**(9), 930 (1986)
3. Charlet, B., Lévine, J., Marino, R.: On dynamic feedback linearization. Syst. Control Lett. **13**(2), 143–151 (1989)
4. Dai, M.D., Eom, K., Kim, C.W.: Nanomechanical mass detection using nonlinear oscillations. Appl. Phys. Lett. **95**(20), 203104 (2009)
5. Dou, S., Strachan, B.S., Shaw, S.W., Jensen, J.S.: Structural optimization for nonlinear dynamic response. Philos. Trans. R. Soc. A **373**:2051, 20140,408 (2015)
6. Habib, G., Grappasonni, C., Kerschen, G.: Passive linearization of nonlinear resonances. J. Appl. Phys. **120**(4), 044901 (2016)
7. Habib, G., Kerschen, G.: A principle of similarity for nonlinear vibration absorbers. Phys. D: Nonlinear Phenom. **332**, 1–8 (2016)
8. Kacem, N., Hentz, S.: Bifurcation topology tuning of a mixed behavior in nonlinear micromechanical resonators. Appl. Phys. Lett. **95**(18), 183104 (2009)
9. Kovacic, I., Rand, R.: About a class of nonlinear oscillators with amplitude-independent frequency. Nonlinear Dyn. **74**(1–2), 455–465 (2013)
10. Kozinsky, I., Postma, H.C., Bargatin, I., Roukes, M.: Tuning nonlinearity, dynamic range, and frequency of nanomechanical resonators. Appl. Phys. Lett. **88**(25), 253101 (2006)
11. Mayet, J., Ulbrich, H.: Tautochronic centrifugal pendulum vibration absorbers: general design and analysis. J. Sound Vib. **333**(3), 711–729 (2014)
12. Mittal, S., Menq, C.H.: Precision motion control of a magnetic suspension actuator using a robust nonlinear compensation scheme. Mech. IEEE/ASME Trans. **2**(4), 268–280 (1997)
13. Nguyen, C.T.: Frequency-selective mems for miniaturized low-power communication devices. Microw. Theory Tech. IEEE Trans. **47**(8), 1486–1503 (1999)
14. Park, S.J., Reines, I., Patel, C., Rebeiz, G.M.: High-rf-mems 4–6-GHz tunable evanescent-mode cavity filter. Microw. Theory Tech. IEEE Trans. **58**(2), 381–389 (2010)
15. Yurke, B., Greywall, D., Pargellis, A., Busch, P.: Theory of amplifier-noise evasion in an oscillator employing a nonlinear resonator. Phys. Rev. A **51**(5), 4211 (1995)

Chapter 13
Tailoring of Hysteresis Across Different Material Scales

Walter Lacarbonara, Michela Talò, Biagio Carboni and Giulia Lanzara

Abstract Hysteresis is discussed as a multi-scale material feature that can strongly affect the dynamic performance of a structure. It is shown that the hysteresis exhibited by assemblies of short wire ropes can be tailored via a synergistic use of different dissipation mechanisms (inter-wire frictional sliding, phase transformations) combined with geometric nonlinearities. The blend of material and geometric nonlinearities is a powerful and promising way to design new advantageous types of hysteretic responses in macro- or micro-scale devices and structures. Indeed, moving from macro-scale structures towards much smaller material scales, carbon nanotubes in nanocomposites are shown to dissipate energy through stick-slip with the polymer chains. The hysteresis of these materials can be largely modified and optimized by adjusting the micro-structural constitutive features. Recent experimental and modeling efforts are discussed in the context of new directions in material design and dynamic behavior of nanocomposites.

13.1 Introduction

A large variety of natural or engineered materials and systems exhibit hysteresis through the looping behavior of the input-output response functions [1]. The macroscopically observed hysteresis is often the result of a combination of complex multi-scale interactions between parts of structural dynamic systems, or it may arise in the material itself. Hysteresis can be caused by local plastic deformations due to internal slippage within the crystalline lattice microstructure of metals, alloys, reticular

W. Lacarbonara (✉) · M. Talò · B. Carboni
Department of Structural and Geotechnical Engineering, Sapienza University of Rome, Via Eudossiana 18, 00184 Rome, Italy
e-mail: walter.lacarbonara@uniroma1.it

G. Lanzara
Department of Engineering, University of RomeTre, Via Vito Volterra 62, 00146 Rome, Italy
e-mail: giulia.lanzara@uniroma3.it

M. Belhaq (ed.), *Recent Trends in Applied Nonlinear Mechanics and Physics*,
Springer Proceedings in Physics 199, https://doi.org/10.1007/978-3-319-63937-6_13

polymers or due to phase transformations in shape memory alloys such as NiTiNOL (Nickel-Titanium Naval Ordnance Laboratory). Often hysteresis is due to friction damping as observed in gears, joints, wire ropes or granular materials. Hysteresis can also result from micro-nano slippage between two or more phases of a composite material or a multifunctional, multi-phase material. Thus, we can define hysteresis as a macroscopically observed phenomenon featured at different material scales.

This fascinating phenomenon is here discussed extensively ranging from the macroscale to the nanoscale to show how the distinct properties of hysteresis can be tailored and engineered towards innovative designs and applications dealing with wire ropes and carbon nanotube nanocomposites.

Wire ropes are load-bearing members which are largely employed in applications requiring the lift of huge masses or the support of long-span decks such as in suspension bridges [2]. Short wire ropes subject to bending or coupled tension-bending can dissipate large amounts of energy through the inter-wire friction developing through the wire-to-wire and rope-to-rope contact areas which, in turn, depend on the shear, longitudinal, and radial stress components. This property makes wire ropes perfect rheological elements in applications requiring restoring forces which provide at the same time stiffness and damping. Recent patents addressed nonlinear hysteretic devices mainly conceived for vibration control purposes [3, 4]. The device of Lacarbonara and Carboni [4] exploits the stiffness and energy dissipation provided by an assembly of hybrid wire ropes made of AISI steel wires and NiTiNOL wires. The energy dissipation is due to the concurrency of inter-wire friction and NiTiNOL phase transformations [5]. The combination of these dissipation mechanisms with the stretching-induced geometric nonlinearity gives rise to the possibility of tailoring the restoring force and the associated hysteresis shape for different applications. In the present chapter, the role of dissipation mechanisms and geometric nonlinearities in the design of an optimized hysteretic response is elucidated. Moreover, the proper modeling tools adopted for the mathematical description of the physical nonlinearity are also discussed. In particular, the results of a finite element computation are discussed to justify the adoption of phenomenological approaches towards wire ropes mechanics and related design problems.

Another interesting class of lightweight materials exhibiting hysteresis shapes is the class of nanostructured polymer composites featuring different kinds of filler in the form of 0D nanoparticles (e.g., silica, nano-oxides and other inorganic particles), 1D nanofibers (e.g., carbon nanotubes, collagen nanofibers, and other nanofibers), and 2D nanolayers (e.g., nanoclay, graphite, graphene, layered silicate). Nanocomposite materials offer the potential for unprecedented improvements in stiffness, toughness, strength, damping and more general multifunctional aspects, without incurring weight penalty [6–12]. The integration of a strong filler into a polymeric hosting matrix is usually dictated by reinforcement purposes. On the other hand, in the last decades, experimental results have shown the potential of several micro- to nano-scale fillers to enhance not only the mechanical properties but also the damping capacity. In nanocmposites, damping mainly arises from the interfacial slippage between the filler and the surrounding matrix [13].

Such interfacial slippage primarily depends on the interfacial shear strength (i.e., the shear stress limit at which the sliding motion is activated at the interfaces). The resulting hysteresis in the stress-strain cycles becomes increasingly larger with an increasing interfacial contact area between the two constituents as is also the case at the macro scale with wire ropes where the amount of dissipation depends on the amount of inter-wire contact area. When the size of the filler approaches the nanometer scale as is the case with carbon nanotubes, for a given volume fraction of the filler, the composite macroscopic hysteretic response becomes more important. Indeed, the nanometer size of the filler is capable of providing a huge specific interfacial surface area through which shear slippage may occur, thus, giving rise to a higher energy absorption capability. Nanofillers have the virtue of modifying and enhancing the hysteresis and strength of the hosting matrices. The main factors affecting the damping capacity of the nanocomposites include the nanofiller aspect ratio, the volume fraction and dispersion, the nature of the interaction forces between the nanofiller and the matrix, as well as the employed manufacturing process [9].

Among all existing nanofillers, carbon nanotubes (CNT) offer the highest ratio between interfacial area and volume fraction. Indeed CNTs exhibit a hollow cylindrical structure with a diameter of a few nanometers and a length ranging from 1 μm to 1 mm thus giving rise to high aspect ratios (L/D). The literature confirmed that CNTs are the most promising candidate fillers to improve the damping capability of polymers even with very low CNT weight fractions [10, 11]. CNTs are known for their excellent elastic properties since the Young modulus can be as high as 1 TPa and the predicted tensile strength can be as high as 100 GPa [12]. However, to exploit their mechanical properties several manufacturing challenges must still be overcome. The interaction forces between CNTs and the surrounding polymer chains are mostly represented by weak van der Waals forces, which can be overcome even when the material is subject to low strains in the elastic region of the hosting matrix. A weak adhesion between the nanotubes and the matrix is the key for the activation of the frictional sliding motion called stick-slip [13, 14], which has the advantage of being reversible in a given range of strain amplitudes. Provided that the fabrication challenges are overcome, compared to other nanofillers, carbon nanotubes can enable a wider tuning of the mechanical and hysteretic properties of the nanocomposites response opening up a wide range of opportunities for the use of strong and highly damped composites [15–20].

Understanding the relationships between the nanocomposites microstructural properties and the macroscopic hysteretic response will pave the way towards unprecedented optimization of the nonlinear material behavior of new composite materials. This chapter will first discuss the hysteresis of wire rope assemblies and its application in the field of vibration absorption and proceed with discussing hysteresis observed in various carbon nanotube nanocomposites under the prevailing loading conditions.

13.2 Hysteresis in Wire Ropes

Wire ropes can be classified according to their cross-sectional geometry resulting from the formation process. There are spiroidal and stranded wire ropes. The first are characterized by an individual strand with a central core wire and a certain number of layers of wires wrapped around. The second type is represented by multiple strands which are wrapped around a central core strand. In principle, an infinite variety of wire ropes can be obtained varying the number, diameter, laying direction of the wires or strands. According to these features the contact area between the wires can be augmented or reduced implying different levels of energy dissipation when the resulting wire ropes are subject to cyclic loads.

The materials constituting the wires play an important role. The material can be elastic, elasto-plastic, pseudo-elastic, etc. For example, the introduction of shape memory alloy wires in combination with classical steel wires entails significant changes in the dissipative features of the ensuing wire ropes [5]. A shape memory alloy, according to its chemical composition, can exhibit material behaviors known as shape recovery effect and pseudo-elasticity.

These properties can be activated varying the thermal state or the stress state of the material. Herein, we will focus on the pseudo-elastic effect observed when the material is subject to a cyclic loading program.

Experimentally observed hysteresis. Figure 13.1 shows the tensile tests performed on an individual NiTiNOL wire, a 7-wire NiTiNOL strand and a mixed NiTiNOL-steel spiroidal wire rope. The force-strain curve for the NiTiNOL wire (see Fig. 13.1a) shows the pseudo-elastic effect typically observed in shape memory alloys. When the load is removed there are no residual strains thanks to the particular crystalline structure of the material. However, at the end of the cycle, a certain amount of energy, given by the area enclosed in the hysteresis loop, is dissipated. On the other hand, the 7-wire NiTiNOL strand in Fig. 13.1b exhibits a small residual strain after unloading. This is due to the frictional sliding between the wires. For the hybrid spiroidal wire rope, the large contact area between the wires provides a large frictional dissipation that is reflected on the residual strain at zero tension. Moreover, the changes in slope along the loading and unloading branches are due to the phase transformations of the shape memory material.

As mentioned, the dissipation occurring in a wire rope is mainly due to inter-wire sliding and its level depends on the normal contact forces between the wires. The literature about wire rope mechanics classifies the contact modes between lateral and radial contact [21]. The lateral or circumferential contact occurs between the wires of the same layer. The associated contact surfaces have a continuous helical shape across the rope length. This type of contact is strongly affected by the manufacturing process and the wear level. Radial contact occurs between the different layers through contact surfaces presenting discontinuous helical shapes across the rope length. These contact modes refer to spiroidal wire ropes but are generally valid also for multiple stranded wire ropes. The hysteresis provided by a wire rope can be selectively modified by

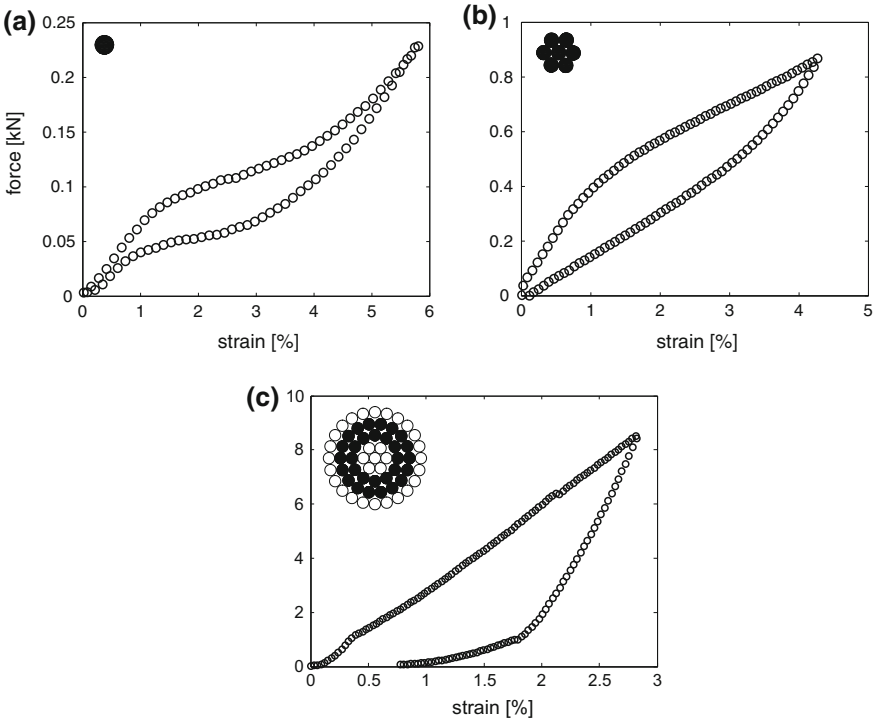

Fig. 13.1 Experimental stress-strain curves obtained via uni-axial tensile tests for **a** an individual NiTiNOL wire with $D = 0.63$ mm, **b** a 7-wire NiTiNOL strand with $D = 1.8$ mm and **c** a mixed spiroidal NiTiNOL steel wire rope with $D = 5.7$ mm. The *black* (*white*) *color* indicates that the wire is made of NiTiNOL (steel)

acting on the internal contact properties and regulating the geometrical wire rope parameters.

The hysteretic response depends also on the loading condition and on the activation of the geometric nonlinear hardening effect. The shape of the hysteresis loops can be regulated combining different types of wire ropes and stress states such as pure bending or coupled tension-bending.

Figure 13.2e, f show the testing setups employed to acquire the restoring forces exhibited by different wire ropes subject to cyclic displacements. These setups are custom made and make use of a linear actuator. The testing setups shown in Fig. 13.2e, f are mounted on the Material Testing System (MTS) available in the Materials and Structures Laboratory at Sapienza University of Rome. One end of the wire rope is vertically displaced while the other end is connected to a load cell that measures the restoring force. Different stress conditions can be implemented according to the horizontal restraint applied to the wire ropes. When a vertical displacement is prescribed, the deflected end of the wire ropes can be free or prevented to slide along the horizontal direction. In the first case the wire rope is subject to pure bending

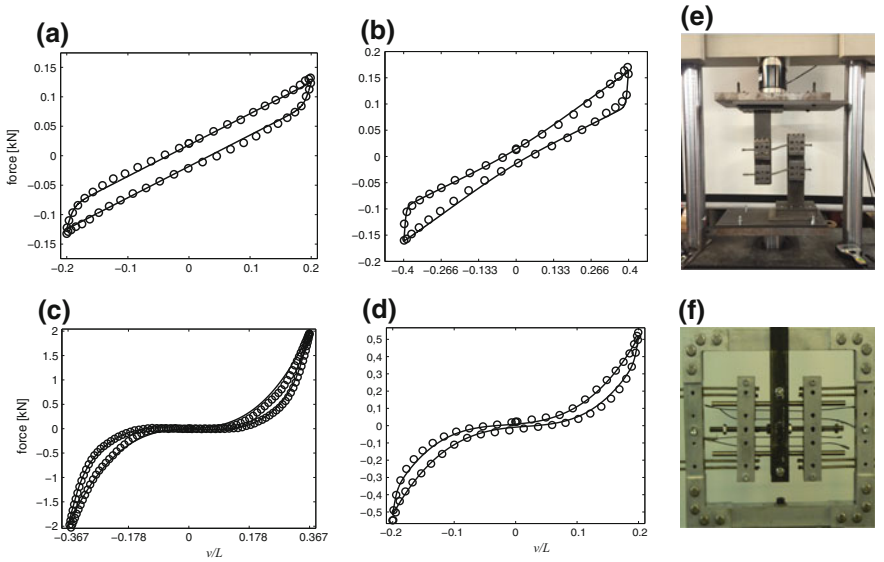

Fig. 13.2 Experimental response curves (*circles*) together with the identified curves (*solid lines*): **a** 8 steel multi-stranded wire ropes with $D = 6$ mm and $L = 100$ mm; **b** 4 mixed NiTiNOL-steel spiral wire ropes with $D = 5.7$ mm and $L = 75$ mm; **c** 8 NiTiNOL 7-wire stranded ropes subject to bending and tension with $D = 1.8$ mm and $L = 56$ mm; **d** 8 steel multi-stranded ropes with $D = 1.8$ mm and $L = 100$ mm subject to bending and tension with 2 additional horizontal NiTiNOL 7-wire strands with $D = 1.8$ mm and $L = 63$ mm. Experimental setups for testing wire ropes assemblies under **e** Bending or tension-bending and **f** With the additional horizontal stiffness provided by secondary wire ropes

states while in the second case the rope is stretched exhibiting a nonlinear geometric stiffness effect of the hardening type. An intermediate stress condition can be implemented introducing an additional horizontal restoring force provided by springs or secondary wire ropes. This testing condition is obtained with the setup shown in Fig. 13.2f. A detailed description of this testing device is given in [5, 22]. The hysteresis loops obtained with different wire rope types and working conditions are shown in Fig. 13.2a–d. Part (a) portrays the hysteresis cycle of steel wire ropes subject to bending. Part (b) shows the hysteretic force of mixed NiTiNOL-steel wire ropes subject to bending. The interaction between friction and phase transformations is revealed by the pinched loop around the origin. When the shape memory material is unloaded and it goes back to the austenitic phase, the return on the elastic branch determines a pinching in the restoring force. Part (c) shows a strong pinching at the origin of the force-displacement cycle and a distinct hardening behavior. This behavior is due to the generated tensile forces in the ropes as a consequence of the horizontal constraint. Part (d) shows a slightly pinched, hardening hysteresis due to NiTiNOL strands subject to coupled bending-tensile loads. The force-displacement cycle in part (d) is obtained introducing the additional horizontal restoring force due

to axially stretched NiTiNOL wires that introduce an additional source of energy dissipation.

Modeling and identification. A fine mechanical modeling of wire ropes is a challenging task mainly because of the large number of wires interacting through contact surfaces with complex geometry. While 3D finite element discretizations can certainly incorporate fine details of the actual geometry and suitably describe inter-wire frictional forces, such a computational approach is very demanding.

By employing Abaqus [23], a steel 19-wires $(1 + 6 + 12)$ strand of diameter $D = 3$ mm and length $L = 65$ mm was discretized into about 3×10^5 8-node tetrahedral elements with linear shape functions. Forward time integrations of the nonlinear equations of motion were performed and a penalty formulation was adopted for the normal and tangential contact problem between the wires. Figure 13.3a shows the finite element model in the undeformed configuration. Each wire end at the root cross section is clamped while the other ends are subject to a transverse displacement time history described by $v(t) = A_1 \sin 2\pi f_1 t$ where $A_1 = 10$ mm, $f_1 = 3.33$ Hz and $t \in [0, 0.3]$ s. The displaced ends are torsionally constrained and kept at the same distance L from the root. In a first set of simulations, the wire rope is initially stress-free while, in the second set, the rope is given an initial pretension through a prescribed longitudinal displacement monotonically increasing up to 0.8 mm. Figure 13.3b shows the contact stresses between the wires while Fig. 13.3c, d depict the total reaction force at the clamp along the transverse direction and the time change of inter-wire contact area for the initially stress-free rope. Figure 13.3e, f describe the force and contact area for the pre-stressed rope.

The hysteresis curve in Fig. 13.3c shows a very pronounced pinching at the origin indicating a low dissipation rate when the strand is unloaded. It is due to the weak contact stresses which are proportional to the axial force in the strand. When the transverse deflection is increased, tension arises in the wires determining a global hardening response together with an increment of the contact forces which in turn gives rise to larger energy dissipation. The same behavior was observed experimentally in Fig. 13.2c [5, 22, 24]. When the wire rope is given a pre-tension, the pinching is negligible and the hystersis loop becomes fatter indicating a greater dissipation due to the larger contact area through which frictional sliding produces dissipation.

The computational time of the Abaqus finite element model exceeds 24 h employing a desktop computer. The heavy computational burden does not allow to use this approach for identification or optimisation purposes. This reason justifies the adoption of much lighter phenomenological models or reduced order models. Indeed phenomenological models can be effectively employed to fit the experimental force-displacement curves by using parameters identification methods such as the Differential Evolution Algorithm [25] or other data-driven strategies [26]. The well-known Bouc-Wen hysteretic model [27, 28] was modified in [5] to describe the pinching at the origin of the force-displacement cycles. The restoring force f depends on the displacement x according to

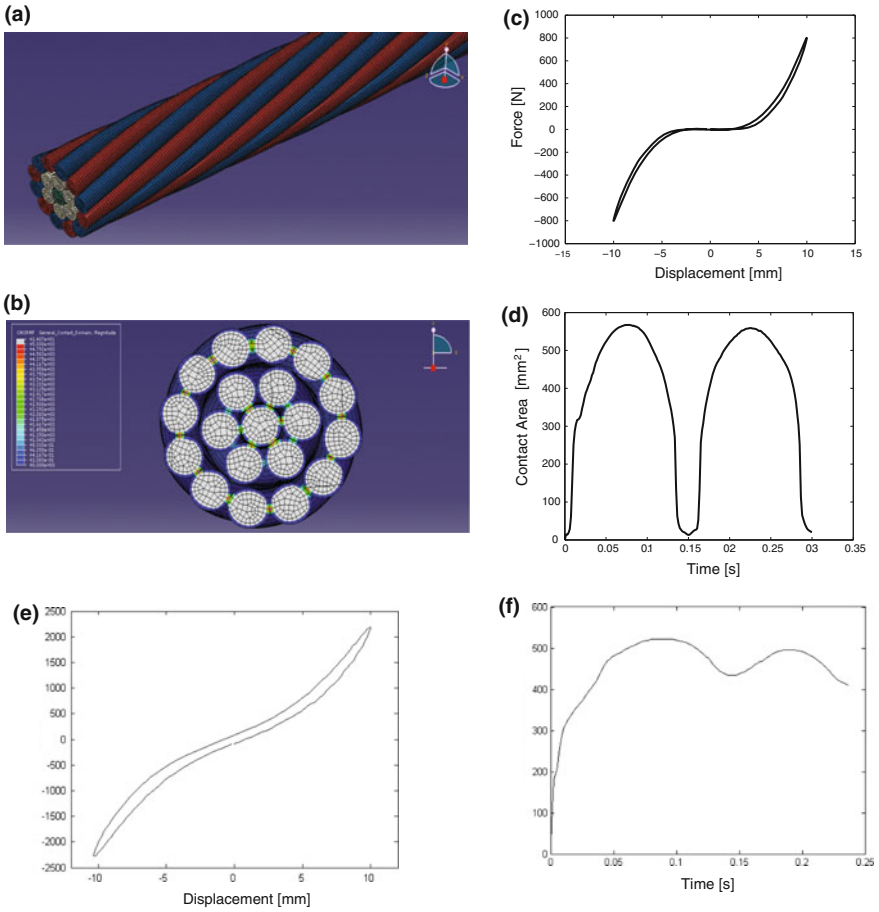

Fig. 13.3 Finite element model of a 19-wire steel strand: **a** Reference configuration; **b** Contour plot of the inter-wire normal contact forces; **c** and **e** Force-displacement cycles of (**c**) stress-free rope and **e** Pre-stressed rope; **d** and **f** Variations with time of the contact area of (**d**) stress-free rope and **f** Pre-stressed rope. The material parameters are: Young's modulus $E = 206$ GPa, Poisson's coefficient $\nu = 0.3$, frictional coefficient $\mu = 0.5$

$$f = k_e x + k_3 x^3 + z, \qquad \dot{z} = \left[k_d h(x) - (\gamma + \beta \text{sgn}(\dot{x} z)\, |z|^n\right] \dot{x} \tag{13.1}$$

where k_e and k_3 represent the elastic linear and cubic stiffness coefficients, respectively, and z is the hysteretic part of the force. The overdot denotes differentiation with respect to time t and (k_d, γ, β, n) are the model parameters regulating the hysteresis loops shape. When $k_3 = 0$, the stiffness at the origin of the cycles is $k_e + k_d$ while past a threshold force the stiffness reaches the plateau value equal to k_e. The pinching function $h(x)$ is given by $h(x) = 1 - \xi \exp(-x^2/x_c)$ with $\xi \in [0, 1)$ regulating the pinching severity and $x_c > 0$ defining the extension of the pinching zone along the

displacement axis. The hysteretic responses shown in Fig. 13.2a–d are accurately identified using (13.1) as shown by the closeness of the solid lines to the experimental measurements. The cubic stiffness k_3 was set to zero for identifying the cycles in Fig. 13.2a, b. Moreover, the pinching function $h(x)$ was set to 1 in Fig. 13.2a. A clear interpretation of the role of each parameter is given in [5, 22].

A good compromise between expensive 3D FE models and phenomenological models is the one-dimensional reduction of a wire rope to a nonlinear hysteretic geometrically exact cylindrical beam model [29]. The generalized hysteretic constitutive relationship was established between the bending moment and the beam curvature within the special Cosserat theory of shearable beams. This approach provides the hysteretic response as well as the internal resultant stresses in the wire rope.

The shape of the restoring forces can be largely varied regulating the geometric and mechanical features. For example, it is possible to change the cross section and material properties of the wire ropes, their number, length, and diameter. Moreover, the presented device [4] allows to tune the geometric nonlinearities and stiffness ratio between the different wire rope components so as to vary the loop shapes.

Hysteretic damping capacity. The damping capacity associated with the obtained constitutive behaviors can be measured by the so-called equivalent damping ratio expressed as

$$\xi_0 = \frac{W_D}{4\pi W_E} \tag{13.2}$$

where W_D denotes the energy dissipated in a loading-unloading cycle and is given by the area enclosed by the force-displacement cycle. W_E indicates the elastic energy stored in an equivalent visco-elastic rope at the end of the loading branch. The evaluation of the stored energy is not unique since it depends on the assumed elastic stiffness of the system. The equivalent damping ratio is meaningful if an equivalent visco-elastic rope (comparison system) is found with a stiffness leading to the same oscillation frequency of the actual hysteretic rope at a given oscillation amplitude. Such stiffness can be set to be the secant stiffness or some other average stiffness over the considered displacement cycle. Figure 13.4 shows the equivalent damping associated with the different constitutive behaviors. All damping curves show a peak at moderately low displacement amplitudes. Thereafter the curves roll off at different rates due to the different evolutions of inter-wire friction and phase transformations at high oscillation amplitudes.

13.2.1 Tailoring the Wire Ropes Damping in Hysteretic Vibration Absorbers

The device proposed in [4] exploits the richness of hysteretic behaviors obtained combining different wire rope assemblies. Such device can be employed as a Tuned

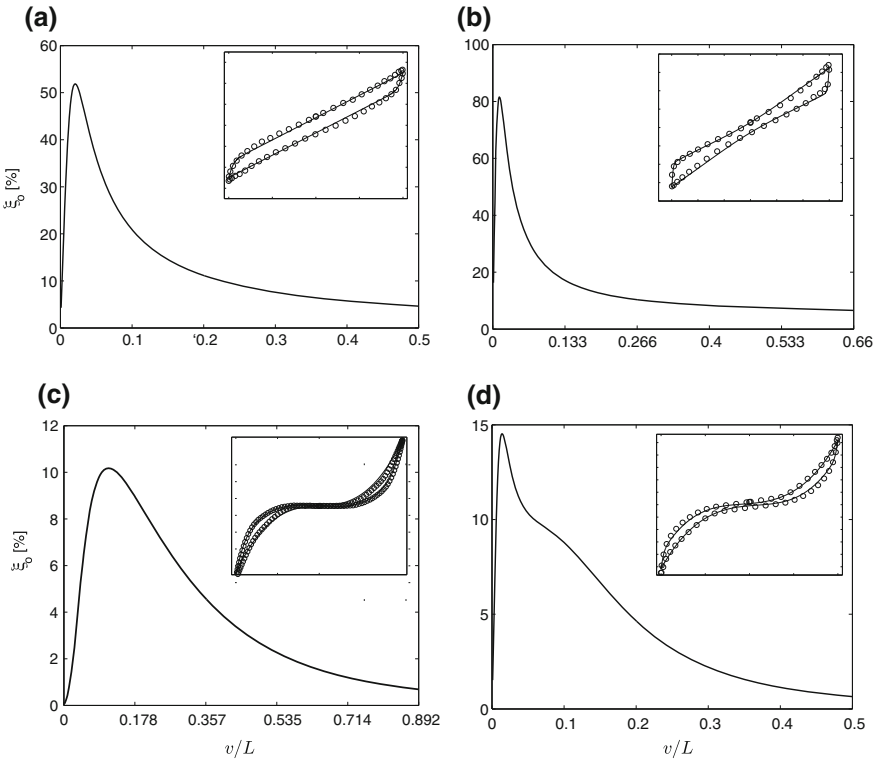

Fig. 13.4 Equivalent damping versus displacement amplitude. The damping curves in parts **a**, **b**, **c** and **d** are referred to the constitutive behaviors shown in Fig. 13.2, respectively

Mass Damper (TMD) for vibration mitigation of structures subject to base motions or direct excitations.

A hysteretic TMD [4] was experimentally investigated in [24] for vibration control of a scaled multi-story building subject to harmonic base excitation. The stiffness and damping of the absorber were tailored to achieve optimal control of the fundamental sway mode of the building. The low-frequency sway modes of a building usually exhibit a linear behavior. In the literature, it is commonly accepted that the optimal stiffness and damping of a TMD designed for mitigating harmonic motions of viscously damped structures must be independent of the displacement amplitude. Many authors provided analytical or empirical expressions to estimate the optimal TMD mechanical parameters [30–35].

The engineering forms according to which vibration absorbers have been realized in the literature comprise reinforced rubber bearings, pistons containing viscous liquids, metal springs in parallel with viscous dampers, devices based on the rolling or sliding friction. The stiffness and damping of these devices exhibit very different behaviors. Invariably, the fundamental drawback is represented by the difficulty of

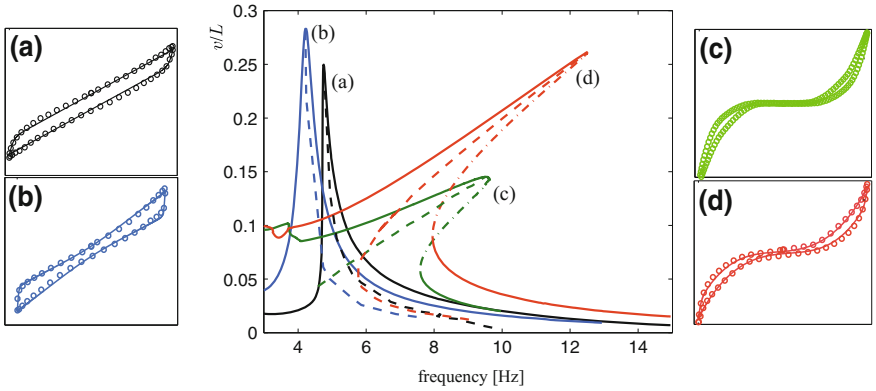

Fig. 13.5 **a** Requency-response curves at various excitation levels for absorbers exhibiting the hysteretic restoring forces labelled (**a**), (**b**), (**c**), (**d**). The *solid* and *dashed-dotted lines* denote the stable and unstable responses, respectively, while the *dashed lines* represent the associated backbone curves

obtaining restoring forces which maintain a constant stiffness and constant damping at large oscillation amplitudes typically attained by the TMD masses oscillating at resonance.

The hysteretic cycle shown in Fig. 13.2b has the peculiarity of providing a large-amplitude displacement range within which both stiffness and damping are nearly constant. This particular feature, as discussed in [24], ensures a good performance of the wire rope-based TMD for controlling the structure dynamics especially at large oscillation amplitudes.

Figure 13.5 shows the frequency-response curves of the different devices whose restoring forces are labelled (a), (b) (c) (d). The devices (a) and (b) exhibit pronounced softening while the devices (c) and (d) are characterized by strong hardening. Of particular interest is the restoring force in Fig. 13.2b. The increment of energy dissipation for increasing oscillation amplitudes due to the NiTiNOL phase transformations makes the ratio between dissipated and elastic energy almost constant. Moreover, the constant stiffness exhibited above a threshold displacement ensures that the resonance frequency also achieves an asymptotic constant value. The other important advantage of the proposed device consists in the fact that both stiffness and damping are provided by the wire ropes without the need of combining multiple rheological elements.

13.3 Hysteresis in Carbon Nanotube Nanocomposites

The hysteresis exhibited by short wire ropes results from a macroscopic frictional sliding between the individual wires. In this section we will discuss the hysteresis observed in nanocomposite materials for which the internal frictional dissipation

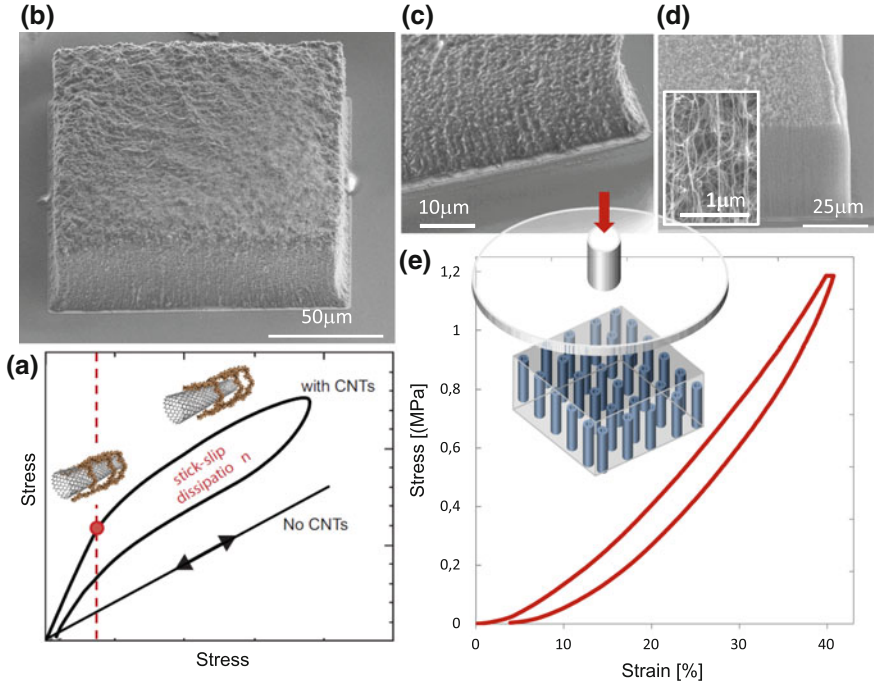

Fig. 13.6 **a** Schematic illustration of the stick-slip phenomenon; **b** CNT/PDMS nanocomposite micropattern; **c** Higher magnification of the nanocomposite; **d** Patterned oriented CNTs before absorption of the hosting matrix and a higher magnification of the same (see inset); **e** Schematic of the test setup and a compressional stress-strain curve

takes place at much smaller scales, namely, at the micro- and nano-scales through sliding between the hosting matrix and the CNTs when the interfacial shear stress reaches the limit value called interfacial shear strength (see Fig. 13.6). A nanocomposite micropillar made of PDMS and a high density array of oriented multi-walled carbon nanotubes (MWNT) was tested under compressional strain cycles in [36]. Forests of oriented MWNTs (35 μm thick) were first grown and patterned in microscaled square pillars (130 μm side) following the procedure described in [36, 37] (see Fig. 13.6d). A thin PDMS layer (Sylgard 182-Dow Corning) was absorbed within the micropillar forming the nanocomposite microstructure (20% CNTs volume fraction) [36, 38]. Figure 13.6b shows the nanocomposite micropillar, while Fig. 13.6c represents a higher magnification of the micropillar in which the good CNTs dispersion within the hosting PDMS matrix is highlighted. The embedded MWNTs are vertically oriented and highly packed (intertube spacing ranging from few nanometers to 250 nm). This is shown in Fig. 13.6d representing the CNTs micropattern before being impregnated with the matrix. Compression tests were performed with a nanoindentation technique using a nanoscratch tester in indentation mode (CSM Instruments). Micropillars were uniformly compressed by means of a flat tip

(2 mm diameter) as shown in Fig. 13.6e. A linear load up to 20 mN at a loading rate of 40 mN/min, reaching nearly 40% compressional strain, was applied to the micropillar and, after a pause of 20s, the sample was fully unloaded at the same speed. The material clearly showed a hysteretic response with a hardening effect during loading. The elastic modulus in the loading cycle was found to be at least one order of magnitude higher than those reported in the literature for pure PDMS samples cured at room temperature [39], and over two orders of magnitude higher in the unloading cycle that is considered to be purely elastic in nanoindentation tests. However, these comparisons are very difficult due to the wide dependence of the PDMS properties on the curing process [39], the ratio of the curing agent [40], the type of elastomer (Sylgard 182 or 184) and the size of the sample [41]. None of the cases reported in the literature corresponds to the presented sample type, size, testing methodology as well as fabrication process (which also includes the addition of solvents to thinner the layer during fabrication). Wide variations are also reported in terms of loading/unloading cycles both in tensile and compression modes. Most commonly a linear elastic response is highlighted up to strains of the order of 50% and a hysteretic response for even larger strains (see, e.g., [39, 40]). It is here observed that the integration of oriented CNTs in the matrix induces a hysteretic response at all strain levels (well below 50%). These loops show an overall wider area especially toward the end of the unloading cycle if compared with the trends reported for higher strains [40, 42]. This effect is certainly related to the oriented CNTs which first affect the PDMS chains distribution within the sample during fabrication, and then affect the overall viscoelastic response. The CNTs in the forest are in fact highly packed forming an array of nanochannels that absorb the polymer chains from the substrate hosting the CNTs micropattern, in agreement with the fabrication procedure. The polymer chains are forced to align along the nanochannels length. Thus, the material becomes a hybrid aggregation of long and aligned fibers (the PDMS chains and the CNTs) that can relatively slide when loaded.

A wider experimental campaign was carried out on macroscopic nanocomposite samples with randomly oriented CNTs. The nancomposite samples were fabricated according to the details given in [19]. A campaign of cyclic tensile and torsional tests was conducted in different testing conditions to investigate hysteresis and the associated damping capacity. Cyclic tensile tests were carried out at increasing strain amplitudes using a Zwick/Roell Universal Testing Machine. Specimen shapes, test speeds and methods were selected according to ISO 527-1 and -2. In particular, dog-bone type-5B nanocomposite specimens were chosen according to ISO 527-2 with an overall length equal to 50 mm, gage length equal to 12 mm, and cross section equal to 2×4 mm^2.

The first investigated macroscale nanocomposite is made of polypropylene (PP), a commodity viscoelastic, thermoplastic polymer with a Young modulus equal to 1.45 GPa. The employed MWNTs have a low aspect ratio (L/D = 155). Other investigated nanocomposites feature engineering polymers, namely, polycarbonate (PC) and polybutylene terephthalate (PBT), with high mechanical properties (E = 3.7 GPa for PBT) and good resistance to chemical agents and heat.

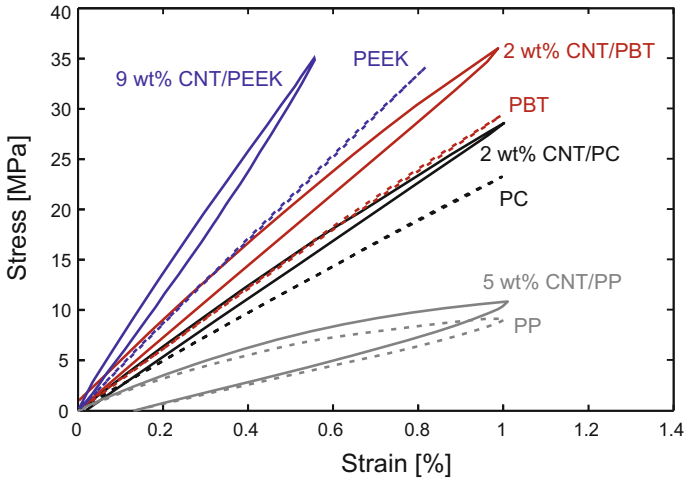

Fig. 13.7 Cyclic tensile tests on PP, PC and PBT nanocomposites showing the influence of different polymer matrices on the ensuing hysteresis loops. The cyclic tests are compared with the tests of Ogasawara et al. [43] carried out on PEEK nanocomposites

A first estimate of the nanocomposites damping capacity can be directly obtained through the tensile loading/unloading cycles. The energy dissipated per cycle W_D is measured as the area enclosed by the loop cycle, while the elastic energy stored in the material W_E is given by the area below the loading branch. Thus, the ratio W_D/W_E can be taken as a measure of the specific damping capacity of the material.

The role of the polymer matrix. Figure 13.7 shows the tensile stress-strain curves compared with the cyclic tests of a high-performance polyether ether ketone (PEEK) nanocomposite, previously investigated by Ogasawara et al. [43]. The shape of the hysteresis loops is controlled by the polymer matrix [44]. The cyclic curve of the PP nanocomposite shows a large enclosed area with a significant residual strain resulting from the pronounced viscous damping properties of the PP viscoelastic polymer, as confirmed by the residual viscous strain at the end of the cycle of the neat PP. On the other hand, the Young moduli of the engineering polymers referred to as PC, PBT and PEEK are higher than that of PP. The very narrow cycles obtained for PC, PBT and PEEK indicate the prevalence of the elastic energy component, since the cycles are mostly closed at the origin given the negligible residual strain at full unloading. For these engineering polymer nanocomposites, the damping capacity can be effectively associated with the internal hysteresis caused by the interfacial sliding motion between CNTs and polymer chains. Indeed, the interfacial shear stress needed to activate the stick-slip phenomenon is lower than the yielding stress in the high-performance polymers, as proved also for other PEEK nanocomposites [43, 45]. In addition, the damping capacity of the PP nanocomposite is not higher than that exhibited by the engineering thermoplastic nanocomposites. Although the area enclosed by the cycle in the CNT/PP nanocomposite appears to be larger compared

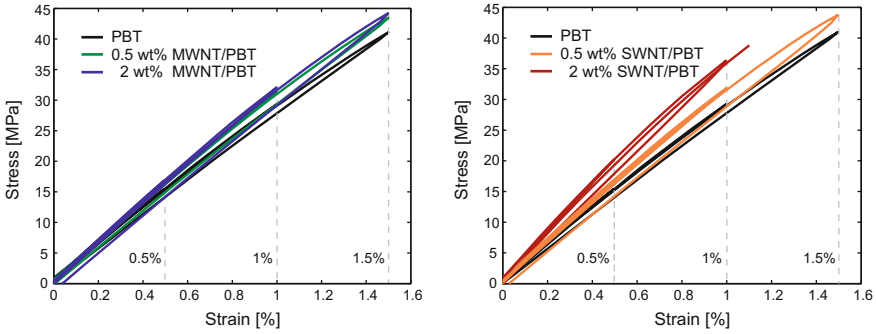

(a) Low aspect ratio MWNTs nanocomposites (b) High aspect ratio SWNTs nanocomposites

Fig. 13.8 Cyclic tensile tests conducted on pure PBT and CNT/PBT nanocomposites showing the influence of different aspect ratio nanofillers. The selected displacement rate was 2 mm/min by increasing the deformation of 0.5% at each loading process. The maximum reached deformation was 1.5% after three loading/unloading cycles

to that of the engineering nanocomposites, the actual damping increment provided by the addition of the CNTs is marginal with respect to the viscous damping component of pure PP. Moreover, the increment of dissipated energy is mainly due to the higher stiffness of the CNT/PP nanocomposite, as testified by the higher slope of the loading branch. This trend indicates that hysteresis observed in thermoplastic nanocomposites is considerably affected by the viscous behavior of the polymer, which may be predominant with respect to the CNT/matrix stick-slip effect. An interpretation of the phenomenon can be given by considering the PP polymer chains mobility and deformability. In soft matrices the polymer chains sliding is triggered by lower shear stresses compared to those needed to activate the stick-slip at the CNT/matrix interfaces. This behavior results in an augmentation of the dissipated energy per cycle, only because the elastic energy stored in the cycle is also increasing. Therefore, the nature of the hosting matrix plays a key role in tailoring the hysteresis of nanocomposite materials, mainly by dictating the shape of the loops.

CNT aspect ratio. The effects of the CNT aspect ratio were investigated in PC and PBT nanocomposites incorporating high aspect ratio single-walled nanotubes (SWNT) with L/D = 2778, in addition to the nanocomposites with low aspect ratio MWNTs (L/D = 155). In all nanocomposites with 0.5 and 2% CNT weight fractions (see Fig. 13.8) there is an increase of the specific damping capacity with respect to the neat polymer. The specific damping capacity increment for the intermediate cycle with 1% strain amplitude is found to be 47% with the addition of 0.5 wt% of MWNTs, and 64% with the addition of 0.5 wt% SWNTs. As expected, the nanocomposite dissipative and mechanical properties are strongly influenced by the CNT aspect ratio. High aspect ratio CNTs provide a larger interfacial area during the activation of the stick-slip phenomenon, thus, SWNT nanocomposites exhibit a more pronounced hysteretic behavior than composites with the lower aspect ratio MWNTs. The drawback of the employed long SWNTs is that good CNT dispersions

in the matrix are harder to pursue. The formation of CNT agglomerates causes stress concentrations. Thus nanocomposites with higher CNTs contents may undergo premature brittle failures, as observed for the 2 wt% SWNT/PBT nanocomposites.

CNT dispersion and functionalization. In addition to the considered thermoplastic nanocomposites, MWNT/epoxy composite samples (i.e., thermosetting matrix) were also tested to understand the influence of the CNT macro- and nano-dispersion on the material macroscopic response. Due to electrostatic and van der Waals attractive interaction forces between the CNTs themselves, they have a tendency to aggregate together. The aggregated CNTs are in the form of bundles or ropes usually with a highly entangled network structure that is difficult to disperse. The homogeneous dispersion of nanofillers within the polymer matrix is a prerequisite of any composite, that may be achieved through mechanical treatments such as shear mixing and ultrasonic dispersion techniques, sometimes combined with chemical treatments [46]. Chemical treatments may consist of (i) non-covalent functionalizations, which do not alter the CNT interface properties but require the use of chemical agents and surfactants to facilitate the CNT dispersion in the surrounding polymer matrix, and (ii) covalent functionalizations, which imply a modification of the chemical interaction forces between the CNTs and the polymer chains by exploiting functional molecules which strengthen the chemical bonds between these two constituents.

Cyclic tensile tests were performed for three epoxy nanocomposites with 0.5 wt% MWNTs content of (see Fig. 13.9). As observed in the light microscopy micrographs (see Fig. 13.9a), the CNT chemical treatment through amino-functionalization turned out to be the most effective treatment to achieve a good CNT dispersion and CNT/matrix adhesion, thus improving the nanocomposite macroscopic elastic response. However, the amino-functional groups strengthened the chemical bonds between the CNTs and epoxy, thus inhibiting or delaying the interfacial stick-slip activation. On the other hand, the effect of mechanical dispersion treatments—(i.e., a milder and a stronger ultrasonication via the ultrasonic bath and the ultrasonic horn, respectively—)led to a slightly improved mechanical response, but preserving and even enhancing the damping capacity. Indeed, the onset of stick-slip interfacial sliding in the non-functionalized nanocomposites occurs when the interfacial van der Waals forces are overcome.

Although various drawbacks may be introduced by the CNT functionalization processes (CNTs damage, shortening, etc.), the engineering of the CNT/matrix interfaces, as a whole, is regarded as a powerful technique to act on the local morphology of the nanotubes and tailor the global nanocomposites material features [47, 48]. For example, the interfacial shear strength (ISS) can be increased by creating covalent bonds between the CNTs and the polymers. This will cause an enhancement of the strength and stiffness of the polymer compound through an improved interfacial load transfer, however the persistence of stick-slip will be lost. On the other hand, the onset of the nanocomposites hysteretic response may be facilitated by reducing the strength of the CNT/matrix interface. Consequently, the resulting nanostructured material will show enhanced damping capacity at relatively low strains, without compromising the mechanical properties of the polymer.

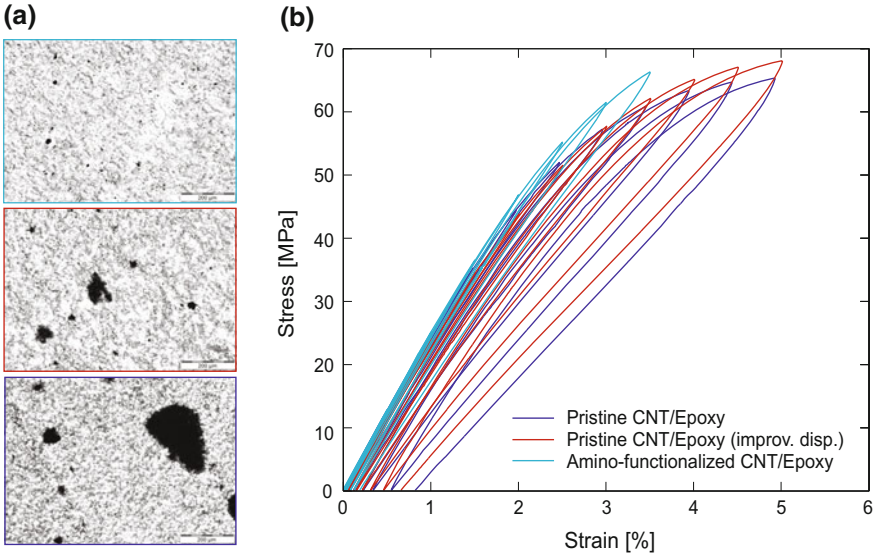

Fig. 13.9 **a** Micrographs of the three nanocomposites denoted by the *blue, red* and *cyan colors*; **b** Cyclic tensile tests on CNT/epoxy nanocomposites obtained via different CNT dispersion treatments: (*blue*) pristine MWNT/epoxy prepared via ultrasonic bath; (*red*) pristine MWNT/epoxy composite prepared via ultrasonic horn; (*cyan*) amino-functionalized MWNT/epoxy composite prepared via ultrasonic horn. The displacement rate was set to 0.2 mm/min and the deformation was increased of 0.5% at each loading cycle until reaching 5%

Strain amplitude-dependent behavior of CNT nanocomposites. After observing the different hysteresis loops via cyclic tensile tests, experimental Dynamic Mechanical Analysis (DMA) tests were carried out to investigate the strain amplitude effect on the damping response of nanocomposites. DMA is a widely used technique by which small deformations or stresses are applied to a sample in a cyclic manner. DMA gives information about the rheology of the material by measuring its viscoelastic properties. The rheology provides a relationship between the inner structure and the macroscopic properties of the nanocomposites, which is the key to the development of new materials. The data collected from the tests may be expressed in terms of storage modulus, loss modulus, or damping. For a given sinusoidal strain time history, the viscoelastic material stress will also vary sinusoidally in time at low strain amplitudes. The stress response will have the same frequency as the input strain but lagging by a phase angle denoted by δ. The phase lag is due to the excess time necessary for molecular motions and relaxations to occur. Dynamic strain and stress are expressed as $\varepsilon = \varepsilon_o \sin(\omega t)$, and $\sigma = \sigma_o \sin(\omega t + \delta)$, respectively, where ω is the angular frequency. The measured stress can be divided into an in-phase component ($\sigma_o \cos\delta$) and an out-of-phase component ($\sigma_o \sin\delta$). Dividing the stress by the strain amplitude, two moduli are derived and defined as E' and E'' for the in-phase and out-of-phase parts, respectively,

$$E' = \frac{\sigma_o}{\varepsilon_o}\cos\delta, \qquad E'' = \frac{\sigma_o}{\varepsilon_o}\sin\delta. \tag{13.3}$$

E' and E'' correspond to the real and imaginary parts of the complex modulus: $E^* = E' + iE''$. The storage modulus E' describes the ability of the material to store potential energy and release it upon deformation. The storage modulus it is associated with the material "stiffness" and is related to the Young modulus. The loss modulus E'' is associated with energy dissipation in the form of heat upon deformation and it is related to "internal friction". The loss modulus is sensitive to different kinds of molecular motions, relaxation processes, transitions, morphology and other structural heterogeneities. Thus, the dynamic properties provide useful information at the molecular level to understand the nanofiller/polymer mechanical behavior. The ratio between the loss modulus and the storage modulus is a measure of the intrinsic damping called loss factor and denoted by $\eta = \tan\delta = E''/E'$. Alternatively, energy concepts can be used. With respect to a steady-state oscillation, η can be described as

$$\eta = \frac{W_D}{2\pi W_E} = \frac{\pi E'' x_o^2}{2\pi(\frac{1}{2}E' x_o^2)} = \frac{E''}{E'}, \tag{13.4}$$

where x_o is the amplitude of the steady-state response, W_D stands for the energy dissipated in a steady-state cycle while W_E represents the stored energy. The loss factor is undoubtedly the most general damping measurement index. The equivalent damping ratio ξ is related to the other damping measures by simple laws: $\eta = \tan\delta = 2\xi$ when damping levels are within $0 < \tan\delta < 0.15$.

DMA tests were carried out using a dynamic thermo-mechanical analyzer (ARES-G2, TA Instruments) to evaluate the variation of (E', E'', η) within selected ranges of the shear strain in torsional mode. The torsional tests provided information about the damping capacity of the nanocomposites, also in terms of the shear stress state that initiated the CNT/matrix stick-slip phenomenon with a significant localization around the contour of the samples cross sections. The strain sweep tests were performed in the strain range from 10^{-4} to 3.5×10^{-2} setting the frequency to 1 Hz, at room temperature. The PC and PBT nanocomposite specimens were rectangular bars with a length of 40 mm and a cross section of $1 \times 9.5\,\text{mm}^2$.

Figure 13.10 shows variations of the damping capacities of CNT/PC and CNT/PBT nanocomposites in a large shear strain range, and provides evidence about the onset of the interfacial stick-slip. Past a critical shear strain value, significant increments of damping ratios are reported for each nanocomposite compared to the neat polymer. These threshold strains identify the onset of the stick-slip phenomenon. More specifically, for low strains, below the threshold strains, the measured damping ratios of nanocomposites are close to the values obtained in the pure matrices and, in some cases, damping is even lower than that exhibited by the polymers. This is because the CNT composites are stiffer that the neat matrices, in which the polymer chains show some mobility and readjustments, even at low strains. However, when the threshold dynamic strain is reached, the energy dissipation in CNT composites is markedly enhanced and it rapidly increases with the dynamic strain [49]. By analyzing the

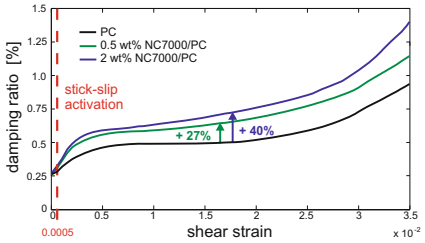

(a) Low aspect ratio MWNT/PC nanocomposites

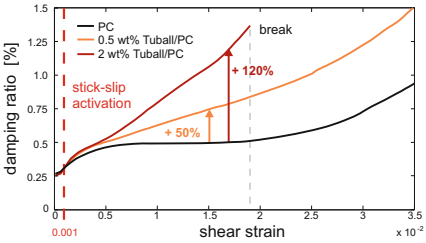

(b) High aspect ratio SWNT/PC nanocomposites

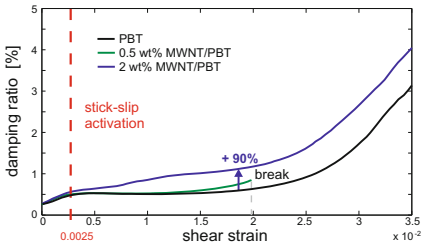

(c) Low aspect ratio MWNT/PBT nanocomposites

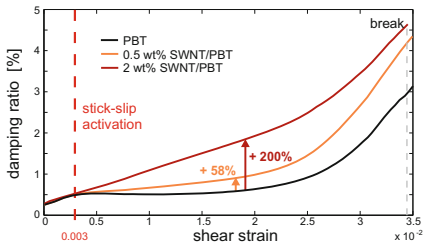

(d) High aspect ratio SWNT/PBT nanocomposites

Fig. 13.10 Damping capacity of the PC and PBT nanocomposites obtained via DMA tests in torsional mode

trend of damping ratio versus shear strain amplitude a threshold strain of 5×10^{-4} is found for MWNT/PC nanocomposite and a threshold strain of 10^{-3} for SWNT/PC nanocomposites, whereas in the CNT/PBT nanocomposites the threshold strain is 2.5×10^{-3} and 3×10^{-3} for MWNT and SWNT nanocomposites, respectively. The threshold strain values provide information about the nanofiller/polymer interactions and suggest that interfaces in SWNT nanocomposites exhibit a better adhesion compared to those of MWNT nanocomposites. The explanation of this behavior is to be found in the nanofiller morphology. TEM analysis reported in [19] highlight the straight and lenghten shape of the SWNTs versus the short and curly shape of the MWNTs. As result, the MWNTs curviness hinders the nanofiller/polymer bonding and make weaker the interfaces in the MWNT nanocomposites.

Besides the dissipation at the interface through stick-slip, additional sources of energy dissipation in nanocomposites at large strain amplitudes could stem from other dissipation phenomena within the matrix. Since it is assumed that the CNTs remain elastic even at large strains, the polymer chains start to relatively slide, especially at the CNTs ends. Furthermore, the way in which the low and high aspect ratio CNTs affect the nanocomposites damping capacity is here highlighted. By adopting high aspect ratio SWNTs, a larger interfacial area is obtained for the stick-slip activation thus providing higher dissipation. When the same CNTs volume fraction is considered, the SWNT/matrix interfacial contact area is estimated to be 5.5 times larger than that available in the MWNT nanocomposites, thus explaining the significantly

higher damping enhancement in all SWNTs nanocomposites. Thus to summarize, at low strain amplitudes, the damping capacity is nearly constant. Above the threshold strain, damping increases with the strain level as a result of the CNT/polymer stick-slip. Moreover, the experimental results show a significant damping improvement by increasing the CNT weight fraction, although the CNT dispersion may become worse. The highest damping enhancement was reported for the 2 wt% SWNT/PBT nanocomposite with 200% increase compared to the neat PBT matrix.

Modeling of hysteresis in CNT nanocomposites. Several analytical/computational models were proposed to describe the nanocomposites nonlinear constitutive behavior. The first efforts aiming at modeling hysteresis in CNT nanocomposites were addressed by Zhou et al. [14], exploiting basic microstructural concepts to describe the interfacial stick-slip in nanocompoites treated as four-phase materials. Li et al. [50] developed a continuum model to describe the interfacial shear stress distribution using a molecular structural mechanics approach and finite element analysis. Interesting friction models for the description of the hysteretic response in CNT nanocomposites were also provided by Huang and Tangpong [51] and by Lin and Lu [52] who modeled the energy dissipation of CNT composites under dynamic loading by considering several crucial aspects, including CNT alignment to optimize the damping response.

Recent advances in the context of smooth hysteresis modeling for nanocomposites were reported in [53, 54] where a multi-scale finite element analysis was carried out to investigate the hysteretic stress-strain behavior of the nanocomposites as well as the influence of the interfacial strength, geometry, volume fraction and elastic properties of the CNTs. In particular, the work of Formica et al. [18, 20] proposed a meso-scale nonlinear incremental constitutive model based on the Eshelby-Mori-Tanaka theory to describe the shear CNT/matrix stick-slip via an inelastic eigenstrain field. The model provided predictions of the hysteretic response in close agreement with experimental results, thus proving its validity.

In the last decade, a huge step forward in modeling the nonlinear response of nanocomposites was taken, also thanks to the progress in nanocomposites manufacturing by which more experimental data were made available to validate the theories. The current goal in analytical modeling is to provide efficient and effective tools able not only to predict the nanocomposites mechanical response, but also to correlate the shape and magnitude of the nanocomposite hysteresis to macro- and micro-structural constitutive parameters. This will enable to design the nanocomposite mechanical properties together with its damping capacity araising from micro-dissipative phenomena, such as the interfacial stick-slip. [20].

13.4 Conclusions

Targeted levels of hysteresis can be achieved in innovative, high-performance structures by either introducing auxiliary point-wise, hysteretic dampers or by leveraging

on the inherent damping capability of nanostructured materials such as carbon nanotube polymer nanocomposites.

This work discussed recent advances in the design of nonlinear rheological devices that make use of dedicated wire ropes which exhibit inter-wire hysteretic frictional damping together with dissipation ensuing from phase transformations in NiTiNOL wires. Moreover, geometric nonlinearities in these devices can be leveraged to conveniently modify the shape of the hysteresis loops thus enabling a wider frequency tuning. The occurrence of friction together with austenitic-martensistic phase tranformations allows to attain energy dissipation over a large displacement range. The possibility to regulate the dissipation level and the effective displacement range makes the rheological device robust for several applications, especially in the field of structural and mechanical vibrations control.

By moving towards a much smaller material scale, desirable hysteresis can be achieved in CNT nanocomposites by taking advantage of the dissipative interfacial stick-slip between the CNTs and the polymer chains. A tailored hysteretic response can be designed through proper choice of the polymer matrix via optimization of the interfacial properties. This can be obtained through an engineering of the interfaces at the micro/nano-scale. Nanoparticle coatings, covalent and non-covalent functionalizations, dispersion treatments and other kinds of surface modifications can be envisioned to selectively modify the interfacial adhesion of the nanofiller with the polymer, and bridge together a variety of structural and nonstructural properties in the same material.

The conducted experimental campaign confirmed that the macroscopic hysteresis can be controlled to within a certain degree in the resulting CNT nanocomposites without compromising the effective stiffness and strength. An increase of 200% in damping capacity was found in randomly oriented 2 wt% SWNT/PBT nanocomposites with a 25% improvement in Young modulus [19]. This opens new perspectives in designing lightweight composites for applications in aerospace and structural engineering as well as in automotive, electronics and biomedical engineering, where also the outstanding electrical and thermal properties of the CNT nanofillers may be conveniently exploited. To mention a few examples, multifunctional nanocomposites—conceived as lightweight, strong, and highly damped composites—can be designed for reconfigurable smart aerostructures or for miniaturized devices, such as microbeam resonators, micropressure sensors and microabsorbers. On the other hand, by exploiting the electrical properties of nanotubes, conductive networks of CNTs may be introduced in polymer based-composite materials to convey thermal gradients and induce a thermomechanical response of viscous polymers via electrical signals. This would allow the design of materials with a thermally activated hysteretic response, which takes advantage of relaxation phenomena in polymer systems. The work here discussed shows that hysteresis can be conceived as a multi-scale feature which can be engineered and delivered through a micro- and nano-structural design of the materials and systems, depending upon the specific needs dictated by new demanding applications.

Acknowledgements Part of the material of this chapter was presented by Walter Lacarbonara in a keynote lecture within the Third International Conference on Structural Nonlinear Dynamics and Diagnosis (CSNDD'2016), Marrakech, Morocco, May 23–25, 2016. This work was partially supported by the European Office of Aerospace Research and Development/Air Force Office of Scientific Research Grant (Grant N. FA9550-14-1-0082 DEF). Dr. Matthew Snyder and Dr. "Les" Lee are gratefully acknowledged for their support and comments.

References

1. Visintin, A.: Differential Models of Hysteresis. Springer, Berlin (1994)
2. Lacarbonara, W.: Nonlinear Structural Mechanics. Theory, Dynamical Phenomena and Modeling. Springer, New York (2013)
3. Vestroni, F., Lacarbonara, W., Carpineto, C.: Hysteretic tuned-mass damper device (TMD) for passive control of mechanical vibrations. Sapienza patent EP 2742254 A1 (2014)
4. Lacarbonara, W., Carboni, B.: Multi-performance hysteretic rheological device. Sapienza pending patent N. PCT/IT2016/000043 (2015)
5. Carboni, B., Lacarbonara, W., Auricchio, F.: Hysteresis of multiconfiguration assemblies of Nitinol and steel strands: experiments and phenomenological identification. J. Eng. Mech. **141**(3), 04014135 (2015)
6. Gibson, R.F.: A review of recent research on mechanics of multifunctional composite materials and structures. Compos. Struct. **92**, 2793–2810 (2010)
7. Li, B., Zhong, W.H.: Review on polymer/graphite nanoplatelet nanocomposites. J. Mater. Sci. **46**, 5595–5614 (2011)
8. Saba, N., Tahir, P.M., Jawaid, M.: A review on potentiality of nano filler/natural fiber filled polymer hybrid composites. Polymers **6**, 2247–2273 (2014)
9. Sun, L., Gibson, R.F., Gordaninejad, F., Suhr, J.: Energy absorption capability of nanocomposites: a review. Compos. Sci. Tech. **69**, 2392–2409 (2009)
10. Koratkar, N.A., Suhr, J., Joshi, A., Kane, R.S., Schadler, L.S., Ajayan, P.M., Bartolucci, S.: Characterizing energy dissipation in single-walled carbon nanotube polycarbonate composites. Appl. Phys. Lett. **87**, 063102 (2005)
11. Suhr J., Koratkar N.A.: Energy dissipation in carbon nanotube composites: a review. J. Mater. Sci. **4**, 4370–4382 (2008)
12. Thostenson, E.T., Ren, Z., Chou, T.W.: Advances in the science and technology of carbon nanotubes and their composites: a review. Compos. Sci. Technol. **61**, 1899–1912 (2001)
13. Rajoria, H., Jalili, N.: Passive vibration damping enhancement using carbon nanotube-epoxy reinforced composites. Compos. Sci. Technol. **65**, 2079–2093 (2005)
14. Zhou, X., Shin, E., Wang, K.W., Bakis, C.E.: Interfacial damping characteristics of carbon nanotube-based composites. Compos. Sci. Technol. **64**, 2425–2437 (2004)
15. Formica, G., Lacarbonara, W., Alessi, R.: Vibrations of carbon nanotube-reinforced composites. J. Sound Vib. **329**, 1875–1889 (2010)
16. Khan, S.U., Li, C.Y., Siddiqui, N.A., Kim, J.K.: Vibration damping characteristics of carbon fiber-reinforced composites containing multi-walled carbon nanotubes. Compos. Sci. Technol. **71**, 1486–1494 (2011)
17. Alnefaie, K.A., Aldousari, S.M., Khashaba, U.A.: New development of self-damping MWCNT composites. Compos. A **52**, 1–11 (2013)
18. Formica, G., Taló, M., Lacarbonara, W.: Nonlinear modeling of carbon nanotube composites dissipation due to interfacial stick-slip. Int. J. Plast **53**, 148–163 (2014)
19. Taló M., Krause B., Pionteck J., Lanzara G., Lacarbonara W.: An updated micromechanical model based on morphological characterization of carbon nanotube nanocomposites. Compos. Part B: Eng. **115**, 70–78 (2016)

20. Formica, G., Lacarbonara, W.: Three-dimensional modeling of interfacial stick-slip in carbon nanotube nanocomposites. Int. J. Plast **53**, 205–218 (2017)
21. Cardou, A., Jolicoeur, C.: Mechanical models of helical strands. Appl. Mech. Rev. **50**(1), 1–14 (1997)
22. Carboni, B., Lacarbonara, W.: Nonlinear dynamic characterization of a new hysteretic device: experiments and computations. Nonlinear Dyn. **83**(1–2), 23–39 (2016)
23. ABAQUS 6.7: Users manual. Inc. and Dassault Systèmes (2007)
24. Carboni, B., Lacarbonara, W.: Nonlinear vibration absorber with pinched hysteresis: theory and experiments. J. Eng. Mech. **142**(5), 04016023 (2016)
25. Storn, R., Price, K.: Differential evolution-a simple and efficient heuristic for global optimization over continuous space. J. Global Optim. **11**(4), 341–359 (1997)
26. Brewick, P.T., Masri, S.F., Carboni, B., Lacarbonara, W.: Data-based nonlinear identification and constitutive modeling of hysteresis in NiTiNOL and steel strands. J. Eng. Mech. **142**, 04016107 (2016)
27. Bouc, R.: Forced vibration of mechanical systems with hysteresis. In: Proceedings of the Fourth Conference on Non-linear Oscillation, Prague, Czechoslovakia (1967)
28. Wen, Y.K.: Method for random vibration of hysteretic systems. J. Eng. Mech. **102**(2), 249–263 (1967)
29. Carboni, B., Lacarbonara, W., Mancini, C.: Hysteretic beam model for steel wire ropes hysteresis identification. Struct. Nonlinear Dyn. Diagn. 261–282 (2015)
30. Den Hartog, J.P., Ormondroyd, J.: Theory of the dynamic vibration absorber. J. Appl. Mech. **50**(4), 11–22 (1928)
31. Den Hartog, J.P.: Mechanical Vibrations. Dover Publications (2013)
32. Randall, S.E., Halsted, D.M., Taylor, D.L.: Optimum vibration absorbers for linear damped systems. J. Mech. Des. **103**(4), 908–913 (1981)
33. Warburton, G.B.: Optimum absorber parameters for various combinations of response and excitation parameters. Earthq. Eng. Struct. Dyn. **10**(3), 381–401 (1982)
34. Tsai, H.C., Lin, G.C.: Optimum tuned-mass dampers for minimizing steady-state response of support-excited and damped systems. Earthq. Eng. Struct. Dyn. **22**(11), 957–973 (1993)
35. Ioi, T., Ikeda, K.: On the dynamic vibration damped absorber of the vibration system. Bull. JSME **21**(151), 64–71 (1978)
36. Lanzara, G.: Realization and analysis of carbon nanotube carpet microstructures, PhD Thesis in Structural Engineering, Sapienza University of Rome (2006)
37. Lanzara, G.: Carbon nanotube micropillars for strain sensing, Paper No. DETC2015-47783, ASME 2015 International Design Engineering Technical Conferences and Computers and Information in Engineering Conference, Boston; 2–5 August 2015, pp. V004T09A027, 7 pages (2015)
38. Lanzara, G., Chang, F.K.: Design and characterization of a carbon-nanotube-reinforced adhesive coating for piezoelectric ceramic discs. Smart Mater. Struct. **18** (2009)
39. Johnston, I.D., McCluskey, D.K., Tan, C.K.L., Tracey, M.C.: Mechanical characterization of bulk Sylgard 184 for microfluidics and microengineering. J. Micromech. Microeng. **24**(7), 035017 (2014)
40. Kim, T.K., Kim, J.K., Jeong, O.C.: Measurement of nonlinear mechanical properties of PDMS elastomer. Microelectron. Eng. **88**, 1982–1985 (2011)
41. Liu, M., Sun, J., Sun, Y., Bock, C., Chen, Q.: Thickness-dependent mechanical properties of polydimethylsiloxane membranes. J. Micromech. Microeng. **19**, 035028 (2009)
42. Samali, B., Attard, M.M., Song, C.: From Materials to Structures: Advancement Through Innovation. CRC Press, Boca Raton (2012)
43. Ogasawara, T., Tsuda, T., Takeda, N.: Stress-strain behavior of multi-walled carbon nanotube/PEEK composites. Compos. Sci. Technol. **71**, 73–78 (2011)
44. Suhr, J., Koratkar, N.A., Keblinski, P., Ajayan, P.: Viscoelasticity in carbon nanotube composites. Nat. Mater. **4**, 134–137 (2005)
45. Dwaikat, M.M.S., Spitas, C., Spitas, V.: A model for elastic hysteresis of unidirectional fibrous nano composites incorporating stick-slip. Mater. Sci. Eng., A **530**, 349–356 (2011)

46. Ma, P.C., Siddiqui, N.A., Marom, G., Kim, J.K.: Dispersion and functionalization of carbon nanotubes for polymer-based nanocomposites: a review. Compos. A **41**, 1345–1367 (2010)
47. Bose, S., Khare, R.A., Moldenaers, P.: Assessing the strengths and weaknesses of various types of pre-treatments of carbon nanotubes on the properties of polymer/carbon nanotubes composites: a critical review. Polymer **51**, 975–993 (2010)
48. Rohini, R., Katti, P., Bose, S.: Tailoring the interface in graphene/thermoset polymer composites: a critical review. Polymer **70**, 17–34 (2015)
49. Gardea, F., Glaz, B., Riddick, J., Lagoudas, D.C., Naraghi, M.: Energy dissipation due to interfacial slip in nanocomposites reinforced with aligned carbon nanotubes. ACS Appl. Mater. Interfaces **7**, 9725–9735 (2015)
50. Li, C., Chou, T.W.: Multiscale modeling of carbon nanotube reinforced polymer composites. J. Nanosci. Nanotechnol. **3**, 423–430 (2003)
51. Huang, Y., Tangpong, X.W.: A distributed friction model for energy dissipation in carbon nanotube-based composites. Commun. Nonlinear Sci. Numer. Simul. **15**, 4171–4180 (2010)
52. Lin, R.M., Lu, C.: Modeling of interfacial friction damping of carbon nanotube-based nanocomposites. Mech. Syst. Signal Process. **24**, 2996–3012 (2010)
53. Spitas, V., Spitas, C., Michelis, P.: Modeling of the elastic damping response of a carbon nanotube-polymer nanocomposite in the stress-strain domain using an elastic energy release approach based on stick-slip. Mech. Adv. Mater. Struct. **20**, 791–800 (2013)
54. Triantafyllou, S.P., Chatzi, E.N.: A hysteretic multiscale formulation for nonlinear dynamic analysis of composite materials. Comput. Mech. **54**, 763–787 (2014)

Chapter 14
Three Ways of Treating a Linear Delay Differential Equation

Si Mohamed Sah and Richard H. Rand

Abstract This work concerns the occurrence of Hopf bifurcations in delay differential equations (DDE). Such bifurcations are associated with the occurrence of pure imaginary characteristic roots in a linearized DDE. In this work we seek the exact analytical conditions for pure imaginary roots, and we compare them with the approximate conditions obtained by using the two variable expansion perturbation method. This method characteristically gives rise to a "slow flow" which contains delayed variables. In analyzing such approximate slow flows, we compare the exact treatment of the slow flow with a further approximation based on replacing the delayed variables in the slow flow with non-delayed variables, thereby reducing the DDE slow flow to an ODE. By comparing these three approaches we are able to assess the accuracy of making the various approximations. We apply this comparison to a linear harmonic oscillator with delayed self-feedback.

Keywords Slow flow · Delay · Hopf bifurcation

14.1 Introduction

It is known that ordinary differential equations (ODEs) are used as models to better understand phenomenon occurring in biology, physics and engineering. Although these models present a good approximation of the observed phenomenon, in many cases they fail to capture the rich dynamics observed in natural or technological systems. Another approach which has gained interest in modeling systems is the inclusion of time delay terms in the differential equations resulting in delay-differential

S.M. Sah (✉)
Nanostructure Physics, KTH Royal Institute of Technology Stockholm, Stockholm, Sweden
e-mail: smsah@kth.se

R.H. Rand
Department of Mathematics, Department of Mechanical & Aerospace Engineering, Cornell University, Ithaca, NY 14853, USA
e-mail: rhr2@cornell.edu

M. Belhaq (ed.), *Recent Trends in Applied Nonlinear Mechanics and Physics*, Springer Proceedings in Physics 199, https://doi.org/10.1007/978-3-319-63937-6_14

equations (DDEs). DDE's have found application in many systems, including rotating machine tool vibrations [7], gene copying dynamics [14], laser dynamics [16] and many other examples.

Despite their simple appearance, DDEs have several features that make their analysis a challenging task. For example, when investigating a DDE by use of a perturbation method, one is often confronted with a slow flow which contains delay terms. It is often argued that since the parameter of perturbation, call it ε, is small, $\varepsilon << 1$, the delay terms which appear in the slow flow may be replaced by the same terms without delay, see e.g. [1, 5, 6, 8, 9, 13, 15, 16]. The purpose of the present paper is to compare the exact Hopf bifurcation curves to the approximate curves obtained by analyzing the slow flow. In particular, we compare the exact treatment of the approximate slow flow with a treatment involving a further approximation based on replacing the slow flow delay terms with terms without delay. We consider the case of a linear delay differential equation and look for the smallest delay T such that the following system has pure imaginary eigenvalues, a setup for a Hopf, depending on the nonlinear terms (omitted here):

$$x'' + x = \varepsilon\, k\, x_d, \qquad \text{where} \qquad x_d = x(t - T) \tag{14.1}$$

To this aim we adopt three methods. The first method consists of solving for the exact solution of the characteristic equation. In the second and third methods, we use a perturbation method, the two variables expansion method, to produce a slow flow. In the second method we keep the delayed variables in the slow flow, while in the third method we replace the delayed variables by non-delayed variables.

14.2 First Method

For the first method we adopt an exact treatment of (14.1) without assuming ε is small. To begin we assume a solution to (14.1) in the form

$$x = \exp(rt) \tag{14.2}$$

Substituting (14.2) into (14.1) yields

$$r^2 + 1 - k\,\varepsilon \exp(-rT) = 0 \tag{14.3}$$

It is known that for a Hopf bifurcation to occur the real parts of a pair of eigenvalues of the characteristic equation, i.e. r's of (14.3), must cross the imaginary axis leading to a changing of sign of this pair of eigenvalues (Rand [10], Strogatz [12]). In other words the origin, which is an equilibrium point for (14.1), changes stability from source to sink or vice-versa. Therefore to find the critical delay T_{cr} causing a Hopf bifurcation, we set $r = i\omega$ giving

$$1 - \omega^2 - k\,\varepsilon \cos \omega t = 0, \qquad \sin \omega t = 0 \tag{14.4}$$

Solving the second equation in (14.4), we obtain $\omega T_{cr} = n\pi, \quad n = 1, 2, 3, \ldots$. However since we are only interested in the smallest delay T causing Hopf bifurcation, we only consider the two solutions $\omega T_{cr} = \pi$ and 2π. Replacing these two solutions in the first equation in (14.4) and solving for ω and T we obtain:

$$\omega = \sqrt{1 + k\,\varepsilon} \tag{14.5}$$

$$T_{cr} = \frac{\pi}{\omega} = \frac{\pi}{\sqrt{1 + k\varepsilon}} \tag{14.6}$$

and

$$\omega = \sqrt{1 - k\,\varepsilon} \tag{14.7}$$

$$T_{cr} = \frac{2\pi}{\omega} = \frac{2\pi}{\sqrt{1 - k\varepsilon}} \tag{14.8}$$

Note that (14.6) and (14.8) are exact values for the delay T for which a Hopf bifurcation may occur. In the two next sections we consider the parameter ε in (14.1) to be small, i.e. $\varepsilon << 1$, and we use a perturbation method to derive a slow flow. We note that using the two variable expansion method gives the same slow flow as would be obtained by using the averaging method [11].

14.3 Second Method

The two variable method posits that the solution depends on two time variables, $x(\xi, \eta)$, where $\xi = t$ and $\eta = \varepsilon t$. Then we have

$$x_d = x(t - T) = x(\xi - T, \eta - \varepsilon T) \tag{14.9}$$

Dropping terms of $O(\varepsilon^2)$, (14.1) becomes

$$x_{\xi\xi} + 2\varepsilon x_{\xi\eta} + x = \varepsilon\, k\, x(\xi - T, \eta - \varepsilon T) \tag{14.10}$$

Expanding x in a power series in ε, $x = x_0 + \varepsilon x_1 + O(\varepsilon^2)$, and collecting terms, we obtain

$$Lx_0 \equiv x_{0\xi\xi} + x_0 = 0 \tag{14.11}$$

$$Lx_1 \equiv k\, x_0(\xi - T, \eta - \varepsilon T) - 2x_{0\xi\eta} \tag{14.12}$$

From (14.11) we have that

$$x_0(\xi, \eta) = A(\eta)\cos\xi + B(\eta)\sin\xi \tag{14.13}$$

In (14.12) we will need $x_0(\xi - T, \eta - \varepsilon T)$:

$$x_0(\xi - T, \eta - \varepsilon T) = A_d\cos(\xi - T) + B_d\sin(\xi - T) \tag{14.14}$$

where $A_d = A(\eta - \varepsilon T)$ and $B_d = B(\eta - \varepsilon T)$.

Substituting (14.13) and (14.14) into (14.12) and eliminating resonant terms gives the slow flow:

$$\frac{dA}{d\eta} = -\frac{k}{2}A_d\sin T - \frac{k}{2}B_d\cos T \tag{14.15}$$

$$\frac{dB}{d\eta} = -\frac{k}{2}B_d\sin T + \frac{k}{2}A_d\cos T \tag{14.16}$$

where $A_d = A(\eta - \varepsilon T)$ and $B_d = B(\eta - \varepsilon T)$. We set

$$A = a\exp(\lambda\eta), \quad B = b\exp(\lambda\eta), \quad A_d = a\exp(\lambda\eta - \varepsilon\lambda T), \quad B_d = b\exp(\lambda\eta - \varepsilon\lambda T) \tag{14.17}$$

where a and b are constants. This gives

$$\begin{bmatrix} -\lambda - \frac{k}{2}\exp(-\lambda\varepsilon T)\sin T & -\frac{k}{2}\exp(-\lambda\varepsilon T)\cos T \\ \frac{k}{2}\exp(-\lambda\varepsilon T)\cos T & -\lambda - \frac{k}{2}\exp(-\lambda\varepsilon T)\sin T \end{bmatrix}\begin{bmatrix} a \\ b \end{bmatrix} = \begin{bmatrix} 0 \\ 0 \end{bmatrix} \tag{14.18}$$

For a nontrivial solution (a, b) we require the determinant to vanish:

$$\left(-\lambda - \frac{k}{2}\exp(-\lambda\varepsilon T)\sin T\right)^2 + \frac{k^2}{4}\exp(-2\lambda\varepsilon T)\cos^2 T = 0 \tag{14.19}$$

We set $\lambda = i\omega$ for a Hopf bifurcation and use Euler's formula $\exp(-i\omega\varepsilon T) = \cos\omega\varepsilon T - i\sin\omega\varepsilon T$. Separating real and imaginary parts we obtain

$$4k^2\cos 2\varepsilon\omega T + 16k\omega\sin T\sin\varepsilon\omega T - 16\omega^2 = 0 \tag{14.20}$$

$$-4k^2\sin 2\varepsilon\omega T + 16k\omega\sin T\cos\varepsilon\omega T = 0 \tag{14.21}$$

At this stage we adopt the technique used in [11] to analytically solve for the pair (ω,T). Following [11] we obtain the exact solutions of (14.20)–(14.21), giving the delay for which Hopf bifurcation occurs

$$T_{cr_1} = \frac{\pi}{1 + \varepsilon\, k/2} \tag{14.22}$$

$$|\varepsilon\, k/2| < 1$$

$$T_{cr_2} = \frac{2\pi}{1 - \varepsilon\, k/2} \tag{14.23}$$

We note that the denominator of (14.22)–(14.23) are just the Taylor expansions to the first order of the exact frequency given by (14.5)–(14.7). In the next section we replace the delayed variables in (14.15)–(14.16), i.e. A_d and B_d, by the non-delayed variables A and B.

14.4 Third Method

The slow flow given by (14.15)–(14.16) is replaced by a slow flow with no delayed variables such that:

$$\frac{dA}{d\eta} = -\frac{k}{2} A \sin T - \frac{k}{2} B \cos T \tag{14.24}$$

$$\frac{dB}{d\eta} = -\frac{k}{2} B \sin T + \frac{k}{2} A \cos T \tag{14.25}$$

In order to find the critical delay we proceed as in the previous section. The corresponding characteristic equation has the form:

$$\lambda^2 + k\,\lambda\, \sin T + \frac{k^2}{4} = 0 \tag{14.26}$$

For a Hopf bifurcation, we require imaginary roots of the characteristic equation. This gives

$$k \sin T = 0 \tag{14.27}$$

Solving the above equation for the critical delay T we obtain:

$$T_{cr} = \pi \tag{14.28}$$

$$T_{cr} = 2\pi \tag{14.29}$$

Figure 14.1 shows a plot of the Hopfs in the $k - T$ parameter plane. From the figure we remark that the exact delay that is obtained from solving (14.4) agrees with the numerical Hopf bifurcation curves (blue) that is obtained by using the DDE-BIFTOOL continuation software [2–4]. The Hopf curves given by the second method offer a good approximation to the numerical Hopf curves, in particular for small values of the feedback magnitude k. However, the curves obtained from the third method do not agree with the numerical Hopf curves.

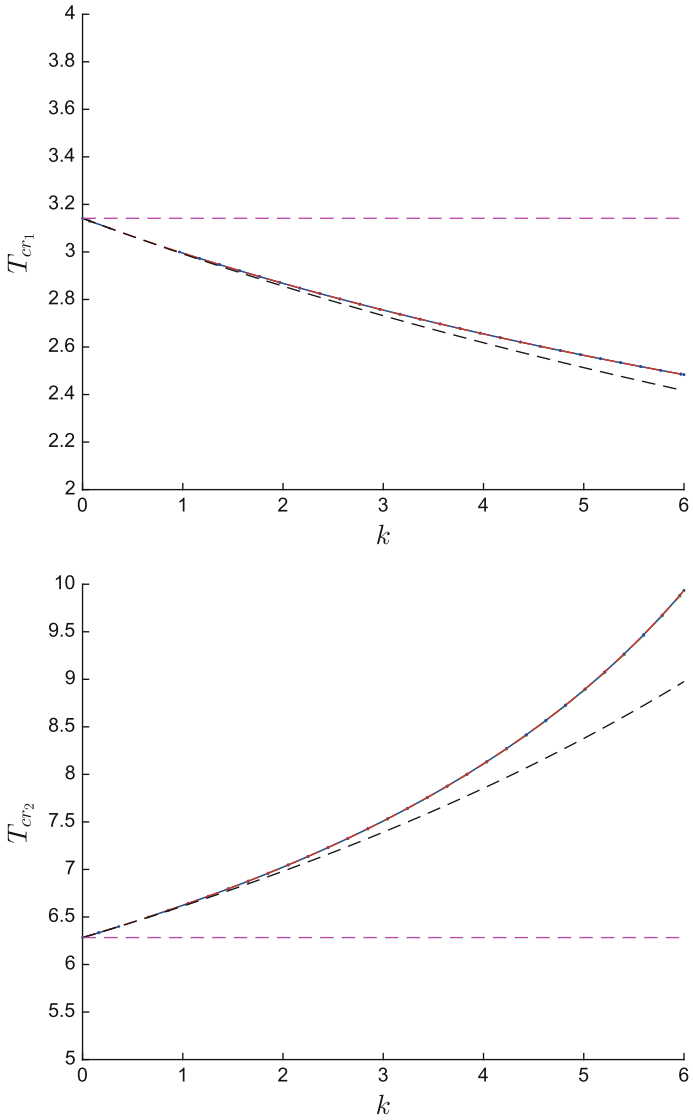

Fig. 14.1 Critical delay versus the feedback magnitude k. *Top*: *blue* (BIFTOOL), *red* (14.6), *black* (14.22), *magenta* (14.28). *Bottom*: *blue* (BIFTOOL), *red* (14.8), *black* (14.23), *magenta* (14.29). Parameter $\varepsilon = 0.1$

14.5 Conclusion

When a DDE with delayed self-feedack is treated using a perturbation method (such as the two variable expansion method, multiple scales, or averaging), the resulting slow flow typically involves delayed variables. In this work we compared the behavior of the resulting DDE slow flow with a related ODE slow flow obtained by replacing the delayed variables in the slow flow with non-delayed variables and comparing the resulting approximate critical delays causing Hopf bifurcation with the exact analytical Hopf curves. We studied a sample system based on the harmonic oscillator with delayed self-feedback, (14.1). We found that replacing the delayed variables in the slow flow by non-delayed variables fails to give a good approximation. However, keeping the delayed variables in the slow flow gives better results.

References

1. Atay, F.M.: Van der Pol's oscillator under delayed feedback. J. Sound Vib. **218**(2), 333–339 (1998)
2. Engelborghs, K., Luzyanina, T., Roose, D.: Numerical bifurcation analysis of delay differential equations using: DDE- BIFTOOL. ACM Trans. Math. Softw. **28**(1), 1–21 (2002)
3. Engelborghs, K., Luzyanina, T., Samaey, G.: DDE-BIFTOOL v. 2.00: a Matlab package for bifurcation analysis of delay differential equations. Technical Report TW-330, Dept. Comp. Sci., K.U. Leuven, Leuven, Belgium (2001)
4. Heckman, C.R.: An introduction to DDE-BIFTOOL is available as Appendix B of the doctoral thesis of Christoffer Heckman: asymptotic and numerical analysis of delay- coupled microbubble oscillators (Doctoral Thesis). Cornell University (2012)
5. Hu, H., Dowell, E.H., Virgin, L.N.: Resonances of a harmonically forced Duffing oscillator with time delay state feedback. Nonlinear Dyn. **15**, 311–327 (1998)
6. Ji, J.C., Leung, A.Y.T.: Resonances of a nonlinear SDOF system with two time-delays on linear feedback control. J. Sound Vib. **253**, 985–1000 (2002)
7. Kalmar-Nagy, T., Stepan, G., Moon, F.C.: Subcritical Hopf bifurcation in the delay equation model for machine tool vibrations. Nonlinear Dyn. **26**, 121–142 (2001)
8. Maccari, A.: The resonances of a parametrically excited van der Pol oscillator to a time delay state feedback. Nonlinear Dyn. **26**, 105–119 (2001)
9. Morrison, T.M., Rand, R.H.: 2:1 Resonance in the delayed nonlinear Mathieu equation. Nonlinear Dyn. **50**, 341–352 (2007)
10. Rand, R.H.: Lecture notes in nonlinear vibrations published on-line by the internet-first university press (2012). http://ecommons.library.cornell.edu/handle/1813/28989
11. Sah, S., Rand, R.: Delay terms in the slow flow. J. Appl. Nonlinear Dyn. **5**(4), 473–486 (2016)
12. Strogatz, S.H.: Nonlinear Dynamics and Chaos: With Applications to Physics, Biology, Chemistry, and Engineering. Addison-Wesley, Reading, Massachusetts (1994)
13. Suchorsky, M.K., Sah, S.M., Rand, R.H.: Using delay to quench undesirable vibrations. Nonlinear Dyn. **62**, 107–116 (2010)
14. Verdugo, A., Rand, R.: Hopf bifurcation in a dde model of gene expression. Commun. Nonlinear Sci. Numer. Simul. **13**, 235–242 (2008)
15. Wahi, P., Chatterjee, A.: Averaging oscillations with small fractional damping and delayed terms. Nonlinear Dyn. **38**, 3–22 (2004)
16. Wirkus, S., Rand, R.H.: The dynamics of two coupled van der Pol oscillators with delay coupling. Nonlinear Dyn. **30**, 205–221 (2002)

Chapter 15
Nonlinear Damping: From Viscous to Hysteretic Dampers

Mikhail E. Semenov, Andrey M. Solovyov, Peter A. Meleshenko and José M. Balthazar

Abstract This paper is dedicated to a brief discussion on the nonlinear damping. We present the particular results for linear and nonlinear viscous dampers, for fractional damper and for the hysteretic damper. As a main purpose we consider the mathematical model of damper with hysteretic properties on the basis of the Ishlinsky-Prandtl model. The numerical results for the observable characteristics such as the force transmission function and the "force-displacement" transmission function are obtained and analyzed both for the cases of the periodic affection as well as for the impulse affection (in the form of δ-function). The comparison of the efficiency of nonlinear viscous damper and hysteretic damper is also presented and discussed.

M.E. Semenov (✉)
Geophysical Survey of Russia Academy of Sciences,
Lenina av. 189, 249035 Obninsk, Russia
e-mail: mkl150@mail.ru

M.E. Semenov · A.M. Solovyov · P.A. Meleshenko
Digital Technologies Department, Voronezh State University,
Universitetskaya, st. 1, 394006 Voronezh, Russia

M.E. Semenov
Applied Mathematics and Mechanics Department, Voronezh State Technical University,
XXletiya Oktyabrya st. 84, 394006 Voronezh, Russia

P.A. Meleshenko
Communication Department, Zhukovsky–Gagarin Air Force Academy,
Starykh Bolshevikov st. 54 "A", 394064 Voronezh, Russia
e-mail: melechp@yandex.ru

J.M. Balthazar
Mechanical Engineering Division Research on Nonlinear Dynamics,
Chaos and Control, Aerospace Science and Technology Department,
Aeronautics Institute of Technology, Praça Mal al Eduardo Gomes 50,
Vila das Acácias, São José dos Campos, São Paulo 12228-900, Brazil

M. Belhaq (ed.), *Recent Trends in Applied Nonlinear Mechanics and Physics*,
Springer Proceedings in Physics 199, https://doi.org/10.1007/978-3-319-63937-6_15

15.1 Introduction

The dampers and damping processes have a long history and especially relevant (both from the fundamental and applied points of view) in the present days due to development of the modern impact-vibrational systems (see, e.g., [1]). The damper is a device used for damping the mechanical, electrical and other modes of vibration arising in the machines and mechanical systems during its operation. Damping is an important task that has a wide range of applications. In general the *damping* is a process whereby the energy is taken from the vibrating system and is being absorbed by the surroundings. The examples of damping include:

- internal forces of a spring;
- viscous force in a fluid;
- electromagnetic damping in galvanometers;
- shock absorber in a car;
- anti seismic damping devices in buildings etc.

In the same time it should be noted that the damping devices are widely used in modern avionics (damper of aero-elastic vibrations, which is the electronic system for automatic cancelation of short-aircraft vibrations that inevitably arise when the flight modes change).

Let us also list the types (relative to the physical nature of damping process) of damping devices, namely: Structural; Coulomb Friction; Elastomer; Active Drivers; Passive Hydraulic; Semi-Active Hydraulic; Adaptive Hydraulic etc.

In the case of oscillations of mechanical systems the model of linear viscous damping (which is based on the energy dissipation due to viscous friction) is widely used. However, this type of damping has a significant drawback, namely the low efficiency outside the region of resonance of the system. One way to solve this problem is to use a nonlinear viscous damper [3, 6, 11, 13, 14, 16] or a damper with hysteretic properties [7, 15] (here we should note the recent work [10] where the effects of nonlinear hysteretic damping on the post-critical behavior of the viscoelastic Beck?s beam are discussed). Here we should also note the interesting works dedicated to experiments with the hysteretic damping systems (see, e.g., [15] and related references, as well as the book [7]). The influence of nonlinear damping effects on the stability of oscillating systems are considered in [9] (see, also the related references). It should also be pointed out the exciting and interesting (generally, from the fundamental point of view) model of viscous damping which is based on the technique of fractional derivatives and can be called as a fractional damping [2, 8, 18, 21]. The interest to the fractional damping is connected with the fact that the systems with such a type of nonlinearity demonstrate the chaotic behavior [23]. Also the fractional damping can be considered as an effective model for the so-called viscoelastic materials that describe the properties of all the materials in the extremely natural way (because there are no pure elastic materials as well as there are no pure viscous materials; all the materials have both the viscous and elastic properties that can be observed at various motion conditions).

Main purpose of this work is to study the dynamics of a mechanical system under various external affections (forced oscillations) in the case of presence of a damping block. Especial interest in this case has a damper with the hysteretic properties. As a mathematical model of such a hysteretic damper we consider the Ishlinsky-Prandtl "converter" which is a type of continual hysterons and can be presented as a system of parallel connected nonlinear links such as "stops" (or hysterons) [5]. Here we should note that the mathematical models of various hysteretic system was considered in a number of works (see, e.g., [4, 12, 17, 22] and related references). However, in these works authors use the phenomenological models of hysteresis (Bouc-Wen model, Duhem model, etc.). In our paper we use the constructive model of hysteresis, namely, the operator technique of Krasnosel'skii-Pokrovskii (see [19, 20]) which has an exact physical meaning in comparison with the phenomenological models.

The paper is organized as follows. In Sect. 15.2 we consider some results for various kinds of damping processes. Also in this section we describe the physical model of the considered mechanical system (car in the cylinder with damping device). Sect. 15.3 is dedicated to hysteretic damping. Namely, in this section we consider the general model for description of hysteretic material based on the Ishlinsky-Prandtl model (such a model is realized by using the operator technique for hysteretic nonlinearities). Also in this section we describe the observable characteristics that allow to make a decision on the efficiency of the various kinds of dampers. In Sect. 15.4 we present the results of numerical simulations for the observable characteristics, namely the force transmission function as well as the "force-displacement" transmission function. Also we present the phase portraits of the considered system for the various kinds of dampers and the response of the considered system on the single pulse affection (in the form of δ-function). This results show the efficiency of the hysteretic damper in comparison with the linear and nonlinear viscous dampers. In the last Sect. 15.5 the main results are summarized.

15.2 Damping

In this section we describe the physical model of the considered mechanical system with the damping device. Also in this section we present some results (namely the equations of motion as well as some observable peculiarities) for various kinds of damping, namely the linear and nonlinear damping, and fractional damping.

15.2.1 Physical System

Let us consider a mechanical system under external affection and in the presence of the damping part $f_d(t)$ as is shown in Fig. 15.1. The system is presented as a cylinder with mass M under external affection $f(t)$ of harmonic nature. In the cylinder there

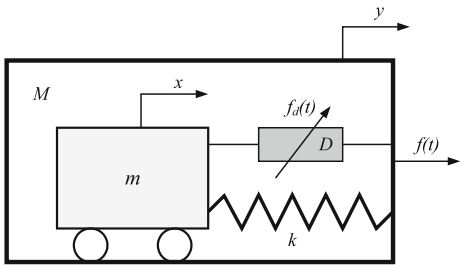

Fig. 15.1 The considered physical system

is a car of mass m (moving without friction in the horizontal plane) connected to the border by a spring with stiffness k. For simplicity we assume that the system is one-dimensional.

Suppose that the affection force $f(t)$ is described by the following relation:

$$f(t) = Y\omega^2 \sin(\omega t), \tag{15.1}$$

where $Y\omega^2$ is an amplitude and ω is a frequency of the affection force.

The equation of motion for considered system is

$$\begin{cases} M\ddot{y} + kz + f_d(t) = f(t), \\ m\ddot{x} - kz - f_d(t) = 0, \\ f(t) = Y\omega^2 \sin(\omega t),\ z(t) = y(t) - x(t). \end{cases} \tag{15.2}$$

Here overdot determines the time derivative and $z(t)$ is a relative displacement.

15.2.2 Linear and Nonlinear Viscous Damping

Let us consider the case of viscous damping. In general case the viscous friction can be described as follows:

$$f_d(t) = c(1 + z(t))^n \dot{z},\ n \geqslant 0, \tag{15.3}$$

where c is a damping coefficient. In the case $n = 0$ we have a linear viscous friction. For $n > 0$ the nonlinear viscous friction takes place [11, 13].

The equation of motion for relative displacement $z(t)$ becomes

$$\ddot{z}(t) + \frac{M+m}{Mm}\left\{c[1 + z(t)]^n \dot{z}(t) + kz(t)\right\} = \frac{Y}{M}\omega^2 \sin(\omega t). \tag{15.4}$$

It is more suitable to introduce the dimensionless variables

$$\Omega = \frac{\omega}{\omega_0},\ \mu = \frac{mM}{m+M},\ A = \frac{Y}{M},\ \tau = \omega_0 t,$$

$$\omega_0 = \sqrt{\frac{k}{\mu}},\ \zeta = \frac{c}{2\omega_0 \mu},\ u = z.$$

After such notations the final equation of motion has the form:

$$\frac{\mathrm{d}^2 u}{\mathrm{d}\tau^2} + 2\zeta(1+u)^n \frac{\mathrm{d}u}{\mathrm{d}\tau} + u = A\Omega^2 \sin(\Omega\tau). \tag{15.5}$$

15.2.3 Fractional Damping

Fractional stiffness and damping is appearing in different contexts in any systems with memory and hysteretic properties (the so-called viscoelastic materials). Such damping is defined by a fractional derivative in contrary to classical viscous damping term with the first order derivative. As the memory of the dynamical system induces extra degree of freedom for the phase space the standard methods of dynamical response analysis and system identification, which relies on the knowledge of system dimensionality cannot be used.

Let us be more specific. The most typical formulation of the problem is to use the fractional derivative term in place of the viscous damper term in the usual damped oscillation. Denoting the amount of the shrinkage of the body under compression by $x(t)$, the restoring force is proportional to $x(t)$. In terms of Fourier transform, the term corresponds to a real coefficient. On the other hand, the damping force due to viscous damper is proportional to the velocity dx/dt, which corresponds to an imaginary coefficient in the Fourier transform. The viscoelastic damping is assumed to be proportional to its fractional derivative $\mathrm{d}^\nu x/\mathrm{d}t^\nu$, $\nu \in R$, $\nu > 0$. Its Fourier transform is proportional to $(i\omega)^\nu$, which has both a real part and an imaginary part, thereby accounting for elasticity and viscousity by a single term.

Let us recall some mathematical definitions. The Riemann–Liouville *fractional integral* of $\chi(t)$(t) is defined by

$$D^{-\mu}\chi(t) = \frac{1}{\Gamma(\mu)} \int_0^t (t-\tau)^{\mu-1} \chi(\tau)\mathrm{d}\tau,\ \Re\mu > 0,$$

where

$$\Gamma(z) = \int_0^\infty t^{z-1} e^{-t} \mathrm{d}t$$

is the standard Euler gamma function.

The Riemann–Liouville *fractional derivative* of $\chi(t)$ is defined by

$$D^\nu \chi(t) = D^n D^{-n+\nu} \chi(t), \ n = \lceil \nu \rceil, \ \nu \neq n,$$

where $D^n \chi(t) = \mathrm{d}^n \chi(t)/\mathrm{d}t^n$ is the usual n-th derivative.

In this way the term $\mathrm{d}u/\mathrm{d}\tau$ in (15.5) should be replaced by the term $D^\nu u(\tau) \equiv \mathrm{d}^\nu u/\mathrm{d}\tau^\nu$.

The solution of such a fractional differential equations will describe the oscillation with viscoelastic damping. This allows us to study the behavior of the solution precisely using the properties of fractional derivatives. In particular, the asymptotic power-law decay is determined by the lowest order derivative $D^{1/n} x(t)$. On the other hand, the initial decrease in the velocity $Dx(t)$ is determined by the therm $D^{2-1/n} x(t)$.

The asymptotic power law decay indicates the lack of characteristic scale, implying fractal structure (this means that the system with fractional damping can be considered as a system with chaotic behavior and has both the fundamental and applied interests). In other words the model with fractional derivative term might well be considered as an effective theory of oscillations with viscoelastic damping.

15.3 Hysteretic Damping

15.3.1 Hysteretic Material

The materials that are used for hysteretic dampers in general are polymers (synthetic rubber). The composition of such materials is chosen appropriately to provide the high damping properties in a specific range of frequencies and temperatures. When the material is damped the energy dissipation occurs within the material itself. Such an effect is caused by friction between the inner layers that are "flow" when the damping occurs. In the case when such a structure is under damping vibrations the hysteresis loop appears in the "stress-strain". The area of the loop determines the energy loss (per unit volume of the body) in one cycle due to damping.

Let us briefly consider a mathematical model of hysteresis (based on the operator technique). The carrier of hysteretic nonlinearities is a converter W with scalar input $u(t)$ and outputs $x(t)$. The state of this converter is a pair $\{u, x\}$, i.e., an input-output pair. Let the set of possible states of the converter W is a strip $\Omega = \Omega(W)$ which is placed between the two horizontal lines Φ_l and Φ_r, as is shown in Fig. 15.2.

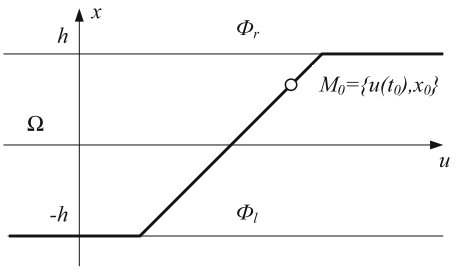

Fig. 15.2 Action of hysteron-nonlinearity

If the input $u(t)$ $(t \geqslant t_0)$ is continuous and monotone then the output can be defined as:

$$x(t) = W[t_0, x_0]u(t) \; (t \geqslant t0) \tag{15.6}$$

so that the variable state $\{u(t), x(t)\}$ is a point in the broken line as is shown in Fig. 15.2 by thick line; this broken line (passing through the initial state $M_0 = \{u(t_0), x_0\}$ and the ends on the lines Φ_l and Φ_r) consists of segment with slope 1 and two horizontal half-lines. In other words, when the input is monotonic the output is determined by the equation:

$$x(t) = \begin{cases} \min\{h, u(t) - u(t_0) + x(t_0)\}, u(t) \text{ nondecreasing}, \\ \max\{-h, u(t) - u(t_0) + x(t_0)\}, u(t) \text{ nonincreasing}. \end{cases} \tag{15.7}$$

To determine the output (15.6) for piecewise monotonic continuous inputs we can use the semigroup identity

$$W[t_0, x_0]u(t) = W[t_1, W[t_0, x_0]u(t_1)]u(t) \; (t_0 \leqslant t_1 \leqslant t). \tag{15.8}$$

The described converter is called as a "stop" or a hysteron. With the special limit construction such a converter can be defined on all the monotonic inputs [5].

In the most common models of elastic-plastic fibers their states are completely determined by the variables of deformation u and stress x. The parameter h in this case is called as the yield strength of the material. Such fibers can be considered as converters with an input in the form of deformation and an output in the form of strain. In the Prandtl model the strain is determined by the deformation in the same manner as in hysteron-nonlinearity, but the trajectories of possible states between the boundary horizontal lines have the slope E which differs from 1 (for small deformations the fiber can be considered as an elastic material with the elastic modulus E).

Let us consider the inverter W which can be presented in the form of a simple flow diagram (without feedback) based on the finite number of hysterons $W^1, \ldots, W^N$ and elementary functional units (as is shown in Fig. 15.3). Usually such converters W are nondeterministic. Their condition can be described (instead of the input-output description) by the set $\{u, z_1, \ldots, z_N\} \in R^{N-1}$, where u is the converter's input and z_j is an output of hysteron W^j in the flow diagram.

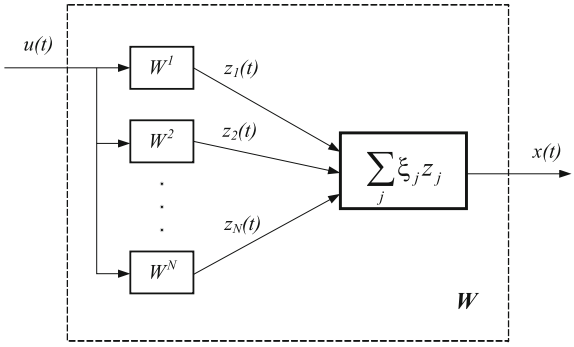

Fig. 15.3 Parallel connection of hysterons

Let us suppose that the hysterons $W^1, \ldots, W^N$ with areas of permissible states $\Omega(W^1), \ldots, \Omega(W^N)$ are determined by the input-output relations

$$z_j(t) = W^j[t_0, z_j(t_0)]u(t)\ (j = 1, \ldots, N). \tag{15.9}$$

Let

$$\Omega(W) = \{\{u, z_1, \ldots, z_N\} : \{u, z_j\} \in \Omega(W^j),\ u \in R^1\}. \tag{15.10}$$

Parallel connection of hysterons W^j with weights ξ_j we call the converter W with an area of permissible states (15.10) such that for every initial state

$$q(t_0) = \{u_0, z_0\} = \{u(t_0), z_1(t_0), \ldots, z_N(t_0)\} \in \Omega(W) \subset R^{N+1} \tag{15.11}$$

all the continuous scalar inputs $u(t)$ $(t \geqslant t_0)$ that satisfy the condition $u(t_0) = u_0$ are allowed. The output is determined by the relation

$$x(t) = W[t_0, z_0]u(t) = \sum_{j=1}^{N} \xi_j W^j[t_0, z_j(t_0)]u(t),\ (t \geqslant t_0). \tag{15.12}$$

The considered converter W is called as Ishlinsky-Prandtl material [6]. Of course the "classical" Ishlinsky-Prandtl converter is determined as a continuos system (sum should be replaced by an integral). However in our numerical simulations it is more appropriate to use the discrete analog of the Ishlinsky-Prandtl converter (15.12). In this way in the following consideration we will call the converter (15.12) as an Ishlinsky-Prandtl converter.

As an example we consider the reaction of the Ishlinsky-Prandtl material on a sinusoidal impact. We use the converter W with the following parameters: $E = 1$, $W^j[t_0, z_j(t_0)] = 0$, $\xi_j = 1$, $W^j : h = \{-j, j\}$, $j = 1, \ldots, 10$ and the input in the form $u(t) = 12 \sin(t)$. "Stress-strain" diagram of such a converter is shown in Fig. 15.4.

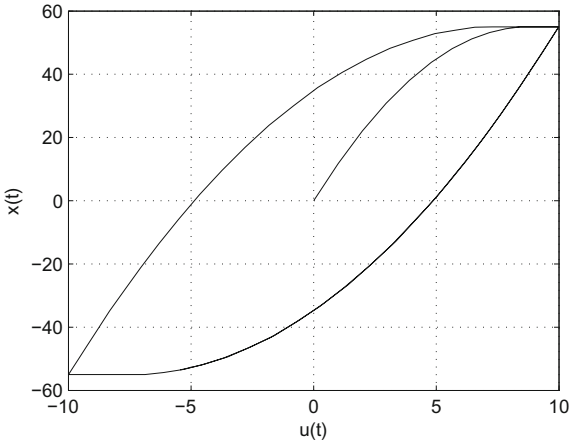

Fig. 15.4 "Stress-strain" diagram for Ishlinsky-Prandtl material

15.3.2 Hysteretic Damping

Now we consider the hysteretic damper. In this case (using the notations introduced above) the damping force can be presented as:

$$f_d(\tau) = W[\tau, z_j(\tau)]u, \ j = \overline{1, N}, \tag{15.13}$$

where W is an Ishlinsky-Prandtl operator which is determined by the relation (15.12).

In this case the equation of motion for the considered system becomes:

$$\frac{\mathrm{d}^2 u}{\mathrm{d}\tau^2} + \alpha W[\tau, z_j(\tau)]u + u = A\Omega^2 \sin(\Omega\tau), \ j = \overline{1, N}, \tag{15.14}$$

where $\alpha = S/k$ and S is an area of damping material's section, k is a spring stiffness.

15.3.3 Main Characteristics

Let us consider the main characteristics reflecting the efficiency of the damper in the resonance system and beyond. Such characteristics are force transmission function and "force-displacement" transmission function.

The *force transmission function* is determined by the ratio of the force applied to the cylinder M and the force applied to the car m (Fig. 15.1). This function reflects the efficiency of suppression of the external affection by the force transmission from an external source to the load. This characteristic is expressed as follows:

$$T_{ff} = \frac{1}{Y\omega^2} \max \left| m\omega_0^2 \frac{\mathrm{d}^2 x}{\mathrm{d}\tau^2} \right|. \tag{15.15}$$

In the case of viscous damper, using the (15.4) and (15.5) we can express the characteristic T_{ff} through the variable u, namely:

$$T_{ff} = \max \left| \frac{m}{(m+M)A\Omega^2} \left[A\Omega^2 \sin(\Omega\tau) - \ddot{u} \right] \right|. \tag{15.16}$$

The *"force-displacement" transmission function* is determined by the relation of the motion of car m relative to the cylinder M and the force applied to the cylinder. This quantity reflects the efficiency of vibration absorption by the ability of the damper to reduce the relative motion of the car under influence of external forces. This characteristic is expressed as

$$T_{fd} = \frac{\max |x(\tau)|}{Y\omega^2}. \tag{15.17}$$

As previously, in the case of viscous damping, using the (15.4) and (15.5) we can express the T_{fd} function in the following form:

$$T_{fd} = \max \left| \frac{A \sin(\Omega\tau) + u}{(m+M)A\Omega^2\omega_0^2} \right|. \tag{15.18}$$

During the following simulations we use these quantities for comparison of the linear viscous, nonlinear viscous and hysteretic dampers.

15.4 Numerical Results

15.4.1 Difference Scheme

The dynamics of the considered system can be simulated using the explicit difference scheme applied to (15.5) and (15.14). Finite-difference equations for viscous damper is:

$$\frac{u_{i+2} - 2u_{i+1} + u_i}{h_\tau^2} + 2\zeta(1 + u_{i+1})^n \frac{u_{i+1} - u_i}{h_\tau} + u_{i+1} = A\Omega^2 \sin(\Omega i h_\tau), \tag{15.19}$$

and for hysteretic damper is:

$$\frac{u_{i+2} - 2u_{i+1} + u_i}{h_\tau^2} + \alpha W[ih_\tau, z_j(ih_\tau)]\varphi_j(t)\Big|_{t=1} + u_{i+1} = A\Omega^2 \sin(\Omega i h_\tau), \tag{15.20}$$

where

$$\varphi_j(t) = (1-t)u_i + tu_{i+1}.$$

Here $i = \overline{0, T}$, $j = \overline{1, N}$, h_τ is a step of a grid by τ axis, N is a number of the Ishlinsky-Prandtl hysterons, T is a time period. Here it should be noted, that the basic properties of the Ishlinsky-Prandtl converter are such that it is not sensitive to behavior of the input state if the last one is monotonic.

The explicit solutions for the viscous damper and for hysteretic damper are:

$$u_{i+2} = A\Omega^2 h_\tau^2 \sin(\Omega i h_\tau) - 2\zeta h_\tau (1+u_{i+1})^n (u_{i+1} - u_i) - h_\tau^2 u_{i+1} + 2u_{i+1} - u_i, \tag{15.21}$$

$$u_{i+2} = A\Omega^2 h_\tau^2 \sin(\Omega i h_\tau) - \alpha h_\tau^2 W[ih_\tau, z_j(ih_\tau)]\varphi_j(t)\Big|_{t=1} - h_\tau^2 u_{i+1} + 2u_{i+1} - u_i, \tag{15.22}$$

respectively.

15.4.2 Simulation Results

We make the numerical simulations using the explicit results (15.21) and (15.22). In order to compare the viscous damper and hysteretic damper we present the numerical results for two characteristics of the system, namely, the force transmission function and "force-displacement" transmission function. For the nonlinear viscous damper we use the following set $n = \{0, 2, 4\}$.

For the hysteretic damper we use the Ishlinsky-Prandtl material (which corresponds to rubber) with the parameters $E = 10000$, $W^j[t_0, z_j(t_0)] = 0$, $\xi_j = 1$, W^j: $h = \{-j, j\}$, $j = 1, \ldots, 50$ (with a step 0.1), $\alpha = 0,0001$.

The characteristics of the mechanical system (per dimensionless units): $M = 1$, $m = 1$, $\zeta = 0.8$, $\omega_0 = 10$; the external affection with parameters $A = 1$, $\omega = 0, \ldots, 30$ (with a step 0.2); parameters of the difference scheme: $h_\tau = 0.0167$, $T = 10000$.

The simulation results are shown in Figs. 15.5 and 15.6. As it can be seen from these figures the linear viscous damper (dark blue curve $n = 0$) has a high efficiency in the resonance region of the system, however outside the resonance region the damping properties sharply decrease. At the same time the nonlinear viscous damper (green $n = 2$ and red $n = 4$ curves) has a wide range of effective use, but loses in efficiency to linear damper in the resonance region of the system.

The hysteretic damper (light blue curve) based on Ishlinsky-Prandtl material has a high efficiency both in the resonance region and beyond. The disadvantage of the hysteretic damper is in decreasing of the ability to reduce the relative movement of car under external forces outside the resonance region of the system.

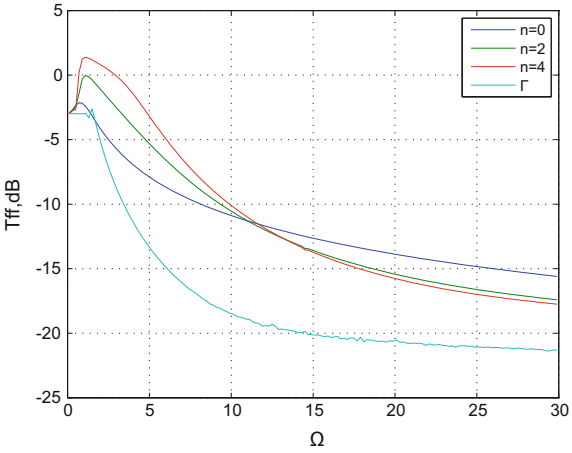

Fig. 15.5 Force transmission function

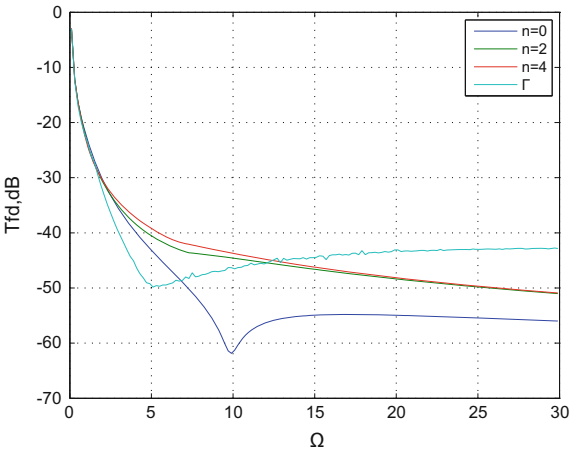

Fig. 15.6 "Force-displacement" transmission function

Let us consider also the phase portraits for the system both for the cases of viscous damper and for hysteretic damper. As the origin of the phase plane we use the instantaneous values of the car's coordinate inside the cylinder $x(\tau)$ and its relative speed $\dot{x}(\tau)$. For the case of viscous damper (for the hysteretic damper we can use the numerical solutions only), using the (15.4) and (15.5) we can write (taking into account the general system of (15.2) together with the corresponding notations):

$$x(\tau) = -\left[A\sin\left(\Omega\tau\right) + u\right]\frac{M}{M+m}, \tag{15.23}$$

$$\dot{x}(\tau) = -\left[A\Omega\cos\left(\Omega\tau\right) + \dot{u}\right]\frac{M}{M+m}. \tag{15.24}$$

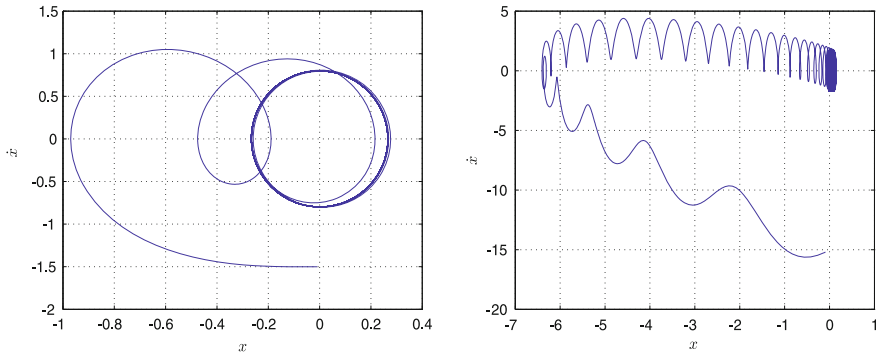

Fig. 15.7 Phase portraits of the system in the case of linear viscous damper ($n = 0$) at $\Omega = 3$ (*left panel*) and $\Omega = 30$ (*right panel*)

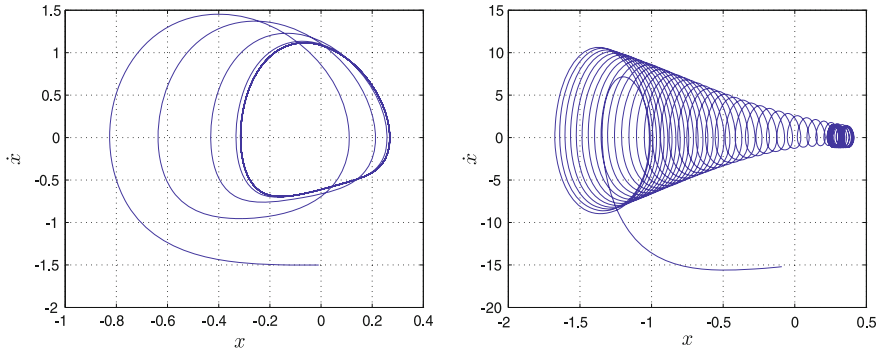

Fig. 15.8 Phase portraits of the system in the case of nonlinear viscous damper ($n = 2$) at $\Omega = 3$ (*left panel*) and $\Omega = 30$ (*right panel*)

The phase portraits of the system under consideration (with various kinds of dampers) are presented in the Figs. 15.7, 15.8, 15.9 and 15.10

Figures show the phase portraits of the system both in the case of viscous (linear and nonlinear) damping and the hysteretic damping. The left panels show the phase portraits in the resonance region, the right panels show the far frequency domain. From the figures it is clear that the hysteretic damper has a greater efficiency (in comparison with the linear and nonlinear viscous dampers) in the resonance region, and beyond. Previously, based on the analysis of transmission functions T_{ff} and T_{fd} we have made some conclusions on the efficiency of hysteretic damper in comparison with the viscous damper. In this way the presented phase portraits are proved our conclusions.

In the final step let us study the dynamics of the system under influence of a pulse affection (we consider the single pulse in the form of δ-function). In this case, the (15.4) for the viscous damper can be rewritten in the following form:

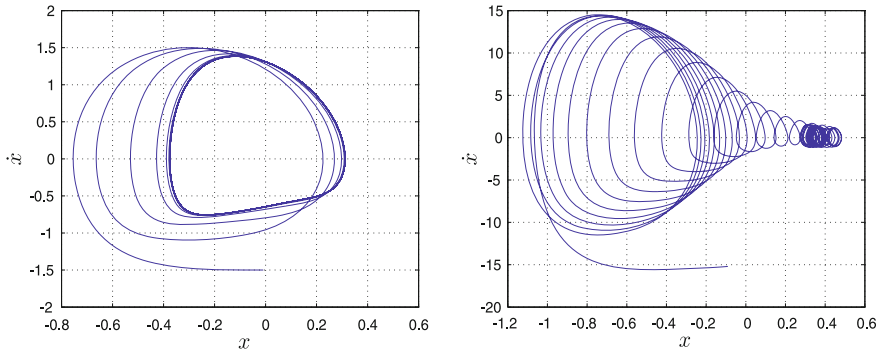

Fig. 15.9 Phase portraits of the system in the case of nonlinear viscous damper ($n = 4$) at $\Omega = 3$ (*left panel*) and $\Omega = 30$ (*right panel*)

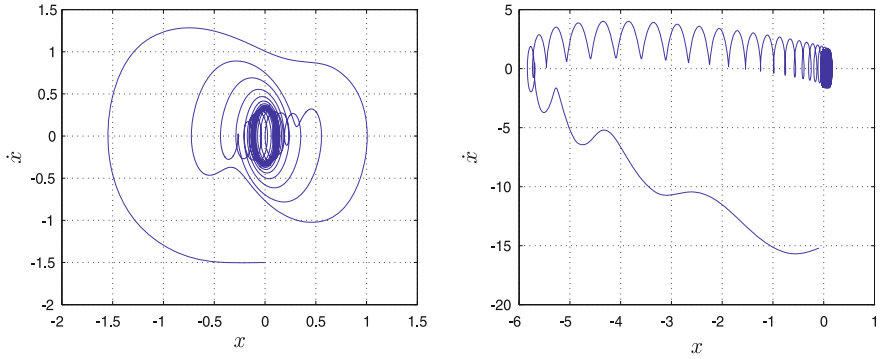

Fig. 15.10 Phase portraits of the system in the case of hysteretic damper at $\Omega = 3$ (*left panel*) and $\Omega = 30$ (*right panel*)

$$\ddot{z}(t) + 2\zeta\omega_0[1 + z(t)]^n \dot{z}(t) + \omega_0^2 z(t) = \delta(t). \tag{15.25}$$

For the hysteretic damper we have:

$$\ddot{z}(t) + \omega_0^2 \left(\alpha W[t, z_j(t)]z(t) + z(t)\right) = \delta(t). \tag{15.26}$$

Figure 15.11 shows the response of the system with viscous and hysteretic dampers to a single pulse.

As it can be seen from the figure, the energy dissipation in the case of hysteretic damper is faster than in the case of linear and nonlinear viscous damper. This fact shows (one more time) the efficiency of hysteretic damper in comparison with the viscous dampers.

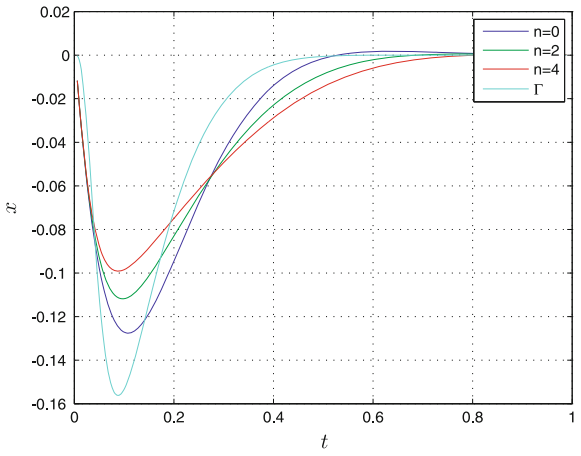

Fig. 15.11 The relative motion of a car $x(t)$ under single pulse affection for various kinds of damping

15.5 Conclusions

This work is considered the various kinds of damping processes that occur in the oscillations of real mechanical systems with damping blocks. Namely we consider the peculiarities of the linear and nonlinear viscous damping as well as the fractional damping, which can be considered as an effective model for the viscoelastic medium. Especial attention in this work we are paid to the hysteretic damper, which constructive model is based on the Ishlinsky-Prandtl model (this model is based on the operator technique for description of the hysteretic nonlinearities; in this way such a model has a great physical meaning in comparison with the phenomenological models based on the functional nonlinearities, such as Bouc-Wen model etc.). We presented the numerical results for the observable characteristics of the system under consideration such as force transmission function and "force-displacement" transmission function both for the cases of hysteretic and viscous (linear and nonlinear) dampers. The phase portraits of the system with various kinds of damping are plotted and analyzed. We have also considered the response of the system with various kinds of damping on the single pulse affection. The obtained results allow to compare the various types of viscous dampers (linear and nonlinear) and hysteretic damper. Based on the obtained numerical results we can formulate the following concluding notes:

- **Linear viscous damper** has a high efficiency in the resonance region of the system, however, outside the resonance region the damping properties sharply decrease.
- **Nonlinear viscous** damping has a wide range of effective use, but loses in efficiency to linear damper in the resonance region of the system.
- **Hysteretic damper** based on the Ishlinsky-Prandtl material **has a high efficiency both in the resonance region and beyond**. The disadvantage of the hysteretic damper is in decreasing of the ability to reduce the relative movement of the car under external forces outside the resonance region of the system.

Acknowledgements Part of the material of this chapter was presented in the Third International Conference on Structural Nonlinear Dynamics and Diagnosis (CSNDD'2016), Marrakech, Morocco, May 23–25, 2016. This work is supported by the RFBR grant 16-08-00312-a.

References

1. Babitsky, V., Krupenin, V.: Vibration of Strongly Nonlinear Discontinuous Systems. Springer, Berlin Heidelberg (2001)
2. Balthazar, J., Brasil, R., Felix, J., Tusset, A., Picirillo, V., Iluik, I., Rocha, R., Nabarrete, A., Oliveira, C.: Dynamics behaviour of an elastic non-ideal (NIS) portal frame, including fractional nonlinearities. J. Phys. Conf. Ser. **721**(1), 012, 004(1)–012, 004(12) (2016)
3. Felix, J., Balthazar, J., Brasil, R., Pontes, B.: On lugre friction model to mitigate nonideal vibrations. J. Comput. Nonlinear Dyn. **4**(3), 034, 503(1)–034, 503(5) (2009). https://doi.org/10.1115/1.3124783
4. Hassani, V., Tjahjowidodo, T., Nho Do, T.: A survey on hysteresis modeling, identification and control. Mech. Syst. Signal Process. **49**(1–2), 209–233 (2014). https://doi.org/10.1016/j.ymssp.2014.04.012
5. Krasnosel'skii, M.A., Pokrovskii, A.V.: Systems with Hysteresis. Springer, Berlin-Heidelberg-New York-Paris-Tokyo (1989)
6. Lang, Z., Billings, S., Yue, R., Li, J.: Output frequency response function of nonlinear Volterra systems. Automatica **43**(5), 805–816 (2007). https://doi.org/10.1016/j.automatica.2006.11.013
7. Latour, M.: Theoretical and Experimental Analysis of Dissipative Beam-to-Column Joints in Moment Resisting Steel Frames. Universal-Publishers (2011)
8. Leung, A., Guo, Z., Yang, H.: Fractional derivative and time delay damper characteristics in Duffing-van der Pol oscillators. Commun. Nonlinear Sci. Numer. Simul. **18**(10), 2900–2915 (2013). https://doi.org/10.1016/j.cnsns.2013.02.013
9. Luongo, A., D'Annibale, F.: Linear and Nonlinear Damping Effects on the Stability of the Ziegler Column, pp. 335–352. Springer International Publishing (2015)
10. Luongo, A.: DAnnibale, F.: Nonlinear hysteretic damping effects on the post-critical behaviour of the visco-elastic Becks beam. Mathematics and Mechanics of Solids (2016). https://doi.org/10.1177/1081286516632381
11. Lv, Q., Yao, Z.: Analysis of the effects of nonlinear viscous damping on vibration isolator. Nonlinear Dyn. **79**(4), 2325–2332 (2015). https://doi.org/10.1007/s11071-014-1814-2
12. Ma, Q., Cui, G., Jiao, T.: Neural-network-based adaptive tracking control for a class of pure-feedback stochastic nonlinear systems with backlash-like hysteresis. Neurocomputing **144**, 501–508 (2014). https://doi.org/10.1016/j.neucom.2014.04.024
13. Milovanovic, Z., Kovacic, I., Brennan, M.: On the displacement transmissibility of a base excited viscously damped nonlinear vibration isolator. J. Vibr. Acoust. **131**(5), 054, 502(1)–054, 502(7) (2009)
14. Peng, Z., Meng, G., Lang, Z., Zhang, W., Chu, F.: Study of the effects of cubic nonlinear damping on vibration isolations using harmonic balance method. Int. J. Non-Linear Mech. **47**(10), 1073–1080 (2012). https://doi.org/10.1016/j.ijnonlinmec.2011.09.013
15. Richards, R.: Comparison of linear, nonlinear, hysteretic, and probabilistic mr damper models. Master's thesis, Faculty of the Virginia Polytechnic Institute and State University (2007)
16. Rigaud, E., Perret-Liaudet, J.: Experiments and numerical results on non-linear vibrations of an impacting hertzian contact. Part 1: harmonic excitation. J. Sound Vib. **265**(2), 289–307 (2003). https://doi.org/10.1016/S0022-460X(02)01262-2
17. Rochdi, Y., Giri, F., Ikhouane, F., Chaoui, F.Z., Rodellar, J.: Parametric identification of nonlinear hysteretic systems. Nonlinear Dyn. **58**(1), 393–404 (2009). https://doi.org/10.1007/s11071-009-9487-y

18. Rüdinger, F.: Tuned mass damper with fractional derivative damping. Eng. Struct. **28**(13), 1774–1779 (2006). https://doi.org/10.1016/j.engstruct.2006.01.006
19. Semenov, M.E., Meleshenko, P.A., Solovyov, A.M., Semenov, A.M.: Hysteretic Nonlinearity in Inverted Pendulum Problem, pp. 463–506. Springer International Publishing (2015)
20. Semenov, M.E., Solovyov, A.M., Meleshenko, P.A.: Elastic inverted pendulum with backlash in suspension: stabilization problem. Nonlinear Dyn. **82**(1), 677–688 (2015). https://doi.org/10.1007/s11071-015-2186-y
21. Syta, A., Litak, G., Lenci, S., Scheffler, M.: Chaotic vibrations of the Duffing system with fractional damping. Chaos **24**(1), 013, 107(1)–013, 107(6) (2014). https://doi.org/10.1063/1.4861942
22. Tu, J.Y., Lin, P.Y., Cheng, T.Y.: Continuous hysteresis model using Duffing-like equation. Nonlinear Dyn. **80**(1), 1039–1049 (2015). https://doi.org/10.1007/s11071-015-1926-3
23. Tusset, A., Balthazar, J., Bassinello, D., Pontes, B., Felix, J.: Statements on chaos control designs, including a fractional order dynamical system, applied to a "MEMS" comb-drive actuator. Nonlinear Dyn. **69**(4), 1837–1857 (2012). https://doi.org/10.1007/s11071-012-0390-6

Index

M. Belhaq (ed.), *Recent Trends in Applied Nonlinear Mechanics and Physics*,
Springer Proceedings in Physics 199, https://doi.org/10.1007/978-3-319-63937-6